Nickel-based Electrocatalysts for Oxygen Evolution in Alkaline Water Electrolysis

Emily Cossar

uOttawa

L'Université canadienne
Canada's university

Thesis submitted

in partial fulfillment of the requirements for the

degree of Doctor of Philosophy in Chemical Engineering

Department of Chemical and Biological Engineering

Faculty of Engineering

University of Ottawa

Abstract

As atmospheric carbon dioxide (CO_2) levels continue to rise due to anthropogenic fossil fuel utilization, the need to develop and employ alternative energy carriers becomes more and more critical. In recent years, interest in hydrogen (H_2) has significantly increased as it is a clean and sustainable, alternative fuel, which can be both produced and utilized without greenhouse gas emissions; H_2 can be produced via water electrolysis powered by renewable energy sources (RES), such as wind and solar energy, then, H_2 can be utilized as a fuel in a hydrogen fuel cell, emitting only water as a by-product. Not only is H_2 a clean alternative fuel, but it also provides an economically feasible way of storing renewable energy so that RES supply can be better regulated according to demand.

Of the existing water electrolysis technologies, not many offer the ability to produce hydrogen both efficiently and at low cost. The alkaline environment of the more commonly employed traditional alkaline electrolyser allows for the use of non-noble metal electrocatalysts, as well as inexpensive cell materials. This process however suffers from an inefficient cell design. Conversely, the proton exchange membrane water electrolyser (PEMWE) utilizes a solid polymer electrolyte membrane, which allows for a compact, low resistance cell design. However, the harsh acidic environment of this device requires expensive platinum group metal (PGM) catalysts and expensive cell components. Anion exchange membrane water electrolysis (AEMWE) is a promising technology for low-cost, efficient H_2 production as it combines the compact cell design of the PEMWE with the favourable alkaline environment of the traditional alkaline electrolyser.

The electrochemical water splitting process is limited by the kinetically unfavourable oxygen evolution half-cell reaction (OER), which requires expensive rare catalysts such as iridium, to efficiently carry out the reaction. Nickel (Ni) is a promising inexpensive and abundant catalyst for the OER in alkaline media, due to its high activity and corrosion resistance. A significant increase in OER activity can be achieved by iron (Fe) incorporation into Ni catalysts. The addition of ceria (CeO_2), a mixed ionic-electronic conductor with favourable oxygen storage and release properties, can also have a positive effect on catalytic performance. While developing electrocatalysts for improved OER performance is important, evaluating the studied materials as anodes in practical AEMWE devices is imperative as it accounts for the efficiency of the catalysts in electrode layers formed using an anion exchange ionomer (AEI). An AEI is a solid polymer

electrolyte that serves as a binder for the particles as well as a hydroxide ion conductor in a catalytic layer of an AEMWE.

The main objectives of this thesis are to (*i*) develop highly active NiFe-based nanoparticle (NP) catalysts with and without CeO_2 for the promotion of the OER in AEMWE devices, and (*ii*) study the effects of commercial AEI type and amount on the efficiency of the produced NiFe-based particles in AEMWE anodes. These objectives will help further understand the behaviour of Ni-based catalysts in AEMWE systems, as well as the effects that catalyst-ionomer interactions can have on anode efficiency in carrying out the OER.

The nanoparticles developed in this work were synthesized by an easily scalable chemical reduction method in ethanol using sodium borohydride. Results show that Ni NPs, which are around 4-6 nm in size, with 10 and 20 at% Fe, provide the highest OER performance. Incorporating small amounts of CeO_2 into the NiFe materials results in better charge and mass transfer of the catalysts, however it introduces an additional ohmic resistance, which prevails over any OER-promoting interactions between NiFe and CeO_2. The best NiFe-based catalysts with and without CeO_2 were evaluated as anodes in a single cell AEMWE in combination with the commercial Fumatech Fumion® ionomer as well as the commercial Ionomr Innovations Aemion™ ionomer. The single-cell AEMWE analysis of the various catalytic layers shows that $Ni_{90}Fe_{10}$ with 15 wt% Fumion® shows the best catalytic performance of 1.72 V at 0.8 A cm^{-2} in 1 M potassium hydroxide (KOH) at 50°C. $Ni_{90}Fe_{10}$ is also the most stable under operating conditions in comparison to the other tested Ni-based materials. While it was found that using 7 wt% Aemion™ provided similar catalytic activity to 15 wt% Fumion®, results show that the Aemion™ ionomer interacts with NiFe to inhibit the formation of NiOOH, the OER active phase. The results of this work highlight the complex interactions between Ni-based nanoparticles and anion exchange ionomers towards the OER and provide possible directions for future research and development in high performing Ni-based anodes for AEMWE.

Résumé

Alors que les niveaux de dioxyde de carbone (CO_2) atmosphérique continuent d'augmenter en raison de l'utilisation anthropique des combustibles fossiles, la nécessité de développer et d'utiliser des vecteurs énergétiques alternatifs devient de plus en plus critique. Ces dernières années, l'intérêt pour l'hydrogène (H_2) a considérablement augmenté, car il s'agit d'un carburant alternatif propre et durable, qui peut être à la fois produit et utilisé sans émission de gaz à effet de serre; l'H_2 peut être produit par électrolyse de l'eau alimentée par des sources d'énergie renouvelables (SER), telles que l'énergie éolienne et solaire, ensuite l'H_2 peut être utilisé comme combustible dans une pile à combustible à l'hydrogène, n'émettant que de l'eau comme sous-produit. Non seulement l'H_2 est un carburant alternatif propre, mais il fournit également un moyen économiquement viable de stocker l'énergie renouvelable, afin que l'approvisionnement de SER puisse être mieux régulé en fonction de la demande.

Parmi les technologies d'électrolyse de l'eau existantes, il y en a peu qui offrent la possibilité de produire de l'hydrogène efficacement et à bas coût. L'environnement alcalin de l'électrolyseur alcalin traditionnel, qui est le procédé d'électrolyse de l'eau le plus couramment utilisé, permet l'utilisation d'électrocatalyseurs faits en métaux non nobles, ainsi que des matériaux de cellule peu coûteux. Ce procédé souffre cependant d'une conception de cellule inefficace. À l'inverse, l'électrolyseur de l'eau à membrane échangeuse de protons (EMEP) utilise une membrane d'électrolyte polymère solide, ce qui permet une conception de cellule compacte et à faible résistance. Cependant, l'environnement acide de ce procédé nécessite des catalyseurs fait en métaux du groupe du platine (MGP) et des composants de cellule coûteux. L'électrolyse de l'eau à membrane échangeuse d'anions (EMEA) est une technologie prometteuse pour la production efficace et à faible coût de l'H_2, car elle combine la conception de cellule compacte du EMEP avec l'environnement basique favorable de l'électrolyseur alcalin traditionnel.

Le processus électrochimique de séparation de l'eau est limité par la réaction de demi-cellule de la production de l'oxygène (RPO), qui est cinétiquement défavorable, et nécessite des catalyseurs de métaux rares et coûteux tels que l'iridium, pour effectuer efficacement la réaction. Le nickel (Ni) est un catalyseur peu coûteux, abondant et prometteur pour la RPO en milieu alcalin, en raison de sa forte activité et de sa résistance à la corrosion. Une augmentation significative de l'activité de la RPO peut être obtenue par l'incorporation de fer (Fe) dans les catalyseurs à base de

Ni. L'ajout du dioxyde de cérium (CeO_2), un conducteur mixte ionique-électronique avec des propriétés favorables de stockage et de libération d'oxygène, peut également avoir un effet positif sur les performances catalytiques. Bien que le développement d'électrocatalyseurs pour améliorer les performances de la RPO soit important, l'évaluation des matériaux étudiés en tant qu'anodes dans les dispositifs d'EMEA pratiques est impérative, car elle tient compte de l'efficacité des catalyseurs dans des couches d'électrodes formées à l'aide d'un ionomère échangeur d'anions (IEA). Un IEA est un électrolyte polymère solide qui sert de liant pour les particules de catalyseur, ainsi que de conducteur d'ions hydroxyde à travers une couche catalytique d'un EMEA.

Les principaux objectifs de cette thèse sont de (*i*) développer des catalyseurs de nanoparticules (NP) à base de Ni et Fe avec et sans CeO_2 pour la promotion de la RPO dans les dispositifs d'EMEA, et (*ii*) étudier les effets du type et de la quantité d'IEA commerciaux sur l'efficacité des particules à base de Ni et Fe produites pour les anodes d'EMEA. Ces objectifs aideront à mieux comprendre le comportement des catalyseurs à base de Ni dans les systèmes d'EMEA, ainsi que les effets que les interactions catalyseur-ionomère peuvent avoir sur l'efficacité de l'anode dans la réalisation de la RPO.

Les nanoparticules développées dans ce travail ont été synthétisées par une méthode qui peut être facilement mise à l'échelle. Cette méthode consiste d'une réduction chimique dans l'éthanol à l'aide de borohydrure de sodium. Les résultats montrent que les NP de Ni, dont la taille est d'environ 4 à 6 nm, avec 10 et 20%at de Fe, offrent les performances de la RPO les plus élevées. L'incorporation de petites quantités de CeO_2 dans les matériaux de Ni et Fe entraîne un meilleur transfert de charge et de masse des catalyseurs, mais elle introduit une résistance ohmique supplémentaire, qui prévaut sur toute interaction entre la phase de Ni et Fe et celle du CeO_2 favorisant la RPO. Les meilleurs catalyseurs à base de Ni et Fe avec et sans CeO_2 ont été évalués en tant qu'anodes dans une cellule unique d'EMEA en combinaison avec l'ionomère commercial Fumatech Fumion® ainsi que l'ionomère commercial Aemion™ de Ionomr Innovations. L'analyse d'EMEA des différentes couches catalytiques montre que le $Ni_{90}Fe_{10}$ avec 15% en masse de Fumion® présente les meilleures performances catalytiques de 1,72V à 0,8A cm^{-2} dans un électrolyte de 1 M d'hydroxyde de potassium (KOH) à 50°C. Le $Ni_{90}Fe_{10}$ est également le plus stable sous les conditions de fonctionnement de l'EMEA par rapport aux autres matériaux à base de Ni. Il a aussi été trouvé que l'utilisation de 7% en masse de l'ionomère Aemion™ fournissait

une activité catalytique similaire à 15% en masse de Fumion®. Cependant, les résultats montrent que l'ionomère Aemion™ interagit avec le Ni et Fe pour inhiber la formation de NiOOH, la phase active de la RPO. Les résultats de ce travail mettent en évidence les interactions complexes entre les nanoparticules à base de Ni et les ionomères échangeurs d'anions vers la RPO et fournissent des orientations possibles pour la recherche et le développement futurs dans les anodes à base de Ni à haute performance pour l'EMEA.

Statement of Contributions of Collaborators

I hereby declare that I am the first author of all chapters written in this thesis.

Chapters 1 and 8 were written solely by me, with editorial comments provided by Dr. Elena Baranova.

Chapter 2 is a literature review adapted from a review paper published in a peer-reviewed academic journal. The chapter is written solely by me with editorial comments provided by Dr. Elena Baranova, who is a co-author on this work. Frédéric Murphy assisted in acquiring the articles pertinent to the review paper as well as extracting relevant data from the summarized articles. All co-authors provided input and reviewed the manuscript.

Chapter 3 is a manuscript published in a peer-reviewed academic journal. Dr. Mohamed S. E. Houache and Zhihao Zhang both provided the lab synthesized Ni nanostructures, which were analyzed in this study, and their accompanying physicochemical characterization. All electrochemical measurements in this study were performed by me. Data analysis was performed by me with assistance from Dr. Elena Baranova. The manuscript was solely written by me, with editorial comments provided by Dr. Elena Baranova, who is a co-author on the manuscript. All co-authors provided input and reviewed the manuscript.

Chapter 4 is a manuscript published in a peer-reviewed academic journal. Material synthesis was done by me, Vu Bao Nguyen and Kushagra Agarwal. TEM and EDS characterization were done by Reza Safari (McMaster University) and Dr. Gianluigi A. Botton (McMaster University). Electrochemical measurements were performed by me, Kushagra Agarwal and Vu Bao Nguyen. Analysis of the TEM and EDS characterization was done by Reza Safari and I with assistance from Dr. Gianluigi A. Botton and Dr. Elena Baranova. The electrochemical data analysis was carried out by me with assistance from Kushagra Agarwal and Dr. Elena Baranova. The manuscript was written solely by me, with editorial comments from Reza Safari, Dr. Elena Baranova and Dr. Gianluigi A. Botton, who are all co-authors on this manuscript. All co-authors provided input and reviewed the manuscript.

Chapter 5 is a manuscript published in a peer-reviewed academic journal. Material synthesis was done by me. SEM imaging was performed by me. Material characterization of the $Ni_{90}Fe_{10}$/ 50

wt% CeO_2 catalyst was performed by Dr. Martin Couillard (Natural Research Council of Canada). Ex-situ electrochemical testing was performed by me. In-situ electrochemical testing was carried out by me with assistance from Dr. Alejandro Oyarce Barnett (SINTEF Industry and Norwegian University of Science and Technology, Norway). Electrochemical impedance fits were done by Dr. Frode Seland (Norwegian University of Science and Technology, Norway). Data analysis was performed by me with assistance from Dr. Elena Baranova, Dr. Alejandro Oyarce Barnett and Dr. Frode Seland. The manuscript was written solely by me with inputs from Dr. Alejandro Barnett, Dr. Frode Seland and Dr. Elena Baranova, who are all co-authors of this work. All co-authors provided input and reviewed the manuscript.

Chapter 6 is a manuscript published in a peer-reviewed academic journal. Material synthesis was done by me. TEM imaging of $Ni_{90}Fe_{10}$, $Ni_{80}Fe_{20}$ and $Ni_{90}Fe_{10}$/ 10 wt% CeO_2 was done by Reza Safari and Dr. Gianluigi A. Botton. BET/BJH measurements were carried out by me. In-situ electrochemical testing was performed by me with assistance from Dr. Alejandro Oyarce Barnett. Electrochemical impedance fits were carried out by Dr. Frode Seland. Analysis of the TEM images was done by Reza Safari and I with assistance from Dr. Elena Baranova and Dr. Gianluigi A. Botton. Analysis of the remaining material characterization and the electrochemical data was done by me with assistance from Dr. Elena Baranova and Dr. Frode Seland. The manuscript was written solely by me, with editorial comments from Reza Safari, Dr. Elena Baranova, Dr. Frode Seland and Dr. Gianluigi A. Botton, who are all co-authors on this work. All co-authors provided input and reviewed the manuscript.

Chapter 7 is a manuscript submitted to a peer-reviewed academic journal. Material synthesis was done by me. SEM imaging was done by me. Ex-situ Raman spectroscopy measurements were performed by Dr. Jaspreet Walia. All electrochemical testing was performed by me, with assistance from Frédéric Murphy. Analysis of the Raman spectroscopy results was carried out by me with guidance from Dr. Jaspreet Walia and Dr. Elena Baranova. All SEM and electrochemical data analysis was done by me with assistance from Dr. Elena Baranova. The manuscript was written solely by me, with editorial comments from Dr. Jaspreet Walia, Dr. Elena Baranova and Dr. Arnaud Weck, who are co-authors on this work. All co-authors provided input and reviewed the manuscript.

Acknowledgements

First and foremost, I would like to thank my thesis supervisor Professor Elena Baranova for her support and guidance throughout my studies. Ever since I first worked under the supervision of Dr. Baranova during my undergraduate studies, she has provided me with amazing opportunities which have allowed me to further both my academic and personal development. Dr. Baranova always encouraged me in my work, which has allowed me to accomplish many things I would not have imagined possible. I have learned so much from Dr. Baranova and consider myself very fortunate to have worked with such a supportive supervisor and role model in engineering.

I would also like to thank Dr. Frode Seland and Dr. Alejandro Barnett for their support and mentorship during my studies. They helped make it possible for me to work two summers at the Norwegian University of Science and Technology (NTNU) and SINTEF in Trondheim, Norway. Working at NTNU and SINTEF allowed me to see a more practical application of electrochemical clean technologies and the importance they have in our future. I am very grateful for the collaboration between Dr. Baranova, Dr. Seland and Dr. Barnett as the research internships I completed in Norway have inspired me to pursue a career in sustainable technologies. I would also like to thank the friends and lab mates that I made in Norway (Tom, Stig, Katie, Alaa, Thulile, Tory,…) for making these trips such an incredible experience.

I would like to thank Professor Gianluigi Botton and Reza Safari from McMaster University for their exceptional work in helping me characterize some of my developed materials. I would also like to thank Dr. Arnaud Weck and Jaspreet Walia for their help characterizing particularly challenging samples of mine using Raman spectroscopy.

I wish to acknowledge funding from the Ni Electro Can project administered from Queen's University and supported by the Natural Sciences and Engineering Research Council of Canada (NSERC) Discovery Frontiers Program. Additionally, I would like to acknowledge funding from the HAPEEL project supported by the Research Council of Norway ENERGIX program, as well as the CANOPENER INTPART project, also supported by the Research Council of Norway. I am also very grateful to have been awarded the NSERC Alexander Graham Bell Canada Graduate Scholarship – Doctoral (CGS-D) as well as funding from the Science and Technology Internship Program (STIP) by Natural Resources Canada (NRCan).

A great portion of my work would not have been possible without the technical staff of the Department of Chemical Engineering. Particularly, during the COVID-19 pandemic, Franco Ziroldo, James Macdermid and Gérard Nina helped me design and build a single cell anion exchange membrane water electrolyser. I am very grateful for the support and assistance that they provided me throughout my studies. I am also very grateful for the help that Francine Pétrin, Sylvie Saindon and Chantal Dubé provided me with for various administrative matters throughout my studies.

I would like to thank my lab mates, Evans, Mohamed, Asma, Chris, Najmeh, Ju, Arash, Frédéric, Tatiana, Kushagra, Natalia, Yasmine and Niloofar for their help, support, and motivation throughout my studies. A particular thanks to Kushagra and Frédéric for helping me with my

experiments. A special thanks goes to Mohamed for his continued guidance and support, ever since I first worked with him during my undergraduate studies.

I would like to thank all the friends that I have made throughout my studies as they have positively impacted my journey through graduate school, and I could not imagine my studies being as enjoyable without them. Fahad, Charbel, Geraldine, Chris P., Chris M., Dean, Sam, Vida, Sean, Curtis, Milad, Amir, Marie, Ali… the list could go on quite a bit. Thank you all for the wonderful environment that you have created for me at the university, and I wish you all the best with your future endeavours.

Finally, I would like to thank my partner Philippe, for his love and support, and for always believing in me. I am forever grateful to have you in my life.

Dedication

I would like to dedicate this thesis to my family, who have shown me that anything is possible if you put your mind to it. To my Mum, Rebecca, for always being there and teaching me to seize opportunities. To my Dad, Douglas, for being a grounding, positive presence in my life, and for guiding me through this journey. To Robert, for always being kind and supportive. And to my sisters, Lydia, Rosie, Rachel, and Kathryn for each being there to support me in their own ways, for always making me smile and for making these last few years amazing. Without all of you, I would not be where I am today.

I love you all very much.
Thank you, and I hope I have made you proud.

Table of Contents

List of Figures

List of Tables

Nomenclature

1.1. Acronyms

AEI	anion exchange ionomer
AEM	anion exchange membrane
AEMWE	anion exchange membrane water electrolysis
AN	anode
BET	Brunauer-Emmett-Teller specific surface area
BJH	Barrett-Joyner-Halender pore size distribution
CA	chronoamperometry
CAT	cathode
CCM	catalyst coated membrane
CCS	catalyst coated surface
CE	counter electrode
CFD	computational fluid dynamics
CP	chronopotentiometry
CV	cyclic voltammetry
DFT	density functional theory
ECSA	electrochemical active surface area [cm^2]
EDS/EDX	energy dispersive x-ray spectroscopy
EELS	electron energy-loss spectroscopy
EIS	electrochemical impedance spectroscopy
GDL	gas diffusion layer

GHG	greenhouse gas
HER	hydrogen evolution reaction
HFR	high frequency resistance
Hg/HgO	mercury/mercury oxide reference electrode
HTE	high temperature electrolysis
LSV	linear sweep voltammetry
MEA	membrane electrode assembly
NP	nanoparticle
OER	oxygen evolution reaction
OCP	open circuit potential [V]
PEC	photoelectrochemical
PEI	proton exchange ionomer
PEM	proton exchange membrane
PEMWE	proton exchange membrane water electrolysis
PGM	platinum group metal
PSD	particle size distribution
PTL	porous transport layer
PV	photovoltaic
RE	reference electrode
RES	renewable energy sources
RHE	reversible hydrogen electrode
RON	research octane number
SCE	saturated calomel electrode

SEM	scanning electron microscopy
SHE	standard hydrogen electrode
SOEC	solid oxide electrolysis cell
STEM	scanning transmission electron microscopy
TEM	transmission electron microscopy
WE	working electrode
XRD	x-ray diffraction

1.2. Symbols – Latin Letters

a_i	activity of the species *i* [-]
C_{dl}	double layer capacitance [F]
c_s	specific capacitance [μF cm^{-2}]
E	voltage [V]
E^0_{rev}	reversible cell voltage [V]
E^0_{AN}	anode standard reduction potential [V]
E^0_{CAT}	cathode standard reduction potential [V]
E_{cell}	cell voltage [V]
F	Faraday's constant [96485 C $mol_{e^-}^{-1}$]
G	Gibb's free energy [kJ mol^{-1}]
H	enthalpy [kJ mol^{-1}]
I	current [A]
I_C	charging current [A]
j	current density [A cm^{-2}]
j_0	exchange current density [A cm^{-2}]
L	inductor term
M	molar [mol L^{-1}]
n	number of electrons transferred per mole of product [mol_{e^-} mol^{-1}]
q	specific charge density [μC cm^{-2}]
Q	charge [C]
Q	constant phase element

R'	universal gas constant [8.314 J $mol^{-1}K^{-1}$]
R	resistance [Ω]
R_{CT}	charge transfer resistance [Ω]
R_{EL}	ohmic resistance [Ω]
RF	roughness factor [-]
R_P	polarization resistance [Ω]
S	entropy [J $mol^{-1}K^{-1}$]
SA	surface area [cm^2]
t	time [s or h]
T	temperature [°C or K]

1.3. Symbols – Greek Letters

α_{AN}	anode charge transfer coefficient [-]
α_{CAT}	cathode charge transfer coefficients [-]
Δ	“change in” [N/A]
η	overpotential [V]
η_{AN}	anode overpotential [V]
η_{CAT}	cathode overpotential [V]
η_{IR}	overpotential from IR losses [V]
v	scan rate [mV s^{-1}]

Chapter 1. General Introduction

1.1 Background and Motivation

Carbon dioxide (CO_2) emissions from the use of fossil fuels have become an increasingly important concern due to their negative effect on the environment. CO_2 is an important contributor to what is known as the "greenhouse gas effect". When CO_2 is emit into the atmosphere, it has a heat trapping effect on the earth; as the sunlight reaches earth's surface, some of its energy is reflected and subsequently absorbed by greenhouse gases such as CO_2, thus resulting in an overall global warming effect[1,2]. While this global warming effect has been known to be associated with drought, shrinking glaciers, heat waves and stronger hurricanes[3], the future effects of increasing CO_2 in the atmosphere are not completely predictable, which makes them a great cause for concern. It is therefore increasingly important to move away from the world's heavy dependence on fossil fuels.

To tackle this problem, in recent years, there has been an increase in the development and implementation of renewable energy sources (RES), such as wind, hydroelectric or solar. However, one major concern for a heavier reliance on these RES, is that their energy is not supplied consistently and as such, economically feasible ways of storing RES must be developed so that renewable energy supplies can be better regulated for use according to need. A promising way to store RES is by using the energy to electrochemically split water into its constituents, hydrogen and oxygen (H_2 and O_2), storing said energy in the chemical bond of di-hydrogen. H_2 is an ideal alternative energy carrier as it can be integrated into a completely sustainable energy system[4]. Once hydrogen is produced via renewable energy powered water electrolysis (green hydrogen), it can be later used in a hydrogen fuel cell, emitting only water as a by-product[5]. This vision of a clean, sustainable energy system is referred to as the "Hydrogen Economy"[6].

The electrochemical splitting of water has been known for over 230 years[7], and over the years, many different technologies have been developed to more efficiently split water. One of the most widely used electrolysis processes is the traditional alkaline electrolysis process, which was first commercialized in 1927 by NEL Hydrogen[8]. This process is advantageous as non-platinum group metal (PGM) catalysts and low-cost cell materials can be utilized due to the alkaline environment of the device, resulting in a decreased capital cost of the system. However, the

traditional electrolysis cell has high ohmic losses from gas bubble formation and the diaphragms used to separate the anode and cathode[8]. The first proton exchange membrane water electrolyser (PEMWE) was reported in 1973, where a solid perfluorinated sulfonic acid membrane was used in place of a liquid electrolyte, resulting in a more efficient, low resistance cell design in comparison to the traditional alkaline electrolyser[8]. The PEMWE system, however, operates in a corrosive acidic environment, requiring the use of PGM metals for electrocatalysts and other cell components[8]. More recently, the anion exchange membrane water electrolyser (AEMWE) has been studied because it is a device which can combine the advantages of the traditional alkaline electrolyser with those of the PEMWE, producing green hydrogen both efficiently and at low cost[8,9]. The AEMWE process utilizes an anion exchange membrane, allowing for an efficient, compact cell configuration, like in the case of the PEMWE. Additionally, the AEMWE process operates in an alkaline environment, like in the case of the traditional alkaline process, allowing for significant capital cost reductions of the cell components in comparison to the PEM electrolysis system[8,9].

The water electrolysis process occurs through two half cell reactions: the oxygen evolution reaction and the hydrogen evolution reaction (OER and HER). The OER half-cell reaction is kinetically unfavourable, requiring expensive rare catalysts such as iridium to efficiently split water[10]. Nickel (Ni) is a promising inexpensive and abundant catalyst for the OER in alkaline media, as it has a high corrosion resistance and can achieve high oxidation states, which are favourable for good OER performance[10–12]. Additionally, researchers have shown that a significant increase in OER activity can be achieved by incorporating iron (Fe) into Ni catalysts[10,13] in amounts ranging from around 1 to 50% Fe, depending on the material. For example, it was observed that in comparison to other transition metals, incorporating Fe into a Ni-based catalyst provided the best OER performance, where the best performing NiFe catalyst contained 10 at% Fe[14]. Pairing a catalyst with a support, can also further enhance the electrochemical activity of a material through metal-support interactions (MSI). Ceria (CeO_2), a mixed ionic-electronic conductive (MIEC) support with oxygen storage and release properties[15], could be combined with Ni-based materials to further enhance OER performance. For example, it has recently been shown that FeOOH/CeO_2 heterolayered nanotubes supported on a nickel foam (NF) have significantly higher oxygen evolution activity in comparison to FeOOH and CeO_2

nanotube arrays on a NF and the NF alone[16], which could be due to an abundance of FeOOH/CeO_2 heterostructure interfaces, as well as the high oxygen storage capacity of CeO_2 in the material.

In AEMWE devices, the compact cell design is achieved using a membrane electrode assembly (MEA), which consists of the anode and cathode catalysts, placed either side of an anion exchange membrane (AEM). Each electrode is then in contact with a gas diffusion layer (GDL), which helps with the transport of reactants and products to and from the electrode surface[17]. In the electrode layers, there is also an anion exchange ionomer (AEI), which serves to bind the catalyst either to the membrane or the GDL, and to conduct hydroxide ions (OH^-) throughout the electrode layer. An optimal MEA is formed with a high amount of "three-phase boundaries", which are the boundaries formed between the catalyst, electrolyte (and by extension polymer electrolyte), and produced gases[17]. In other words, an efficient MEA is one where efficient hydroxide ion, electron, reactant, and product transport occurs. As an important part of the anode catalytic layer, the choice of type and amount of ionomer used can significantly affect the electrochemical performance of the evaluated catalysts. For example, when pairing different loadings (10, 20, 30 wt%) of the commercial Fumatech FAA-3-Br ionomer with a commercial IrO_2 anode catalyst in an AEMWE, it is observed that employing 20 wt% AEI, offers the best AEMWE performance by balancing electrode morphology and catalyst active site coverage[18].

1.2 Project Objectives and Hypothesis

The overall goal of this thesis is to develop and optimize nickel-based nanostructured electrocatalysts for the promotion of the oxygen evolution reaction in anion exchange membrane water electrolysis for more efficient and low-cost green hydrogen production. This was attempted by studying the effects of iron and ceria incorporation into nickel-based catalysts to enhance OER performance, and by evaluating the effects of ionomeric binders on the efficiency of the OER catalysts in AEMWE anode electrode layers.

Based on these primary objectives, the main hypotheses of this thesis are:

1. Incorporating optimized amounts of Fe and CeO_2 into Ni nanoparticle catalysts will modify the properties of the Ni OER-active phase, and in turn promote the reaction.

2. Studying the effects of anion exchange ionomer nominal loading and type will result in improved anode catalytic layer architecture, with better catalyst utilization for more efficient and stable oxygen production.

The following detailed objectives were used to fulfill the overall goals of this thesis

1. Perform a comparative study of established methods used to quantify the electrochemical active surface area (ECSA) of Ni materials to determine whether a single suitable method exists, or whether the best method to employ depends on the materials studied. Evaluate the ECSA methods using polycrystalline Ni and various Ni nanostructures to better assess the applicability of the methods.
2. Synthesize Ni-based nanoparticles using an easily scalable chemical reduction method, with varying amounts of Fe ($Ni_{100-x}Fe_x$/ 50 wt% CeO_2, where x=0, 5, 10, 20, 40 at%) and CeO_2 (NiFe/ y wt% CeO_2, where y=0, 5, 7, 10, 20, 50 wt%) for enhanced OER in alkaline media.
3. Study the physicochemical properties (particle size, morphology, phase, elemental distribution, etc) of the synthesized catalysts using modern analytical techniques, such as Scanning and Transmission Electron Microscopy (SEM, TEM or STEM), X-ray Diffraction (XRD), Electron Energy-Loss Spectroscopy (EELS), Energy Dispersive X-ray Spectroscopy (EDS), Brunauer-Emmett-Teller (BET) specific surface area measurements and Barrett-Joyner-Halender (BJH) pore size distribution measurements.
4. Investigate the three-electrode cell electrochemical activity and stability of the synthesized Ni-based catalysts for OER in alkaline media using cyclic voltammetry (CV), chronoamperometry (CA), chronopotentiometry (CP), electrochemical impedance spectroscopy (EIS) and linear sweep voltammetry (LSV).
5. Design and construct a single-cell AEMWE to further evaluate the performance of the Ni-based materials in a practical electrolyser device with simultaneous oxygen and hydrogen production.
6. Scale up the synthesis of the most stable and active OER catalysts to evaluate their electrochemical performance in an AEMWE. Utilize electrochemical techniques such as EIS, CP and polarization curve measurements to evaluate the electrochemical activity of

the anode catalysts in the electrolyser. Evaluate the morphology of the produced anode catalytic layers using SEM.

7. Study the effects of varying the nominal loading of commercially available anion exchange ionomers on the performance of the best Ni-based anode electrocatalysts in an AEMWE. Employ Particle Size Distribution (PSD) measurements of catalyst inks and SEM of the catalytic layers to evaluate the effects of ionomer content on the resulting electrode morphology. Utilize ex-situ Raman spectroscopy to understand the surface chemistry of the prepared catalytic layers.

1.3 Thesis Structure

This thesis is made up of 8 chapters, where the current chapter, Chapter 1, covers the General Introduction to the thesis work. Chapter 2 then covers a topical literature review for the presented research. Chapters 3 to 7 all present independent research articles, which were either submitted to or published in peer-reviewed academic journals. As a result of this article-based thesis structure, repetition of certain elements and ideas, such as experimental methodology, was inevitable. Finally, Chapter 8 provides a general discussion and conclusions of the presented work and provides recommendations for future work of this thesis. The cited literature is presented as bibliographies at the end of each chapter. Below is a more detailed description of what is covered in each chapter of this thesis.

Chapter 1 - General Introduction

This chapter covers the background and motivation of this thesis work, along with the key research objectives.

Chapter 2 – Literature Review

This chapter provides a literature review relevant to the thesis work. A discussion of the use of hydrogen as an alternative fuel is provided, along with a comparison of various water electrolysis technologies used to produce hydrogen in a clean and sustainable way. Amongst the discussed types of water electrolysis is anion exchange membrane water electrolysis, a technology which shows immense promise in producing H_2 both efficiently and at low cost. The review then covers a detailed summary of recent research progress (from 2015 onwards) on the development of Ni particle-based anodes used with anion exchange ionomers tested in AEMWE devices. An

analysis of the synthesis and electrode preparation methods is provided to comment on the feasibility of industrializing the production of Ni-based AEMWE anodes. Finally, the impact of ionomeric binder type and loading is evaluated in the summarized articles to show that future catalyst and ionomer development must account for how the two of them work together in catalyzing the OER.

Chapter 3 - Comparison of Electrochemical Active Surface Area Methods for Various Nickel Nanostructures

In this chapter, a comparative study of four previously established ECSA methods is carried out to determine whether a single most appropriate method for calculating the ECSA exists for Ni-based materials. The ECSA is an important parameter to assess the intrinsic activity of an electrocatalyst. To perform an extensive study, five Ni materials were evaluated: polycrystalline Ni as well as 4 different Ni nanostructures. The results of the applied ECSA methods were analyzed in combination with the physicochemical properties of the catalysts obtained using SEM, TEM and XRD. Overall, the detailed analysis performed in the study shows that the ECSA method to apply will depend strongly on the type of Ni under study.

Chapter 4 - Highly Active Nickel-iron Nanoparticles with and without Ceria for the Oxygen Evolution Reaction

This chapter covers an investigation into the incorporation of Fe and CeO_2 into Ni nanoparticle catalysts for the promotion of the OER in alkaline media. The studied catalysts were synthesized using an easily scalable method, namely, chemical reduction in ethanol using sodium borohydride. The iron content was first optimized in a $Ni_{100-x}Fe_x$/ 50 wt% CeO_2 catalyst, then the mass percentage of ceria in the $Ni_{100-x}Fe_x$/ 50 wt% CeO_2 materials was optimized for the best two Fe contents. Using TEM and EDS, it was possible to determine that the produced spherical particles are around 4-6 nm in size, where the Ni and Fe phases are co-distributed, while the ceria containing materials show CeO_2 separately agglomerated. Electrochemical testing in a three-electrode electrochemical cell in 1 M potassium hydroxide (KOH) shows that the $Ni_{80}Fe_{20}$ electrode is the most active material, while the $Ni_{90}Fe_{10}$ electrode is the most stable. Finally, results show that CeO_2 does not improve or hinder the OER of the Ni-based materials.

Chapter 5 - The Performance of Nickel and Nickel-Iron catalysts Evaluated as Anodes in Anion Exchange Membrane Water Electrolysis

In this chapter, a preliminary evaluation of the $Ni_{100-x}Fe_x$/ y wt% CeO_2 materials developed in Chapter 4 was carried out in a single cell AEMWE. The tested materials included Ni, $Ni_{90}Fe_{10}$ and $Ni_{90}Fe_{10}$/ 50 wt% CeO_2. The anode electrode layers were prepared using 7 wt% of the commercial Fumatech Fumion® FAA-3-SOLUT-10 anion exchange ionomer, based on a previously established procedure for the preparation of iridium black benchmark anode electrodes. In this work, the $Ni_{90}Fe_{10}$ electrode shows the most promising performance of all Ni-based materials in an AEMWE and is also competitive with the Ir black benchmark electrode. Electrochemical impedance results indicate that incorporating CeO_2 into the Ni-based catalysts has beneficial effects on the charge transfer resistance of the anode layers. However, CeO_2 introduces a large ohmic resistance to the system, indicating the need to optimize the CeO_2 content from 50 wt% to improve the electrical conductivity of the ceria-containing anode catalytic layers.

Chapter 6 - Ionomer Content Optimization in Nickel-iron-based Anodes with and without Ceria for Anion Exchange Membrane Water Electrolysis

Following the preliminary AEMWE evaluation of the $Ni_{100-x}Fe_x$/ y wt% CeO_2 catalysts in Chapter 5, this chapter covers the optimization of the Fumatech Fumion® FAA-3-SOLUT-10 ionomer content in said Ni-based anode catalytic layers. Fumion® loadings of 7, 15, 25, 35 and 45 wt% were evaluated. Based on PSD measurements of the catalyst inks, SEM images of the prepared anode catalytic layers and AEMWE performance of the anodes with different amounts of ionomer, it was found that 15 wt% Fumion® provided the best AEMWE performance and the strongest particle adhesion of the catalysts in the anode layers. When evaluating the performance and short-term durability of various $Ni_{100-x}Fe_x$/ y wt% CeO_2 electrodes ($Ni_{90}Fe_{10}$, $Ni_{80}Fe_{20}$, both with and without 10 wt% CeO_2, based on the material optimization study in Chapter 4) with 15 wt% Fumion®, it was found that the $Ni_{90}Fe_{10}$ electrode was the most active and stable anode of the Ni-based materials. While in this study a more optimal amount of CeO_2 of 10 wt% was employed with the NiFe catalysts, the CeO_2-containing layers continued to show a higher ohmic resistance. They did however continue to show beneficial effects on the charge transfer of the anode layers. Furthermore, during the preliminary durability testing, signs of maintained mass transfer over time were observed when CeO_2 was incorporated into the anode layers.

Chapter 7 - Study of the Aemion^{TM} Ionomer in Nickel-Iron Anodes for Anion Exchange Membrane Water Electrolysis

Having identified in Chapters 4 to 6 that the $Ni_{90}Fe_{10}$ catalyst is the most promising studied Ni-based anode in AEMWE, the performance of said catalyst was evaluated in combination with a more durable commercial anion exchange ionomer, namely the Aemion^{TM} ionomer from Ionomr Innovations. This chapter therefore covers a detailed three-electrode cell investigation on the effects of the Aemion^{TM} ionomer as a binder for $Ni_{90}Fe_{10}$ nanoparticles for OER in alkaline media. Results indicate that in comparison to the Fumion® ionomer and the widely used Nafion^{TM} ionomer, the Aemion^{TM} ionomer inhibits the $Ni(OH)_2$/NiOOH redox transition peaks, which in turn results in lower OER activity with continued CV cycling. This effect was proposed to be related to negative catalyst-ionomer interactions between $Ni_{90}Fe_{10}$ and Aemion^{TM} and was found to be permanent. The effects of different nominal loadings (7, 15, 25, 35 wt%) of the Aemion^{TM} ionomer were also evaluated with the $Ni_{90}Fe_{10}$ anode catalyst in a single cell AEMWE, where it was found that having 7 wt% Aemion^{TM} provided the best AEMWE performance, comparable to that of $Ni_{90}Fe_{10}$ with 15 wt% Fumion®. The SEM analysis of the prepared electrodes with Aemion^{TM} show poor electrode layer morphology, which was suggested to be related to the poor stability of the catalyst ink dispersions and the electrode fabrication conditions. Finally, ex-situ Raman spectroscopy was used to analyze the $Ni_{90}Fe_{10}$ anode layers with Aemion^{TM} before and after polarization, showing that after electrolysis, the electrode mostly remains in the $Ni(OH)_2$ phase, supporting the CV results.

Chapter 8 – General Discussion, Conclusions and Recommendations

This chapter provides a general discussion of the presented thesis work, summarizing the main conclusions and contributions of the thesis. Finally, recommendations for future work of this thesis are provided.

References

[1] Earth Science Communications Team, "The Causes of Climate Change," *NASA's Jet Propulsion Laboratory*, **2022**, accessed on February 14, 2022, https://climate.nasa.gov/causes/.

[2] Earth Science Communications Team, "Carbon Dioxide," *NASA's Jet Propulsion Laboratory*, **2022**, accessed on February 14, 2022, https://climate.nasa.gov/vital-signs/carbon-dioxide/.

[3] Earth Science Communications Team, "The Effects of Climate Change," *NASA's Jet Propulsion Laboratory*, **2022**, accessed on February 14, 2022, https://climate.nasa.gov/effects.

[4] D. M. F. Santos, C. A. C. Sequeira, *Quim. Nova* **2013**, *36*, 1176.

[5] I. Katsounaros, S. Cherevko, A. R. Zeradjanin, K. J. J. Mayrhofer, *Angew. Chemie - Int. Ed.* **2014**, *53*, 102.

[6] D. Clark, N. Brandon, What's the "hydrogen economy"? *Guardian* **2012**.

[7] T. Smolinka, H. Bergmann, J. Garche, M. Kusnezoff, "Chapter 4 - The history of water electrolysis from its beginnings to the present," *Electrochemical Power Sources: Fundamentals, Systems, and Applications: Hydrogen Production by Water Electrolysis*, T. Smolinka, J. Garche, Eds., Elsevier **2022**, p. 83.

[8] R. Abbasi, B. P. Setzler, S. Lin, J. Wang, Y. Zhao, H. Xu, B. Pivovar, B. Tian, X. Chen, G. Wu, Y. Yan, *Adv. Mater.* **2019**, *31*, 1805876.

[9] I. Vincent, D. Bessarabov, *Renew. Sustain. Energy Rev.* **2018**, *81*, 1690.

[10] M. Gong, H. Dai, *Nano Res.* **2015**, *8*, 23.

[11] M. Tahir, L. Pan, F. Idrees, X. Zhang, L. Wang, J. J. Zou, Z. L. Wang, *Nano Energy* **2017**, *37*, 136.

[12] M. E. G. Lyons, M. P. Brandon, *Int. J. Electrochem. Sci.* **2008**, *3*, 1386.

[13] F. Dionigi, P. Strasser, *Adv. Energy Mater.* **2016**, *6*, 1600621.

[14] X. Li, F. C. Walsh, D. Pletcher, *Phys. Chem. Chem. Phys.* **2011**, *13*, 1162.

[15] C. Panaritis, M. Edake, M. Couillard, R. Einakchi, E. A. Baranova, *J. CO2 Util.* **2018**, *26*, 350.

[16] J.-X. Feng, S.-H. Ye, H. Xu, Y.-X. Tong, G.-R. Li, *Adv. Mater.* **2016**, *28*, 4698.

[17] B. Bladergroen, H. Su, S. Pasupathi, V. Linkov, "Overview of Membrane Electrode Assembly Preparation Methods for Solid Polymer Electrolyte Electrolyzer," *Electrolysis*, **2012**.

[18] J. E. Park, S. Y. Kang, S. H. Oh, J. K. Kim, M. S. Lim, C. Y. Ahn, Y. H. Cho, Y. E. Sung, *Electrochim. Acta* **2019**, *295*, 99.

Chapter 2. Nickel-based Anodes in Anion Exchange Membrane Water Electrolysis: A Review

Emily Cossar[a], Frédéric Murphy[a], Elena A. Baranova[a*]

[a] *Department of Chemical and Biological Engineering, Centre for Catalysis Research and Innovation (CCRI) University of Ottawa,161 Louis-Pasteur Ottawa, Canada, K1N 6N5*

Chapter adapted from a review paper published in: *J. Chem. Technol. Biotechnol.,* **2022,** https://doi.org/10.1002/jctb.7094.

Supplementary information for this chapter is found in Appendix A.

Abstract

Anion exchange membrane water electrolysis (AEMWE) is a promising technology for efficiently producing low-cost hydrogen (H_2). It operates in an alkaline environment, allowing for inexpensive cell materials and non-noble metal electrocatalysts, and it utilizes an anion exchange membrane permitting a low resistance cell design in comparison to the traditional alkaline electrolysis process. Of the two half-cell reactions in AEMWE, the oxygen evolution reaction (OER) is kinetically sluggish, requiring an electrocatalyst to promote the reaction. Nickel (Ni) is a promising non-noble metal catalyst for OER due to its high stability, low cost, and activity in alkaline media. In an AEMWE, Ni particles form a catalytic layer bound together using an anion exchange ionomer (AEI), which also serves to provide hydroxide ion transport throughout the layer. In this review, reports of lab synthesized Ni particle-based anode catalytic layers with AEIs, used specifically in AEMWE devices, are summarized from 2015 onwards to highlight the recent research and development of active Ni-based AEMWE anodes. The synthesis and electrode fabrication method for the anodes is analyzed to offer a perspective on the feasibility of industrial scale AEMWE. As ionomeric binders are an important component of AEMWE anodes, the ionomer type and loading used with the Ni-based particles is also summarized with a focus on how those parameters affect catalytic performance. In addition to recapitulating and discussing the current progress of Ni particle-based anode catalytic layers in AEMWE, this review culminates in suggestions for future research and development avenues to better develop high-performing AEMWE anodes.

2.1 Introduction

In the 18th century, the start of Industrial Revolution allowed the world population to dive into their money-driven materialistic way of living[1,2]. This way of life was possible due to the burning of fossil fuels to generate energy. At the time, the impact that burning fossil fuels had on the environment was not much cause for concern. However, a catastrophic and continuous increase in greenhouse gas (GHG) emissions to the atmosphere was observed over the years since the start of the Industrial Revolution[3,4]. Such gases include carbon dioxide, nitrous oxide, and methane, all of which are known environmental pollutants. The reason greenhouse gases are taking a major toll on the environment is that they cause a heat trapping effect on the earth by not letting incident energy from the sun escape the atmosphere[2,5]. Increasing the earth's average temperature has resulted in effects such as drought and sea ice melting, and the worst may still be yet to come. Many advances are being made in the field of carbon capture and utilization[6] to slow or ideally stop the effects of global warming. Nevertheless, to properly deal with climate change, a new energy carrier must be used.

Recently, interest in H_2 as a green alternative fuel has increased. Although hydrogen is an attractive fuel, one major concern to the public is whether it will be a safe fuel to use. A comparison of the properties of H_2, gasoline and diesel are summarized in Table 2.1 below. In comparison to gasoline and diesel, hydrogen is more flammable that the other two fuels, showing a low flash point, wide flammability range[7,8]. However, H_2 has the highest auto-ignition temperature of 585°C and the highest research octane number (RON) of >130 [7], which dictates the fuel's resistance to detonation upon compression. Furthermore, H_2 does not have any long-term health effects[8], whereas gasoline can be carcinogenic due to the benzene present in the mixture that makes up the fuel[9].

***Table 2.1 Properties of hydrogen, gasoline, and diesel fuel*[7–12].**

Property	Hydrogen	Gasoline	Diesel
Colour	none	straw coloured	straw coloured
Odour	no	yes, characteristic	yes, characteristic
Phase	gas	liquid	liquid
NFPA code			
Health	0	1	0
Flammability	4	3	2
Reactivity	0	0	0
Energy density [MJ kg^{-1}]	143	46.4	45.4
Energy density [MJ L^{-1}]	0.0107*	34.2	34.6
RON	>130	87	30
Auto-ignition [°C]	585	246-280	210
Flash Point [°C]	-231	-45	62
Flammability Range in air [%]	4 - 75	1 - 7.6	0.6 - 5.5

* value reported at ambient pressure. H_2 has an energy density of 5.6 and 10.1 MJ L^{-1} in its liquid and compressed (to 700 bar) state, respectively.

In addition to being a clean and sustainable fuel, hydrogen is an attractive fuel for use due to its high mass energy density of 143 MJ/kg, which is just over 3x that of the other hydrocarbon fuels. A problem can however arise because contrary to liquid hydrocarbon fuels, H_2 is not very dense in its natural state[7], meaning that challenges arise where its storage is concerned. Of the available hydrogen storage technique, H_2 is most commonly stored as a compressed gas or as a liquid[10]. Each of those methods has their drawbacks whether it be the safety concerns associated to storing H_2 at high pressures of 700 bar or the energy required to liquefy hydrogen to be stored in a cryogenic tank at 21 K[10]. Hydrogen is also an attractive fuel because emission-free hydrogen-powered fuel cell electric vehicles are more clean and efficient than gasoline-fed internal combustion engines[13,14]. With that information summarized, it is possible to say that H_2 is as safe and attractive for use than traditional hydrocarbon fuels. It also has the very important advantage of being a clean energy carrier when produced by renewably powered water electrolysers.

Although hydrogen it is one of the most abundant elements on earth, it is not commonly found in its elemental state. As such, many methods have been developed for producing hydrogen [11,15,16]. The most common ways of producing H_2 are natural gas steam reforming, partial hydrocarbon oxidation and coal gasification, which together account for around 96% of the global H_2 production. All those mentioned methods produce high GHG emissions. The remaining 4% of

H_2 production occurs via water electrolysis, a carbon-free process[11,16–18]. Although fossil fuel-based methods for producing hydrogen may currently have a higher H_2 output, the environmental impact resulting from the carbon-based feedstock is too high to sustain over time[15,16,19]. As such, it is important to move towards clean H_2 generation for a sustainably future.

The clean utilization of H_2 as a fuel can be nicely described by the ideal of the "Hydrogen Economy", which explains the implementation of an energy cycle based on using hydrogen as the energy carrier of a completely sustainable system[20,21]. In short, renewably sourced energy, whether it be wind, tidal or solar, is used to produce hydrogen through water electrolysis. During electrolysis, the energy supplied to the system, is captured in the bonds formed in H_2. Once made, the H_2 is either immediately used to generate power in hydrogen fuel cells or is stored for later use. Not only do hydrogen fuel cells only emit water as a by-product but storing renewable energy in hydrogen solves the imbalance that occurs between renewable energy supply and demand.

2.2 Water Electrolysis

Water electrolysis, or electrochemical water splitting, is a process that uses electrical energy to convert water into oxygen and hydrogen through two half-cell reactions: the oxygen evolution reaction (OER) and the hydrogen evolution reaction (HER). The two half-cell reactions combine to yield the overall reaction shown in Reaction 2.1:

$$H_2O + \text{energy} \rightarrow H_2 + \frac{1}{2}O_2 \qquad \textbf{\textit{Reaction 2.1}}$$

Both the OER and HER have their own theoretical reduction voltage which together, describe the theoretical minimum amount of energy required to split water. This voltage is 1.23 V vs the reversible hydrogen electrode (RHE) at room temperature[21]. When running the water electrolysis process, various cell resistances and inefficiencies make the actual amount of energy required to split water much higher that the theoretical amount of 1.23 V. This extra input energy is referred to as the cell overpotential. Researchers have been studying various types of water electrolysis processes as well as changing their cell components and configurations to minimize the overpotential for water electrolysis[21–26].

Multiple different water electrolysis processes have been studied[15,20–23,26,27]. The most common methods to split water include high temperature electrolysis (HTE) using solid oxide

electrolysis cells (SOEC), photoelectrochemical (PEC) electrolysis, proton exchange membrane (PEM) electrolysis, traditional alkaline electrolysis, and anion exchange membrane (AEM) electrolysis.

2.2.1 High Temperature Electrolysis

HTE using SOEC is a process in which water is heated to steam at around 650-1000°C, which subsequently dissociates into H_2 and O_2[11,18]. As shown in Reactions 2.2 and 2.3 below, water goes into the cathode where hydrogen and oxygen anions are produced. Then, the anions migrate through a solid oxide electrolyte to the anode side of the cell to produce oxygen and generate electrons[20]. This process has an overall efficiency of around 40-60% with a voltage efficiency of around 81-86% when operating at moderately high currents of 0.3-2.0 A cm^{-2} at 0.7-1.5 V[15,18,20,26,28].

$$cathode: H_2O + 2e^- \rightarrow H_2 + O^{2-} \qquad \textbf{\textit{Reaction 2.2}}$$

$$anode: O^{2-} \rightarrow \frac{1}{2}O_2 + 2e^- \qquad \textbf{\textit{Reaction 2.3}}$$

HTE using SOEC can be fully sustainable and generally requires less electrical energy input than other electrolysis processes due to more favourable thermodynamics at higher operating temperatures. However, finding the appropriate materials to construct a SOEC and properly operating and maintaining the process safely, can be challenging at such high operating temperatures[20,21,26]. The process can present issues due to corrosion, sealing and thermal cycling[22].

2.2.2 Photoelectrochemical Electrolysis

PEC electrolysis processes are similar to photovoltaic (PV) electrolysis systems, however they combine the photovoltaic cell, which is in charge of transforming solar energy to electrical energy, and the electrolyser which uses the produced electrical energy to split water[20,21]. The PEC system therefore has a more favourable, compact design. During the PEC electrolytic process, the photocatalysts in an aqueous environment will absorb solar energy, creating an electron-hole pair. The charge that is obtained is then is used to split water[11]. The specific half-cell reaction in this process depends on the type of photocatalyst being used. For example, a system consisting of a TiO_2 anode and a Pt counter electrode would follow the mechanism below[29]. In Reaction 2.4, the

electron-hole pair is created, then O_2 is produced at the anode in Reaction 2.5, while H_2 is produced at the cathode in Reaction 2.6.

$$TiO_2 + 2h\upsilon \rightarrow 2e^- + 2h^+ \qquad \textbf{\textit{Reaction 2.4}}$$

$$anode: H_2O + 2h^+ \rightarrow \frac{1}{2}O_2 + 2H^+ \qquad \textbf{\textit{Reaction 2.5}}$$

$$cathode: 2H^+ + 2e^- \rightarrow H_2 \qquad \textbf{\textit{Reaction 2.6}}$$

The overall process yields efficiencies around 2-12%[15,20,27,30]. Those efficiency values make photovoltaic processes 25x more expensive that the fossil fuel alternative[11], therefore solar electrolytic cells are not yet efficient and feasible for industrial scale operation.

2.2.3 Traditional Alkaline Water Electrolysis

Alkaline electrolysers are one of the most industrially suitable electrolytic processes for producing hydrogen. In the alkaline process, hydroxide ions participate in the two half cell reactions as shown in Reactions 2.7 and 2.8[21].

$$cathode: 2H_2O + 2e^- \rightarrow H_2 + OH^- \qquad \textbf{\textit{Reaction 2.7}}$$

$$anode: 2OH^- \rightarrow \frac{1}{2}O_2 + H_2O + 2e^- \qquad \textbf{\textit{Reaction 2.8}}$$

Traditional alkaline electrolysers consist of electrode sheets held in a compartment containing highly concentrated KOH solution (~ 20 - 40 wt%), where the anode and cathode are separated by a diaphragm, which is made of asbestos, a ceramic or a microporous material[26,31,32]. This electrolyser configuration possesses gaps between the electrodes and the diaphragm, making the process inefficient due to high ohmic losses from the electrolyte, separator, gas bubble formation and circuitry[20,21,26]. Additionally, the employed diaphragm does not completely separate the gases, which can be problematic due to the low explosion limit of hydrogen in oxygen of 4 mol% H_2[32–34]. The high system losses of the traditional alkaline cell means it can only operate at low currents of 0.2-0.5 A cm^{-2} at 1.8-2.4 V and 60-80°C with voltage efficiencies of around 59-82%[18,28,35], making the operating cost of the process rather high. The alkaline environment does, however, come with its advantages; non-noble metal catalysts are very corrosion resistant in alkaline media, which allows for the use of an economical, active catalyst[18,23,31,36].

2.2.4 Proton Exchange Membrane Electrolysis

Proton exchange membrane water electrolysis (PEMWE) is an electrolytic process that offers a new cell design in an acidic environment. The cell consists of two endplates or bipolar plates on either side of the unit, immediately followed by two gas diffusion layers (GDL), which serve as current collectors, and a membrane electrode assembly (MEA) that is placed between the GDLs[26]. The MEA consists of a proton exchange membrane with the anode and cathode catalysts deposited either directly on the membrane [catalyst coated membrane (CCM) configuration], or on the GDLs [catalyst coated surface (CCS) method]. When using particle-base catalytic layers, proton exchange ionomers (PEI) are often used to bind the particles and to conduct protons (H^+). This electrolysis cell configuration is known as the "zero-gap" configuration, which results in a lower cell resistance due to the small inter-electrode gap resulting in a compact cell design[22]. The two reactions that take place in a PEMWE and are shown in Reactions 2.9 and 2.10 below[21].

$$cathode: 2H^+ + 2e^- \rightarrow H_2 \qquad \textbf{\textit{Reaction 2.9}}$$

$$anode: H_2O \rightarrow \frac{1}{2}O_2 + 2H^+ + 2e^- \qquad \textbf{\textit{Reaction 2.10}}$$

Employing a solid polymer electrolyte membrane instead of a diaphragm in the PEMWE process provides many operational advantages in comparison to the traditional alkaline electrolysis cell design, such as improved process efficiency, higher current density operation, lower gas crossover and differential pressure operation[23,26,31,32,37]. Although the PEMWE system possesses a favourable cell configuration and a high voltage efficiency of around 65-82% at moderately high currents of 0.6-2.2 A cm^{-2} at 1.8-2.2 V and 50-84°C[18,28,35], it does have its drawbacks. PEMWE occurs in an acidic environment with expensive membranes and ionomers such as Nafion™, requiring the use of noble metal catalysts and expensive cell components (bipolar plates, current collectors, etc.)[22,23,32]. Traditionally, the cathode is a platinum (Pt) -based material, while the anode is either a ruthenium (Ru) or iridium (Ir) metal or metal-oxide. At a cost of around 42, 22 and 161 CAD g^{-1} for Pt, Ru and Ir, respectively[38], this process is not ideal for industrial scale operation. Furthermore, while the Ru anode is more economical and better performing than Ir, it oxidizes easily at the potentials required for OER, which make it highly unstable[26].

2.2.5 Anion Exchange Membrane Water Electrolysis

Anion exchange membrane water electrolysis (AEMWE) is an emerging technology, used for its ability to produce hydrogen both efficiently and at low cost by combining the advantages of both PEMWE and traditional alkaline electrolysis. In AEMWE, water and electrons combine at the cathode to produce hydrogen and hydroxide ions as shown by Reaction 2.7. The hydroxide ions then migrate across the AEM to the anode, where they are used to produce oxygen, water, and electrons as shown by Reaction 2.8. In AEMWE, particle-based catalytic layers are formed using anion exchange ionomers (AEI) to bind the particles and to conduct OH^- ions through catalytic layer. Similar to PEMWE, using AEMs allows for an efficient compact cell design, which results in the same operational advantages of the PEMWE[28,33,39]. Figure 2.1 provides a side-by-side comparison of the traditional alkaline, PEM and AEM electrolysis processes.

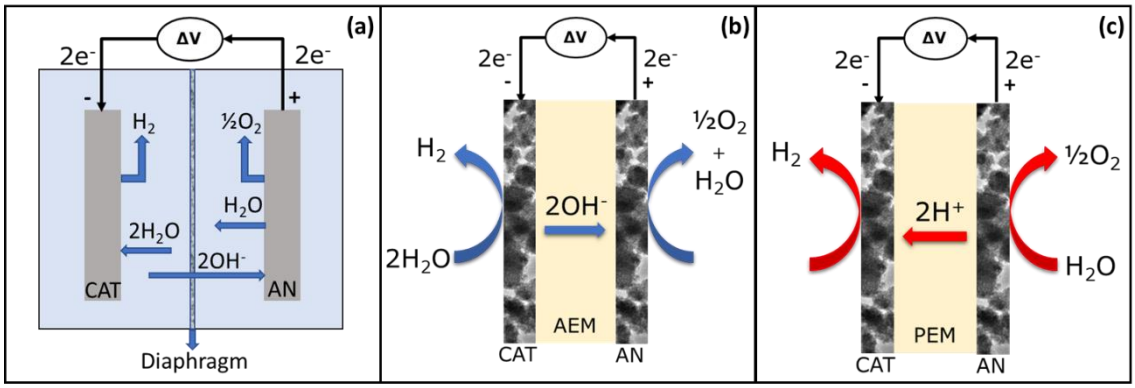

Figure 2.1: Schematic of the (a) traditional alkaline, (b) anion exchange membrane (AEM) and (c) proton exchange membrane (PEM) water electrolysis processes.

Like the traditional alkaline electrolyser, the AEMWE system operates in an alkaline environment, allowing for the use of low-cost non-noble metal catalysts and cell materials, such as nickel (Ni)[28,32,33,39], which is around 0.030 CAD g^{-1}[38], over 5000 x less expensive than iridium. Additionally, the use of an AEM allows for the use of low concentration alkaline electrolyte or distilled water[23,32], which are both more favourable to the high alkalinity of the traditional alkaline process. In AEMWE, membranes and ionomers are commonly made with hydrocarbon backbones and cationic groups for hydroxide ion conduction[23,32,33,40,41], which provides a more economically and environmentally favourable option to the PEMWE perfluorinated membranes such as Nafion™, which releases hydrogen fluoride (HF) upon chemical decomposition[33,42]. AEMWE, therefore, aims to combine the low-cost advantage of the traditional alkaline process with the high

efficiency the PEMWE process to result in a highly efficient, cost-effective green hydrogen production method. The AEMWE process typically operates between 0.2-1.0 A cm^{-2} at 1.8-2.2 V and 50-60°C. One draw important back to the AEMWE process is that it is currently still under Research and Development (R&D), compared to the PEMWE which is a mature technology for small scale operation[23,32]. Table 2.2 provides a side-by side comparison of some of the key advantages and disadvantages raised in the provided discussion of the electrolysis systems, along with their typical operating conditions and process efficiencies.

Table 2.2: Comparison of various water electrolysis systems.

Electrolysis System	Advantages	Disadvantages	Typical operating conditions	% Efficiency
High Temperature (HTE) [15,18,20,26,28]	• Favourable thermodynamics	• Expensive materials of construction • High temperature operation	650 – 1000°C 0.3 – 2.0 A cm^{-2} 0.7 – 1.5 V	~40 – 60[a] ~81 – 86[b]
Photoelectrochemical (PEC) [15,20,27,30]	• Solar powered	• Low process efficiency	---	~2 – 12[c]
Proton Exchange Membrane (PEM) [18,20,28,35]	• "zero-gap" cell design • Higher performance	• Expensive cell materials	50 – 84°C 0.6 – 2.2 A cm^{-2} 1.8 – 2.2 V	~67 – 82[b]
Traditional Alkaline [18,20,28,35]	• Low-cost cell materials	• Traditional cell design (high ohmic losses)	60 – 80°C 0.2 – 0.5 A cm^{-2} 1.8 – 2.4 V	~62 – 82[b]
Anion Exchange Membrane (AEM) [31]	• "zero-gap" cell design • Low-cost cell materials	• At laboratory R&D stage	50 – 60°C 0.2 – 1.0 A cm^{-2} 1.8 – 2.2 V	R&D

[a]net efficiency
[b]voltage efficiency
[c]efficiency based on hydrogen yield

Overall, in comparison to all water electrolysis systems, the AEM water electrolysis system is one of the most promising future green H_2 technologies because it occurs at moderate operating conditions, utilizes an attractive low resistance cell configuration and the alkaline environment allows the use of non-noble metal cell components, resulting in important cost savings.

2.2.6 Thermodynamics of Water Electrolysis

The water splitting process is an endothermic, thermodynamically unfavourable process with an enthalpy (ΔH) of 286 kJ mol_{H2}^{-1} positive Gibb's free energy (ΔG) of 238 kJ mol_{H2}^{-1} at ambient temperatures and atmospheric pressure[18]. It also has a change in entropy (ΔS) of 163.4 J mol_{H2}^{-1} K^{-1}, due to the increase in disorder going from a liquid to a gaseous phase[18]. It is, therefore, necessary to drive the decomposition of water by overcoming what is referred to as the equilibrium or reversible cell voltage, E^0_{rev}, which is related to the Gibb's Free Energy of the reaction, number of electrons transferred in the water splitting reaction, n=2 mol_{e-} mol_{H2}^{-1}, and Faraday's constant, F=96485 C mol_{e-}^{-1}, as shown in Equation 2.1.

$$E^0_{rev} = \frac{-\Delta G}{nF} \qquad \textit{Equation 2.1}$$

The equilibrium voltage is also the difference between the anode and cathode standard reduction potentials, E^0_{AN} and E^0_{CAT}, respectively, as shown by Equation 2.2 below[22].

$$E^0_{rev} = E^0_{AN} - E^0_{CAT} \qquad \textit{Equation 2.2}$$

In an alkaline environment at pH 14, the cell potential at the anode side is -0.83 V vs the standard hydrogen electrode (SHE), while the cell potential at the cathode side is 0.40 V vs SHE. This means that at ambient temperature and atmospheric pressure, the thermodynamic minimum cell voltage required to split water, E^0_{rev}, is 1.23 V. When operating at non-standard conditions, the equilibrium cell voltage is adjusted using the Nernst equation (Equation 2.3) as follows[18,43]:

$$E_{rev} = E^0_{rev} + \frac{R'T}{nF} \ln \frac{a^2_{H_2} a_{O_2}}{a^2_{H_2O}} \qquad \textit{Equation 2.3}$$

Where R' represents the universal gas constant [8.314 J $mol^{-1}K^{-1}$], T the temperature [K], and a is the activities of the species involved in the water splitting process.

In practical electrolytic processes, there are many reasons for which the actual cell voltage required to carry out the reaction E_{cell}, is much higher than the reversible cell voltage. This is due to cell overpotential, η, or in other words the excess energy required for the reaction to occur. The cell overpotential can stem from various sources, such as the activation losses for the anode and cathode half-cell reactions to occur (η_{AN} and η_{CAT}, respectively) as well as ohmic or IR losses (η_{IR}),

which are associated to resistances to transport of ions in the electrolyte, transport of bubbles in the system, the membrane, as well as electrical circuitry[18,20,22,26,43]. Equation 2.4 shows how the anode, cathode and IR losses affect the cell potential of an electrolysis cell.

$$E_{cell} = E_{rev} + |\eta_{AN}| + |\eta_{CAT}| + |\eta_{IR}| \qquad \textit{Equation 2.4}$$

Although IR losses can contribute significantly to the total cell overpotential, energy losses due to activation losses on both the anode and cathode are generally most important[18,22,26].

The activation polarization of the anode and cathode are the amount of excess energy required for electron transfer at the electrode interface[18] at a certain applied current, and can be described using the Butler-Volmer equation. At high enough overpotentials and in the absence of mass transfer limitations, the Butler-Volmer equation can be simplified to the Tafel equation, shown by Equations 2.5 and 2.6, which described the charge transfer or kinetics occurring at the anode and cathode, respectively.

$$\eta_{AN} = m \cdot \log(j) + b = \frac{2.303RT}{\alpha_{AN} nF} \log(j) - \frac{2.303RT}{\alpha_{AN} nF} \log(j_0) \qquad \textit{Equation 2.5}$$

$$|\eta_{CAT}| = m \cdot \log(|j|) + b = \frac{2.303RT}{\alpha_{CAT} nF} \log(|j|) - \frac{2.303RT}{\alpha_{CAT} nF} \log(j_0) \qquad \textit{Equation 2.6}$$

In Equations 2.5 and 2.6, α_{AN} and α_{CAT} are the anode and cathode charge transfer coefficients, which describe the current response to changes in overpotential, or more specifically the fraction of overpotential that serves to lower the reaction kinetic energy barrier at the electrode-electrolyte interface[18]. j_0 is the exchange current density of the reaction, which represents the reaction rate under equilibrium potential, or rather when the reaction overpotential is zero. The term *m* shown in Equations 2.5 and 2.6 represents the Tafel slope with units of mV dec^{-1}, is often used to describe the efficiency of catalysts in carrying out the OER or HER. The lower the Tafel slope, the less energy is input into the system to carry out the reaction.

2.3 Anode Catalytic Layers in AEMWE

In AEMWE, in comparison to the hydrogen evolution reaction at the cathode, the oxygen evolution reaction at the anode presents a complex mechanism of multiple electron transfer steps. This means that the overpotential required at the anode is larger than that at the cathode, making the anode a crucial cell component to optimize[18,44,45]. As previously mentioned, common catalysts

used as anodes in AEMWE cells are non-noble metal catalysts, due to their high activity and stability in an alkaline environment, as well as their favourable cost in comparison to their noble metal performance equivalent[23,31,32,46]. Various transition metals have been evaluated for oxygen evolution in alkaline media showing that Ni-based catalysts, among other first row transition metal-based catalysts, are some of the most promising materials for enhanced oxygen evolution[32,44,46–53]. This is likely due to the relative conductivity of nickel, and its ability to easily transition from $Ni(OH)_2$ to the OER-active NiOOH phase under applied currents[47,48,52], and to nickel's more favourable bond strength of reaction intermediates, which can be related to its relative number of d electrons in the metal cation[52,54].

When forming an anode layer in AEMWE, two general groups can be used. The first group, Group A, is one consisting of the modification or enhancement of a porous support, often the GDL used in the AEMWE cell, usually formed, and utilized without the use of an ionomer. These catalytic layers can be produced using multiple methods such as further enhancing the surface area of a Ni mesh by hot-dip galvanization in a zinc bath with subsequent leaching in potassium hydroxide[55], corrosion induced coating of a Ni foam in an Fe precursor solution[56], compressing and sintering Ni powders into a Ni foam[57], electrodeposition onto a conductive porous support (carbon paper, Ti foil) from a Ni or Ni-based precursor solution[58,59], magnetron sputtering from a Ni target onto a carbon paper[60], and more complex methods such as coprecipitation (electrodeposition and electrophoretic deposition) of metal precursor salts and powders onto a Ni mesh, followed by further activation of the catalytic layer by thermal decomposition of Ni and Co precursor salts[61,62].

The second group, Group B, is one where catalyst layers are particle-based, formed either by coating particles from a catalyst ink onto a GDL or directly onto a membrane using an AEI to bind the particles to the GDL/membrane, and to facilitate hydroxide ion conduction throughout the catalytic layer[46,63–80]. In this method, a wide variety of catalyst synthesis methods can be used to produce active particles or powders, then an electrode fabrication method must be used to cast or deposit the particles, along with the ionomer onto the GDL or membrane. One of the most common electrode fabrication methods is spray coating of a catalyst ink, which is a well mixed dispersion of the catalyst and ionomer in a solvent. However, many other electrode fabrication methods exist, such as dry spraying (layer deposition from dry powder followed by passing it

through a calender, then hot rolling/pressing it), doctor blade or decal transfer of an ink, painting of an ink, screen printing of an ink, and spreading of a paste[78,81]. A representative diagram of both groups of catalytic layer preparation is shown in Figure 2.2.

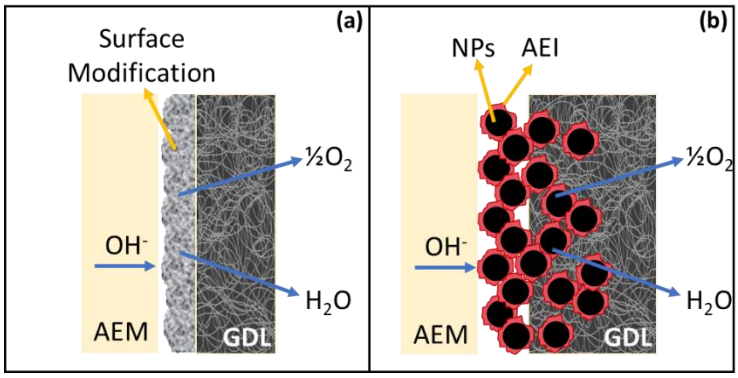

Figure 2.2: Representative diagram of the anode layer of (a) surface modified porous supports (Group A) and (b) particle-based layers with ionomers (Group B).

One of the biggest advantages of the modified surface catalytic layers (Group A), is that anode layers can more easily be produced at large scale as they often require less processing steps. By directly modifying the anode GDL of the AEMWE to form the anode catalytic layer, both producing a novel anode catalytic structure and casting it onto the GDL are combined, cutting down a significant step in comparison to the particle-based catalytic layers (Group B). Techniques such as electrodeposition also allow for the formation of uniform films on various substrates at varying production scales[18]. Additionally, depending on the electrode preparation technique, a more stable contact can be formed between the GDL and the catalysts, promoting stability at high current densities and for long-term operation[71]. In terms of disadvantages, depending on the selected method, the energy and operating conditions required to form the catalytic layer may be unfavourable for industrial scale production. Additionally, in certain Group A catalytic layers, such as those formed by magnetron sputtering, employing thicker catalyst layers can be disadvantageous due to the lack of an ionomer to aid with ionic transport[81,82].

Particle-based catalyst layers on the other hand (Group B), are advantageous as they allow for the tunable formation of a porous anode layer with high access to active sites. Not only can accessible active sites be significantly increased with the choice of a catalyst with a large surface to volume ratio, but the method of electrode fabrication, along with the choice and amount of ionomer can impact the porosity of the formed catalytic layer[83], which can lead to more efficient

anode performance. Additionally, with the ionomer connecting particles and creating channels throughout the catalytic layer for ion and mass transport, the catalyst loading can be optimized for enhanced performance. While common electrode fabrication techniques for particle-based layers may not be particularly complex or energy demanding, similar disadvantages as in Group A are still present as the selected particle synthesis method will dramatically impact the feasibility of producing large scale anodes for AEMWE. Furthermore, while ionomers can be advantageous in particle-based anodes, they are not necessarily very stable[78,84], impacting the overall anode performance over time.

As evident from Figure 2.2b, the catalyst and ionomer in particle-based anodes must work closely to carry out the OER. It is, therefore, imperative to properly pair catalyst and ionomer together, in the right amounts, to yield an efficient AEMWE anode with optimal amounts of three-phase boundaries[81] and optimal interactions between the reactants (OH^-), products (H_2O and O_2) and electrons. The aim of this review is to summarize and highlight recent (from 2015 onwards) research efforts on the development of lab synthesized Ni particle-based anode catalytic layers utilizing AEIs tested in AEMWE systems. While some authors have tested their lab synthesized particles in two-electrode alkaline water electrolyser configurations[85,86], the focus here will be on catalysts tested specifically in AEMWE devices as they are more practical. Both catalytic layers formed by coating particles on a GDL, or a membrane will be examined, and an analysis of their potential for industrialization will be provided. Additionally, an overview of the use of AEIs in Ni particle-based anode catalytic layers will be provided, covering the effects of ionomer loading and type on the electrochemical performance of the Ni anode catalysts.

It should be noted that particles can also be deposited without the use of an ionomer, such as in the case of electrophoretic deposition[61,62] or the compressing and sintering of Ni powders into a Ni foam[57], however for the purpose of this review, directly depositing particles onto a GDL without the use of an ionomer will be considered as a Group A catalytic layer, or rather a surface modified GDL. Additionally, Group A catalytic layers, where ionomers are added on top of the modified surface, will not be considered in this analysis. Such a case was used in the work of Xiao *et al.*[71], where they prepare fluoride-incorporated self-supported Fe_xNi_yOOH nanosheet arrays by dissolved oxygen and galvanostatic corrosion onto a compressed Ni foam, then dip-coated the prepared layers into an ionomer solution to provide OH^- transport.

2.3.1 Ni Particle-based Anodes Layers in AEMWE

To highlight recent research efforts in the development and testing of lab synthesized Ni-based particles as anodes in AEMWE devices, the following section provides an overview of said Ni OER catalysts, used in combination with an ionomeric binder in an AEMWE. While particle-based catalytic layers will strongly depend on the ionomer selection, the reported role and impact of the ionomers used will not be discussed until Section 2.3.2 of this review. To offer a perspective on the potential of industrialization of these catalysts as large-scale electrolysis anodes, their synthesis method and method of electrode fabrication is summarized in Tables 2.3 and 2.4, with supplemental information on all methodology provided in Tables A.1 and A.2. The best-achieved performance reported in the summarized articles is also provided in Tables 2.3 and 2.4. While many factors affect anode performance in an AEMWE, for the sake of simplicity, only the anode (AN) loading, current density, *i*, voltage, *E*, temperature, *T*, and electrolyte type and concentration are reported. The cathode (CAT) catalyst material has also been identified as being either PGM or non-PGM.

Table 2.3: Part 1: Ni-based anode catalyst synthesis, electrode fabrication and associated AEMWE performance.

Ni-based AN	Particle Synthesis	Electrode Fabrication	AN loading [mg cm^{-2}]	CAT Type	*i* [A cm^{-2}]	*E* [V]	*T* [°C]	Electrolyte	Ref.# (year)
$NiCoO_x$, $NiFeO_xH_y$, **$NiCoO_x$:Fe**, $NiCoFeO_x$ NPs	*Hydrothermal method* at 150°C for 3 h	Spray coat ink, then additional ionomer onto a Pt-coated sintered titanium frit at 80°C.	3	PGM	0.9	2.39	50	nanopure H_2O at AN	[46] (2019)
Fe_xNi_yOOH-20F powder	*Hydrothermal method* at 100°C for 12 h.	Spray coat ink onto both sides of a compressed Ni foam.	4.8	PGM	0.13	1.8	80	water	[71] (2021)
Ni, $Ni_{90}Fe_{10}$, $Ni_{90}Fe_{10}$/50 wt% CeO_2 NPs	*Chemical reduction* using $NaBH_4$ at RT.	Spray coat ink onto a membrane at 60°C.	6	PGM	1.32	1.80	50	1 M KOH	[63] (2019)
Ni, **$Ni_{90}Fe_{10}$**, $Ni_{80}Fe_{20}$, $Ni_{90}Fe_{10}$/ 10 wt% CeO_2, $Ni_{80}Fe_{20}$/ 10 wt% CeO_2 NPs		Spray coat ink onto a gold-coated titanium felt at 60°C.	5	PGM	0.8	1.72	50	1 M KOH	[66] (2021)
Ni_2Fe_1 nanofoam	*Chemical reduction* using $NaBH_4$ at RT.	Paint ink onto a platinized titanium GDL.	3	PGM	5.3	1.8	60	1 M NaOH	[80] (2020)
NiO nanosheets	*Chemical reduction* using $NaBH_4$. Anneal in air at 500°C for 6 h.	Spray coat ink onto a carbon paper GDL at 60°C.	5	PGM	~ 0.03	2*	RT	1 M KOH	[64] (2020)
$NiCo_2O_4$ particles	*Coprecipitation using NaOH*. Calcinate at 325°C for 4 h.	Spray coat ink onto a Ni foam GDL on a hot plate.	10	non-PGM	0.135	1.85	50	10 wt% KOH	[73] (2017)
$NiCo_2O_4$ particles		Spray coat ink onto a Ni foam GDL or **membrane** at 50°C.	10	non-PGM	0.147	2	45	10 wt% KOH	[78] (2019)
$NiCo_2O_4$ particles		Spray coat ink onto a Ni foam at 120°C. Heat CCS to 325°C for 15 min.	10	non-PGM	0.12	1.8	65	10 wt% KOH	[70] (2016)
$Ni_{0.6}Co_{0.2}Fe_{0.2}$ particles	*Laboratory synthesized**	Spray coat ink, then additional ionomer onto a Au-coated Ti felt at 60°C.	5	non-PGM	1.15	2	50	1 M KOH	[87] (2021)

Notes: In bold is the material or the specifications for which the performance is reported. *Synthesis method not specified.

Table 2.4: Part 2: Ni-based anode catalyst synthesis, electrode fabrication and associated AEMWE performance.

Ni-based AN	Particle Synthesis	Electrode Fabrication	AN loading [mg cm^{-2}]	CAT Type	*i* [A cm^{-2}]	*E* [V]	*T* [°C]	Electr-olyte	Ref.# (year)
NiFe (2:1)-LDH/KB (2/1)	*Gelation-deflocculation method* at RT, letting sln sit for a few days	Spray coat ink onto a carbon paper.	2.5	PGM	1	1.59	80	1 M KOH	[76] (2020)
NiFe-BTC-GNPs MOF	*Chemical reduction* at 85°C for 24 h under stirring. Extensive material recovery protocol.	Coat ink onto a nickel foam. Hot press the CCS + membrane 5 MPa at 40°C for 2-3 min.	2.5	non-PGM	1.15	1.85	70	0.1 M KOH	[77] (2020)
$Ni_{0.9}Fe_{0.1}Co_{1.975}Li_{0.025}O_4$, $Ni_{0.9}Fe_{0.1}Co_2O_4$ particles	*Electrochemical precipitation* by applying 10 V for 1 h. Calcinate at 325°C for 4 h in air.	Spray coat ink onto a Ni foam GDL on a hot plate. Sinter CCS at 325°C for 15 min.	10	non-PGM	0.143	1.85	50	10 wt% KOH	[79] (2018)
$NiMnO_x$ NPs	*Oxalate method*, adding H_2O_2 at 80°C to form precipitate. Calcinate at 350°C for 120 min.	Spray coat ink onto a membrane.	3	PGM	0.53	2	80	1 M KOH	[65] (2020)
$NiFeO_x$ 70wt% / KB, $NiFe_2O_x$ 70 wt%/KB NPs	*Oxalate method*, adding H_2O_2 at 80°C to form precipitate. Calcinate at 450°C for 120 min.	Spray coat ink onto a carbon cloth backing GDL.	2.5	PGM	0.65	2	50	1 M KOH to AN, N_2 at CAT	[67] (2020)
$NiMn_2O_4$ (20 wt%)/CNF, **$NiCo_2O_4$ (40 wt%)/CNF** fibers	*Electrospinning method* applying 17 kV to the sln jet at 21°C and <40% RH. Stabilize at 270°C in air for 30 min. Carbonize at 900°C for 1 h in He. Oxidize at 350°C in static air for 1 h.	Spray coat ink onto a carbon cloth backing GDL.	~2.5 - 3	PGM	0.303	1.8	50	6 M KOH to AN, N_2 at CAT	[68] (2019)
$NiCo_2O_4$ particles	*Thermal decomposition* at 338 K (65°C). Calcinate at 648 K (375°C) for 20 h. Ball mill for 12 h.	Spray coat ink onto a **Ti fibre felt GDL** or coat ink onto a membrane.	10	PGM	0.1	1.65	60	0.1 M NaOH	[69] (2018)
commercial $NiFe_2O_4$ NPs	N/A	Spray coat ink onto a stainless fiber paper.	2	non-PGM	1	1.9	60	1 M KOH	[72] (2017)
commercial $NiFe_2O_4$ NPs	N/A	Spray coat ink onto a Ni fiber paper. Dry CCS at 80°C for 20 min.	2	non-PGM	2	2.13	60	1 M KOH	[74] (2020)
commercial $NiFe_2O_4$ NPs	N/A	Spray coat ink onto a 316L sintered SS fiber felt. Dry CCS at 80°C for 20 min.	2	non-PGM	1	1.9	60	1 M KOH	[75] (2017)

Notes: In bold is the material or the specifications for which the performance is reported. "sln" is short for solution.

In a recent study, multiple Ni-based catalysts were studied in both a three-electrode cell and an AEMWE to observe changes in their relative catalytic behaviour[46]. The authors also tested some Co-based catalysts and an IrO_x benchmark catalyst. The catalysts were synthesized via modified hydrothermal method, and for AEMWE testing, the synthesized catalyst inks were spray coated onto a Pt-coated Ti frit, with an extra layer of ionomer added on top. Of all the tested Ni-based catalysts, $NiFeO_xH_y$ was the most active OER catalysts in a three-electrode cell in 1 M KOH, however when tested in an AEMWE with nanopure water at the anode, this catalyst exhibited the worst performance. Conversely, the NiCo-based materials, which did not perform as well in a three-electrode cell, showed high AEMWE activity. In the study, the authors observed that a high electrical conductivity of the as-synthesized catalysts generally correlated to high activity in a water-fed AEMWE, where other variables such as catalyst composition and catalyst interactions with the ionomer may slightly alter this trend. Of the tested catalysts, $NiCoO_x$:Fe exhibited the highest performance in an AEMWE of around 0.9 A cm^{-2} at 2.39 V at 50°C in nanopure water using a Pt black cathode, which was better than IrO_x. In this material, the Fe was added to $NiCoO_x$ after the hydrothermal synthesis by adsorption from a $FeCl_2$ aqueous solution. While adding Fe by adsorption to $NiCoO_x$ slightly increased AEMWE activity in comparison to the one-step hydrothermally-prepared $NiCoFeO_x$, the performance of $NiCoO_x$:Fe more severely degraded over their 3 h stability test at 200 mA cm^{-2}, which was proposed to be due to Fe dissolution under OER conditions. Long-term catalyst stability is another important issue to address in industrial catalysis, as is briefly discussed in a review on durability-limiting factors in AEMWE[84].

In our previous works[63,66,88], we tested various NiFe-based nanoparticles with and without CeO_2 in both a three-electrode cell and a single-cell AEMWE using a 60 wt% Pt/C cathode. For comparison, commercial Ir black was also tested as an anode in the AEMWE. The materials were synthesized by chemical reduction of the precursors in ethanol by adding $NaBH_4$ and the electrodes were prepared by spray coating a catalyst ink onto either a membrane[63] or a gold-coated Ti GDL[66]. When evaluating various combinations of Fe and CeO_2 incorporation into the Ni catalysts in a three-electrode cell in 1 M KOH[88], it was observed that the $Ni_{80}Fe_{20}$ catalyst was the best performing of all catalyst, including Ir black, while the $Ni_{90}Fe_{10}$ catalyst was the most stable Ni-based material. Interestingly, in an AEMWE at 50°C in 1 M KOH[66], the $Ni_{80}Fe_{20}$ catalyst showed poor performance, while the $Ni_{90}Fe_{10}$ electrode showed the best performance of the tested Ni-based materials achieving 0.8 A cm^{-2} at 1.72 V. In the electrolyser, Ir black was better performing

than all Ni-based materials. The poor performance of the $Ni_{80}Fe_{20}$ electrode in the electrolyser was suggested to be related to the instability of Fe when present in higher amounts under operating conditions. Like in the three-electrode cell testing, the preliminary durability of the materials with 10 at% Fe was more stable than the materials with 20 at% Fe in an AEMWE tested at 0.5 A cm^{-2} in 0.1 M KOH for 12 h, which was proposed to be from increased Fe dissolution under operating currents. With respects to the ceria-containing materials, their overall catalytic activity was generally lower than their metallic equivalents, possibly due to the low electronic conductivity of CeO_2 introducing an additional ohmic resistance to the materials. However, evidence of decreased charge transfer resistance with the CeO_2-containing materials was observed in the AEMWE experiments, likely due to beneficial electronic effects that CeO_2 has on NiFe. Furthermore, when operating in 0.1 M KOH[66], the $Ni_{80}Fe_{20}$/ 10 wt% CeO_2 catalyst showed the best Ni-based AEMWE performance after IR-correction, which was suggested to be related to ceria's reducibility and oxygen storage capacity, promoting electrochemical activity by favourably altering the local pH of the electrode surface within the catalyst layer.

Similar to our above-mentioned work, other authors[64,80] have investigated chemical reduction using $NaBH_4$ as a synthesis route to producing Ni-based catalysts for OER in AEMWE devices. Li *et al.*[80] developed 3D porous Ni_xFe_y nanofoams (NF) in their previous work[89], by injecting a Ni and Fe precursor solution into an $NaBH_4$ solution under stirring at RT, as opposed to adding the $NaBH_4$ solution to the precursor salt solution. In their work, they showed that of the tested Ni and Fe compositions, the Ni_2Fe_1 NF electrode had the highest OER performance in a three-electrode cell in 1 M KOH. As such, more recently[80] they used the active Ni_2Fe_1 NFs in a study where they investigated the impact of synthesized AEIs on AEMWE anode performance. In their work, the electrodes were prepared by painting a catalyst ink onto a platinized Ti GDL. When using a PtRu/C cathode, they achieved a current of 5.3 A cm^{-2} at 1.8 V in 1 M NaOH at 60°C. They also tested their cell configurations in pure water at 85°C, where the Ni_2Fe_1 NF anode achieved currents of 2.7 and 0.906 A cm^{-2} at 1.8 V when paired with a PtRu/C and Ni_9Mo_1/C cathodes, respectively.

In another study[73], multiple Ni-Co spinel oxide catalyst synthesis routes were investigated for the promotion of the OER in alkaline media. The synthesis methods include coprecipitation by NaOH, thermal decomposition of hydroxides, microemulsion, sol-gel, coprecipitation by NH_4OH

and thermal decomposition of nitrate. Each of these methods was followed by catalyst calcination at an optimized temperature of 325°C for 4 h. Of the 6 tested synthesis routes, the coprecipitation by NaOH method to produce Ni-Co oxides yielded the highest OER activity in a three-electrode cell in 1 M KOH. With the synthesis method established, the authors proceeded to evaluate the effects of electrocatalyst composition on OER activity, finding that the $NiCo_2O_4$ catalyst was the best performing material, likely due to its catalyst surface composition, allowing for a higher occurrence of non-stoichiometric sites for charge transfer, and its higher electron conductivity. To evaluate the performance of the optimized catalyst in an AEMWE, the authors spray coated the material onto a Ni foam GDL using three different ionomeric binders. In 10 wt% KOH at 50°C, the $NiCo_2O_4$ anode catalyst, paired with an anion-selective binder, achieved a current density of 0.135 A cm^{-2} at 1.85 V using a Ni foam cathode.

In a recent study[67], NiFe-based OER catalysts made via the "oxalate method" were investigated in an AEMWE. This patented synthesis method[90] involves dissolving precursor salts in water at 60°C with added oxalic acid, then neutralizing the solution with NaOH. Then, hydrogen peroxide is added to the solution at 80°C and the metal precipitate is formed. The obtained material is calcinated at 450°C for 120 minutes. In this work, the authors form the anode electrolysis layer by spray coating the NiFe-based anodes with 30 wt% ketjen black (KB) onto a carbon cloth backing. They evaluated two compositions of the NiFe catalyst, namely $NiFeO_x$/KB and $NiFe_2O_x$/KB. The $NiFeO_x$/KB outperformed the electrode with higher iron content, reaching a current of 0.65 A cm^{-2} at 2 V and 50°C, using a Pt/C cathode and feeding 1 M KOH to the anode and humidified N_2 to the cathode. However, performance degradation of the $NiFeO_x$/KB electrode was evident over a 500-h accelerated stability test at 25°C, cycling between 1 and 1.8 V. As for the $NiFe_2O_x$/KB electrode, its AEMWE performance showed strong activation control in its polarization curves, which was proposed to be related to differences in adsorption strength of oxygen species onto the catalyst, or differences in the synergistic role of the phases in the material in catalysing the reaction.

An original, one-pot procedure to synthesize nanometer-sized NiFe (2:1) layered double hydroxides (LDH) was reported, and the application of said materials as OER catalysts in a three-electrode cell and in an AEMWE with a Pt/C cathode was evaluated[76]. The NiFe-LDH synthesis method involved a spontaneous gelation-deflocculation method at RT, a process which takes a few

days to occur, and the material was used as an anode in an AEMWE by spray coating the NiFe-LDH/KB (2/1) onto a carbon paper GDL. In a three-electrode cell configuration, the NiFe-LDH material showed higher OER performance than the selected commercial IrO_x reference electrode in 1 M KOH electrolyte. This high performance was suggested to be related to the material's higher surface area, owing to its small size. These results are consistent with the AEMWE experiments, showing that the NiFe-based anode outperformed IrO_x, achieving a current of 1 A cm^{-2} at 1.59 V in 1 M KOH at 80°C. The NiFe-LDH material was also more stable that IrO_x under operating conditions of 1 A cm^{-2} at 80°C for several hours. The authors do, however, recommend replacing the KB carbon support used along with their NiFe-LDH by an oxidation-resistant material to further improve electrode stability.

Recently, graphene-nanoplatelet-supported NiFe metal-organic frameworks (MOF) were reported as active and stable anodes in AEMWE[77]. The material was synthesized by first mixing Ni and Fe precursors, graphene powder (GNP) and trimesic acid (BTC) into H_2O: N,N-dimethylformamide (DMF):EtOH (1:1:1), then heating the reaction solution to 85°C for 24 h under stirring. The resulting NiFe-BTC-GNP MOF material was evaluated in a three-electrode cell in 1 M KOH and compared to Ni-BTC and NiFe-BTC, as well as commercial IrO_2 and an electrodeposited NiFe LDH. Of all the tested catalysts, the NiFe-BTC-GNP electrode provided the highest OER performance, which was ascribed to the synergistic effect between Ni and Fe in promoting the reaction, as well as the high electrical conductivity and specific surface area of the GNPs, promoting electron transfer and increasing access to active sites. The authors evaluated the NiFe-BTC-GNP MOF as an anode in AEMWE with a $MoNi_4/MoO_2$ nanoparticle cathode, where the MEA was formed by hot pressing, at 5 MPa and 40°C, the anode and cathode CCS electrodes to a pre-treated membrane. The non-PGM cell achieved 1.15 A cm^{-2} at 1.85 V in 0.1 M KOH at 70°C. In this study, AEMWE performance was also evaluated in ultrapure water, however the authors introduced an additional OH^- transport pathway to regenerate the MEA conductivity and pH gradient during operation. The non-PGM cell achieved 0.54 A cm^{-2} at 1.85 V at 70°C in ultrapure water with the additional OH^- pathway. Additionally, in this cell configuration, AEMWE performance was relatively stable under an applied voltage of 1.85 V for around 72 h at 50°C with a degradation rate of 0.27 mA h^{-1}.

Other methods were used to synthesize Ni-based particles for AEMWE applications, such as the electrochemical synthesis of Li-doped NiFeCo oxides[79], the electrospinning method to produce $NiMn_2O_4$ and $NiCo_2O_4$ oxide particles supported on carbon nanofibers (CNF)[68] and the thermal decomposition method to produce $NiCo_2O_4$ particles[69]. We refer the reader to their works for more details on their studies. We have also summarized the performance of a few commercial Ni-based particle anodes in Table 2.4 for the reader's reference.

When analyzing the particle synthesis methods from a chemical or process engineering point of view, practicality and safety in producing the materials is very important. Procedures which require large energy inputs, such as operating at high temperatures or pressures, will increase the operating cost of producing the Ni-based anodes. Additionally, operating at more severe operating conditions can be hazardous and unfavourable when handling large scale equipment. A few observations with respects to the operating conditions of the synthesis methods can be made following the analysis of the articles in Tables 2.3 and 2.4. The chemical reduction, coprecipitation using NaOH, gelation-deflocculation and electrochemical precipitation methods occur at room temperature, which can be safer and more economical than processes requiring heat, such as the hydrothermal method or the thermal decomposition method. However, in some cases, a calcination step followed the initial synthesis step to further treat the catalysts, adding a heat requirement to the catalyst preparation steps. Calcinating a material at an optimal temperature can be essential further modifying the properties of an electrocatalyst for optimal electrochemical performance[73,91,92], indicating a potential trade-off between the energy require to develop a material and the activity of the resulting catalyst. Additionally, some materials can require multiple thermal treatments in their production, such as in the case of the electrospun $NiMn_2O_4$ and $NiCo_2O_4$ oxide particles supported on carbon nanofibers (CNF)[68]. Not only can additional processing increase the overall energy requirement of the process, but it can also increase the man-power requirement to produce the Ni anode materials, which will in turn increase the operating cost of the process. In the case of the electrochemical precipitation and the electrospinning methods, external power supply was necessary to produce the particles. When producing the $Ni_{0.9}Fe_{0.1}Co_{1.975}Li_{0.025}O_4$ particles[79], 10 V was applied to the precursor solution for 1 h to precipitate the material. When producing the electrospun $NiMn_2O_4$ and $NiCo_2O_4$ oxide particles supported on carbon nanofibers (CNF)[68], an electrical field of 17 kV was applied to the solution

jet. Applied voltage is another parameter to account for when assessing energy requirements at industrial scale.

In terms of electrode preparation methods, most of the above-mentioned authors are spray coating a catalyst ink onto a GDL or a membrane. In comparison to painting a catalyst layer for example, spray coating a catalyst ink can aid in the formation of a more favourable porous catalytic layer by controlling the evaporation rate of the catalyst ink as it is deposited onto the target surface. The evaporation rate of the solvent in the ink can be controlled with the conditions of the spraying apparatus as well as the temperature of the target support. This temperature can however be limited to the thermal stability of the membrane and ionomer used. Having a more porous layer can help with mass transport throughout the catalytic layer and help provide better access to active sites. While spray coating can produce efficient catalytic layers, further research could be done on evaluating and comparing the electrochemical performance of different electrode preparation methods for a same catalyst to find a more optimal catalyst layer architecture, maximizing the potential of the electrocatalyst in an AEMWE[81]. Another very important consideration for the formation of optimal catalyst layers is the formulation and preparation method of the catalyst ink used in fabricating the electrode. Multiple complex interactions occur between the constituents of a catalyst ink, which can affect the resulting microstructure of the catalyst layer and its electrochemical performance[93]. These complex systems are further discussed in a recent review of fuel-cell catalyst layer inks by Weber's research group[93]. Additionally, the mixing method of the catalyst ink must also be carefully considered to produce an optimal ink dispersion, while not damaging the ink constituents (catalyst and ionomeric binder). Most authors use a form of ultrasonication (ultrasonic bath or probe) to mix their catalyst ink, however some use stirring[46], or ball-milling[76].

While much research into the development of novel Ni-based materials for oxygen evolution in alkaline media has been done[18,36,44,50,51,94], not many of those produced catalysts were subsequently tested in a working AEMWE. While very informative, simply using the three-electrode cell performance of novel catalysts to determine whether they are active or not, can be misleading in the development of active catalysts in an AEMWE system as many additional factors are introduced when moving to the AEM electrolyzer. Factors that can influence the electrochemical performance of a catalyst in an AEMWE could be related to the design of the

MEA, the materials used for the MEA or other cell components, or the selected operating conditions of the electrolyser[81]. Every type and composition of electrocatalyst can also respond different to the new factors it is exposed to in an AEMWE. The presence of these additional factors is clear in the summarized articles where the relative activity of the tested catalysts in a three-electrode cell is not always consistent with the relative activity of the catalysts in an AEMWE. Such is the case for example, for our $Ni_{80}Fe_{20}$ catalyst[66,88], as previously discussed. This topic was addressed in the works of Boettcher's research group[46], where they observed that the electrical conductivity of a catalyst is likely a better activity descriptor for assessing the activity of a catalyst in an water-fed AEMWE. It is, therefore, important to test multiple versions of developed materials in an AEMWE, and not simply the best performing catalyst based on the results found in a three-electrode cell electrochemical evaluation. Since it is more economical and time saving to simply test the best few catalysts in an AEMWE, researchers should also further investigate other activity descriptors for assessing potential for active anodes in an AEMWE. In this way, the most active catalysts for AEMWE can be more accurately identified. This was touched on in a recent study covering the establishment of baseline three-electrode cell OER performance in alkaline media, in an effort to better project device-level performance of analyzed catalysts[95]. Furthermore, utilizing techniques, such as the in-situ half-cell AEMWE analysis with reference electrodes from the works of Faid *et al.*[64], could be very useful for better understanding the electrochemical performance of the novel anode catalysts when in an electrolysis cell.

It should be noted that as there are many inconsistent electrolyser variables and experimental parameters between the summarized articles, electrochemical performance in an AEMWE between the studies will not be directly compared. One of the parameters that can significantly affect cell performance is the selected cathode material. Many authors studying anode electrocatalysts will select a PGM-based cathode to provide a more reliable performance. While utilizing PGM cathodes to study AEMWE anodes is informative, pairing Ni-based anodes with active non-PGM cathodes will provide a more realistic performance indication of an economically feasible AEM electrolyser. Finally, it should also be noted that the particle washing, and recovery methods were not discussed, however they too would be considered when industrializing a catalyst synthesis method.

2.3.2 Ionomers used with Ni Particle-based Layers in AEMWE

As previously mentioned, when using particles as catalysts in polymer electrolyte membrane water electrolysis devices, an ionomer is required to bind the catalytic layer, either directly on the membrane, or on the GDL. Ionomers are polymer electrolytes with functional groups which serve to conduct ions through the catalytic layer. More specifically, the ionomer is responsible for creating a porous network with effective three-phase boundaries to improve the utilization of the catalyst and gas permeability in the electrode layer for enhanced electrochemical performance[33,96,97]. The three-phase boundary in the catalytic layers is found between the catalyst (solid), the electrolyte and ionomer (liquid) and the produced O_2 and H_2 (gas). In PEMWE, the most commonly used ionomer is DuPont's Nafion, as it is very mechanically and electrochemically stable due to its hydrophobic polytetrafluoroethylene (PTFE) backbone and hydrophilic sulfonic acid side chain functional groups, which conduct protons[96,98]. In AEMWE, most ionomers are developed with the goal of being as performing or better than Nafion. In AEM electrolysis, ionomers are commonly made using a hydrocarbon-based backbone with quaternary ammonium or imidazolium cationic functional groups for hydroxide ion conduction throughout the catalytic layer[32,41,97].

From a catalyst performance point of view, appropriately selecting the amount and type of ionomer used is imperative for creating a strong, stable and active catalytic layer. When considering the amount of ionomer being used in a catalytic layer, having too little can result in poor connectivity and pore formation, which can reduce ion and mass transport through the layer, as well as poor electrode durability through catalyst detachment due to lack of adhesion of the particles. Too much ionomer on the other hand can result in the blocking of active sites of the catalyst, increased mass transport and electronic resistances and poor durability due to the detachment of the catalyst from the overhydration of the catalytic layer[66,83,99]. When considering the type of ionomer to employ, it is important to consider how the ionomer will interact with the catalyst under operating conditions. The influence of ionomers on electrochemical performance will vary for every combination of catalyst and ionomer[41]. For example, the effects of different membrane-ionomer combinations on the AEMWE performance of a cobalt nanoparticle anode catalyst was recently investigated[100]. The authors observe that when using an ETFE ionomer [tetrafluoroethylene backbone and benzyl trimethylammonium (BTMA)-based cation], there is a

reduction in capacitance and redox response in the CV of the Co nanoparticles, which was suggested to be related to differences in catalyst-ionomer integration and a lower access to Co active sites. Additionally, when using the "Gen 2-Gen 2" ionomer and membrane (both perfluorinated backbone and hexyl trimethylammonium (HTMA)-based cation), the Co^{3+}/Co^{4+} transition was absent at 60°C in 0.1 M potassium bicarbonate electrolyte. This phenomenon was particular to those operating conditions and was proposed to be due to the structure of the Gen-2 ionomer and how it interacts with the catalyst surface.

One reported interaction between AEIs and catalysts under OER currents is the oxidation of phenyl. Phenyl group oxidation in a quaternized biphenylene (BPN) ionomer over a 100 h durability test at 2.1 V in an AEMWE at 80°C with an IrO_2 anode catalyst is studied[101]. The authors found evidence of the phenolic proton when analyzing the BPN ionomer by proton nuclear magnetic resonance spectroscopy (^{1}H NMR) after the durability test and explained that this is problematic for AEMWE operation because phenol is acidic in nature and can neutralize the quaternized hydroxide groups in the ionomer, reducing the local pH in the vicinity of the electrode surface. Additionally, as phenol is covalently bonded to the ionomer, it can be difficult to remove it from the catalyst-ionomer interface. In this study, the authors also performed three-electrode cell OER experiments and NMR spectroscopy to analyze the effects of catalyst type on phenyl oxidation of a benzyltrimethylammonium hydroxide (BTMAOH) electrolyte. For all the tested catalysts, they observed lower current densities at higher potentials in BTMAOH in comparison to KOH and suggest this to be related to the formation of acidic phenol intermediate. They also determine that the phenyl oxidation rate is lower on the non-PGM $La_{0.85}Sr_{0.15}CoO_3$ catalyst, in comparison to Pt/C and IrO_2, which is likely due to weaker interactions of phenyl with the non-PGM catalyst.

Tables 2.5 and 2.6 summarizes the ionomers that have been tested with previously provided lab synthesized Ni-based particles used as anodes in AEMWE. More specifically, the type of ionomer (conducting ion and name of polymer) used with the Ni-based anodes, along with the tested ionomer loadings is provided. For the information of the reader, the type of membranes employed in the AEMWE devices is also summarized.

Table 2.5: Part 1: Ni-based anode ionomer type and loading, as well as membrane used in AEMWE testing.

Ni-based AN	AN Ionomer Type and Name	AN Ionomer loading [wt%]	Membrane Type and Name	ref.# (year)
$NiCoO_x$, $NiFeO_xH_y$, $CoFeO_x$, **$NiCoO_x$:Fe**, $NiCoFeO_x$, Co_3O_4 NPs	anionic - Fumatech FAA-3	12.5, **15**, 20 (2.5, **5**, 10 in ink, **10 on top)**	anionic - Fumatech FAA-3	[46] (2019)
Fe_xNi_yOOH-20F powder	anionic - poly(aryl piperidinium) (PAP-TP-85)	30	anionic - poly(aryl piperidinium) (PAP-TP-85)	[71] (2021)
Ni, $Ni_{90}Fe_{10}$, $Ni_{90}Fe_{10}$/50 wt% CeO_2 NPs	anionic - Fumatech Fumion FAA-3	7	anionic - Fumatech fumasep FAA-3PE-30	[63] (2019)
Ni, **$Ni_{90}Fe_{10}$**, $Ni_{80}Fe_{20}$, $Ni_{90}Fe_{10}$/ 10 wt% CeO_2, $Ni_{80}Fe_{20}$/ 10 wt% CeO_2 NPs	anionic - Fumatech Fumion FAA-3	7, **15**, 25, 35, 45	anionic - Fumatech fumasep FAA-3PE-30	[66] (2021)
Ni_2Fe_1 nanofoam	anionic - trimethyl ammonium functionalized polystyrene (TMA-x, where x = 53, **70** mol% of quaternized benzyl ammonium)	11.1, 15.8, **20.0**, 27.3	anionic -hexamethyl trimethyl ammonium-functionalized Diels–Alder polyphenylene (HTMA-DAPP)	[80] (2020)
NiO nanosheets	anionic - Fumatech Fumion FAA-3	10, 20, 30, 40	anionic - Fumatech Fumapem-3-PE-30	[64] (2020)
$NiCo_2O_4$ particles	**anionic -quaternized polyphenylene oxide (qPPO)** neutral - polytetrafluoroethylene (PTFE) cationic – Nafion	15	anionic - (27.3 wt% low density polyethylene, 6.7 wt% poly(ethylene glycol-*ran*-propylene glycol), 66 wt% ANEX particles, Dowex Marathon A)	[73] (2017)
$NiCo_2O_4$ particles	anionic - PSEBS-CM-DABCO	10	anionic - chloromethylated polystyrene-block-poly(ethylene-ran-butylene)-block-polystyrene (PSEBS-CM) with 1,4-diazabicyclo[2.2.2]octane (DABCO) functional groups	[78] (2019)
$NiCo_2O_4$ particles	neutral - polytetrafluoroethylene (PTFE)	5, **15**, 25	anionic - low-density polyethylene and water-soluble poly(ethylene glycol-*ran*-propylene glycol) (PEG-PPG) blended with anion-selective resins (styrene-divinyl benzene copolymer matrix with quaternary ammonium functional groups)	[70] (2016)
$Ni_{0.6}Co_{0.2}Fe_{0.2}$ particles	cationic - Nafion anionic - Fumatech Fumion FAA-3	20 wt% (**10 wt% Nafion in layer*** + 10 wt% Fumion on top)	anionic - Fumatech Fumapem-3-PE-30	[87] (2021)

Note: In bold is the material or the specifications for which the performance is reported in Tables 2.3 and 2.4 and shows the optimal ionomer loading found in the studies. *Ratio of Nafion vs Fumion in the catalytic layer was optimized where only using Nafion provided the best AEMWE performance.

Table 2.6: Part 2: Ni-based anode ionomer type and loading, as well as membrane used in AEMWE testing.

Ni-based AN	AN Ionomer Type and Name	AN Ionomer loading [wt%]	Membrane Type and Name	ref.# (year)
NiFe (2:1)-LDH/KB (2/1)	cationic - Nafion	not specified	anionic - Dioxide Materials Sustainion X37-50 grade T	[76] (2020)
NiFe-BTC-GNPs MOF	anionic - not specified	not specified	anionic - Fumatech FAA-3-PK-130	[77] (2020)
$Ni_{0.9}Fe_{0.1}Co_{1.975}Li_{0.025}O_4$, $Ni_{0.9}Fe_{0.1}Co_2O_4$ particles	neutral - polytetrafluoroethylene (PTFE)	15	anionic - (27.3 wt% low-density polyethylene, 6.7 wt% poly(ethylene glycol-ran-propylene glycol), 66 wt% ANEX particles, Dowex Marathon A)	[79] (2018)
$NiMnO_x$ NPs	anionic - Fumatech FAA3-50	not specified	anionic - Fumatech FAA3-50	[65] (2020)
$NiFeO_x$ 70wt% / KB, $NiFe_2O_x$ 70 wt%/KB NPs	anionic - not specified	33	anionic - Dioxide Materials Sustainion™ X37-50	[67] (2020)
$NiMn_2O_4$ (20 wt%)/CNF, **$NiCo_2O_4$ (40 wt%)/CNF** fibers	anionic - Fumatech FAA3-50	33	anionic - Fumatech FAA3-50	[68] (2019)
$NiCo_2O_4$ particles	anionic - chloromethylated polystyrene-b-poly(ethylene/butylene)-b-polystyrene (SEBS) with amination using trimethylamine (TMA)	10	anionic - radiation grafted low-density polyethylene with vinylbenzyl chloride (LDPE-g-VBC) with amination using trimethylamine (TMA)	[69] (2018)
commercial $NiFe_2O_4$ NPs	cationic - Nafion	not specified	anionic - Dioxide Materials Sustainion™ X37-50	[72] (2017)
commercial $NiFe_2O_4$ NPs	cationic - Nafion	not specified	anionic - Tokuyama A-201 **anionic - Dioxide Materials Sustainion®** anionic - Ionomr Innovations AemionTM	[74] (2020)
commercial $NiFe_2O_4$ NPs	cationic - Nafion	not specified	**anionic - Dioxide Materials Sustainion® 37-50** anionic - Fumatech Fumasep FAS-50 anionic - Fumatech Fumasep FAPQ-375 anionic - Astom Neosepta ACM anionic - Membranes International AMI-7001 cationic - Nafion® 115 cationic - PBI Performance Products Incorporated Celazole® PBI	[75] (2017)

Note: In bold is the material or the specifications for which the performance is reported in Tables 2.3 and 2.4 and shows the optimal ionomer loading found in the studies.

In our recent work[66], we investigated the effects of the Fumatech Fumion FAA-3 ionomer content in Ni-based nanoparticle anodes in AEMWE. Ionomer nominal loadings of 7, 15, 25, 35 and 45 wt% were studied for optimal ink formulations, anode layer morphology and electrochemical performance. When analyzing the particle size distribution of the Ni catalyst inks, it was observed that having 15 wt% ionomer resulted in a unimodal distribution of particles or agglomerates, which is likely beneficial to forming an improved catalytic layer as the hand-spraying of the ink using air brush would be more continuous and efficient. The formed catalytic layers were visually analyzed showing that when using high ionomer amounts of 35 and 45 wt%, the structure of the catalytic layers was lost due to overhydration and excessive swelling when exchanged in 1 M KOH. When further analyzing the more stable 7, 15 and 25 wt% ionomer electrodes using scanning electron microscopy (SEM), it was observed that when less ionomer is used, there is more texture and pores in the as-prepared catalytic layers, potentially exposing more active sites, however providing less mechanical stability to the electrode. When more ionomer is used, the electrode surface is smoother and likely more durable, however fewer active sites are likely exposed due to ionomer coating of the particles and agglomerates. These observations were further validated when testing the 7, 15 and 25 wt% electrodes in an AEMWE cell. The 15 wt% electrode showed the best overall AEMWE performance, followed by the 25 wt% electrode. It was however also found that the 15 wt% electrode was the only anode to have enough ionomer to maintain the structural integrity of the catalytic layer under the imposed shear stress of the electrolyzer, and not too much ionomer to have catalyst loss due to excessive swelling when exposed to the alkaline electrolyte.

The importance of catalyst-ionomer interactions in Ni-based catalytic layers are discussed in terms of electrode stability in the works of Boettcher *et al*.[46]. In their work, they evaluated the Fumatech Fumion FAA-3 ionomer distribution and content used in the catalyst ink of their electrodes finding that 5 wt% ionomer in the catalyst ink with an additional 10 wt% added on top of the catalytic layer provided the best and most stable AEMWE performance. When performing a short-term stability test of their anode catalysts at 200 mA cm^{-2} for 3 h at 50°C in nanopure water, they observed a common degradation mechanism between all materials and attributed it to the ionomer in the catalytic layer. By performing two-electrode voltammetry before and after the stability test, they were able to identify a loss in pseudo-capacitance features for every electrode

over the stability test, which was suggested to be related to a loss of connectivity of the anode catalyst and the ionomer.

Recently, Faid *et al.*[64] also evaluated the effects of Fumatech Fumion FAA-3 ionomer content on the electrochemical activity of a NiO anode catalyst. They studied the effects of ionomer loading in a three-electrode cell (17, 33, 44, 50 wt% ionomer) as well as in an AEMWE equipped with reference electrodes for in-situ half-cell measurements (10, 20, 30, 40 wt% ionomer). In both cell configurations, they observed that varying the ionomer loading with the NiO catalyst did not have a significant impact on oxygen evolution activity. These results are supported by their SEM analysis of the post-*mortem* AEMWE anode layers, showing that no obvious changes in morphology are observed for increasing ionomer content with the NiO catalyst. In their work, they also compared OER activity of the NiO catalyst using the Nafion and Fumion FAA-3 ionomers in a three-electrode cell. When using the Fumion ionomer, there was a decrease in OER activity in comparison to Nafion, which they proposed to be related to phenyl adsorption of the Fumion ionomer backbone as well as any oxidation products formed under OER conditions.

The use of a trimethyl ammonium (TMA) functionalized polystyrene ionomer with different amounts of quaternized benzyl ammonium at the anode of an AEMWE with pure water flowing through the system has been recently investigated[80]. After determining that the TMA-70 (TMA ionomer with 70 mol% quaternized benzyl ammonium) ionomer was the best performing with an IrO_2 anode catalyst, the authors evaluated the effects of TMA-70 ionomer loading on a NiFe nanofoam anode, finding that 20 wt% provided the best AEMWE activity. When investigating the stability of the TMA-70 ionomer with the Ni-based catalyst, they observed that particles are washed out of the electrodes, likely due to the high IEC of the ionomer, which increases with increasing mol% of quaternized benzyl ammonium. An improvement of stability was obtained when using the TMA-53 ionomer, which has a lower IEC and therefore higher resulting binding strength of the catalyst particles. In this study, the authors also investigated the effects of phenyl groups in the backbone of the ionomer used with an IrO_2 catalyst. When comparing the TMA-53 ionomer to a hexamethyl trimethyl ammonium-functionalized Diels-Alder polyphenylene (HTMA-DAPP) ionomer of equivalent IEC, they observed that the TMA-53 ionomer, with a phenyl-free backbone, showed higher AEMWE performance than the HTMA-DAPP ionomer in pure water. The authors also studied the extent of phenyl oxidation on the

HTMA-DAPP ionomer by measuring the pH and ohmic resistance of a tetramethylammonium hydroxide (TMAOH) solution with varying amounts of phenol, which represents varying amounts of phenol formation on the ionomer backbone. For an equivalent of 25% phenyl oxidation of the ionomer backbone, the TMAOH solution pH and conductivity decreased from 14.2 to 11.4 and 165 to 25 mS cm^{-1}, respectively, which may affect the efficiency of the catalyst in the anode layer. This highlights the benefits of using ionomeric binders with phenyl-free backbones.

The AEMWE performance of different types of ionomeric binders with a $NiCo_2O_4$ anode catalyst was studied[73]. The authors employed a hydrophilic anionic binder made of quaternized polyphenylene oxide (qPPO), a hydrophobic electroneutral or inert binder, PTFE, and a hydrophilic cationic binder, Nafion, and evaluated them all with a loading of 15 wt%. Under the same operating conditions of 50°C and 10 wt% KOH, the qPPO ionomer exhibited the best AEMWE performance. This was attributed to the anion-selective binder offering ionic connection between the catalyst and the membrane, which increases three-phase contact in the catalytic layer. In comparison to the hydrophobic PTFE ionomer, the hydrophilic Nafion ionomer better facilitated rapid gas removal from the catalytic layer. However, as a cation-selective ionomer, Nafion does not provide OH^- transport. When evaluating the short-term stability of the MEAs over 7 h at 225 mA cm^{-2}, the PTFE ionomer showed the best stability, while the qPPO ionomer showed the fastest degradation. This was proposed to be due to the insufficient mechanical stability of the qPPO ionomer under operating conditions. The stability test of the PTFE electrode was further continued for 135 h at 225 mA cm^{-2}. During this test, the authors observed a degradation rate of 0.34 mV h^{-1} and attributed the observed performance loss to a decreasing catalyst particle size over time and the partial irreversible oxidation to Ni^{3+} on the catalyst surface.

Overall, interesting work has been carried out with respects to optimizing the ionomer loading and type for Ni-based electrocatalysts as anodes in AEMWE. When optimizing the ionomer content, the optimal amount is generally found to be around 15-20 wt%. This loading generally provides a balance between ohmic, polarization and mass transport resistances through the catalytic layer, catalyst active site coverage as well as electrode morphology and durability, and is in line with the optimal amount of ionomer reported in literature for other AEMWE anode catalysts[40,83,99,102,103]. It is interesting to note however that in some cases[64], no effects of ionomer content on anode performance in AEMWE was observed. These variations in catalyst performance

with ionomer content is a clear indication of the importance of ionomer loading optimization for every studied catalyst under its specific set of AEMWE operating conditions. It should also be noted that the optimal ionomer content may not only depend on the catalyst used but also the operating conditions of the electrolyser (temperature, pressure, electrolyte type, electrolyte feed method, etc).

It was also observed that some authors[46,87] apply ionomeric binders in the catalytic layer by directly adding it into the catalyst ink, then apply supplemental ionomer on top of the catalytic layer. It is observed that adding extra ionomer on top of the catalytic layer is needed for more stable AEMWE performance[46]. These results indicate that ionomer distribution in catalytic layers is another parameter which should be investigated for enhanced AEMWE performance. Faid *et al.*[87] studied the effects of varying the Nafion to Fumion ratio of the ionomer found in catalyst layer. Results indicated that having 10 wt% Nafion in the catalytic layer provided the best AEMWE performance. They then added 10 wt% Fumion on top of the catalytic layer. By utilizing two ionomers in two configurations, they were able to achieve improved particle adhesion and water transport in the catalytic layer from the Nafion ionomer and improved ionic conductivity and contact resistance between the CCS and the anion exchange membrane from the Fumion ionomer. These results indicate that combining ionomers with different properties could serve to further promote AEMWE performance. We refer the reader to the work of Faid *et al.*[87] for an analysis of catalyst-ionomer and electrolyte interactions on a Ni-MoO_2 HER electrocatalyst as a AEMWE cathode.

In terms of the nature of the studied ionomers, as expected, most authors use anion conducting ionomers with the Ni-based catalysts, where a few use the neutral PTFE ionomer and others use the cationic Nafion ionomer. Using AEIs is expected as they have the ability to both bind the catalytic layer and conduct OH^- ions to the active catalyst sites. While AEIs can show higher AEMWE performance than Nafion or PTFE, they do not always offer good stability under operating conditions[73]. This can be problematic when assessing a catalyst's long-term durability in an AEMWE device. While researchers may use more durable ionomers such as Nafion or PTFE to study catalysts in AEMWE, it is important to realize that the observed activity and durability of the catalyst may be very different when using a more economically and environmentally

favourable AEI and as such, further optimization of the catalytic layer may be required to reach acceptable electrolysis performance.

Based on the summarized studies of Ni-particle based anodes in AEMWE, there are no studies that evaluate the effects of various anion-conducting ionomers on AEMWE performance, like in the previously overviewed work on Co nanoparticle anodes[100]. As catalysts can interact differently with different ionomers, evaluating many AEIs with a same catalyst can help explain why some ionomers may work better than others with a certain catalyst. This may therefore help researchers better understand how best to pair catalysts with ionomers for enhanced AEMWE performance and may help better guide future research in catalyst and AEI development. On a similar note, as ionomers and catalysts must work together to carry out the electrolytic process, it would be useful to develop them together more closely. For example, ionomers are often evaluated using PGM anode catalysts, then assumed to work similarly with non-PGM catalysts, which is not necessarily the case. Finally, it should be noted that most of the ionomers summarized in Tables 2.5 and 2.6 are commercial, likely due to their established performance and properties. While utilizing a more reliable ionomer can be advantageous, companies do not often disclose the ionomer chemistry of their product, which may pose a challenge when trying to understand specific catalyst-ionomer interactions.

2.4 Summary and Perspective

Anion-exchange membrane water electrolysis is a technology which combines the compact cell design of the PEM water electrolyser with the economical advantages of the traditional alkaline electrolyser to result in an device that can efficiently produce green hydrogen at low cost. An important component of the AEMWE cell is the anode catalytic layer, which is responsible for carrying out the kinetically unfavourable oxygen evolution reaction. Nickel is one of the most favourable OER electrocatalysts owing to its high activity and stability in an alkaline environment. A summary of the development of Ni nano-structured, particle-based anodes in AEMWE devices was provided in this review to highlight recent progress in the field and provide guidance for future research. Of the summarized articles, most use particle synthesis methods with moderate operating conditions and relatively simple operating steps, making them attractive for safe, large-scale production of Ni AEMWE anode particles. Utilizing more easily scalable synthesis methods for future anode catalyst development is imperative for the realization of the AEMWE process on an

industrial scale. When preparing anodes for AEMWE, most authors use a catalyst ink spray-coating technique, which can form favourable porous anode layers, however not many explore different electrode fabrication techniques to yield better AEMWE performance through the tuning of the electrode layer architecture. Further studying electrode fabrication techniques is recommended to result in the best utilization of the anode catalysts. Additionally, preparing appropriate ink formulations for the employed electrode fabrication technique must also be carefully considered to form optimal high performing catalytic layers.

With respects to overall catalyst development, this review demonstrates the need to test more Ni-based OER catalysts in an AEMWE, because the electrolyser environment introduces multiple factors to the evaluated anode catalysts in comparison to a three-electrode electrochemical cell. Understanding how the AEMWE environment can affect the electrocatalysts' performance is necessary to finding the most active materials. Since it can be economically unfeasible and time consuming to test many materials in an electrolyser, it is also important to further investigate other activity descriptors for highly active AEMWE anodes. As such, active anode catalysts can be better identified and the fine tuning of high performing anode catalysts for use in an AEMWE can be more strategically completed. It is also suggested to pair experimental testing with modelling to help better understand the AEMWE systems and guide future research. For example, density functional theory (DFT) calculations can be used to understand the OER reaction mechanism of the studied materials. Additionally, computational fluid dynamics (CFD) could be used to study electrolyte and gas bubble flow in AEMWE devices to better design membrane electrode assemblies and components of the electrolyser hardware.

In particle-based catalytic layers, anionic binders are required to bind the particles to the catalytic layer, while also forming three-phase boundaries and a pathway for hydroxide ions throughout the electrode layer. The analysis of ionomers used with the Ni-based anodes provide a clear indication that ionomer loading, and distribution within the catalytic layer must be carefully studied to yield high activity of the Ni particle-based anodes, while also providing good mechanical stability of the electrode layer. The optimal loading and distribution of ionomer can vary between catalysts and with different operating conditions. It is also important to consider testing multiple ionomers with the Ni-based materials to further understand how they interact with each other to carry out the OER in an AEMWE device. Further understanding these catalyst-

ionomer interactions can help researchers better understand which ionomers to pair with which catalysts and help better direct future research in producing high performing Ni-based catalysts and ionomers. Finally, it could be of interest to further investigate mixing or pairing ionomers with different properties together, to yield high AEMWE performance and good long-term durability of the studied anode catalysts.

Acknowledgements

This research was conducted as part of the Engineered Nickel Catalysts for Electrochemical Clean Energy project administered from Queen's University and supported by Grant number RGPNM 477963-2015 under the Natural Sciences and Engineering Research Council of Canada (NSERC) Discovery Frontiers Program. Additional funding was also provided by NSERC's Alexander Graham Bell Canada Graduate Scholarship – Doctoral (CGS D).

References

[1] History, “Industrial Revolution,” *History*, **2018**, accessed on March 17, 2018, https://www.history.com/topics/industrial-revolution.

[2] W. W. Kellog, R. Schware, *Climate Change and Society: Consequence of Increasing Atmospheric Carbon Dioxide*, Westview Press, **1981**.

[3] American Chemical Society, “What are the greenhouse gas changes since the Industrial Revolution?,” accessed on May 26, 2020, https://www.acs.org/content/acs/en/climatescience/greenhousegases/industrialrevolution.html.

[4] Earth Science Communications Team, “Carbon Dioxide,” *NASA’s Jet Propulsion Laboratory*, **2022**, accessed on February 14, 2022, https://climate.nasa.gov/vital-signs/carbon-dioxide/.

[5] Earth Science Communications Team, “The Causes of Climate Change,” *NASA’s Jet Propulsion Laboratory*, **2022**, accessed on February 14, 2022, https://climate.nasa.gov/causes/.

[6] P. Markewitz, W. Kuckshinrichs, W. Leitner, J. Linssen, P. Zapp, R. Bongartz, A. Schreiber, T. E. Müller, *Energy Environ. Sci.* **2012**, *5*, 7281.

[7] K. Mazloomi, C. Gomes, *Renew. Sustain. Energy Rev.* **2012**, *16*, 3024.

[8] Voltaix Inc., MSDS Document Number -H000; Material Safety Data Sheet for Hydrogen **1996**, 1–12.

[9] HESS, Material Safety Data Sheet MSDS No. 9950; All Grades Gasoline , All Grades **2007**, 1–9.

[10] A. Zuttel, *Naturwissenschaften* **2004**, *91*, 157.

[11] I. Dincer, C. Acar, *Int. J. Hydrogen Energy* **2014**, *40*, 11094.

[12] Phillips Petroleum Company, Manufacturer MSDS #: 0041 Name : NO . 2 DIESEL FUEL **2002**, 1–9.

[13] Alternative Fuels Data Center, "Hydrogen Basics," *U. S. Department of Energy*, **2022**, accessed on February 22, 2022, https://afdc.energy.gov/fuels/hydrogen_basics.html#:~:text=In fact%2C a fuel cell,emissions and are less efficient.

[14] Alternative Fuels Data Center, "Fuel Cell Electric Vehicles," *U. S. Department of Energy*, **2022**, accessed on February 22, 2022, https://afdc.energy.gov/vehicles/fuel_cell.html.

[15] J. D. Holladay, J. Hu, D. L. King, Y. Wang, *Catal. Today* **2009**, *139*, 244.

[16] R. Kothari, D. Buddhi, R. L. Sawhney, *Renew. Sustain. Energy Rev.* **2008**, *12*, 553.

[17] M. Balat, *Energy Sources, Part A* **2009**, *31*, 39.

[18] A. L. Santos, M.-J. Cebola, D. M. F. Santos, *Energies* **2021**, *14*, 3193.

[19] E. Cetinkaya, I. Dincer, G. F. Naterer, *Int. J. Hydrogen Energy* **2012**, *37*, 2071.

[20] K. Zeng, D. Zhang, *Prog. Energy Combust. Sci.* **2010**, *36*, 307.

[21] D. M. F. Santos, C. A. C. Sequeira, *Quim. Nova* **2013**, *36*, 1176.

[22] R. Phillips, C. W. Dunnill, *RSC Adv.* **2016**, *6*, 100643.

[23] I. Vincent, D. Bessarabov, *Renew. Sustain. Energy Rev.* **2018**, *81*, 1690.

[24] M. K. Cho, A. Lim, S. Y. Lee, H. Kim, S. J. Yoo, Y. Sung, H. S. Park, J. H. Jang, *J. Electrochem. Sci. Technol.* **2017**, *8*, 183.

[25] M. Bodner, A. Hofer, V. Hacker, *Wiley Interdiscip. Rev. Energy Environ.* **2015**, *4*, 365.

[26] M. M. Rashid, M. K. Al Mesfer, H. Naseem, M. Danish, *Int. J. Eng. Adv. Technol.* **2015**, *4*, 80.

[27] J. Turner, G. Sverdrup, M. K. Mann, P.-C. Maness, B. Kroposki, M. Ghirardi, R. J. Evans, D. Blake, *Int. J. energy Res.* **2008**, *32*, 379.

[28] M. David, C. Ocampo-martínez, R. Sánchez-peña, *J. Energy Storage* **2019**, *23*, 392.

[29] M. R. Pai, A. M. Banerjee, A. K. Tripathi, S. R. Bharadwaj, "Fundamentals and applications of the photocatalytic water splitting reaction," *Functional Materials*, Elsevier Inc. **2012**, p.

579.

[30] S. Licht, B. Wang, S. Mukerji, T. Soga, M. Umeno, H. Tributsch, *Int. J. Hydrogen Energy* **2001**, *26*, 653.

[31] H. A. Miller, K. Bouzek, J. Hnat, S. Loos, C. I. Bernäcker, T. Weißgärber, L. Röntzsch, J. Meier-Haack, *Sustain. Energy Fuels* **2020**, *4*, 2114.

[32] C. Li, J.-B. Baek, *Nano Energy* **2021**, *87*, 106162.

[33] D. Henkensmeier, M. Najibah, C. Harms, J. Žitka, J. Hnát, K. Bouzek, *J. Electrochem. Energy Convers. Storage* **2021**, *18*, 024001.

[34] V. Schröder, B. Emonts, H. Janßen, H. P. Schulze, *Chem. Eng. Technol.* **2004**, *27*, 847.

[35] O. Schmidt, A. Gambhir, I. Staffell, A. Hawkes, J. Nelson, S. Few, *Int. J. Hydrogen Energy* **2017**, *42*, 30470.

[36] M. I. Jamesh, X. Sun, *J. Power Sources* **2018**, *400*, 31.

[37] Y. Leng, G. Chen, A. J. Mendoza, T. B. Tighe, M. A. Hickner, C.-Y. Wang, *J. Am. Chem. Soc.* **2012**, *134*, 9054.

[38] Daily Metal Prices, "Metal Spot Prices by Currency," **2022**, accessed on February 3, 2022, https://www.dailymetalprice.com/metalpricescurr.php.

[39] K. E. Ayers, E. B. Anderson, C. B. Capuano, M. Niedzwiecki, M. A. Hickner, C.-Y. Wang, Y. Leng, W. Zhao, *ECS Trans.* **2013**, *45*, 121.

[40] S. Koch, P. A. Heizmann, S. K. Kilian, B. Britton, S. Holdcroft, M. Breitwieser, S. Vierrath, *J. Mater. Chem. A* **2021**, *9*, 15744.

[41] J. R. Varcoe, P. Atanassov, D. R. Dekel, A. M. Herring, M. A. Hickner, P. A. Kohl, A. R. Kucernak, W. E. Mustain, K. Nijmeijer, K. Scott, T. Xu, L. Zhuang, *Energy Environ. Sci.* **2014**, *7*, 3135.

[42] A. Kusoglu, A. Z. Weber, *Chem. Rev.* **2017**, *117*, 987.

[43] D. Pletcher, X. Li, *Int. J. Hydrogen Energy* **2011**, *36*, 15089.

[44] M. Gong, H. Dai, *Nano Res.* **2015**, *8*, 23.

[45] Z. Chen, C. X. Kronawitter, X. Yang, Y. W. Yeh, N. Yao, B. E. Koel, *Phys. Chem. Chem. Phys.* **2017**, *19*, 31545.

[46] D. Xu, M. B. Stevens, M. R. Cosby, S. Z. Oener, A. M. Smith, L. J. Enman, K. E. Ayers, C. B. Capuano, J. N. Renner, N. Danilovic, Y. Li, H. Wang, Q. Zhang, S. W. Boettcher, *ACS Catal.* **2019**, *9*, 7.

[47] L. Trotochaud, J. K. Ranney, K. N. Williams, S. W. Boettcher, *J. Am. Chem. Soc.* **2012**, *134*, 17253.

[48] M. S. Burke, L. J. Enman, A. S. Batchellor, S. Zou, S. W. Boettcher, *Chem. Mater.* **2015**, *27*, 7549.

[49] M. S. Burke, S. Zou, L. J. Enman, J. E. Kellon, C. A. Gabor, E. Pledger, S. W. Boettcher, *Phys. Chem. Lett.* **2015**, *6*, 3737.

[50] F. Dionigi, P. Strasser, *Adv. Energy Mater.* **2016**, *6*, 1600621.

[51] M. Tahir, L. Pan, F. Idrees, X. Zhang, L. Wang, J. J. Zou, Z. L. Wang, *Nano Energy* **2017**, *37*, 136.

[52] M. E. G. Lyons, M. P. Brandon, *J. Electroanal. Chem.* **2010**, *641*, 119.

[53] X. Li, F. C. Walsh, D. Pletcher, *Phys. Chem. Chem. Phys.* **2011**, *13*, 1162.

[54] J. O. Bockris, T. Otagawa, *J. Electrochem. Soc.* **1984**, *131*, 290.

[55] M. Schalenbach, O. Kasian, K. J. J. Mayrhofer, *Int. J. Hydrogen Energy* **2018**, *43*, 11932.

[56] J. Lee, H. Jung, Y. S. Park, S. Woo, N. Kwon, Y. Xing, S. H. Oh, S. M. Choi, J. W. Han, B. Lim, *Chem. Eng. J.* **2021**, *420*, 127670.

[57] J. H. Kim, J. N. Lee, C. Y. Yoo, K. B. Lee, W. M. Lee, *Int. J. Hydrogen Energy* **2015**, *40*, 10720.

[58] S. H. Ahn, S. J. Yoo, H. J. Kim, D. Henkensmeier, S. W. Nam, S. K. Kim, J. H. Jang, *Appl. Catal. B Environ.* **2016**, *180*, 674.

[59] P. Ganesan, A. Sivanantham, S. Shanmugam, *ACS Appl. Mater. Interfaces* **2017**, *9*, 12416.

[60] E. López-Fernández, J. Gil-Rostra, J. P. Espinós, A. R. González-Elipe, A. De Lucas Consuegra, F. Yubero, *ACS Catal.* **2020**, *10*, 6159.

[61] V. N. Kuleshov, N. V Kuleshov, S. A. Grigoriev, E. Y. Udris, P. Millet, A. S. Grigoriev, *Int. J. Hydrogen Energy* **2016**, *41*, 36.

[62] N. V. Kuleshov, V. N. Kuleshov, S. A. Dovbysh, S. A. Grigoriev, S. V. Kurochkin, P. Millet, *Int. J. Hydrogen Energy* **2019**, *44*, 29441.

[63] E. Cossar, A. O. Barnett, F. Seland, E. A. Baranova, *Catalysts* **2019**, *9*, 814.

[64] A. Y. Faid, L. Xie, A. O. Barnett, F. Seland, D. Kirk, S. Sunde, *Int. J. Hydrogen Energy* **2020**, *45*, 28272.

[65] A. Carbone, S. C. Zignani, I. Gatto, S. Trocino, A. S. Aricò, *Int. J. Hydrogen Energy* **2020**, *45*, 9285.

[66] E. Cossar, A. O. Barnett, F. Seland, R. Safari, G. A. Botton, E. A. Baranova, *J. Power Sources* **2021**, *514*, 230563.

[67] S. C. Zignani, M. Lo Faro, S. Trocino, A. S. Aricò, *Energies* **2020**, *13*, 1720.

[68] C. Busacca, S. C. Zignani, A. Di Blasi, O. Di Blasi, M. Lo Faro, V. Antonucci, A. S. Aricò, *Int. J. Hydrogen Energy* **2019**, *44*, 20987.

[69] G. Gupta, K. Scott, M. Mamlouk, *J. Power Sources* **2018**, *375*, 387.

[70] R. A. Tufa, E. Rugiero, D. Chanda, J. Hnàt, W. van Baak, J. Veerman, E. Fontananova, G. Di Profio, E. Drioli, K. Bouzek, E. Curcio, *J. Memb. Sci.* **2016**, *514*, 155.

[71] J. Xiao, A. M. Oliveira, L. Wang, Y. Zhao, T. Wang, J. Wang, B. P. Setzler, Y. Yan, *ACS Catal.* **2021**, *11*, 264.

[72] Z. Liu, S. D. Sajjad, Y. Gao, J. J. Kaczur, R. I. Masel, *ECS Trans.* **2017**, *77*, 71.

[73] D. Chanda, J. Hnát, T. Bystron, M. Paidar, K. Bouzek, *J. Power Sources* **2017**, *347*, 247.

[74] I. V Pushkareva, A. S. Pushkarev, S. A. Grigoriev, P. Modisha, D. G. Bessarabov, *Int. J.*

Hydrogen Energy **2020**, *45*, 26070.

[75] Z. Liu, S. D. Sajjad, Y. Gao, H. Yang, J. J. Kaczur, R. I. Masel, *Int. J. Hydrogen Energy* **2017**, *42*, 29661.

[76] H. Koshikawa, H. Murase, T. Hayashi, K. Nakajima, H. Mashiko, S. Shiraishi, Y. Tsuji, *ACS Catal.* **2020**, *10*, 1886.

[77] P. Thangavel, M. Ha, S. Kumaraguru, A. Meena, A. N. Singh, A. M. Harzandi, K. S. Kim, *Energy Environ. Sci.* **2020**, *13*, 3447.

[78] J. Hnát, M. Plevova, R. A. Tufa, J. Zitka, M. Paidar, K. Bouzek, *Int. J. Hydrogen Energy* **2019**, *44*, 17493.

[79] D. Chanda, S. Basu, *Int. J. Hydrogen Energy* **2018**, *43*, 21999.

[80] D. Li, E. J. Park, W. Zhu, Q. Shi, Y. Zhou, H. Tian, Y. Lin, A. Serov, B. Zulevi, E. D. Baca, C. Fujimoto, H. T. Chung, Y. S. Kim, *Nat. Energy* **2020**, *5*, 378.

[81] B. Bladergroen, H. Su, S. Pasupathi, V. Linkov, "Overview of Membrane Electrode Assembly Preparation Methods for Solid Polymer Electrolyte Electrolyzer," *Electrolysis*, **2012**.

[82] S. Hirano, J. Kim, S. Srinivasan, *Electrochim. Acta* **1997**, *42*, 1587.

[83] J. E. Park, S. Y. Kang, S. H. Oh, J. K. Kim, M. S. Lim, C. Y. Ahn, Y. H. Cho, Y. E. Sung, *Electrochim. Acta* **2019**, *295*, 99.

[84] D. Li, A. R. Motz, C. Bae, C. Fujimoto, G. Yang, F. Y. Zhang, K. E. Ayers, Y. S. Kim, *Energy Environ. Sci.* **2021**, *14*, 3393.

[85] Y. Li, B. Huang, Y. Sun, M. Luo, Y. Yang, Y. Qin, L. Wang, C. Li, F. Lv, W. Zhang, S. Guo, *Small* **2019**, *15*, 1804212.

[86] P. W. Menezes, C. Panda, S. Loos, F. Bunschei-bruns, C. Walter, M. Schwarze, X. Deng, H. Dau, M. Driess, *Energy Environ. Sci.* **2018**, *11*, 1287.

[87] A. Y. Faid, A. O. Barnett, F. Seland, S. Sunde, *ACS Appl. Energy Mater.* **2021**, *4*, 3327.

[88] E. Cossar, K. Agarwal, V. B. Nguyen, R. Safari, G. A. Botton, E. A. Baranova,

Electrocatalysis **2021**.

[89] S. Fu, J. Song, C. Zhu, G.-L. Xu, K. Amine, C. Sun, X. Li, M. H. Engelhard, D. Du, Y. Lin, *Nano Energy* **2018**, *44*, 319.

[90] WO2004049491 (**2004**), invs.: AS Arico, LR Gullo, D La Rosa, S Siracusano, AB Lopes Corriera Tavares, A Sin Xicola.

[91] B. Chi, J. Li, Y. Han, Y. Chen, *Int. J. Hydrogen Energy* **2004**, *29*, 605.

[92] E. O. Nwanebu, N. Abou Harb, R. Gharbi, S. Omanovic, *Solid State Sci.* **2021**, *119*, 106703.

[93] S. A. Berlinger, S. Garg, A. Z. Weber, *Curr. Opin. Electrochem.* **2021**, *29*, 100744.

[94] V. Vij, S. Sultan, A. M. Harzandi, A. Meena, J. N. Tiwari, W. Lee, T. Yoon, K. S. Kim, *ACS Catal.* **2017**, *7*, 7196.

[95] G. C. Anderson, B. S. Pivovar, S. M. Alia, *J. Electrochem. Soc.* **2020**, *167*, 044503.

[96] N. Chen, Y. M. Lee, *Prog. Polym. Sci.* **2021**, *113*, 101345.

[97] R. Abbasi, B. P. Setzler, S. Lin, J. Wang, Y. Zhao, H. Xu, B. Pivovar, B. Tian, X. Chen, G. Wu, Y. Yan, *Adv. Mater.* **2019**, *31*, 1805876.

[98] G.-F. Li, D. Yang, P. Y. A. Chuang, *ACS Catal.* **2018**, *8*, 11688.

[99] I. Vincent, A. Kruger, D. Bessarabov, *Int. J. Hydrogen Energy* **2017**, *42*, 10752.

[100] S. Ghoshal, B. S. Pivovar, S. M. Alia, *J. Power Sources* **2021**, *488*, 229433.

[101] D. Li, I. Matanovic, A. S. Lee, E. J. Park, C. Fujimoto, H. T. Chung, Y. S. Kim, *ACS Appl. Mater. Interfaces* **2019**, *11*, 9696.

[102] M. K. Cho, H. Y. Park, H. J. Lee, H. J. Kim, A. Lim, D. Henkensmeier, S. J. Yoo, J. Y. Kim, S. Y. Lee, H. S. Park, J. H. Jang, *J. Power Sources* **2018**, *382*, 22.

[103] M. K. Cho, H. Park, S. Choe, S. J. Yoo, J. Y. Kim, H.-J. Kim, D. Henkensmeier, S. Y. Lee, Y. Sung, H. S. Park, J. Hyun Jang, *J. Power Sources* **2017**, *347*, 283.

Chapter 3. Comparison of Electrochemical Active Surface Area Methods for Various Nickel Nanostructures

Emily Cossar, Mohamed S. E. Houache, Zhihao Zhang, Elena A. Baranova*

Department of Chemical and Biological Engineering, Centre for Catalysis Research and Innovation (CCRI) University of Ottawa,161 Louis-Pasteur Ottawa, Canada, K1N 6N5

Chapter as published in: *J. Electroanal. Chem.* **2020**, *870*, 114246, http://dx.doi.org/10.1016/j.jelechem.2020.114246.

Supplementary information for this chapter is found in Appendix B.

Abstract

Electrochemical processes, such as energy conversion and storage, water electrolysis and other electrocatalytic processes call for expensive noble metal catalysts to provide efficient performance of their systems. The use of those expensive catalysts does not allow for feasible industrial scale operation of such processes. Non-noble metals such as nickel (Ni), provide an industrially feasible alternative to noble metal catalysts because they are inexpensive yet still have high catalytic performance. When evaluating electrochemical performance, it is imperative to quantify the electrochemical active surface area (ECSA) of the materials, however for Ni-based materials, this has proven to be quite challenging. In this study, four ECSA methods are compared for four Ni-based nanostructured catalysts as well as polycrystalline Ni, to determine whether one method is more representative than the other, or whether the appropriate method depends on the type of Ni being used. The tested methods were carried out in an alkaline environment and were based on (i) the double layer capacitance obtained through non-faradaic charging by cyclic voltammetry as well as the charge associated to (ii) the α-$Ni(OH)_2$ oxidation peak, (iii) the β-NiOOH reduction peak and finally (iv) the β-NiOOH reduction peak in the presence of oxalic acid. The methods were applied to Ni wire, various shaped Ni nanoparticles (NPs) such as triangle, urchin and spherical, as well as Ni foams. Electrochemical results of this study, along with scanning and transmission electron microscopy (SEM and TEM) and X-ray diffraction (XRD) analyses are reported and a detailed discussion on the applicability of the methods is provided.

3.1 Introduction

Nickel (Ni) is a very widely applied catalyst in alkaline electrochemistry due to its high stability in the alkaline environment and promising catalytic activity resulting from its interesting surface oxidation properties [1–3]. Researchers have been developing Ni-based materials for the efficient alkaline hydrogen fuels cells [4–6], high performing alkaline water electrolysers [7–10], and for other electrochemical processes such as the selective glycerol electrooxidation to value added chemicals [11–13].

The surface oxidation properties of Ni have been thoroughly studied to better understand the metal and its intrinsic activity [3,14–19]. The Bode diagram [20] is most widely used to describe nickel's oxidation mechanism. Although the diagram has been extensively covered and paired with cyclic voltammograms (CVs) [15,18,19], a short summary will be given here to aid in the understanding of this study. As shown in Figure B.1 of the Supplementary Information (S. I.), once metallic Ni is submerged in an alkaline environment, it transforms into the unstable α-$Ni(OH)_2$ phase. It then irreversibly restructures into the β-$Ni(OH)_2$ and once anodic polarization is applied, it oxidizes to the β-NiOOH phase. That last transition is reversible. A more detailed explanation of the Bode oxidation process with respect to a CV of a metallic Ni surface is covered in Section B.1 of the S. I.

When evaluating electrochemical performance of Ni-based materials it is imperative to know the electrochemical active surface area (ECSA) of the material you are working with in order to compare intrinsic catalytic activity between catalysts. Knowing the ECSA will allow you to quantify the area of the reacting interface and will allow for a more accurate performance comparison of a certain metals. [21] For some materials, it can be rather straightforward to calculate the active surface area of the catalyst. For example, for platinum catalysts, the active surface area can be reproducibly obtained by measuring the charge associated to one monolayer of under potential deposited hydrogen (UPD-H) desorption in a CV [22–25]. Unfortunately, the complexity of Ni electrochemistry calls for assumptions and estimations when trying to estimate the active surface area, rendering the obtained values misrepresentative of the activity of a certain Ni material.

Machado *et al.*[26] introduced an "Alpha" ECSA method for bulk Ni. This method was further developed by Alsabet *et al.*[14]. In this method, the charge of the oxidation peak of the α-$Ni(OH)_2$ transformation in 0.5 M KOH is used to calculate the ECSA. In their calculations, the authors assumed a specific charge density of 514 μC cm^{-2} for the formation of one monolayer of α-$Ni(OH)_2$.Versions of this method were also applied to commercial Ni foams [27,28].

Hall *et al.* [29] later developed an "Oxalate" method for determining the ECSA. In this method, the charge of the reduction peak of the β-NiOOH transformation in a 0.1 M KOH and 0.08 M oxalic acid solution is used to calculate the ECSA. In their study, the authors showed that by running a CV at high scan rates (≥150 mVs^{-1}), the Ni surface remains in an unstable phase analogous to the α-$Ni(OH)_2$ phase, and forms a monolayer of a Ni-oxalate complex [$Ni(OH)_{2-x}(C_2O_4)_{x(ads)}$] in the anodic region. The ECSA is calculated by measuring the charge of the reduction of the Ni-oxalate complex. It is assumed that the specific charge density of Ni in this environment is 195 μC cm^{-2}. This Oxalate method was further investigated by van Drunen *et al.* [30] for commercial Ni foams.

McCrory *et al.* [31,32] used two methods based on the electrochemical double layer to calculate the ECSA for many oxygen evolution catalysts, including Ni. In the first method, CVs were run over a 100 mV window around the open circuit potential (OCP) at various scan rates in order to obtain the double layer capacitance from the slope of the charging current vs. the scan rate. The second method is carried out by running electrochemical impedance spectroscopy (EIS) in a frequency-dependant impedance zone and pairing the response to a modified Randles circuit to obtain the double layer capacitance value. In both methods, the ECSA is obtained by dividing the obtained double layer capacitance by a specific capacitance value of 40 μF cm^{-2} in 1 M NaOH. Both methods provided ECSA values within 15% of each other. The authors also report that using different theoretical capacitance values could yield ECSA results that are off by a factor of 7. Many other authors used capacitance-based methods in alkaline media to calculate the ECSA of Ni [14,28,33–35], some applying their methods to Ni bimetallic or composite catalysts . It is to be noted that measuring the ECSA with these capacitance-based methods does not account for the dependence of double layer charging on pH for oxide materials[21], and it assumes that metal oxide catalysts are equally conductive to their respective metals[31].

Ho *et al.* [33] developed a method to measure the active surface area of Ni and NiCo materials for the OER region. Their method is carried out by charging their electrodes in the OER region to fill the electrode surface with one monolayer overpotential deposited oxygen (OPD O) species. Next, they measured the galvanic discharge over time of the monolayer of OPD O species. Integrating that plot yielded a charge, $Q_{OPD,\,O}$, for the OER discharge process which was related to the active surface area by assuming a surface charge density of 420 μC cm^{-2}. Although they list four additional assumptions required to carry out the calculations, their ECSA results were concurrent with the activity found in CV experiments. This method was later used for nickel, cobalt and iron electrodes for OER [18,36].

Conway *et al.* [37] carried out a study on the potential dependence of the surface coverage of hydrogen atoms on Ni electrodes, once steady state polarization has been obtained through continuous faradaic cycling. Sheng *et al.* [38] referenced this work when calculating the ECSA using the reduction peak of the α-$Ni(OH)_2$ species. Analogous to this work, the "Beta" method for calculating the ECSA in the Ni^{2+}/Ni^{3+} region can be carried out by cycling at a higher scan rate of 100 mVs^{-1}, for enough cycles to reach a steady state reduction of the β-NiOOH species in the anodic region of the CV shown in Figure B.1 of the S.I. Although though the peak associated to the oxidation of β-$Ni(OH)_2$ will continue to increase, the stable reduction peak of β-NiOOH is meant to indicate the reduction of one monolayer of the oxidised Ni surface that is in the active phase for OER. Therefore, by using the charge associated to that peak and the theoretical surface charge of 420 μC cm^{-2} [33,36], the ECSA can be obtained.

Despite the number of ECSA methods that can be applied for Ni-based materials, there is no consensus on the most accurate and reliable method, meaning there are issues related to the applicability of each method. As the ECSA of a material depends on its morphology, synthesis, surface composition and size, this study will compare the most easily and generally applicable methods to various shapes Ni-based materials. The analysed methods will include the "Alpha", "Oxalate", "Capacitance" and "Beta" methods, where the Capacitance method is applied using CV experiments at different scan rates. The four methods will be applied to a polycrystalline Ni wire, Ni nanofoams and Ni spherical, urchin and triangle nanoparticles (NPs). These materials were selected as they are metallic Ni or Ni-oxide-based yet have different morphologies and therefore different electrochemical behaviour. The goal of this study is to evaluate and understand the Ni

materials, then to compare the ECSA results of all four methods for every Ni material, to determine whether one of the tested methods is more representative than the other, or whether the appropriate method depends on the type of Ni being used.

3.2 Materials and Methods

3.2.1 Material Synthesis

3.2.1.1 Ni Spherical

The spherical Ni NPs were synthesized by chemical reduction in ethanol using sodium borohydride as the reducing agent [10]. As with all synthesis methods that will be covered in this paper, the glassware was first washed using the Aqua Regia procedure (2:1 HCl: HNO_3, 37 %, 70%, respectively, Fisher Scientific, Hampton, NH, USA). A nickel chloride hexahydrate ($NiCl_2 \cdot 6H_2O$, 99.999%, Sigma Aldrich, St. Louis, MO, USA) precursor salt was dissolved in ethanol (EtOH, 99%, Greenfield, Grayslake, IL, USA) at room temperature by magnetic stirring for around 45 minutes. The solution concentration was around 14 mmol L^{-1}. Once dissolved, the nickel precursor salt was reduced using sodium borohydride powder ($NaBH_4$, ≥98%, ACROS, Geel, Belgium) that was dissolved in around 5 mL of EtOH solution. Two moles of $NaBH_4$ was used to reduce each mole of Ni precursor salt. The resulting suspension of Ni NPs was stirred for another 30 minutes, after which it was centrifuged at 6000 rpm for 10 minutes, then the reaction liquid was decanted out. The resulting nanoparticles were washed with ethanol three times. The remaining ethanol in the NP sample was removed using a freeze drier for around 15 hours.

3.2.1.2 Ni Foams

The Ni foams were prepared by polyol method in glycerol [39]. First, a nickel nitrate hexahydrate [$Ni(NO_3)_2 \cdot 6H_2O$, 99.999%, Sigma Aldrich, St. Louis, MO, USA] precursor salt was dissolved in glycerol ($C_3H_8O_3$, ≥99%, Sigma Aldrich, St. Louis, MO, USA) at 60°C with magnetic stirring for 12 hours. The concentration of the solution was 40 mM. The flask was then mounted to a reflux system and its temperature was slowly raised to 290°C over approximately 30 minutes. Once at 290°C, the reflux was maintained for around 40 minutes. Once the foams were floating in the reaction solution, the reflux was continued for around 20 more minutes to ensure complete reduction of the precursor salt. The solution was then decanted by holding the foams with an exterior magnetic against the flask. Finally, the foams were washed 5x with ethanol and dried in

an oven at 60°C. To increase the activity of the Ni foams, an oxidation/reduction procedure was used. First, they were oxidized under air (high purity mixture of 20% O_2 and 80% N_2, Linde, ON, Canada) for 2 hours at 600°C. Then the were reduced for 4 hours under hydrogen (H_2, ≥99.996%, Linde, ON, Canada) at 300°C.

3.2.1.3 Ni Urchin

The urchin-like NPs were synthesized by polyol method in ethylene glycol [12,40]. First, 0.357 g of $NiCl_2 \cdot 6H_2O$ was placed in ethylene glycol at a concentration of 50 mM. Then, the solution was mounted to a reflux system and raised to 100°C with magnetic stirring. Once at 100°C, 1.7 mL of 0.1 M hydrazine hydrate ($N_2H_4 \cdot H_2O$, 50-60%, Sigma Aldrich, St. Louis, MO, USA) was added to the reaction solution after 2 minutes had passed. After another 2 minutes had passed, 4.5 mL of 0.5 M sodium hydroxide (NaOH, 97%, Fisher Scientific, Hampton, NH, USA) was added to the system. The reflux was continued for approximately 20 minutes after the solution had turned black. The solution was decanted and then the particles were washed 3x with ethanol using the centrifuge at 6000 rpm for 10 mins. The remainder of the ethanol in the sample after washing was removed by air drying. All aqueous solutions were prepared with ultrapure water

3.2.1.4 Ni Triangle

The Ni triangle particles were synthesized the same way as the urchin-like particles, however the concentration of sodium hydroxide used in the synthesis was 0.1 M.

3.2.2 Material Characterization

The scanning electron micrograph (SEM) of the Ni foams were taken on the Joel JSM-7500F Field emission scanning electro microscope (Peabody, MA, USA) at a voltage of 3 kV. The transmission electron micrographs (TEM) of the Ni spherical, urchin and triangle particles were obtained with the JEOL JEM 2100F Field Emission Transmission Electron Microscope (Tokyo, Japan) at 200 kV. X-ray Diffraction data was gathered on the Rigaku Ultima IV multi-purpose diffractometer (Tokyo, Japan) using copper Kα radiation (λ=1.5418 Å) set to 40 kV and 44 mA. The 2θ range of the XRD spectra was 20-80° and the rate was 0.5° 2θ min^{-1}.

3.2.3 Electrochemical Methods

3.2.3.1 Cell Setup

All electrochemical testing was done in a conventional three-electrode glass cell with a Pt mesh counter electrode. The working electrode used for benchmark testing was a Ni wire (0.5 mm O.D., 99.99%, Sigma Aldrich, St. Louis, MO, USA), which was polished with 500-grit sand paper, 30-micron alumina (Al_2O_3, Carveth Metallurgical Limited, Canada) and 3-micron alumina (Al_2O_3, Buehler, Lake Bluff, IL, USA), then sonicated for 10 minutes in ultrapure water. The working electrode used for testing the nanomaterials consisted of 10 μL of a catalyst ink deposited on a glassy carbon electrode (Pine Research, Durham, NC, USA) with a geometric surface area, *SA*, of 0.196 cm^2. The catalyst ink was prepared with 6 mg of metal, 1 mL of ultrapure water, 200 μL of isopropanol (IPA, 99.9%, Fisher Scientific, Hampton, NH, USA) and 100 μL of Nafion® (~5%, Sigma Aldrich, St. Louis, MO, USA), and then was sonicated for around 5 minutes. The glassy carbon surface was polished with 30-micron and 3-micron alumina, then rinsed with ethanol and ultrapure water (Milli-Q® Millipore, 18.2 MΩ cm at 293 K) prior to the ink deposition. The electrolytes were prepared with ultrapure water. The reference electrodes used in this study will be specified during the explanation of each method since specific reference electrodes were required for some of the methods. All experiments were run at room temperature and were carried out using the Bio-Logic Potentiostat/Galvanostat, which was paired with the EC labs software (Bio-Logic Science Instruments, Seyssinet-Pariset, France).

3.2.3.2 The "Alpha" Method

As mentioned in the introduction, the Alpha method utilizes the charge associated to the α-$Ni(OH)_2$ oxidation peak in an alkaline environment. In this study, this method was performed on a fresh electrode. Before performing the Alpha method, each electrode was electrochemically reduced by running a chronoamperogram (CA) at -1.446 V vs SCE for 5 mins, then a CA at -0.946 V vs SCE at 10 minutes [14] in 0.1 M potassium hydroxide (KOH, ≥85%, Sigma Aldrich, St. Louis, MO, USA) + 0.08 M oxalic acid dihydrate ($C_2H_2O_4 \cdot H_2O$, 99.5-102.5%, Fisher Scientific, Hampton, NH, USA). The Alpha method was carried out by running a cyclic voltammogram (CV) from -1.096 to -0.546 V vs the saturated calomel electrode (SCE, Koslow Scientific, Englewood, NJ, USA) for 10 cycles at a scan rate of 50 mVs^{-1}. The charge, *Q*, of α-$Ni(OH)_2$ oxidation peak was obtained using Equation B.1, by numerically integrating the experimental data of the peak in

the tenth CV cycle over a 200 mV window (from -0.8 to -0.6 V vs SCE), as shown in Figure B.2 of the S. I.. This window was selected to encompass the α-$Ni(OH)_2$ peak of each material. The specific charge density, *q*, used in this method is 514 μC cm^{-2} [14,26]. The electrochemical active surface area, *ECSA*, and geometric relative roughness factor, *RF*, of the electrodes were then obtained with Equations 3.1 and 3.2 using the geometric surface area, *SA*, of the electrodes. The *SA* of the Ni wire was 0.159 cm^2, while the *SA* for the nanostructures was 0.196 cm^2.

$$\mathrm{ECSA}[\mathrm{cm}^2] = \frac{\mathrm{Q}[\mu\mathrm{C}]}{\mathrm{q}\left[\frac{\mu\mathrm{C}}{\mathrm{cm}^2}\right]} \qquad \textbf{\textit{Equation 3.1}}$$

$$\mathrm{RF}[-] = \frac{\mathrm{ECSA}\,[\mathrm{cm}^2]}{\mathrm{SA}\,[\mathrm{cm}^2]} \qquad \textbf{\textit{Equation 3.2}}$$

Note that the original Alpha method [14,26], is run in 0.5 M KOH, however based on the results shown in Figure B.3 of the S. I., the cathodic region is unaffected by the addition of the oxalate salt to the KOH electrolyte. This result supports the findings of Hall *et al.* [29]. Furthermore, in order to better compare all active surface area methods to one another, all experiments in this study are conducted using a base of 0.1 M KOH to avoid effects due to changes in electrolyte molarity. Current densities in CVs can change with electrolyte concentration, meaning that active surface areas can change with electrolyte concentration. 0.1 M KOH was selected as the KOH concentration for the study based on the Oxalate method, which was developed with a very specific electrolyte.

3.2.3.3 The "Oxalate" Method

The Oxalate method utilizes the charge of the reduction of the β-NiOOH peak in an alkaline environment in the presence of oxalic acid to estimate the ECSA. In this study, the Oxalate method was run immediately after the Alpha method (same electrode) to minimize the error obtained from using a new deposition. This method was done by running a CV from -1.096 to 0.575 V vs SCE for 2 cycles at 150 mVs^{-1}. Note that the CV in this method should be bound by the start of the oxygen evolution reaction (OER). Therefore, in some cases, the anodic bound of the CV was extended to accommodate high overpotentials for OER. Specific bounds for the CVs can be found in Table B.1 of the S. I. In this method, the ECSA and RF were calculated using Equations B.1,

3.1 and 3.2, however the charge, Q, was based on the reduction peak in the anodic region of the graph, marking the reduction of a nickel-oxalate complex $[Ni(OH)_{(2-x)}(C_2O_4)_x]$ [29]. This peak was integrated over a 350 mV region (from 0.425 to 0.075 V vs SCE) as shown in Figure B.4. Note that this area was chosen to encompass the cathodic charge of every material, which varied due to different reaction overpotentials. The specific charge density associated with nickel in this method is 195 μC cm^{-2} [29]. This method requires the presence of the α-$Ni(OH)_2$ phase when starting the first CV scan to ensure the electrode remains in an alpha-like phase in the anodic region of the CV. The presence of the α-$Ni(OH)_2$ peak in the first CV scan is shown in Figure B.5 of the S. I.

3.2.3.4 The "Capacitance" Method

As previously mentioned, the Capacitance method consisted of cycling the Ni-based electrodes at different scan rates in a non-faradaic charging process to estimate the ECSA. In this study, this method was performed on a fresh electrode. This method was carried out by running a series of CVs at different scan rates (5, 10, 20, 50, 100, 150, 200, 300, 400 mVs^{-1}) ± 50 mV around the open circuit potential (OCP) that is particular for each electrode. A summary of the average open circuit values for each material is shown in Table B.2 of the S. I. This method was performed in 0.1 M KOH using a mercury/mercury oxide reference electrode (Hg/HgO, Koslow Scientific, Englewood, NJ, USA). With the data from the CVs, it was possible to determine the charging current, I_c, of the electrodes at each scan rates, as shown by Equation 3.3.

$$I_C[A] = \left|\left(I_{anodic} - I_{cathodic}\right)\right|_{OCP} \qquad \textbf{\textit{Equation 3.3}}$$

It is then possible to obtain a double layer capacitance value, C_{dl}, by plotting a graph of charging current vs. scan rate and calculating the slope as shown by Equation 3.4.

$$\text{Slope} = C_{dl}[F] = \frac{\Delta I_C[A]}{\Delta v[Vs^{-1}]} \qquad \textbf{\textit{Equation 3.4}}$$

Finally, the *ECSA* can be calculated using the specific capacitance, c_s, of 40 μFcm^{-2} [31,32] and Equation 3.5. The *RF* is calculated with Equation 3.2.

$$ECSA[cm^2] = \frac{C_{dl}[\mu F]}{c_s\left[\frac{\mu F}{cm^2}\right]} \qquad \textbf{\textit{Equation 3.5}}$$

3.2.3.5 The "Beta" Method

The Beta method consisted of integrating the β-NiOOH reduction peak once steady state polarization was reached at a high scan rate. This method was run immediately after the capacitance method (same electrode) to, once again, minimize the error obtained from using a new deposition. Before running the method, the electrodes were treated with the reduction procedure explained above, however since the beta method was run with the Hg/HgO electrode, the reduction procedure was a CA at -1.3 V for 5 mins, followed by a CA at -0.8 V vs Hg/HgO. Once the electrodes were electrochemically reduced, the Beta method was carried out by running 100 CV cycles from 0.1 to 0.7 V vs Hg/HgO at 100 mVs^{-1}. Similar to the Oxalate method, the CVs here are also bound by the OER. The catalyst specific CV regions are summarized in Table B.3 of the S. I. The *ECSA* and *RF* for this method were calculated using the β-NiOOH reduction peak of the 100^{th} cycle over a 430 mV window (from 0.57 to 0.14 V vs Hg/HgO) as shown in Figure B.6, and Equations B.1, 3.1 and 3.2. This area was selected to include the full cathodic charge of every material, which varied due to different reaction overpotentials. In this method, the specific charge density used is 420 μC cm^{-2} [33,36].

3.3 Results and Discussion

3.3.1 XRD

Figure 3.1 shows XRD results for all nanostructured materials. As it can be seen, the Ni foams as well as the Ni triangle and urchin NPs consist of metallic Ni, while the Ni spherical NPs show some metallic Ni features but mostly the β-$Ni(OH)_2$ phase [3,41].

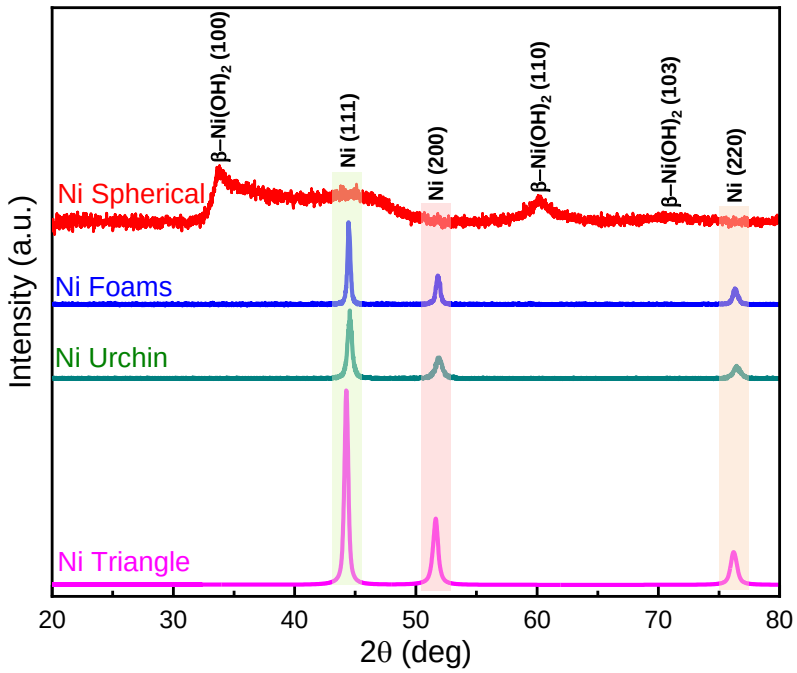

Figure 3.1: XRD patterns of Ni spherical (red), Ni foams (blue), Ni urchin (green) and Ni triangle (magenta) NPs [3,41]***.***

3.3.2 SEM/TEM

Figure 3.2 shows TEM images for the Ni spherical NPs (Figure 3.2a), SEM images for the Ni foams (Figure 3.2b) and TEM images for the Ni urchin and triangle particles (Figure 3.2c and d, respectively). Using the scale in the image, it is possible to see that the spherical NPs are around 4-6 nm in size, while the urchin and triangle NPs are around 130 and 150 nm, respectively. The Ni foams present wire-like structure less than 2 μm in diameter, that breaks down into a porous nanostructure. For other images of the Ni nanostructures, see Figure B.7 in the supplementary information.

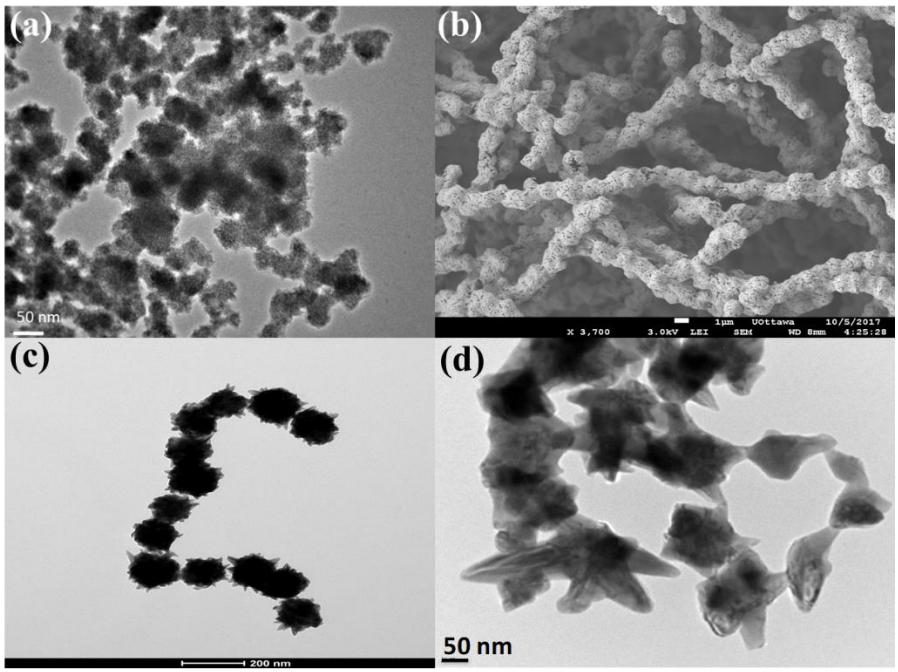

Figure 3.2: Ni nanostructures (a) TEM of Ni spherical, (b) SEM of Ni foams, (c) TEM of Ni urchin, and (d) TEM of Ni triangle.

3.3.3 Electrochemical Methods

3.3.3.1 The "Alpha" Method

Figure 3.3 shows the CV results for the Alpha method. ECSA values for all methods are reported in Table 3.1. The standard error obtained between trials for calculating the ECSA of a certain method is presented in Table B.4 of the S. I. See Table B.5 for the reported RF values and their respective standard errors. Based on the current densities for the formation α-$Ni(OH)_2$ transformation and the values in Table 3.1, the Ni triangle NPs holds the highest ECSA value, which is followed by the Ni urchin NPs, then the Ni foams and wire. It is important to observe that the spherical particles do not show an α-$Ni(OH)_2$ feature since the material is synthesized mostly in the β-$Ni(OH)_2$ state. As the transition from the β-$Ni(OH)_2$ back to the α-$Ni(OH)_2$ phase is irreversible, it is not possible to electrochemically reduce the spherical NPs back to metallic Ni to get a value for the Alpha ECSA value.

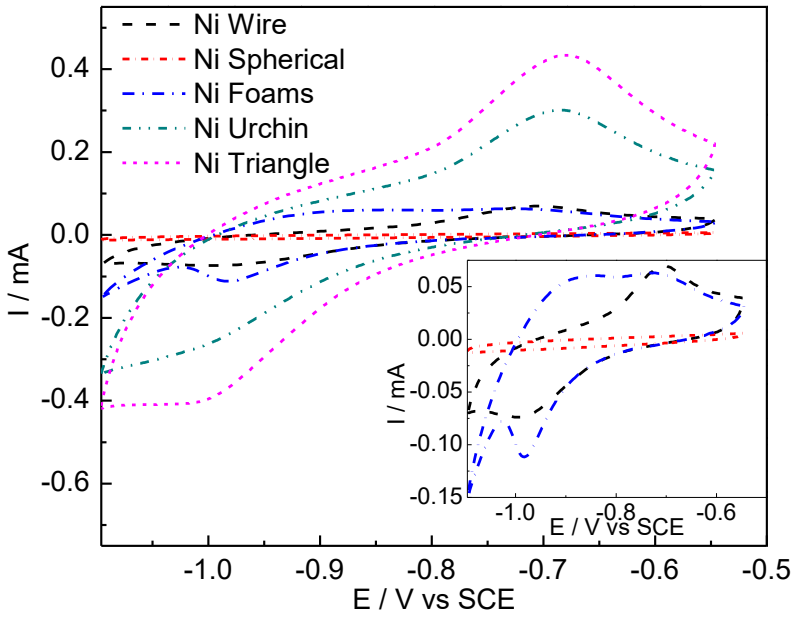

Figure 3.3: The Alpha method; Cycle 10 of CVs from -1.096 to -0.546 V vs SCE in 0.1 M KOH + 0.08 M $C_2H_2O_4$ run at a scan rate of 50 mVs^{-1}. Catalysts; Ni wire (black), Ni spherical (red), Ni foams (blue), Ni urchin (green) and Ni triangle (magenta). The inset figure shows details of the plots with lower currents.

3.3.3.2 The "Oxalate" Method

Figure 3.4 shows the CV results for the Oxalate method. As expected from their very small particle size, the Ni spherical particles show a very large current in the anodic region of the CV. It is however important to remember the theory behind the Oxalate method; the authors state that they start from a metallic Ni phase and cycle at a high scan rate, keeping the electrode in an unstable alpha-like phase in the anodic region [29]. The assumption that the electrode retains its alpha-like form brings the question of how representative the Oxalate method can be for surfaces that are already in the stable β-$Ni(OH)_2$ phase. Then, following a similar trend to the Alpha method, the Ni triangle particles have the next highest ECSA values, followed by the urchin NPs, the foams and the wire.

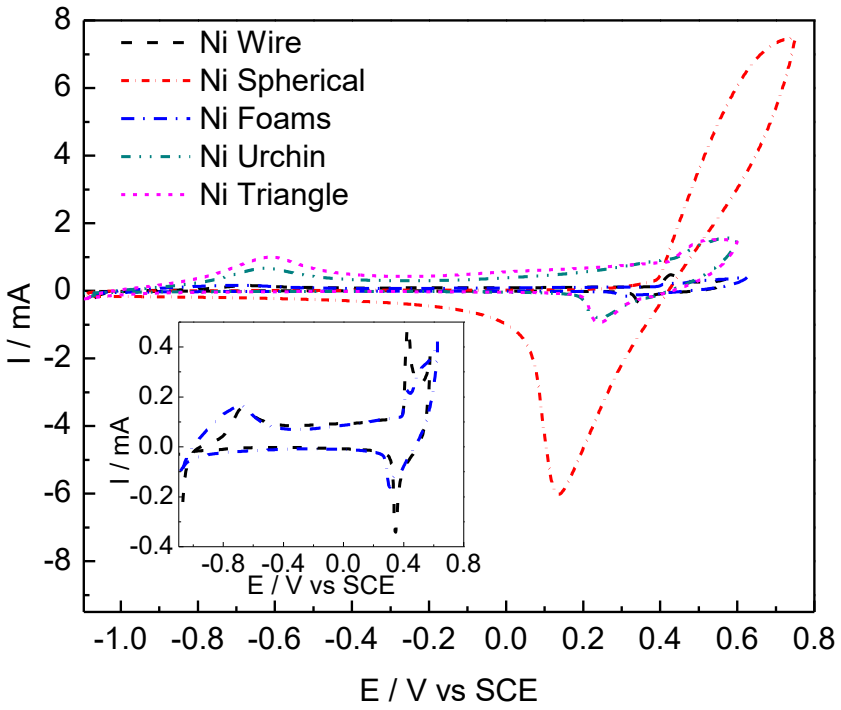

Figure 3.4: The Oxalate method; Cycle 1 of CVs from -1.096 to 0.575 V* vs SCE in 0.1 M KOH + 0.08 M $C_2H_2O_4$ run at a scan rate of 150 mVs^{-1}. Catalysts; Ni wire (black), Ni spherical (red), Ni foams (blue), Ni urchin (green) and Ni triangle (magenta). The inset figure shows details of the plots with lower currents. *Range specified for Ni wire; see Table B.1 for more details.

3.3.3.3 The "Capacitance" Method

Figure 3.5 shows the regressions used to calculate the double layer capacitance of the Ni electrodes from the charging current vs scan rate plot. Based on the math explained in Section 3.2.3.4, the higher the slope shown on Figure 3.5, the higher the ECSA. Contrary to what is expected from the Ni spherical NPs, the material showed a very low ECSA, which is possibly an effect of the surface oxidation state or the very small particle size. Interestingly, in this method, the Ni urchin NPs show an ECSA that is significantly higher than the triangle NPs, which is contrary to the results obtained from the Alpha and Oxalate methods. This however correlates nicely with the expected result of the urchin particles yielding a higher ECSA based on their lower specific surface area compared to the triangle NPs. The Capacitance method also results in a much higher value for the ECSA of the Ni foams compared to the Ni wire, which may be due to a better represented contribution from the micropores in the foam structure.

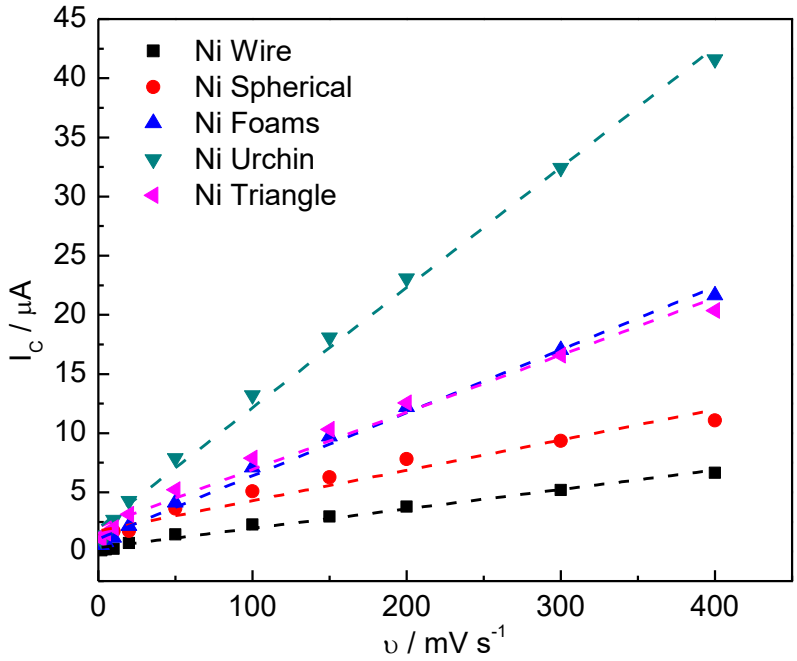

Figure 3.5: The Capacitance method; Experimental data of charging current vs scan rate as well as a linear regression of each data set in dotted lines, obtained from CV experiments done ± 50 mV around the OCP* in 0.1 M KOH. Catalysts; Ni wire (black), Ni spherical (red), Ni foams (blue), Ni urchin (green) and Ni triangle (magenta). *See Table B.2 for OCP values.

3.3.3.4 The "Beta" Method

Figure 3.6 shows the CV profiles for the Beta method. This method seems to show the most appropriate ECSA values for the Ni materials. For a decreasing particle size, the ECSA increases. Then, in accordance to the Capacitance method, the Ni foams are more active than the Ni wire, which is an expected result considering their three-dimensional structure. Furthermore, although the Ni spherical particles show a lower ECSA value using the Beta method compared to the Oxalate method, the obtained value with the Beta method could be more representative of the Ni spherical activity as it does not require a metallic Ni electrode to be applied.

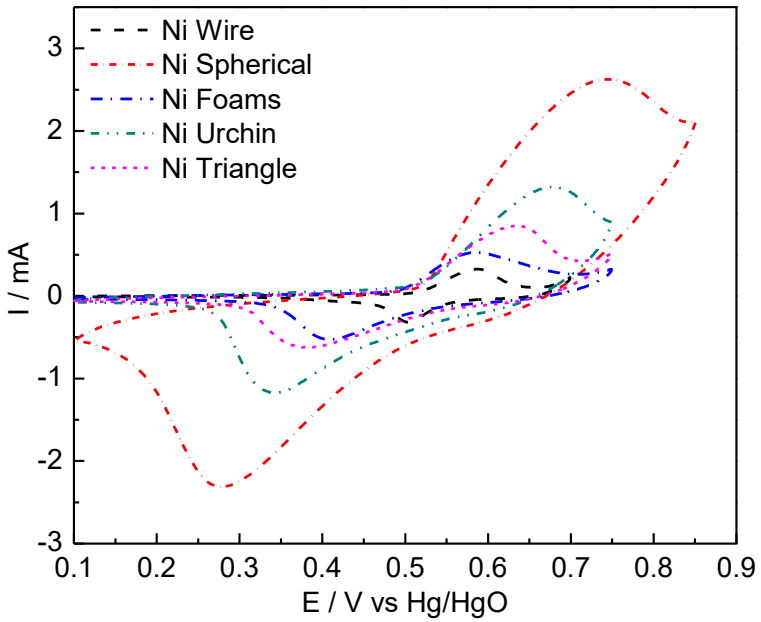

Figure 3.6: The Beta method; Cycle 100 of CVs from 0.1, 0.7 V* vs Hg/HgO in 0.1 M KOH run at a scan rate of 100 mVs^{-1}. Catalysts; Ni wire (black), Ni spherical (red), Ni foams (blue), Ni urchin (green) and Ni triangle (magenta). *Range specified for Ni wire; see Table B.3 for more details.

Table 3.1: Summary of electrochemical active surface area (ECSA) values.

Material	$ECSA_{alpha}$ [cm^2]	$ECSA_{oxalate}$ [cm^2]	$ECSA_{capacitance}$ [cm^2]	$ECSA_{beta}$ [cm^2]
Ni Wire	0.42	0.74	0.43	0.75
Ni Foams	0.43	0.75	1.19	2.09
Ni Triangle	2.48	3.55	1.27	2.93
Ni Urchin	1.86	3.39	2.62	5.08
Ni Spherical	N/A	21.90	0.47	13.37

3.3.3.5 Discussion of all ECSA Methods

Although the Alpha method is relatively reproducible, it does require the metallic state of Ni to be applied. This is therefore limiting when working with Ni-oxide species. Similarly, the Oxalate method was developed on a metallic Ni surface and the theory is based on remaining in an a state with α-$Ni(OH)_2$ -like character, making the obtained ECSA values likely less representative for oxide materials. The Oxalate method also works on the assumption that at 150 mVs^{-1}, a limiting cathodic charge is obtained in the first CV scan. To confirm applicability of the

method, the cathodic charge vs scan rate was measured for each electrode and summarized in Figure B.8 of the S. I. In Figure B.8, a limiting cathodic charge is more or less attained for all electrodes, however the cathodic charge of Ni spherical particles continues to change in a more significant way all the way until 400 mVs^{-1}, once again causing uncertainty in the obtained ECSA values for that material. In the Alpha and Oxalate methods, the ECSA for the urchin particles is smaller than the triangles NPs, despite the smaller physical size of the urchin NPs. This could be due to the higher NaOH concentration that was used in the synthesis of the urchin particles. It is possible that there are some inactive oxide species on the layer.

The Oxalate method also presents some disadvantages, particularly in the destruction of the electrode. As shown in Figure 3.7, applying the Oxalate method causes irreversible modification of the Ni surfaces, likely due to contamination from oxalate species. Note that the CVs in Figure 3.7 are in 0.1 M KOH. In Figure 3.7a, the reduction procedure of a CA at -1.446 V vs SCE for 5 mins, then a CA at -0.946 V vs SCE at 10 minutes was applied in an attempt to electrochemically reverse the adsorption of the oxalate species and "reset" the electrode. With the same goal in mind, in Figure 3.7b, simple anodic cycling after applying the Oxalate method was employed to try to rid its surface of any oxalate species. As shown in the CVs after the Oxalate method, there are electrochemically irreversible changes that occur on the electrode surface, as shown by the appearance of a new reduction peak and shifts in the oxidation peak maximum (Figure 3.7a) or current densities. As such, electrochemical test using the Oxalate method will need to be carried out with a different ink deposition than the one used to calculate the ECSA.

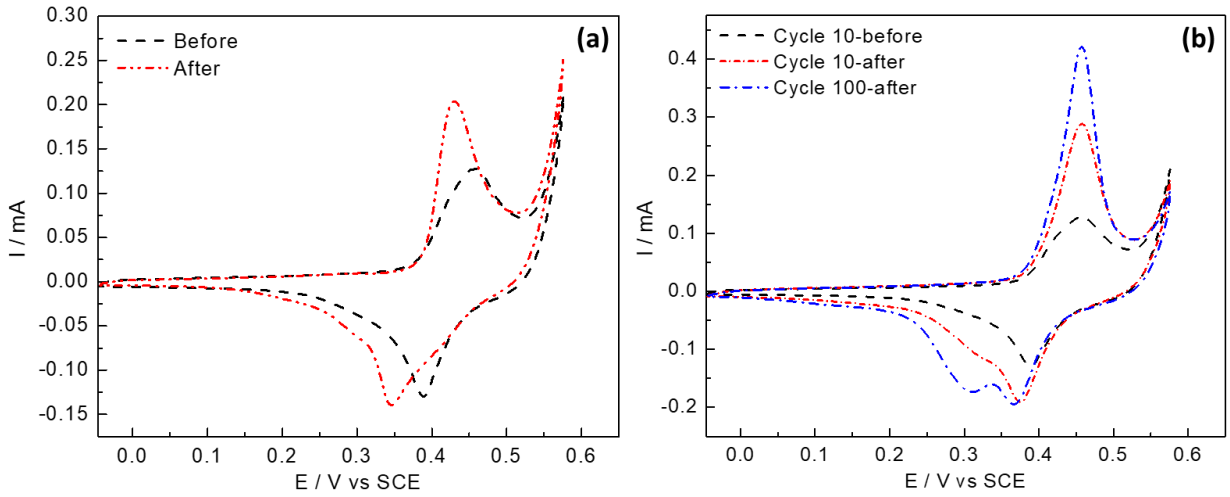

Figure 3.7: CVs for Ni wire from -0.046 to 0.575 V vs SCE in 0.1 M KOH run at a scan rate of 50 mVs^{-1} before and after the application of the Oxalate method. (a) Shows Cycle 10 before the Oxalate method and then after the method with the electrochemical reduction of the electrode, and (b) shows Cycle 10 before the Oxalate method and then Cycle 10 and 100 after the method.

The Capacitance method generally shows values that correlate well with the expected ECSA of each material based on their relative size, however the surface response of the spherical particles to the double layer charging process was not properly representing the activity of the small particles. This is likely due to the spherical Ni being nanoparticles of such a small size and that it is a mixture of metal and metal hydroxide species, indicating that it will present different behaviour depending on the exposed surfaces during polarization. As the oxide portion of the material is not conductive, it will not be in electronic contact with the current collector, therefore utilizing double layer charging the quantify the ECSA of this material will not be representative of the intrinsic activity of the particles. To confirm this, the Ni spherical particles were supported on 70 wt% carbon to allow for conduction through the catalyst. As shown in Table 3.2 and Figure B.9 of the S. I., supporting the Ni particles with carbon resulted in a very high ECSA obtained through the capacitance method, indicating a much better double layer response for that sample. Note that supporting Ni on carbon can modify catalytic activity in many ways, therefore the Ni/C results will not be further analyzed for this Ni ECSA study. Additionally, the metallic content in the carbon supported electrode is different, adding more differences to experimental conditions. For more details, on the Ni spherical / 70 wt% C experiments, see Section B.8 in the S. I.

Table 3.2: The Capacitance method; Comparison of Ni spherical NPs with and without a carbon support.

Ni Structure	**ECSA**$_{capacitance}$ [cm^2]	**RF**$_{capacitance}$ [-]
Ni Spherical	0.47	2.41
Ni Spherical / 70 wt% C	25.55	130.36

In comparison to the Alpha and Oxalate methods, which showed that the foams and the Ni wire had very similar ECSAs, the Capacitance method seems to be able to properly quantify the porous structure of the metallic Ni foams. Despite the poor results obtained for the unsupported Ni spherical particles, the Capacitance method is still advantageous because it does not change the nature of the electrode surface; there are no additional species required in the electrolyte, and since cycling is done by charging and discharging the electrochemical double layer, therefore no faradaic processes will occur. As for the Beta method, it shows a nice correlation between the size of the particles, and the obtained ECSA values. This method is however only favourable when working on the OER because it requires the transition into the Ni^{3+} state.

As explained in the above discussion, every method seems to offer its advantages and disadvantages. By looking only at the ECSA values for the Ni wire, which is used as a benchmark electrode in this study, it is possible to see that the Alpha and Capacitance methods may under estimate the ECSA values, however those ECSA values are only around 20-25% lower than what was obtained with the Oxalate and Beta methods. It is important to note that a direct comparison between methods will only be possible for the Ni wire electrode as it is a pure metallic surface. As mentioned in Section 3.3.1, the spherical Ni particles are synthesized mostly in the β-$Ni(OH)_2$ state, resulting in a lack of the α-$Ni(OH)_2$ transition peak in its CV shown in Figure 3.3. Although the rest of the nanomaterials were found to be metallic Ni in the XRD measurements and showed the α-$Ni(OH)_2$ transition peak in Figure 3.3, the form of their CVs indicates a small presence of Ni-oxides.

Another source of error in the study can come from the selection of the integration window used for the Oxalate and the Beta methods since the reduction peaks used to calculate the ECSA occurred at different potentials for the different types of Ni due to the different phases present in each sample. To study this effect, the ECSA of both methods was evaluated using two different ways: (a) calculating the ECSA values over a larger, identical potential window position, as

described in Sections 3.2.3.3 and 3.2.3.5 and (b) integrating over a smaller window around the reduction peak of Ni^{3+}, a window which was particular to each material. For the Oxalate and Beta methods, this potential window size was 125 and 200 mV, respectively. These alternate windows are shown in Table B.6 of the S.I. As shown in Table B.7 of the S. I., changing the integration window does not change the relative trends of the ECSA values. Choosing a smaller window only results in slightly lower ECSA values. Roughness factor values obtained using the smaller integration windows are reported in Table B.8. For more information, see the S. I.

Another important consideration when evaluating the results is that each synthesis method was prepared at different experimental conditions and in the presence of different chemicals, meaning that although each method had a cleaning procedure to remove impurities, it is possible that trace amounts of impurities in certain materials are interfering with certain ECSA methods. Finally, when looking at the accuracy of every method, it is important not to overlook the most important applied assumption; the use of a theoretical value of either a Ni surface charge density or capacitance. Theoretical surface charge and capacitance values should be determined specifically for every material, whether it be a Ni material or a Ni bimetallic catalyst. The values used in this study and throughout literature are reported for metallic Ni surfaces, therefore the ECSA methods are technically all limited to pure Ni surfaces. It is probable that only a small error is introduced by applying the theoretical charge density or capacitance of metallic Ni to other Ni surfaces, however, that error would increase when dealing with Ni bimetallic, or other Ni composite materials. Other researchers have applied the Capacitance method to Ni composite catalysts, however they acknowledge the inaccuracy that comes when applying the theoretical specific capacitance of Ni to other materials [31,32,34]. However, as the Capacitance method does not utilise characteristic peaks of the Ni electrode, it is possible that the Capacitance method is the best to use with other Ni-based catalysts.

It is to be noted that throughout the discussion, ECSA and RF values in this study are not compared to literature values as the materials used are synthesized using different methods and used in different amounts, therefore any comparison would not be informative for the purpose of this study.

3.4 Conclusions

Based on electrochemical active surface area methods that are presented in literature, the Alpha, Oxalate, Capacitance and Beta methods were successfully analyzed and compared for Ni wire, Ni foams as well as for shape-specific spherical, urchin and triangle Ni NPs. When looking at the results for the benchmark Ni wire electrode, the obtained ECSA values are relatively consistent between methods, which is expected for the pure metallic Ni surface. For the methods that were successfully applied to the various Ni structures, ECSA results are in nice correlation with the relative size of the particles, showing that the Ni wire has the lowest ECSA, which is followed by the Ni foams, the urchin and triangle NPs and finally the spherical NPs. This study has shown that there is not one ECSA method that should be used over the other. The Alpha method provides a precise estimation of the ECSA but cannot be applied to Ni oxide electrodes. The Oxalate method well represents the ECSA of the materials, however it is harder to reproduce, and requires a new catalyst for subsequent electrochemical experiments. Furthermore, like the Alpha method, the ECSA values obtained using the Oxalate method should not be trusted for Ni oxide species. The Capacitance method is a very promising ECSA method however some concerns arose when using the spherical particles due to their non-conductive inhomogeneous surface, resulting in inconsistent double layer charging. The Capacitance method is however the most favourable for activity comparisons of Ni composite materials because it does not use any transition peaks specific to Ni to calculate the ECSA. Finally, the Beta method provides representative ECSA values however the method is limited to electrodes used in OER applications.

Acknowledgements

This research was conducted as part of the Engineered Nickel Catalysts for Electrochemical Clean Energy project administered from Queen's University and supported by Grant number RGPNM 477963-2015 under the Natural Sciences and Engineering Research Council of Canada (NSERC) Discovery Frontiers Program. Additional funding was also provided by NSERC's Alexander Graham Bell Canada Graduate Scholarship – Doctoral (CGS D), as well as the Science and Technology Internship Program (STIP) by Natural Resources Canada (NRCan) for Green Jobs in Natural Resources.

References

[1] A. Seghiouer, J. Chevalet, A. Barhoun, F. Lantelme, *J. Electroanal. Chem.* **1998**, *442*, 113.

[2] M. Tahir, L. Pan, F. Idrees, X. Zhang, L. Wang, J. J. Zou, Z. L. Wang, *Nano Energy* **2017**, *37*, 136.

[3] D. S. Hall, D. J. Lockwood, C. Bock, B. R. MacDougall, *Proc. R. Soc. A Math. Phys. Eng. Sci.* **2014**, *471*, 20140792.

[4] Y. Kiros, S. Schwartz, *J. Power Sources* **2000**, *87*, 101.

[5] Z. Zhuang, S. A. Giles, J. Zheng, G. R. Jenness, S. Caratzoulas, D. G. Vlachos, Y. Yan, *Nat. Commun.* **2016**, *7*, 1.

[6] G. A. Goenaga, A. L. Roy, N. M. Cantillo, S. Foister, T. A. Zawodzinski Jr., *J. Power Sources* **2018**, *395*, 148.

[7] M. Gong, H. Dai, *Nano Res.* **2015**, *8*, 23.

[8] M. Gong, D. Y. Wang, C. C. Chen, B. J. Hwang, H. Dai, *Nano Res.* **2016**, *9*, 28.

[9] A. Faid, A. Oyarce Barnett, F. Seland, S. Sunde, *Catalysts* **2018**, *8*, 614.

[10] E. Cossar, A. O. Barnett, F. Seland, E. A. Baranova, *Catalysts* **2019**, *9*, 814.

[11] M. S. E. Houache, E. Cossar, S. Ntais, E. A. Baranova, *J. Power Sources* **2018**, *375*, 310.

[12] M. S. E. Houache, K. Hughes, A. Ahmed, R. Safari, H. Liu, G. A. Botton, E. A. Baranova, *ACS Sustain. Chem. Eng.* **2019**, *7*, 14425.

[13] M. S. E. Houache, K. Hughes, E. A. Baranova, *Sustain. Energy Fuels* **2019**, *3*, 1892.

[14] M. Alsabet, M. Grden, G. Jerkiewicz, *Electrocatalysis* **2011**, *2*, 317.

[15] M. Alsabet, M. Grden, G. Jerkiewicz, **2014**, *5*, 136.

[16] M. Alsabet, M. Grdeń, G. Jerkiewicz, *Electrocatalysis* **2015**, *6*, 60.

[17] D. S. Hall, D. J. Lockwood, S. Poirier, C. Bock, B. R. MacDougall, *J. Phys. Chem. A* **2012**, *116*, 6771.

[18] M. E. G. Lyons, M. P. Brandon, *Int. J. Electrochem. Sci.* **2008**, *3*, 1386.

[19] D. S. Hall, C. Bock, B. R. MacDougall, *J. Electrochem. Soc.* **2013**, *160*, F235.

[20] H. Bode, K. Dehmelt, J. White, *Electrochim. Acta* **1966**, *11*, 1079.

[21] S. Trasatti, O. A. Petrii, *Pure Appl. Chem.* **1991**, *63*, 711.

[22] S. Ntais, A. Serov, N. I. Andersen, A. J. Roy, E. Cossar, A. Allagui, Z. Lu, X. Cui, E. A. Baranova, P. Atanassov, *Electrochim. Acta* **2016**, *222*, 1455.

[23] G. Jerkiewicz, *Electrocatalysis* **2010**, *1*, 179.

[24] M. Shao, J. H. Odell, S. Il Choi, Y. Xia, *Electrochem. commun.* **2013**, *31*, 46.

[25] A. P. Yadav, *Int. J. Chem. Stud.* **2013**, *1*, 215.

[26] S. A. S. Machado, L. A. Avaca, *Electrochim. Acta* **1994**, *39*, 1385.

[27] M. Grden, M. Alsabet, G. Jerkiewicz, *ACS Appl. Mater. Interfaces* **2012**, *4*, 3012.

[28] J. Van Drunen, B. Kinkead, M. C. P. Wang, E. Sourty, B. D. Gates, G. Jerkiewicz, *ACS Appl. Mater. Interfaces* **2013**, *5*, 6712.

[29] D. S. Hall, C. Bock, B. R. MacDougall, *J. Electrochem. Soc.* **2014**, *161*, H787.

[30] J. van Drunen, A. F. B. Barbosa, G. Tremiliosi-Filho, *Electrocatalysis* **2015**, *6*, 481.

[31] C. C. L. McCrory, S. Jung, J. C. Peters, T. F. Jaramillo, *J. Am. Chem. Soc.* **2013**, *135*, 16977.

[32] C. C. L. McCrory, S. Jung, I. M. Ferrer, S. M. Chatman, J. C. Peters, T. F. Jaramillo, *J. Am. Chem. Soc.* **2015**, *137*, 4347.

[33] J. C. K. Ho, D. L. Piron, *J. Appl. Electrochem.* **1996**, *26*, 515.

[34] M. J. Gira, K. P. Tkacz, J. R. Hampton, *Nano Converg.* **2016**, *3*, 1.

[35] G. Li, L. Anderson, Y. Chen, M. Pan, P. A. Chuang, *Sustain. Energy Fuels* **2018**, *2*, 237.

[36] M. E. G. Lyons, M. P. Brandon, *J. Electroanal. Chem.* **2010**, *641*, 119.

[37] B. E. Conway, L. Bai, *J. Chem. Soc. Faraday Trans. 1 Phys. Chem. Condens. Phases* **1985**, *81*, 1841.

[38] W. Sheng, M. Myint, J. G. Chen, Y. Yan, *Energy Environ. Sci.* **2013**, *6*, 1509.

[39] W. Ni, H. Bin Wu, B. Wang, R. Xu, X. W. Lou, *Small* **2012**, *8*, 3432.

[40] S. H. Wu, D. H. Chen, *J. Colloid Interface Sci.* **2003**, *259*, 282.

[41] H. Wang, X. Kou, J. Zhang, J. Li, *Bull. Mater. Sci.* **2008**, *31*, 97.

Chapter 4. Highly Active Nickel-iron Nanoparticles with and without Ceria for the Oxygen Evolution Reaction

Emily Cossar[a], Kushagra Agarwal[a], Vu Bao Nguyen[a], Reza Safari[b], Gianluigi A. Botton[b] and Elena A. Baranova[a*]

[a] *Department of Chemical and Biological Engineering, Centre for Catalysis Research and Innovation (CCRI), University of Ottawa, 161 Louis-Pasteur Ottawa, Canada, K1N 6N5*

[b] *Department of Materials Science Engineering, McMaster University, 1280 Main St. W., Hamilton, Ontario, Canada L8S 4L8*

Chapter as published in: *Electrocatalysis* **2021**, https://doi.org/10.1007/s12678-021-00674-7.

Supplementary information for this chapter is found in Appendix C.

Abstract

Anion exchange membrane water electrolysis (AEMWE) is an attractive technology for hydrogen (H_2) production. This process, however, is kinetically hindered by the oxygen evolution half-cell reaction (OER). Nickel (Ni) -based materials in combination with iron (Fe) have been considered a promising option to enhance activity towards OER in alkaline media. Studies have also shown that incorporating ceria (CeO_2) into electrocatalysts can help promote the OER. This study investigates the OER activity of bimetallic Ni-Fe spherical nanoparticles, with and without ceria, synthesized by chemical reduction in ethanol using sodium borohydride. First, the iron content is studied for $Ni_{100-x}Fe_x$/50 wt% CeO_2 (x=0, 5, 10, 20, 40 at%), then the ceria content is studied for the best two iron compositions, namely, $Ni_{80}Fe_{20}$/ y wt% CeO_2 and $Ni_{90}Fe_{10}$/ y wt%CeO_2 (y=0, 5, 7, 10, 20 and 50 wt%). Transmission electron microscopy (TEM) and energy dispersive spectroscopy (EDS) characterization shows spherical particles 4-6 nm in size, where Ni and Fe are co-distributed, and ceria is separately agglomerated. Electrochemical characterization in 1 M KOH shows that at 10 mA cm^{-2}, the $Ni_{80}Fe_{20}$ catalyst achieved the lowest overpotential for OER of 269 mV, which better performing than the iridium black benchmark, as well as similar NiFe materials reported in literature. Stability testing indicates that the $Ni_{90}Fe_{10}$ catalyst is the most stable material with almost no change in overpotential over 12 h at 10 mA cm^{-2}. This study shows that the addition of CeO_2 to the catalysts does not significantly improve or impede OER activity.

Graphical Abstract

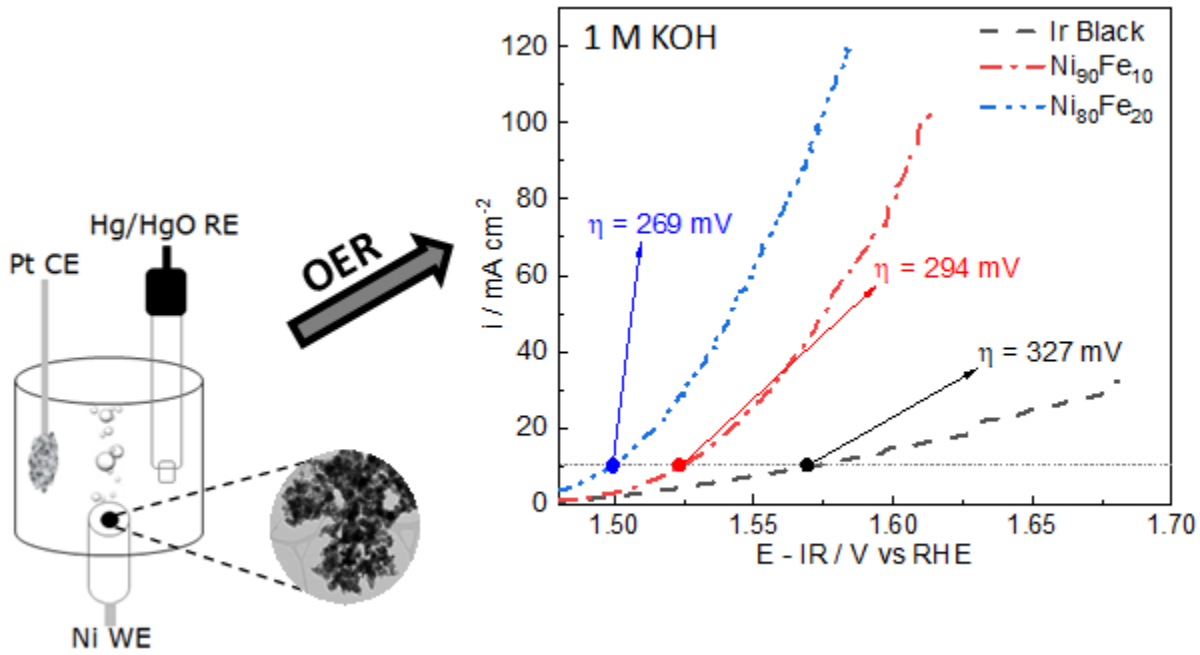

4.1 Introduction

Hydrogen (H_2) is one of the most promising clean alternative energy carriers for many reasons including its high mass energy density of 143 MJ kg^{-1}[1], three times that of gasoline or diesel, and its ability to be utilized in a completely sustainable manner; H_2 can be produced by water electrolysis, powered by renewable energy sources, and then the stored energy can be released and used in a fuel cell, emitting only water as a by-product[2]. Amongst the many types of water splitting reactions, anion exchange membrane water electrolysers (AEMWE) are the most feasible technology for efficient, clean hydrogen production because they combine the advantages from both the proton exchange membrane water electrolysis (PEMWE) system and the traditional alkaline water electrolysis system[3–5].

While the traditional alkaline electrolysis system employs a porous diaphragm separator, the AEMWE system employs the use of a polymer electrolyte membrane, which results in a reduces cell resistance and better separation of the produced gases, thus allowing for high operational efficiency and improved safety[6,7]. Although the PEMWE also delivers efficient performance using the zero-gap cell design, its acidic environment requires the use of noble metal catalysts for the anode and cathode, as well as expensive cell components, such as perfluorinated membranes and titanium-based current collectors[4,7,8]. The AEMWE system on the other hand allows for the use low-cost non-noble catalysts and cell components, resulting in dramatic cost savings.

The AEMWE process occurs through two half-cell reactions: the oxygen (O_2) and the hydrogen evolution reactions (OER and HER), shown respectively in Reactions 4.1 and 4.2 below[2].

$$2OH^- \rightarrow H_2O + \tfrac{1}{2}O_2 + 2e^- \; ; E^0 = 0.40 \text{ V vs SHE} \qquad \textbf{\textit{Reaction 4.1}}$$

$$2H_2O + 2e^- \rightarrow H_2 + 2OH^- \; ; E^0 = -0.83 \text{ V vs SHE} \qquad \textbf{\textit{Reaction 4.2}}$$

The OER has sluggish kinetics in comparison to the HER because for each molecule of O_2 produced, twice as many electron transfer steps need to occur and twice as many hydroxide ions (OH^-) ions need to participate in the reaction[5,9]. An example of a conventional OER mechanism in alkaline media is shown by Reactions 4.3-4.6[10–12], however other proposed or commonly used mechanisms have been reported[13–15].

$$OH^- + * \rightarrow OH^* + e^-$$ ***Reaction 4.3***

$$OH^* + OH^- \rightarrow O^* + H_2O + e^-$$ ***Reaction 4.4***

$$O^* + OH^- \rightarrow OOH^* + e^-$$ ***Reaction 4.5***

$$OOH^* + OH^- \rightarrow * + H_2O + e^- + O_2 \uparrow$$ ***Reaction 4.6***

Nickel (Ni) has been investigated as a catalyst to improve the OER as it is an inexpensive and abundant catalyst with high activity and stability in an alkaline environment[16]. Like other transition metals, Ni has high achievable oxidation states as described by the Bode diagram[17,18], one of which is the β-NiOOH state, which is said to be the most active phase towards the OER[15]. Many studies have shown that iron (Fe) in combination with Ni make some of the highest performing OER catalysts[15,16,19–25]. Some attribute this increase in OER activity to the introduction of the Fe active site. For example, when incorporating over 4.7% Fe into NiFe layered double hydroxide materials, it was found that the active site of the catalyst changed from Ni to Fe, increasing the turnover frequency of the catalyst 20-200 fold[22]. Similarly, a study on electrodeposited $Ni_{1-x}Fe_xOOH$ catalysts showed that there was a 500 fold increase in OER activity with Fe contents up to 25%, owing to the Fe^{3+} active site within the $Ni_{1-x}Fe_xOOH$[23]. On the other hand, others claim Ni remains the active site, while Fe serves as a promoter to Ni. For example, when studying Fe-doped electrodeposited Ni borate films, the increase in OER activity was found to stem from a more easily accessible Ni^{4+} active state when anodizing the electrode with 5-10% Fe present[24]. Density functional theory (DFT) calculations have also been applied to Fe-doped NiOOH systems for OER[25]. It was found that the (Ni,Fe)OOH system is bifunctional where both Ni and Fe work in synergy to catalyze the OER; Fe^{4+} helps form an active O radical species, while Ni^{4+} serves to subsequently catalyze O-O coupling, showing each metal helping with elemental steps of the OER mechanism. A summary of NiFe catalysts studied for the OER in 1 M KOH is shown in Table 4.1. Along with their reported reaction overpotential at 10 mA cm^{-2} is their synthesis method. Further discussion of the data in this table is found in Section 4.3.2.1.

Table 4.1: Summary of OER performance of related NiFe materials in 1 M KOH. Reference numbers are as follows: Ref. A [20]***, Ref. B*** [26]***, Ref. C*** [27]***, Ref. D**** [28]***, Ref. E*** [29]***, Ref. F*** [30]***, Ref. G*** [31]***, Ref. H*** [32] ***and Ref. I*** [33]

Ref Number	Material	η at 10 mA cm^{-2} [mV]	Tafel slope [$mVdec^{-1}$]	Synthesis Method
this work $Ni_{90}Fe_{10}$	$Ni_{90}Fe_{10}$	294	42	chemical reduction
this work $Ni_{80}Fe_{20}$	$Ni_{80}Fe_{20}$	269	43	chemical reduction
Ref. A [20]	$Ni_{0.9}Fe_{0.1}O_x$	336	30	thin film deposition by spin coating
Ref. B [26]	$Ni_{0.88}Fe_{0.12}(OH)_2$	348	41.5	modified hydrothermal method
Ref. C [27]	$Ni_{0.75}Fe_{0.25}(OH)_x$	310	68	coordinated etching and precipitation using a Cu_2O template
Ref. D* [28]	$Ni_{32}Fe_1$ oxide	291	58	hard templating using spent tea leaves as the template
Ref. E [29]	$Fe:Ni(OH)_2$	280	40	electrodeposition of $Ni(OH)_2$ film, Fe incorporation by aging
Ref. F [30]	NiFe (3:1) LDH	302	40	hydrothermal process, then liquid phase exfoliation
Ref. G [31]	NiFe (4:1) LDH	331	58	electrodeposition of NiFe nanoplates
Ref. H [32]	$Ni_{78}Fe_{22}$ LDH	280	47.6	pulsed-laser ablation in liquids
Ref. I [33]	NiFe LDH	290	228	seed-assisted hydrothermal method

*Results obtained in Fe-free 1 M KOH.

Cerium oxide or ceria (CeO_2) is a mixed ionic-electronic conducting (MIEC) support that has been widely used in multiple applications due to its ability to efficiently store and release oxygen [34]. Ceria's ability to easily transform between Ce^{4+} and Ce^{3+} and form oxygen vacancies make it a material with unique properties, which are particularly useful for oxidation reactions[35]. The addition of CeO_2 to a metal catalyst either in the form of a co-catalyst or as a support leads to the modification electronic properties of the metal[36]. Furthermore, the interaction between ceria and water has been investigated using density functional theory (DFT)[37–39]. It has been demonstrated that if oxygen vacancies are present at the ceria surface, the binding energy of water

is stronger, indicating an attractive interaction between water molecules and oxygen vacancies[39], which could lead to OER promotion.

The use of ceria to enhance the OER on various metal catalysts has been reported[40–45]. It was observed the addition of ceria in FeOOH/CeO_2 (1:1) heterolayered nanotubes (HLNT) supported on a Ni nanofoam (NF) resulted in higher OER currents at lower overpotentials, in addition to maintaining good catalytic stability over 50 h[40]. Similarly, adding 6.9% CeO_2 to a copper oxide (CuO_x) catalyst resulted in a 3.3 times higher OER current, while also showing improved stability over 5 h, due to the uniform distribution of Ce^{4+} or small CeO_x clusters throughout the CuO_x sample[41]. Finally, incorporating less than 10% ceria into iridium-ruthenium oxide catalysts was shown to promote the electrocatalytic properties and intrinsic efficiency of the active sites of the catalysts for OER in acidic media due to the oxygen mobility of ceria in the samples[45].

In this work we prepare various compositions of bimetallic NiFe catalysts with and without CeO_2 by an easily scalable chemical reduction synthesis method in ethanol using sodium borohydride. The goal of the study was first to optimize the amount of iron, then the amount of ceria, used in the materials to find high performing OER catalysts in alkaline media. All electrochemical testing was performed in 1 M KOH and the best 6 catalysts were also tested in 0.1 M KOH. Additionally, durability experiments were performed on the best 6 catalysts by cyclic voltammetry for 300 cycles and by chronopotentiometry for 12 h.

4.2 Materials and Methods

4.2.1 Material Synthesis

The bimetallic NiFe materials with and without ceria were made by chemical reduction in ethanol using sodium borohydride. This synthesis method was used in our previous work[18] when testing some of the NiFe materials as anodes in single AEMWE cells. Whether the goal was to synthesize, Ni, NiFe or NiFe/CeO_2, the procedure for this easily scalable method is the same. To make the materials, the required amount of nickel chloride hexahydrate ($NiCl_2 \cdot 6H_2O$, 99.999%, Sigma Aldrich, St. Louis, MO, USA), iron sulphate heptahydrate ($FeSO_4 \cdot 7H_2O$, ≥99%, Sigma Aldrich, St. Louis, MO, USA) precursor salts as well as cerium oxide nanopowder (CeO_2, 99.5%, 15 to 30 nm, 30 to 50 m^2 $g^{-}1$, Alfa Aesar, Haverhill, MA, USA) are first dissolved in ethanol

(EtOH, 99%, Greenfield, Grayslake, IL, USA) by magnetic stirring each in their own Erlenmeyer flask that was previously cleaned with the Aqua Regia procedure [2:1 by volume of hydrochloric acid to nitric acid (HCl 37%, HNO_3 70%, Sigma Aldrich, St. Louis, MO, USA)]. The three components are then mixed and chemically reduced using sodium borohydride ($NaBH_4$, ≥98%, ACROS, Geel, Belgium) that was dissolved in water (Milli-Q® Millipore, 18.2 MΩ cm at 293 K). The nanoparticles (NPs) are then removed from the reaction solution by centrifuge at 6000 rpm for 10 mins and subsequently washes 3x with ethanol using the same centrifuge settings. Finally, the materials are freeze dried over night.

As the goal of this work was to optimize the amount of iron and ceria in the Ni-based catalysts, two sets of material synthesis were done. The first set covered testing $Ni_{100-x}Fe_x$/ 50 wt% CeO_2 for x=0, 5, 10, 20 and 40 at% to optimize the Fe content in a Ni/50 wt% catalyst. The second set was used to optimize the ceria content on the best two performing NiFe catalysts, namely, $Ni_{90}Fe_{10}$/ 50 wt% CeO_2 and $Ni_{80}Fe_{20}$/ 50 wt% CeO_2. Therefore, in addition to the data collected using 50 wt% CeO_2, the materials were also tested with 20, 10, 7 and 5 and 0 wt% CeO_2.

4.2.2 Material Characterization

The NiFe-based particles were characterized using transmission electron microscopy (TEM) and energy dispersive spectroscopy (EDS). The TEM images were taken using the Philips CM12 at an operating voltage of 120 kV. The EDS mapping was performed using the JOEL JEM 2010 FETEM at 200 keV. For this method, all X-rays were collected through an EDS detector, then all spectra and images were analysed and extracted using an INCA software, included in the same system.

4.2.3 Electrochemical Characterization

4.2.3.1 Cell Setup

Electrochemical OER testing was carried out in a Teflon three-electrode cell where the working electrode (WE) was facing upward for ease of bubble evolution. A representation of the OER cell is shown in Figure C.1 of the Supplementary Information (SI). Prior to testing, the WE (London Scientific Limited, St. Thomas, ON, CAN) was polished with 30-micron alumina (Al_2O_3, Carveth Metallurgical Limited, Canada) and 3-micron alumina (Al_2O_3, Buehler, Lake Bluff, IL, USA) then it was wiped with EtOH and Milli-Q® water. For all electrochemical testing, the

working electrode's glassy carbon (GC) surface area of 0.196 cm^2 was covered with 5 µL catalyst ink, which was dried in an oven at 60°C for 5 mins. The ink consisted of 6 mg of catalyst, 1 mL of Milli-Q® water, 200 µL of isopropanol (IPA, 99.9% Fisher Scientific, Hampton, NH, USA) and 100 µL of Nafion® (~5%, Sigma Aldrich, St. Louis, MO, USA), all of which was mixed using an ultrasonic bath (40 kHz Ultrasonic Bath 15337409, Fischer Scientific, Hampton, NH, USA) for 5 mins. This resulted in an electrode loading of around 118 µg cm^{-2}. The counter electrode used was a Pt mesh and the reference electrode was a mercury/mercury oxide (Hg/HgO, Koslow Scientific Company, Englewood, NJ, USA) electrode. Testing was done at room temperature (RT) in both 1 and 0.1 M potassium hydroxide (KOH, ≥85%, Sigma Aldrich, St. Louis, MO, USA). Although it has been shown that iron impurities present in reagent grade KOH can affect the results of electrochemical OER testing on Ni electrodes[29,46,47], for practical purposes, the electrolyte in this study was not further purified. All experiments were controlled using EC labs software with the Bio-Logic Potentiostat/Galvanostat(Bio-Logic Science Instruments, Seyssinet, France).

4.2.3.2 Electrochemical Testing

A series of tests were carried out to properly evaluate the OER activity of the synthesized materials. First, to calculate the ohmic losses of the system, potentiostatic electrochemical impedance spectroscopy (EIS) experiments were carried out around the OCP of each electrode using a sinusoidal amplitude of 5 mV from 50 kHz to 0.1 Hz. Then, to pre-treat the electrode[48] before OER testing, a chronoamperometry (CA) experiments were carried out at -1.3 V for 5 mins then at -0.8 V for 10 mins. To evaluate the OER, cyclic voltammetry (CV) experiments were done between 0.1 and 0.8 V vs Hg/HgO for 10 cycles at 25 mV s^{-1}, then linear sweep voltammetry (LSV) experiments were done between 0.3 and 0.8 V vs Hg/HgO for 1 sweep at 1 mV s^{-1}. Cycle 10 of the CVs are reported unless otherwise indicated. To test the preliminary electrode durability and mechanical integrity of the best performing electrodes, the CVs mentioned above were repeated for 300 cycles and chronopotentiometry (CP) measurements were done at 10 mA cm^{-2} for 12 h. Note that all presented currents were normalized using the geometric surface area of the electrode. The electrochemical active surface area (ECSA) was not used to analyze the data as there are many uncertainties, assumptions and estimations involved in calculating the ECSA of Ni-based materials[49]. By using the geometric surface area to normalize the data, no results can be skewed due to poorly estimated ECSA values. Furthermore, to analyze the results, graphs were

converted to the reference hydrogen electrode (RHE) using Equations 4.1 and 4.2 for data obtained in 1 and 0.1 M KOH, respectively. These calculations are further elaborated on in our previous work[18].

$$E_{RHE} = E_{Hg/HgO} + 0.925 \quad \textit{Equation 4.1}$$

$$E_{RHE} = E_{Hg/HgO} + 0.866 \quad \textit{Equation 4.2}$$

4.3 Results and Discussion

4.3.1 TEM and EDS

Figure 4.1 shows TEM images for $Ni_{90}Fe_{10}$ (Figure 4.1a), $Ni_{80}Fe_{20}$ (Figure 4.1b), $Ni_{90}Fe_{10}$/10 wt% CeO_2 (Figure 4.1c) and $Ni_{80}Fe_{20}$/7 wt% CeO_2 (Figure 4.1d), while Figures 4.2 and 4.3 show EDS mapping for $Ni_{90}Fe_{10}$ (Figure 4.2a, b, c), $Ni_{80}Fe_{20}$ (Figure 4.2d, e, f), $Ni_{90}Fe_{10}$/10 wt% CeO_2 (Figure 4.3a, b, c, d) and $Ni_{80}Fe_{20}$/7 wt% CeO_2 (Figure 4.3e, f, g, h). When inspecting the TEM micrography for the $Ni_{90}Fe_{10}$ particles, it is difficult to see each individual particle as they agglomerate very easily, however in some areas, agglomerates with smaller single particles surrounding them can be found. Due to the low iron content, the big agglomerates are likely Ni, while the small particles around the agglomerates are a mix of Ni and Fe. This is supported by the EDS mapping shown in Figure 4.2b and c, where it is possible to visualize that the $Ni_{90}Fe_{10}$ sample has a co-distribution of Ni and Fe throughout the material, with more Ni present that Fe. The $Ni_{80}Fe_{20}$ sample shown in Figure 4.1b has a similar structure to $Ni_{90}Fe_{10}$, however it has an additional flake-like phase. Through EDS mapping it was possible to determine that this sample also has a co-distribution of Ni and Fe in both the particle/agglomerate phase and the flake-like phase.

As for the samples containing CeO_2 shown in Figure 4.1c and d as well as Figure 4.3, it seems that the larger size of commercial CeO_2 particles (15 – 30 nm with a specific surface area of 30 – 50 $m^2 g^{-1}$), prevent it from evenly distributing itself within the metallic content. It is once again difficult to identify, from inspection of the TEM images, the different phases of the sample. However, in some areas, it is possible to recognize larger clusters, later identified as CeO_2 particles, which are surrounded by the smaller particles and agglomerates of Ni and Fe. The EDS mapping in Figure 4.3 supports the identification of phases from the TEM images showing that Ni and Fe

are co-distributed in one area, while CeO_2 is agglomerated separately in other areas. Other characterization of some of these samples is available in our previous work[18].

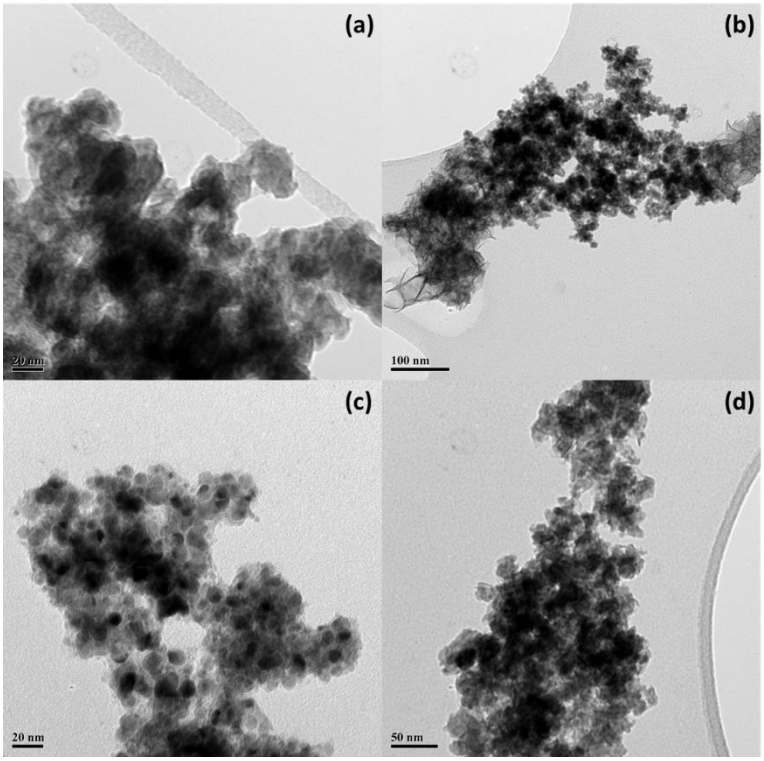

Figure 4.1: TEM of (a) $Ni_{90}Fe_{10}$, (b) $Ni_{80}Fe_{20}$, (c) $Ni_{90}Fe_{10}$/10 wt% CeO_2 and (d) $Ni_{80}Fe_{20}$/7 wt% CeO_2 NPs.

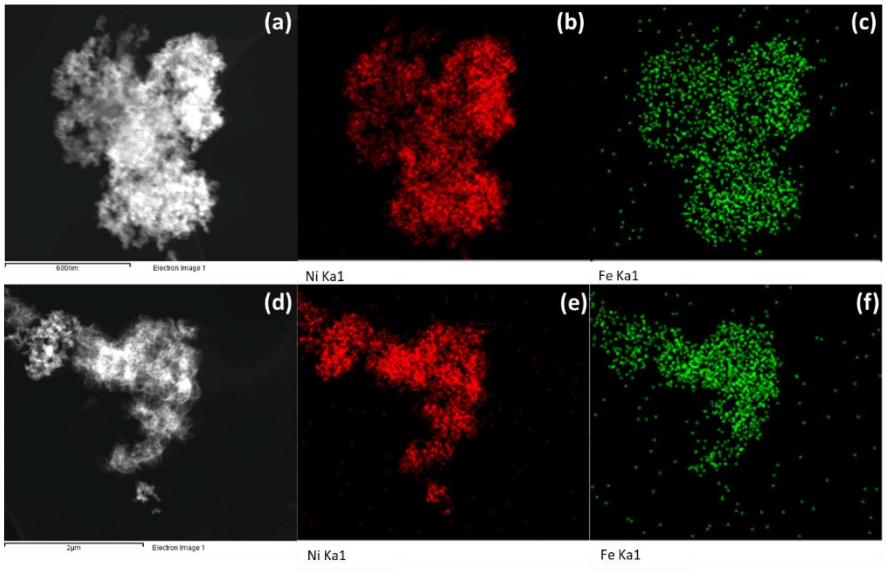

Figure 4.2: EDS mapping of (a, b, c) $Ni_{90}Fe_{10}$ (d, e, f) $Ni_{80}Fe_{20}$ NPs, where (a, d) show the analysed image, (b, e) show the Ni content and (c, f) show the Fe content.

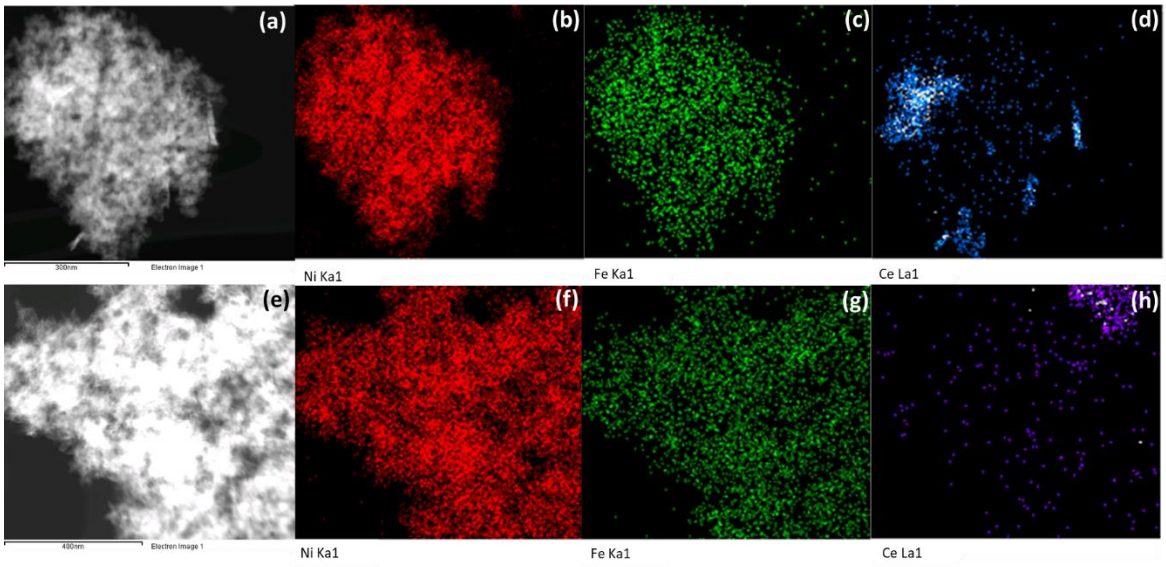

Figure 4.3: EDS mapping of (a, b, c, d) $Ni_{90}Fe_{10}$/ 10 wt% CeO_2 and (e, f, g, h)) $Ni_{80}Fe_{20}$/ 7 wt% CeO_2 NPs, where (a, e) show the analysed image, (b, f) show the Ni content, (c, g) show the Fe content and (d, h) show the Ce content.

4.3.2 Electrochemical Characterization

4.3.2.1 Evaluation of OER Performance

Different atomic fractions of Fe were tested in $Ni_{100-x}Fe_x$/ 50 wt% CeO_2 (x=0, 5, 10, 20 and 40 at%) materials to find the optimal composition. Results obtained from CV and LSV testing are shown in Figure 4.4 and key information is summarized in Table 4.2. For comparison, data for monometallic Ni is also included in Figure 4.4 and Table 4.2. To see how the Ni/ 50 wt% CeO_2 catalyst compares to Ni and CeO_2 alone, see Figure C.2 in the SI. Information on where the Tafel slopes were calculated in Figure 4.4b is shown in Figure C.3 of the SI.

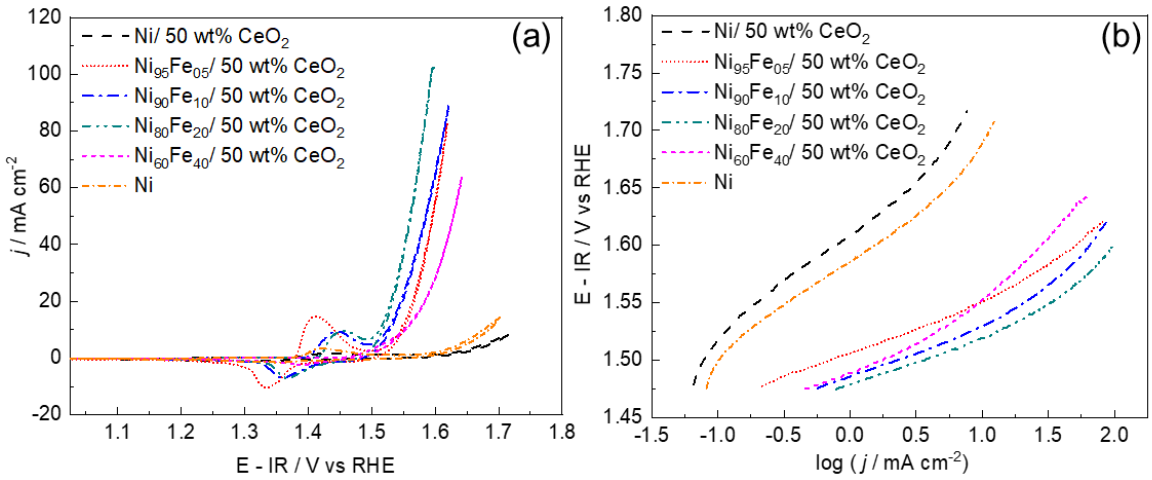

Figure 4.4: (a) Cyclic voltammetry run at 25 mV s^{-1} and (b) Tafel plot obtained from linear sweep voltammetry run at 1 mV s^{-1} in 1 M KOH at RT for the $Ni_{100-x}Fe_x$/ 50 wt% CeO_2 (x = 0, 5, 10, 20, 40 at%) catalysts as well as Ni, as indicated in the figure.

Table 4.2: Summary of OER performance for $Ni_{100-x}Fe_x$/50 wt% CeO_2 (x=0, 5, 10, 20, 40 at%) as well as Ni in 1 M KOH obtained from Figure 4.4b. η = overpotential.

Material	**η at 10 mA cm^{-2} [mV]**	**η at 80 mA cm^{-2} [mV]**	**Tafel Slope [mV dec^{-1}]**
Ni	445	N/A*	75
Ni/ 50 wt% CeO_2	N/A*	N/A*	79
$Ni_{95}Fe_{05}$/ 50 wt% CeO_2	321	391	41
$Ni_{90}Fe_{10}$/ 50 wt% CeO_2	299	384	41
$Ni_{80}Fe_{20}$/ 50 wt% CeO_2	289	357	40
$Ni_{60}Fe_{40}$/ 50 wt% CeO_2	323	N/A*	46

*current not attained

When looking at the transition peaks of $Ni(OH)_2$/NiOOH, it is possible to observe that the oxidation peak of $Ni(OH)_2$ to NiOOH shifts to a more positive potential as more iron is incorporated to the catalyst. This trend is commonly reported in literature[21,29,50], and is characteristic of NiFe bimetallic materials as the Fe hydroxide species is less readily oxidized than the Ni hydroxide species[21]. In addition to having an effect on the $Ni(OH)_2$/NiOOH transition peak, incorporation of only 5 at% Fe into the Ni/50 wt% CeO_2 dramatically increases the OER current and negatively shifts the estimated onset potential (potential where the OER current starts to rise) by around 70 mV. While the $Ni_{95}Fe_{05}$/ 50 wt% CeO_2 catalyst reached 10 mA cm^{-2} at 321 mV, the Ni/50 wt% CeO_2 catalyst did not perform well enough to reach that same current. When further increasing the iron content to 10 and 20 at%, the OER activity increased where the 20 at% sample showed the lowest overpotential at 10 mA cm^{-2} of 289 mV. The high activity of the 20 at% sample is also reflected in its low Tafel slope of 40 mV dec^{-1}, however the rest of the catalysts, aside from the Ni/ 50 wt% CeO_2 catalyst, show similar Tafel slopes. These results are in accordance with literature where it was found that around 10 - 20% iron incorporation into Ni catalysts shows the best OER activity[22,23,27,51]. Tian *et al.* [27] synthesized Fe-modulated nickel hydroxide hollow nanocubes with various Fe compositions and found that the optimal composition was 25% Fe, showing an overpotential of around 310 mV and a Tafel slope of 68 mV dec^{-1}. Zhang *et al*.[51] synthesized Ni-Fe/ nitrogen-doped nanocarbon hybrids (NiFe/NC) and found that 10% Fe was the optimal OER catalyst showing overpotentials of 330 mV at 10 mA cm^{-2} and a Tafel slope of 45 mV dec^{-1}. The $Ni_{90}Fe_{10}$/ 50 wt% CeO_2 and $Ni_{80}Fe_{20}$/ 50 wt% CeO_2 materials are quite competitive with those reported values. Further increasing the Fe content to 40 at% has a negative effect on OER activity, a result commonly found in literature when increasing the Fe content over

around 20-50%[22,23,27,51–54]. The overall obtained trend in OER activity with increasing Fe content has been previously studied and the initial increased OER activity has been attributed to Fe incorporation into the NiOOH species, while the limit found with a further increase of Fe into the catalyst has been attributed to the segregation of a less active Fe-rich phase[23,29].

In our previous work[18], we observed that using 50 wt% CeO_2 in an anode of a single cell AEMWE induced quite a high cell resistance, however incorporating CeO_2 did show interesting advantages such as improved charge transfer. Based on these results and what was found in literature regarding optimal amounts of CeO_2 in OER catalysts[41,45], it was evident that the ceria content had to be optimized. As the $Ni_{90}Fe_{10}$ and $Ni_{80}Fe_{20}$ catalysts with 50 wt% CeO_2 are the best performing samples, they were both used to optimize the CeO_2 content. CVs and LSV evaluating the 50, 20, 10, 7 and 5 and 0 wt% CeO_2 for the $Ni_{90}Fe_{10}$ and $Ni_{80}Fe_{20}$ catalysts are shown in Figures 4.5 and 4.6, respectively, and key information from those graphs is shown in Tables 4.3 and 4.4, respectively. Information on the Tafel slope calculations is found in Figure C.4 and C.5 of the SI for the $Ni_{90}Fe_{10}$ and $Ni_{80}Fe_{20}$ catalyst, respectively.

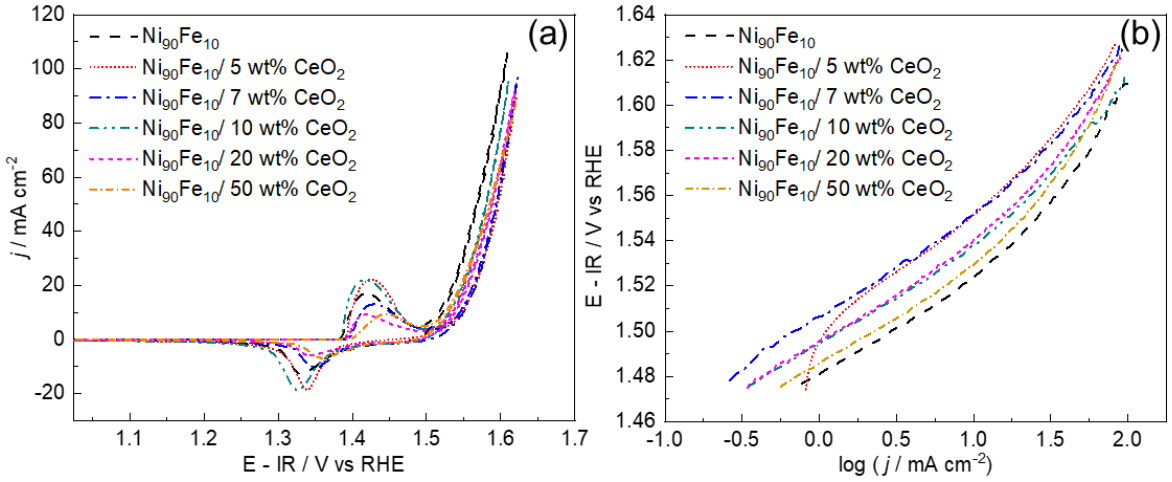

Figure 4.5: (a) Cyclic voltammetry run at 25 mV s^{-1} and (b) Tafel plot obtained from linear sweep voltammetry run at 1 mV s^{-1} in 1 M KOH at RT for the $Ni_{90}Fe_{10}$/ y wt% CeO_2 (y=0, 5, 7, 10, 20, 50 wt%) catalysts, as indicated in the figure.

Table 4.3: Summary of OER performance for $Ni_{90}Fe_{10}$/ y wt% CeO_2 (y=0, 5, 7, 10, 20, 50 wt%) in 1 M KOH obtained from Figure 4.5b. η = overpotential.

Material	**η at 10 mA cm^{-2} [mV]**	**η at 80 mA cm^{-2} [mV]**	**Tafel Slope [mV dec^{-1}]**
$Ni_{90}Fe_{10}$	294	370	42
$Ni_{90}Fe_{10}$/ 5 wt% CeO_2	321	395	51
$Ni_{90}Fe_{10}$/ 7 wt% CeO_2	322	390	47
$Ni_{90}Fe_{10}$/ 10 wt% CeO_2	308	373	40
$Ni_{90}Fe_{10}$/ 20 wt% CeO_2	310	386	41
$Ni_{90}Fe_{10}$/ 50 wt% CeO_2	299	384	41

For the $Ni_{90}Fe_{10}$ with CeO_2 catalysts, the $Ni_{90}Fe_{10}$ catalyst with 0 wt% CeO_2 is the best performing catalyst showing the lowest overpotential at both 10 and 80 mA cm^{-2}. All $Ni_{90}Fe_{10}$/ y CeO_2 (y=0, 5, 7, 10, 20, 50 wt%) materials have a low Tafel slope in the range of around 40 – 50 mV dec^{-1} indicating that the amount of ceria in the catalyst does not affect the reaction mechanism. At lower currents, the 50 wt% sample shows close performance to the $Ni_{90}Fe_{10}$ sample with an overpotential at 10 mA cm^{-2} increasing by only 5 mV. At higher currents however, the $Ni_{90}Fe_{10}$/10 wt% CeO_2 sample is competitive with the metallic catalyst showing an overpotential of 373 at 80 mA cm^{-2}, only 3 mV higher than that for the $Ni_{90}Fe_{10}$ catalyst. When decreasing ceria content from 50 wt% to 10 wt% it is generally observed that catalytic activity is slightly increasing. However, apart from the $Ni_{90}Fe_{10}$ catalyst with 0 wt% CeO_2, decreasing ceria content under 10 wt% does not continue to further promote OER performance. The low performance of the samples with 5 and 7 wt% CeO_2 is evident by looking at the reaction overpotentials at 10 and 80 mA cm^{-2}, as well as the Tafel slopes, which are around 50 mV dec^{-1}.

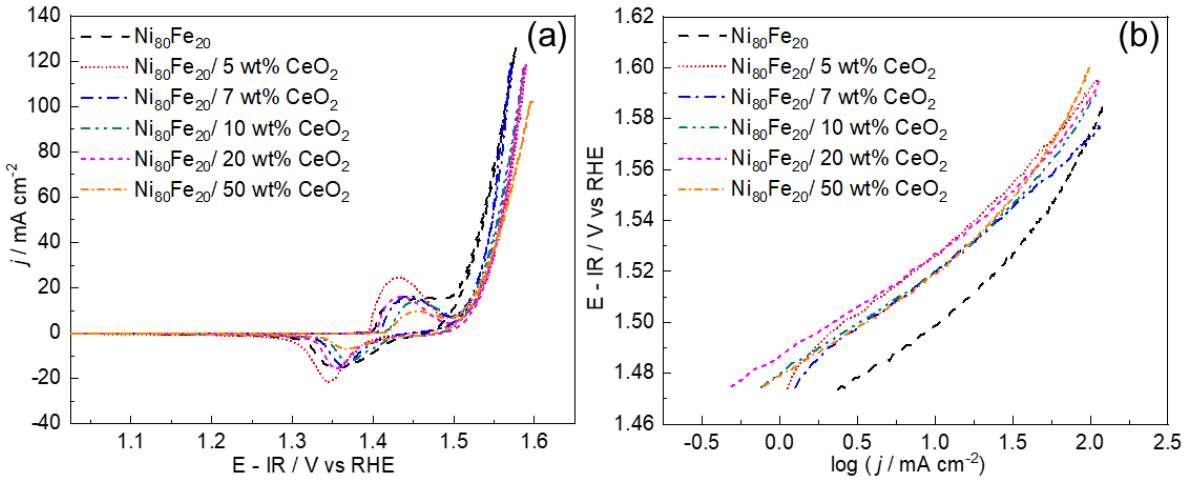

Figure 4.6: (a) Cyclic voltammetry run at 25 mV s^{-1} and (b) Tafel plot obtained from linear sweep voltammetry run at 1 mV s^{-1} in 1 M KOH at RT for the $Ni_{80}Fe_{20}$/ y wt% CeO_2 (y=0, 5, 7, 10, 20, 50 wt%) catalysts, as indicated in the figure.

Table 4.4: Summary of OER performance for $Ni_{80}Fe_{20}$/ y wt% CeO_2 (y=0, 5, 7, 10, 20, 50 wt%) in 1 M KOH obtained from Figure 4.6b. η = overpotential.

Material	**η at 10 mA cm^{-2} [mV]**	**η at 80 mA cm^{-2} [mV]**	**Tafel Slope [mV dec^{-1}]**
$Ni_{80}Fe_{20}$	269	332	43
$Ni_{80}Fe_{20}$/ 5 wt% CeO_2	296	354	50
$Ni_{80}Fe_{20}$/ 7 wt% CeO_2	290	337	47
$Ni_{80}Fe_{20}$/ 10 wt% CeO_2	290	346	41
$Ni_{80}Fe_{20}$/ 20 wt% CeO_2	297	349	40
$Ni_{80}Fe_{20}$/ 50 wt% CeO_2	289	357	40

For the $Ni_{80}Fe_{20}$ with ceria samples, similar results were obtained to the $Ni_{90}Fe_{10}$ catalysts especially with respects to the obtained Tafel slopes. The $Ni_{80}Fe_{20}$ samples do however show lower OER overpotentials that the $Ni_{90}Fe_{10}$ samples. When analyzing the effect of ceria content in the $Ni_{80}Fe_{20}$ samples, the catalyst with 0 wt% CeO_2 is the best performing material showing low overpotentials of 269 and 332 mV at 10 and 80 mA cm^{-2}, respectively. At low currents, the 5, 7 and 50 wt% CeO_2 samples show the next best OER activity, all showing a reaction overpotential of around 290 mV at 10 mA cm^{-2}, around 20 mV higher than the $Ni_{80}Fe_{20}$ sample with no ceria. At higher currents, the $Ni_{80}Fe_{20}$/ 7 wt% CeO_2 sample is the second-best performing catalyst

showing an overpotential 337 mV 80 mA cm^{-2}, only 5 mV higher than the $Ni_{80}Fe_{20}$ sample. Once again, it seems decreasing the ceria content increases OER activity, however in the case of the $Ni_{80}Fe_{20}$ material, it seems an optimum has been found with around 7 wt% CeO_2. Interestingly, the Tafel slope of the 7 wt% sample is slightly higher than some of the other catalysts, indicating quite a competitive performance between the catalysts.

As shown in Figures 4.5a and 4.6a, adding CeO_2 to the NiFe catalysts affects the $Ni(OH)_2$/NiOOH redox peaks. This effect was observed earlier[55] when the authors showed that incorporating CeO_x into their gold-supported NiO_x catalyst shifts the $Ni(OH)_2$/NiOOH redox peaks to higher overpotentials as more CeO_x is added. Although the change in our study does not clearly demonstrate CeO_x shifting the peaks to higher potentials, it is important to note that, as discussed above, Fe incorporation into Ni catalysts induces a similar visual change in CV behaviour, therefore it is possible that here, the observed effects of Fe and CeO_x are competing. It should be noted that while Fe and CeO_2 could similarly modify the Ni redox peaks, they may not do so for the same reasons. Fe is likely inducing an electronic effect on Ni, while CeO_2 is likely inducing a combination of a geometric effect, an electronic effect and an effect related to the oxygen vacancies of the material and its oxygen storage and release properties.

Overall, ceria does not promote or hinder the oxygen evolution reaction in our study, however, having larger quantities of CeO_2 in the Ni-based catalysts results in lower OER activity. This result has been reported in literature for similar catalysts[55,56], and the lower OER activity with increasing CeO_2 content could be due to the low electronic conductivity of ceria. While we have previously observed that adding ceria provides more favourable charge transfer in a single cell AEMWE[18], we have also observed an increased cell ohmic resistance compared to the Ni and NiFe catalysts, which affects the bulk conductivity in the catalyst layer. Despite IR-correcting the OER data in this work to remove the ohmic resistance of the system, it is possible that the effects related to the low conductivity of ceria in the drop-cast electrode are still present. Thus, the added ohmic resistance introduced by CeO_2 prevails over an electronic effect between the NiFe and CeO_2 phases. This can also result in reduced interactions between water molecules and ceria's surface oxygen vacancies.

Of the tested materials, the $Ni_{90}Fe_{10}$, $Ni_{80}Fe_{20}$, $Ni_{90}Fe_{10}$/10 wt% CeO_2 and $Ni_{80}Fe_{20}$/ 7 wt% CeO_2 are the best performing. For comparison, in Figure 4.7, those 4 catalysts along with the

$Ni_{90}Fe_{10}$/ 7 wt% $CeO_2$and the $Ni_{80}Fe_{20}$/ 10 wt% CeO_2 catalysts were placed alongside an Ir black commercial benchmark catalyst. Details on how the Tafel slope was calculated are shown in Figure C.6 of the SI. It is important to note that at these small quantities, CeO_2 is likely not acting as a support but rather as a catalyst promoter. This is in accordance with the EDS analysis in Figure 4.3 that shows that CeO_2 is not evenly distributed throughout the NiFe samples.

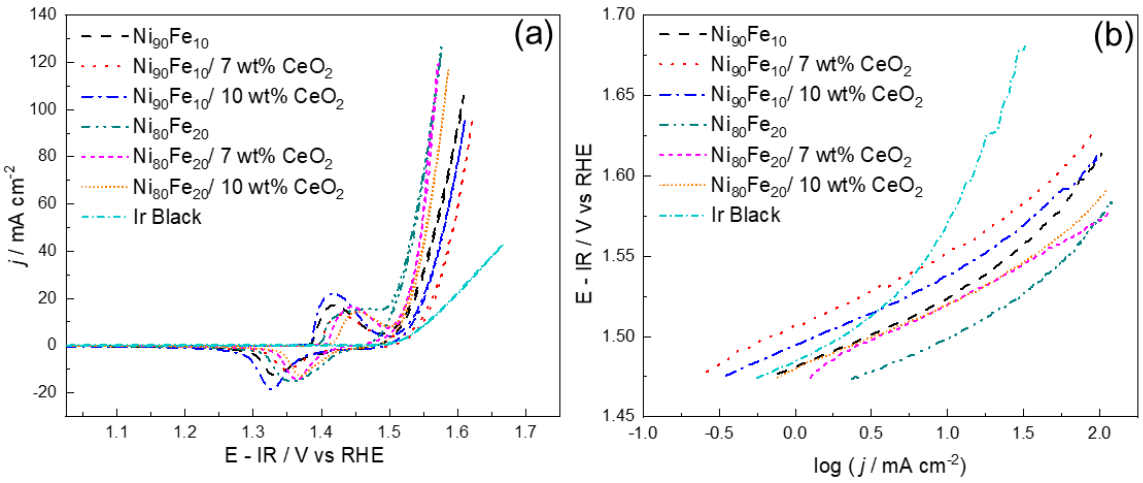

Figure 4.7: (a) Cyclic voltammetry run at 25 mV s^{-1} and (b) Tafel plot obtained from linear sweep voltammetry run at 1 mV s^{-1} in 1 M KOH at RT for Ir black as well as $Ni_{90}Fe_{10}$/ y wt% CeO_2 and $Ni_{80}Fe_{20}$/ y wt% CeO_2 (y=0, 7, 10 wt%) catalysts, as indicated in the figure.

As mentioned with the data presented above, all Ni-based materials perform similarly, with the $Ni_{80}Fe_{20}$ materials showing slightly higher performance than the $Ni_{90}Fe_{10}$ materials. In comparison to the Ni-based catalysts, Ir black does not have a fast rise in its current, achieving 10 mA cm^{-2} at an overpotential of 327 mV and not reaching 80 mA cm^{-2}. Ir also has a higher estimated onset overpotential, however its Tafel slope of 47 mV $dec^{-1}$is close to that of the Ni-based materials.

Figure 4.8 shows a comparison of the OER performance of similar NiFe-based materials founds in literature[20,26–33]. Data used to produce this figure is summarized in Table 4.1 in Section 4.1. It is important to note that the literature search was solely limited to NiFe materials (i.e. without the addition of other metals, supports or promoters), studied in 1 M KOH, using an electrochemically inert substrate. Other NiFe-based materials[33,57–60] do have higher reported OER activity, however they did not fit into the criteria of the search. As can be seen in Figure 4.8, the

$Ni_{90}Fe_{10}$ and $Ni_{80}Fe_{20}$ are very competitive with other reported materials, where the $Ni_{80}Fe_{20}$ outperforms them all in terms of achieved overpotential at 10 mA cm^{-2}.

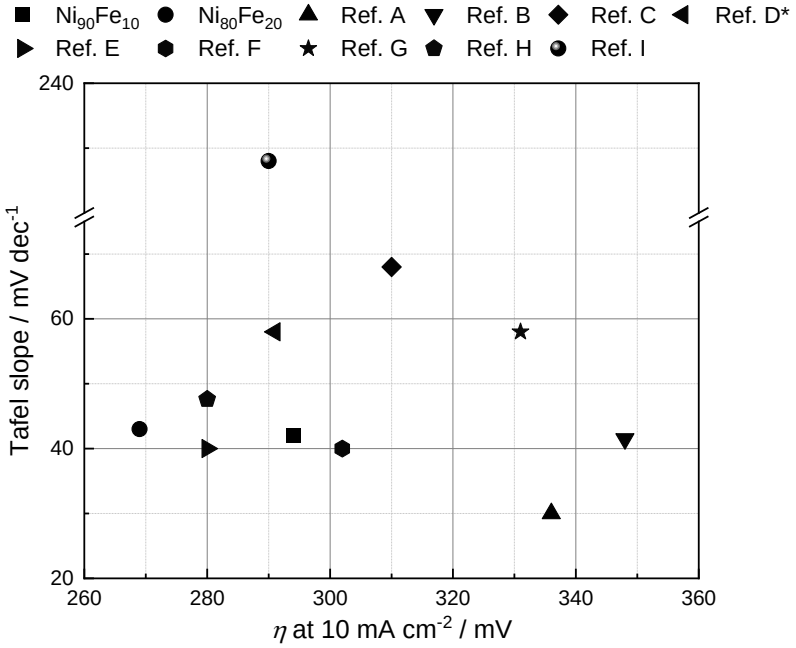

Figure 4.8: Comparison of the OER performance achieved in this study vs. the OER performance found in literature for similar materials in 1 M KOH. *Results for this reference obtained in Fe-free 1 M KOH. Reference numbers are as follows: Ref. A [20]***, Ref. B*** [26]***, Ref. C*** [27]***, Ref. D**** [28]***, Ref. E*** [29]***, Ref. F*** [30]***, Ref. G*** [31]***, Ref. H*** [32] ***and Ref. I*** [33]***.***

The $Ni_{90}Fe_{10}$ and $Ni_{80}Fe_{20}$ catalysts with 0, 7 and 10 wt% CeO_2 were also tested in 0.1 M KOH as shown in Figure 4.9. Data from Figure 4.9 is summarized in Table 4.5. The region where the Tafel slope was calculated is shown in Figure C.7 of the SI.

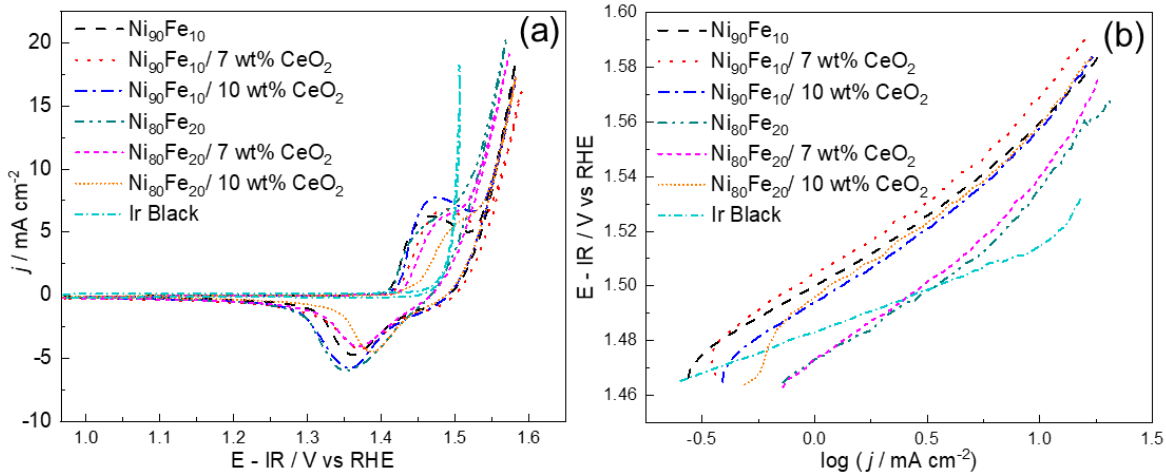

Figure 4.9: (a) Cyclic voltammetry run at 25 mV s^{-1} and (b) Tafel plot obtained from linear sweep run at 1 mV s^{-1} in 0.1 M KOH at RT for Ir black as well as $Ni_{90}Fe_{10}$/ y wt% CeO_2 and $Ni_{80}Fe_{20}$/ y wt% CeO_2 (y=0, 7, 10 wt%) catalysts, as indicated in the figure.

Table 4.5: Summary of OER performance for Ir black as well as $Ni_{90}Fe_{10}$/ y wt% CeO_2 and $Ni_{80}Fe_{20}$/ y wt% CeO_2 (y=0, 7, 10 wt%) catalysts in 0.1 M KOH obtained from Figure 4.9b. η = overpotential.

Material	η at 10 mA cm^{-2} [mV]	Tafel Slope [mV dec^{-1}]
$Ni_{90}Fe_{10}$	330	48
$Ni_{90}Fe_{10}$/ 7 wt% CeO_2	339	52
$Ni_{90}Fe_{10}$/ 10 wt% CeO_2	328	55
$Ni_{80}Fe_{20}$	306	52
$Ni_{80}Fe_{20}$/ 7 wt% CeO_2	310	57
$Ni_{80}Fe_{20}$/ 10 wt% CeO_2	329	56
Ir Black	284	30

Similar to what was seen in 1 M KOH, the $Ni_{80}Fe_{20}$ samples show slightly lower overpotentials than the $Ni_{90}Fe_{10}$ samples. With 0 wt% CeO_2, the $Ni_{90}Fe_{10}$ catalyst shows an overpotential at 10 mA cm^{-2} that is 24 mV higher than that of $Ni_{80}Fe_{20}$. As for the best ceria-containing samples, the $Ni_{80}Fe_{20}$/ 7 wt% catalyst shows high OER activity with an overpotential of 310 mV at 10 mA cm^{-2}, which is 18 mV lower than the $Ni_{90}Fe_{10}$/ 10 wt% CeO_2 material's overpotential of 328 mV. Interestingly the $Ni_{90}Fe_{10}$ catalysts have slightly lower Tafel slopes than the $Ni_{80}Fe_{20}$ catalysts, with the lowest Ni-based Tafel slope of 48 mV dec^{-1} found for $Ni_{90}Fe_{10}$ without CeO_2. The Tafel slope values are however very similar to one another, indicating once more, no change in reaction mechanism between the samples. The reported performance of the Ni-

based materials, particularly the $Ni_{80}Fe_{20}$ catalyst, remains competitive with what is reported in literature in a lower pH environment (0.1 M). Kim *et al.* [61] fabricated a nanoporous Ni electrode by cadmium dissolution and subsequently deposited 18% Fe onto the porous Ni electrocatalyst. This catalyst showed an overpotential of 290 mV at 10 mA cm^{-2} and a Tafel slope of 38 mV dec^{-1} in 0.1 M NaOH. Görlin *et al.* [62] prepared a $Ni_{65}Fe_{35}$ catalyst by physically mixing $Ni(OH)_2$ and FeOOH materials together, and their catalyst shows an overpotential of 298 mV at 10 mA cm^{-2} and a Tafel slope of 37 mV dec^{-1} in 0.1 M KOH. Contrary to what was observed in 1 M KOH, Ir black shows a better performance in comparison to the Ni-based materials in 0.1 M KOH. It attains a current of 10 mA cm^{-2} at an overpotential of 284 mV and with a low Tafel slope of 30 mV dec^{-1}. The observed relative activity of Ir in comparison to the Ni-based materials in 1 and 0.1 M KOH is in agreement with literature data[63,64], where Ir electrodes do not exhibit a dramatic increase in OER current with increasing pH, likely due to its poor stability in a high pH environment[65].

4.3.2.2 Preliminary Durability in Oxygen Evolving Currents

In addition to OER activity, the catalysts stability over time is another important parameter to evaluate. As shown in Figure 4.10, the durability of the $Ni_{90}Fe_{10}$ and $Ni_{80}Fe_{20}$ with 0, 7 and 10 wt% CeO_2 catalysts was tested by chronopotentiometry for 12 h and by continuous CV cycling for 300 cycles. Although more rigorous conditions are recommended for evaluating Ni stability by CV cycling[66], the analysis presented below is sufficient for a preliminary indication of electrode durability and mechanical integrity. The change in potential over time from the CP and the change of current with cycling from the CVs is tabulated in Table 4.6.

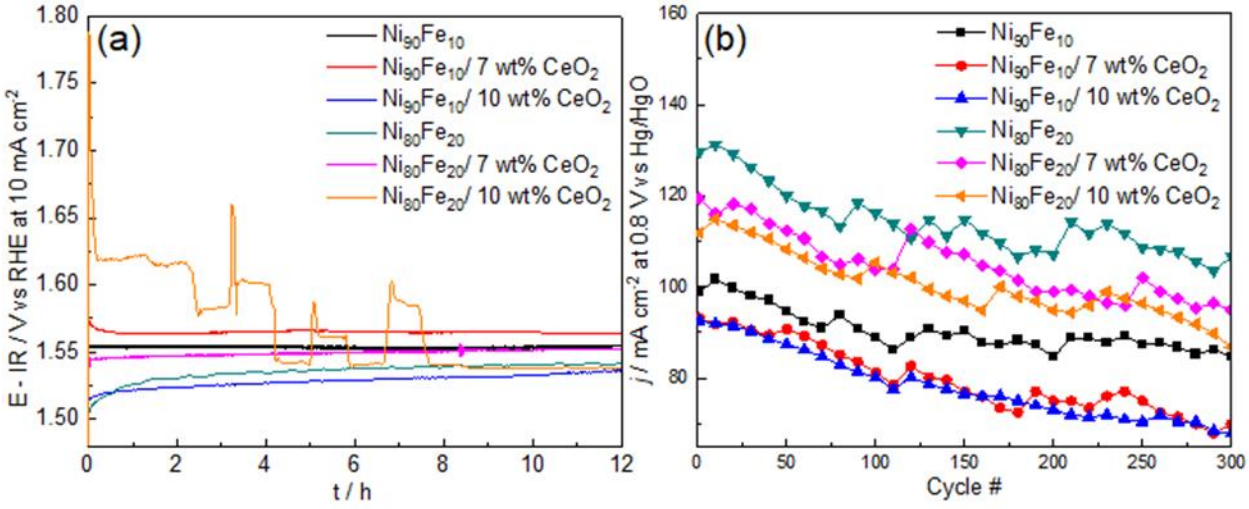

Figure 4.10: (a) Chronopotentiometry and (b) Current density at 0.8 V vs Hg/HgO vs Cycle # obtained from cyclic voltammetry run at 25 mV s^{-1} in 1 M KOH at RT for the $Ni_{90}Fe_{10}$/ y wt% CeO_2 and $Ni_{80}Fe_{20}$/ y wt% CeO_2 (y=0, 7, 10 wt%) catalysts, as indicated in the figure.

Table 4.6: Change in performance over time obtained through durability experiments in 1 M KOH obtained from Figure 4.10.

Material	**(*E-IR*) Drift [mV h^{-1}]**	**%Δ *I* over 300 cycles**
$Ni_{90}Fe_{10}$	-0.1	-14.1
$Ni_{90}Fe_{10}$/ 7 wt% CeO_2	-0.6	-24.7
$Ni_{90}Fe_{10}$/ 10 wt% CeO_2	1.8	-26.9
$Ni_{80}Fe_{20}$	3.2	-17.7
$Ni_{80}Fe_{20}$/ 7 wt% CeO_2	0.7	-20.2
$Ni_{80}Fe_{20}$/ 10 wt% CeO_2	-20.9	-22.3

When considering the CPs shown in Figure 4.10a, the most stable catalysts are the $Ni_{90}Fe_{10}$ materials. When comparing the CPs of $Ni_{90}Fe_{10}$ and $Ni_{80}Fe_{20}$, it can be observed that the drift in potential of the $Ni_{80}Fe_{20}$ catalyst is high in the first 2 hours of testing, while the drift of the $Ni_{90}Fe_{10}$ catalyst does not change significantly. This could be an indication of initial Fe dissolution from the sample with a higher starting iron content. Additionally, in comparison to the $Ni_{80}Fe_{20}$ materials with 0 and 7 wt% CeO_2 which show a positive potential drift over time, the $Ni_{90}Fe_{10}$ catalysts with 0 and 7 wt% CeO_2 catalysts both show a negative drift, indicating a slight increase of performance over time. This result is particularly interesting for the $Ni_{90}Fe_{10}$/ 7 wt% CeO_2

sample because it showed slightly lower performance than the other $Ni_{90}Fe_{10}$ samples during the OER performance evaluation experiments. The increase in performance over time of $Ni_{90}Fe_{10}$ and $Ni_{90}Fe_{10}$/ 7 wt% CeO_2 could be due to Fe incorporation into the Ni WE from impurities in the reagent grade KOH[47], however Speck et *al.* [67] also found evidence of Fe leaching out of their $FeNiO_x$ film during 24 h stability measurements at similar operating conditions and currents, so one could negate the other.

Overall, adding ceria to the catalysts does not significantly alter the stability of the NiFe materials, however, it is interesting to observe that adding 7 wt % CeO_2 to the $Ni_{90}Fe_{10}$ and $Ni_{80}Fe_{20}$ electrodes showed a slight improvement in observed voltage drift of 0.5 and 2.5 mV h^{-1}, respectively, in electrode durability over time in the CP experiments. This effect was not found when increasing the CeO_2 amount to 10 wt%, as is further discussed below for the $Ni_{80}Fe_{20}$/ 10 wt% CeO_2 catalyst, which show poor stability over 12 h at 10 mA cm^{-2}. A similar results was obtained during stability experiments carried out by Chen *et al.*[41] on their Ce-modified CuO_x catalysts for 5 h at 5 mA cm^{-2}; in comparison to their pure copper sample and the 10.3 at% Ce-modified sample, the 6.9 at% Ce-modified sample showed a significantly improved stability over time.

When it comes to the CV cycling, the $Ni_{90}Fe_{10}$ electrode is once again the most stable catalyst, showing only a 14% decrease in current over 300 cycles. This performance is followed by the $Ni_{80}Fe_{20}$ electrode, which only shows a 18% decrease in current with cycling. On average, it can be observed that the Ni-based catalysts are not stable over CV cycling. Kuroda *et al.*[66] explain that the bounds that are selected for CV durability experiments can alter the observed stability of a catalyst. For example, they demonstrate that cycling Ni between 0.5 and 1.8 V vs RHE will show significant electrode degradation, while cycling between 1.4 and 1.8 V vs RHE, will not. The reason for this is that when a larger potential window is used, the NiOOH formed in the OER region will be discharged during the reverse scan, which can cause severe electrode degradation. Although in our study we are only cycling between 1.025 and 1.725 V vs RHE (0.1 to 0.8 V vs Hg/HgO in 1 M KOH), it is possible that some electrode degradation is occurring due to the discharging of the electrode during the reverse scan.

When analyzing the data of the $Ni_{80}Fe_{20}$ materials, what is quickly evident in Figure 4.10a is the odd behaviour of the $Ni_{80}Fe_{20}$/ 10 wt% CeO_2. In comparison to the other Ni-based catalysts,

it is extremely unstable showing a change in potential of 14% over 12 hours. This test was repeated as shown in Figure C.8 of the SI, showing once again a very unstable catalyst, meaning that the $Ni_{80}Fe_{20}$/ 10 wt% CeO_2 catalyst has trouble maintaining oxygen evolving currents over time. This effect could be due to the specific amount of iron and ceria in comparison to Ni in that sample, and how that affects the way each component interacts with each other, especially as both the samples with less ceria ($Ni_{80}Fe_{20}$/ 7 wt% CeO_2) and with less iron ($Ni_{90}Fe_{10}$/ 10 wt% CeO_2) are stable. Enman *et al.*[56] tested the stability over 50 CV cycles of $Ni_{0.85}Ce_{0.15}O_xH_y$ and $Ni_{0.65}Ce_{0.35}O_xH_y$ catalysts prepared by spin-cast deposition and compared their activity to a sample with no Ce. They found that the sample with 35% Ce evolved from being 4x more active to as active as NiO_xH_y, while the sample with 15 % Ce evolved from being 8x to 2x more active than NiO_xH_y, although it was reported that continued cycling of the latter sample may further decrease its activity to that of NiO_xH_y. This result shows that altering the amounts of ceria in comparison to nickel can affect catalyst stability or the degradation rate of the electrode. Reasons for this decrease in activity over time could be due in some part to phase segregation of CeO_2 with a continued applied current[56,68,69], a component which was found to be redox inactive at higher currents (8 mA cm^{-2}) in a $Ni_{0.3}Fe_{0.07}Co_{0.2}Ce_{0.43}O_x$ catalyst studied by Favaro *et al.*[69]. This hypothesis may support the results in Figure 4.10b, where the stability of the $Ni_{80}Fe_{20}$/ 10 wt% CeO_2 catalyst, evaluated through CV cycling (i.e. not at constant high currents), is shown to be arguably as stable as the other catalysts. However, determining why the $Ni_{80}Fe_{20}$/ 10 wt% CeO_2 sample is particularly unstable in comparison to the other catalysts would require further evaluation of both the physicochemical properties and electrochemical activities of many more ratios of Ni:Fe:CeO_2, and is therefore out of the scope of this study.

4.4 Conclusions

In this study, the iron and ceria content of a bimetallic NiFe with and without ceria catalyst was optimized to produce a highly active oxygen evolution reaction catalysts for applications in alkaline water electrolysis. When studying the effects of Fe in a $Ni_{100-x}Fe_x$/ 50 wt% CeO_2 (x=0, 5, 10, 20, 40 at%) catalyst, it was found that the material with 20 at% Fe showed the best OER activity, while the material containing 10 at% Fe was a competitive second-best catalyst. When optimizing ceria content in $Ni_{90}Fe_{10}$/ y wt% CeO_2 and $Ni_{80}Fe_{20}$/ y wt% CeO_2 (y=0, 5, 7, 10, 20, 50 wt%), although amounts of 7 and 10 wt% for the $Ni_{80}Fe_{20}$ and $Ni_{90}Fe_{10}$ catalysts, respectively,

were found to be optimal, it was found that in the case of both $Ni_{80}Fe_{20}$ and $Ni_{90}Fe_{10}$, having no ceria present showed the highest OER activity. This result is likely due to the larger size of ceria in comparison to the metallic nanoparticles, making it difficult for the two phases to mix as seen in the physicochemical characterization of the samples, thus making it difficult to observe any induced promotional effects of CeO_2 on the NiFe OER species. Nevertheless, the best Ni-based materials outperformed Ir black in 1 M KOH and showed comparable performance in 0.1 M KOH. Additionally, in comparison to similar NiFe materials found in literature, the $Ni_{80}Fe_{20}$ material showed the lowest overpotential for OER of 269 mV at 10 mA cm^{-2} in 1 M KOH. Stability results indicate that the $Ni_{90}Fe_{10}$ catalyst is overall the most stable material. It was observed that adding 7 wt% ceria to both $Ni_{90}Fe_{10}$ and $Ni_{80}Fe_{20}$ helped improve the stability during the CP experiments. This increase in stability, however, was not found to be significant. Overall, the addition of CeO_2 to the Ni-based catalysts in this study does not hinder OER activity, however it does not promote OER activity or stability either. Both the $Ni_{90}Fe_{10}$ and $Ni_{80}Fe_{20}$ catalysts show good promise for highly active anodes in anion exchange membrane water electrolysis, where the $Ni_{90}Fe_{10}$ catalyst has the added advantage of better durability over time.

Acknowledgments

This research was conducted as part of the Engineered Nickel Catalysts for Electrochemical Clean Energy project administered from Queen's University and supported by Grant number RGPNM 477963-2015 under the Natural Sciences and Engineering Research Council of Canada (NSERC) Discovery Frontiers Program. Additional funding was also provided by NSERC's Alexander Graham Bell Canada Graduate Scholarship – Doctoral (CGS D).

References

[1] K. Mazloomi, C. Gomes, *Renew. Sustain. Energy Rev.* **2012**, *16*, 3024.

[2] D. M. F. Santos, C. A. C. Sequeira, *Quim. Nova* **2013**, *36*, 1176.

[3] M. K. Cho, A. Lim, S. Y. Lee, H. Kim, S. J. Yoo, Y. Sung, H. S. Park, J. H. Jang, *J. Electrochem. Sci. Technol.* **2017**, *8*, 183.

[4] I. Vincent, D. Bessarabov, *Renew. Sustain. Energy Rev.* **2018**, *81*, 1690.

[5] H. A. Miller, K. Bouzek, J. Hnat, S. Loos, C. I. Bernäcker, T. Weißgärber, L. Röntzsch, J. Meier-Haack, *Sustain. Energy Fuels* **2020**, *4*, 2114.

[6] R. Phillips, C. W. Dunnill, *RSC Adv.* **2016**, *6*, 100643.

[7] M. K. Cho, H. Park, S. Choe, S. J. Yoo, J. Y. Kim, H.-J. Kim, D. Henkensmeier, S. Y. Lee, Y. Sung, H. S. Park, J. Hyun Jang, *J. Power Sources* **2017**, *347*, 283.

[8] M. Carmo, D. L. Fritz, J. Mergel, D. Stolten, *Int. J. Hydrogen Energy* **2013**, *38*, 4901.

[9] G. Li, L. Anderson, Y. Chen, M. Pan, P. A. Chuang, *Sustain. Energy Fuels* **2018**, *2*, 237.

[10] N. Alzate-Carvajal, L. M. Bolivar-Pineda, V. Meza-Laguna, V. A. Basiuk, E. V. Basiuk, E. A. Baranova, *ChemElectroChem* **2020**, *7*, 428.

[11] O. Diaz-Morales, D. Ferrus-Suspedra, M. T. M. Koper, *Chem. Sci.* **2016**, *7*, 2639.

[12] E. Fabbri, T. J. Schmidt, *ACS Catal.* **2018**, *8*, 9765.

[13] M. E. G. Lyons, M. P. Brandon, *Int. J. Electrochem. Sci.* **2008**, *3*, 1386.

[14] J. O. M. Bockris, *J. Chem. Phys.* **1956**, *24*, 817.

[15] E. Fabbri, A. Habereder, K. Waltar, R. Kötz, T. J. Schmidt, *Catal. Sci. Technol.* **2014**, *4*, 3800.

[16] M. Tahir, L. Pan, F. Idrees, X. Zhang, L. Wang, J. J. Zou, Z. L. Wang, *Nano Energy* **2017**, *37*, 136.

[17] H. Bode, K. Dehmelt, J. White, *Electrochim. Acta* **1966**, *11*, 1079.

[18] E. Cossar, A. O. Barnett, F. Seland, E. A. Baranova, *Catalysts* **2019**, *9*, 814.

[19] M. Gong, H. Dai, *Nano Res.* **2015**, *8*, 23.

[20] L. Trotochaud, J. K. Ranney, K. N. Williams, S. W. Boettcher, *J. Am. Chem. Soc.* **2012**, *134*, 17253.

[21] X. Li, F. C. Walsh, D. Pletcher, *Phys. Chem. Chem. Phys.* **2011**, *13*, 1162.

[22] S. Lee, L. Bai, X. Hu, *Angew. Chemie - Int. Ed.* **2020**, *59*, 8072.

[23] D. Friebel, M. W. Louie, M. Bajdich, K. E. Sanwald, Y. Cai, A. M. Wise, M. Cheng, D. Sokaras, T. Weng, R. Alonso-mori, R. C. Davis, J. R. Bargar, J. K. Nørskov, A. Nilsson, A. T. Bell, *J. Am. Chem. Soc.* **2015**, *137*, 1305.

[24] N. Li, D. K. Bediako, R. G. Hadt, D. Hayes, T. J. Kempa, F. Von Cube, D. C. Bell, L. X. Chen, D. G. Nocera, *Proc. Natl. Acad. Sci. U. S. A.* **2017**, *114*, 1486.

[25] H. Xiao, H. Shin, W. A. Goddard, *Proc. Natl. Acad. Sci. U. S. A.* **2018**, *115*, 5872.

[26] D. Xu, M. B. Stevens, M. R. Cosby, S. Z. Oener, A. M. Smith, L. J. Enman, K. E. Ayers, C. B. Capuano, J. N. Renner, N. Danilovic, Y. Li, H. Wang, Q. Zhang, S. W. Boettcher, *ACS Catal.* **2019**, *9*, 7.

[27] T. Tian, M. Zheng, J. Lin, X. Meng, Y. Ding, *Chem. Commun.* **2019**, *55*, 1044.

[28] M. Yu, G. Moon, E. Bill, H. Tüysüz, *ACS Appl. Energy Mater.* **2019**, *2*, 1199.

[29] S. Klaus, Y. Cai, M. W. Louie, L. Trotochaud, A. T. Bell, *J. Phys. Chem. C* **2015**, *119*, 7243.

[30] F. Song, X. Hu, *Nat. Commun.* **2014**, *5*, 4477.

[31] X. Yu, M. Zhang, W. Yuan, G. Shi, *J. Mater. Chem. A* **2015**, *3*, 6921.

[32] B. M. Hunter, J. D. Blakemore, M. Deimund, H. B. Gray, J. R. Winkler, A. M. Múller, *J. Am. Chem. Soc.* **2014**, *136*, 13118.

[33] Q. Chen, R. Wang, M. Yu, Y. Zeng, F. Lu, X. Kuang, X. Lu, *Electrochim. Acta* **2017**, *247*, 666.

[34] T. Montini, M. Melchionna, M. Monai, P. Fornasiero, *ACS Chem. Rev.* **2016**, *116*, 5987.

[35] H. A. E. Dole, E. A. Baranova, *ChemCatChem* **2016**, *8*, 1977.

[36] *Catalysis by Ceria and Related Materials*, A. Trovarelli, P. Fornasiero, Eds., 2nd edition, Imperial College Press, London, **2013**.

[37] M. B. Watkins, A. S. Foster, A. L. Shluger, *J. Phys. Chem. C* **2007**, *111*, 15337.

[38] H. T. Chen, Y. M. Choi, M. Liu, M. C. Lin, *ChemPhysChem* **2007**, *8*, 849.

[39] M. Fronzi, S. Piccinin, B. Delley, E. Traversa, C. Stampfl, *Phys. Chem. Chem. Phys.* **2009**, *11*, 9188.

[40] J.-X. Feng, S.-H. Ye, H. Xu, Y.-X. Tong, G.-R. Li, *Adv. Mater.* **2016**, *28*, 4698.

[41] Z. Chen, C. X. Kronawitter, X. Yang, Y. W. Yeh, N. Yao, B. E. Koel, *Phys. Chem. Chem. Phys.* **2017**, *19*, 31545.

[42] C. C. L. McCrory, S. Jung, J. C. Peters, T. F. Jaramillo, *J. Am. Chem. Soc.* **2013**, *135*, 16977.

[43] J. A. Haber, Y. Cai, S. Jung, C. Xiang, S. Mitrovic, J. Jin, A. T. Bell, J. M. Gregoire, *Energy Environ. Sci.* **2014**, *7*, 682.

[44] J. A. Haber, C. Xiang, D. Guevarra, S. Jung, J. Jin, J. M. Gregoire, *ChemElectroChem* **2014**, *1*, 524.

[45] T. Audichon, S. Morisset, T. W. Napporn, K. B. Kokoh, C. Comminges, C. Morais, *ChemElectroChem* **2015**, *2*, 1128.

[46] D. A. Corrigan, *J. Electrochem. Soc.* **2006**, *134*, 377.

[47] L. Trotochaud, S. L. Young, J. K. Ranney, S. W. Boettcher, *J. Am. Chem. Soc.* **2014**, *136*, 6744.

[48] M. Alsabet, M. Grden, G. Jerkiewicz, *Electrocatalysis* **2011**, *2*, 317.

[49] E. Cossar, M. S. E. Houache, Z. Zhang, E. A. Baranova, *J. Electroanal. Chem.* **2020**, *870*, 114246.

[50] M. W. Louie, A. T. Bell, *J. Am. Chem. Soc.* **2013**, *135*, 12329.

[51] X. Zhang, H. Xu, X. Li, Y. Li, T. Yang, Y. Liang, *ACS Catal.* **2016**, *6*, 580.

[52] M. Görlin, P. Chernev, J. F. De Araújo, T. Reier, S. Dresp, B. Paul, R. Krähnert, H. Dau, P. Strasser, *J. Am. Chem. Soc.* **2016**, *138*, 5603.

[53] M. Gorlin, J. F. De Araujo, H. Schmies, D. Bernsmeier, S. Dresp, M. Gliech, Z. Jusys, P. Chernev, R. Kraehnert, H. Dau, P. Strasser, *J. Am. Chem. Soc.* **2017**, *139*, 2070.

[54] M. Wang, J. Jiang, L. Ai, *ACS Sustain. Chem. Eng.* **2018**, *6*, 6117.

[55] J. W. D. Ng, M. García-Melchor, M. Bajdich, P. Chakthranont, C. Kirk, A. Vojvodic, T. F. Jaramillo, *Nat. Energy* **2016**, *1*, 16053.

[56] L. J. Enman, M. S. Burke, A. S. Batchellor, S. W. Boettcher, *ACS Catal.* **2016**, *6*, 2416.

[57] P. Thangavel, M. Ha, S. Kumaraguru, A. Meena, A. N. Singh, A. M. Harzandi, K. S. Kim, *Energy Environ. Sci.* **2020**, *13*, 3447.

[58] Z. Li, M. Shao, H. An, Z. Wang, S. Xu, M. Wei, D. G. Evans, X. Duan, *Chem. Sci.* **2015**, *6*, 6624.

[59] H. Koshikawa, H. Murase, T. Hayashi, K. Nakajima, H. Mashiko, S. Shiraishi, Y. Tsuji, *ACS Catal.* **2020**, *10*, 1886.

[60] F. Dionigi, P. Strasser, *Adv. Energy Mater.* **2016**, *6*, 1600621.

[61] J. Kim, D. H. Youn, K. Kawashima, J. Lin, H. Lim, C. B. Mullins, *Appl. Catal. B Environ.* **2018**, *225*, 1.

[62] M. Görlin, P. Chernev, P. Paciok, C.-W. Tai, J. F. De Arau, T. Reier, M. Heggen, R. Dunin-borkowski, P. Strasser, *Chem. Commun.* **2019**, *55*, 818.

[63] Y. Pi, N. Zhang, S. Guo, J. Guo, X. Huang, *Nano Lett.* **2016**, *16*, 4424.

[64] M. Gong, Y. Li, H. Wang, Y. Liang, J. Z. Wu, J. Zhou, J. Wang, T. Regier, F. Wei, H. Dai, *J. Am. Chem. Soc.* **2013**, *135*, 8452.

[65] Y. Zhao, N. M. Vargas-Barbosa, E. A. Hernandez-Pagan, T. E. Mallouk, *Small* **2011**, *7*, 2087.

[66] Y. Kuroda, T. Nishimoto, S. Mitsushima, *Electrochim. Acta* **2019**, *323*, 134812.

[67] F. D. Speck, K. E. Dettelbach, R. S. Sherbo, D. A. Salvatore, A. Huang, C. P. Berlinguette, *Chem* **2017**, *2*, 590.

[68] J. A. Haber, E. Anzenburg, J. Yano, C. Kisielowski, J. M. Gregoire, *Adv. Energy Mater.* **2015**, *5*, 1402307.

[69] M. Favaro, W. S. Drisdell, M. A. Marcus, J. M. Gregoire, E. J. Crumlin, J. A. Haber, J. Yano, *ACS Catal.* **2017**, *7*, 1248.

Chapter 5. The Performance of Nickel and Nickel-Iron Catalysts Evaluated as Anodes in Anion Exchange Membrane Water Electrolysis

Emily Cossar[1], Alejandro Oyarce Barnett[2,3,*], Frode Seland[4] and Elena A. Baranova[1,*]

[1] *Department of Chemical and Biological Engineering, Centre for Catalysis Research and Innovation (CCRI), University of Ottawa, 161 Louis-Pasteur Ottawa ON K1N 6N5, Canada*

[2] *SINTEF Industry, Sustainable Energy Technology Department, New Energy Solutions Group, Trondheim NO-7491, Norway*

[3] *Department of Energy and Process Engineering, Norwegian University of Science and Technology, Trondheim NO-7491, Norway*

[4] *Department of Materials Science and Engineering, Norwegian University of Science and Technology Trondheim NO-7491, Norway*

Chapter as published in: *Catalysts* **2019**, *9*, 814, doi:10.3390/catal9100814.

Supplementary information for this chapter is found in Appendix D.

Abstract

Anion exchange membrane water electrolysis (AEMWE) is an efficient, cost-effective solution to renewable energy storage. The process includes oxygen and hydrogen evolution reactions (OER and HER); the OER is kinetically unfavourable. Studies have shown that nickel (Ni)- iron (Fe) catalysts enhance activity towards OER, and cerium oxide (CeO_2) supports have shown positive effects on catalytic performance. This study covers the preliminary evaluation of Ni, $Ni_{90}Fe_{10}$ (at%) and $Ni_{90}Fe_{10}/CeO_2$ (50 wt%) nanoparticles (NPs), synthesized by chemical reduction, as OER catalysts in AEMWE using commercial membranes. Transmission electron microscopy (TEM) images of the Ni-based NPs indicate NPs roughly 4–6 nm in size. Three-electrode cell measurements indicate that $Ni_{90}Fe_{10}$ is the most active non-noble metal catalyst in 1 and 0.1 M KOH. AEMWE measurements of the anodes show cells achieving overall cell voltages between

1.85 and 1.90 V at 2 A cm^{-2} in 1 M KOH at 50 °C, which is comparable to the selected iridium-black reference catalyst. In 0.1 M KOH, the AEMWE cell containing $Ni_{90}Fe_{10}$ attained the lowest voltage of 1.99 V at 2 A cm^{-2}. Electrochemical impedance spectroscopy (EIS) of the AEMWE cells using $Ni_{90}Fe_{10}/CeO_2$ showed a higher ohmic resistance than all catalysts, indicating the need for support optimization.

Graphical Abstract

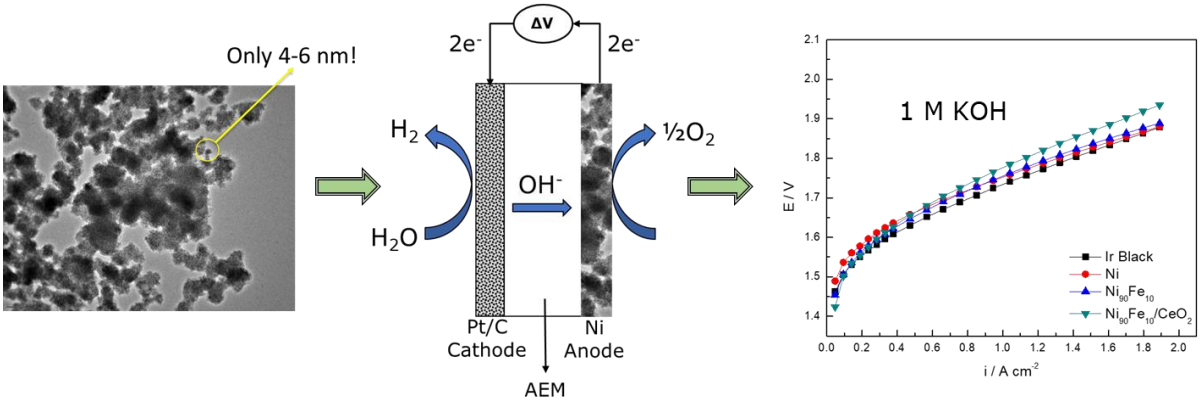

5.1 Introduction

As global warming and climate change concerns continue to rise, the concept of a "hydrogen economy" is becoming more and more important. This ideal is based on using hydrogen (H_2) as a clean, renewable fuel [1]. H_2 can also be used to store renewable energy through water electrolysis [2]. Water electrolysis utilizing anion exchange membranes (AEMs) is an emerging water electrolysis technology, used for its ability to produce hydrogen both efficiently and at low cost. Compared to traditional alkaline water electrolysis, which employ porous diaphragm separators, solid polymer electrolytes may provide certain advantages, such as lower gas crossover, improved efficiency, higher current densities, differential pressure operation and improved operation dynamics [3]. Unlike other solid polymer electrolyser technologies, such as proton exchange membrane water electrolysis (PEMWE), anion exchange membrane water electrolysis (AEMWE) technology has the potential to operate without expensive noble-metal catalysts, such as iridium, ruthenium and platinum, in addition to low-cost materials for bipolar plates and current collectors. AEMWE, therefore, aims to combine the low costs of alkaline electrolysis with the high efficiency and flexibility of the proton exchange membrane (PEM) electrolysis design [3].

The theoretical thermodynamic potential for water electrolysis is 1.23 V at room temperature. To achieve a low activation overvoltage during electrolysis's operation, high performing oxygen and hydrogen evolving catalysts are required. As the goal of water electrolysis is its industrialization, catalyst cost is imperative. As such, the development of active non-noble metal catalysts is crucial to further develop and establish AEMWE technology. The number of studies addressing performance improvements through the development of new AEM materials, catalysts and membrane electrode assemblies (MEAs) have increased in recent years [4–13]. However, the water splitting performance reported for AEMWE is still lower than that of PEMWE [14,15], particularly when employing non-noble metal catalysts and lower concentrations of alkaline solutions, or water [16].

The water electrolysis process occurs through two simultaneously occurring half-cell reactions: the oxygen evolution reaction (OER) on the anode and the hydrogen evolution reaction (HER) on the cathode. OER kinetics are more sluggish than HER kinetics [17]; therefore, the performance of water electrolysers heavily depends on the OER. Generally, the OER activity of non-noble electrocatalysts is high in alkaline environments [14]. Non-noble metal oxides are, therefore, of interest as catalysts for AEMWE. More specifically, catalysts based on Ni or Co (hydroxides, oxides, spinels, perovskites and pyrochlores) show good activity towards the OER in alkaline media. Ni-based electrocatalysts have been particularly well investigated, and include different ratios of Ni–iron (Fe), Ni–chromium (Cr) and Ni–molybdenum (Mo) oxide catalysts [6,18–23], amongst other bimetallics and alloys. Li et al. [18] studied various electrodeposited, Ni-bimetallic catalysts for OER. Among all tested metals, the NiFe catalyst showed the highest promotional effect, achieving the lowest overpotential of 256 mV at 0.5 A cm^{-2} with 10% iron incorporation. Similarly, Trotochaud et al. [20] tested multiple metal and mixed-metal oxide catalysts prepared by spin coating for OER. Their study showed that the $Ni_{90}Fe_{10}O_x$ catalyst obtained the lowest overpotential of 297 mV at 1 mA cm^{-2}.

The most widely accepted description of the Ni oxidation steps in alkaline media is through the Bode diagram, a simplified version of which is shown in Figure 5.1 below [24].

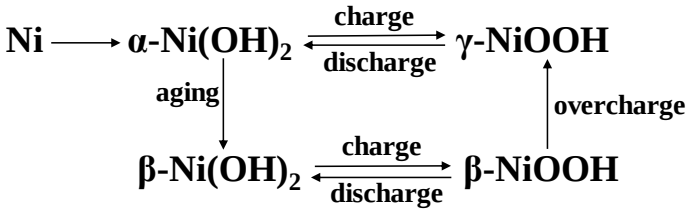

Figure 5.1: Nickel oxidation steps in alkaline media.

In an alkaline environment, nickel is first oxidized to the unstable α-$Ni(OH)_2$ (about –0.5 V versus Hg/HgO or ~0.43 V versus RHE at pH 14). Prolonged exposure to an alkaline environment or slight anodic polarization brings it to the stable β-$Ni(OH)_2$ phase. Further polarization induces the

oxidative deprotonation of β-$Ni(OH)_2$ to β-NiOOH (~0.45 V versus Hg/HgO or ~1.38 V versus RHE at pH 14), the active phase for OER [17]. Finally, further increasing the electrode potential will overcharge the nickel catalyst and bring it to the γ-NiOOH phase, which is believed to be the highest-achievable Ni oxidation phase. It is most commonly assumed that the β-NiOOH oxidation phase is most active towards the OER [17]. This oxidative deprotonation process to generate the catalytic species for the OER is not particular for nickel; it has been reported that cobalt, iron and manganese-based catalysts also deprotonate prior to oxygen evolution, in processes that are strongly pH-dependent [25–29].

Ceria (CeO_2) is an ionically conducting support that has been widely studied and applied in various electrochemical applications due to the advantageous metal support interactions (MSIs) that it may provide [30–32]. The MSIs occur through the unique properties of CeO_2, such as oxygen storage and release properties, and good ionic conductivity [33–35]. Using CeO_2 as a catalyst support can modify a catalyst's dispersion, minimize a catalyst's agglomeration and increase a catalyst's surface area. There are very few reports dealing with CeO_2 supports for non-noble metal catalysts for OER. Chen et al. [34] reported that the incorporation of CeO_2 into a copper oxide catalyst increased OER activity through strong electronic interactions between Ce^{4+} and Cu ions. They reported an optimal cerium content of 6.9%; further increasing the Ce content resulted in a less optimal Ce^{4+} distribution, and subsequently lower OER activity. Feng et al. [33] studied the incorporation of CeO_2 into FeOOH heterolayered nanotubes and concluded that the enhancement of OER's performance obtained through the incorporation of ceria into their catalyst was likely the result of the increased FeOOH/CeO_2 interfaces as well as the high oxygen storage capacity of the material. Haber et al. [36] developed a $Ni_{0.3}Fe_{0.07}Co_{0.2}Ce_{0.43}O_x$ catalyst exhibiting good activity (overpotential of 370 mV at 10 mA cm^{-2} in 1 M NaOH) and stability towards OER. Said catalyst was further studied by Favaro et al. [35], who concluded that the incorporation of ceria into the catalyst does provide unique promotional catalytic properties towards OER. Finally, McCrory et

al. [37], showed that their $NiCeO_x$ material had the highest overpotential for OER compared to IrO_x and NiO_x, $NiFeO_x$, amongst other bimetallic electrocatalysts in 1 M NaOH. Preliminary cyclic voltammograms of the effect of ceria incorporation into the Ni catalyst are shown in Figure D.1 of the Supplementary Information.

With respect to AEMWE studies, Seetharaman et al. [38] studied graphene oxide (GO) modified NiO electrode as an OER catalyst with enhanced electron conductivity and catalytic activity. A NiZnS ternary alloy was used at the cathode. The initial AEMWE performance of the electrodeposited catalysts on Ni foams was evaluated in the study. A Selemion™ AMV membrane (Asahi Glass Co. Ltd.) was used to prepare the membrane electrode assemblies (MEAs) and was sandwiched between the coated, foam electrodes. The AEMWE cell tests were performed using deionized water and concentrations of an alkaline solution [potassium hydroxide (KOH)] ranging from 0 to 5.36 M. They also tested various operating temperatures ranging from 30 to 80 °C. Increasing the concentration of the alkaline solution improved the initial cell performance, with current densities of approximately 65 and 140 mA cm^{-2} observed for pure water and 5.36 M KOH, respectively, at 1.8 V and 30 °C. When using the 5.36 M electrolyte and holding the system at 1.8 V, the current density increased from 100 to 380 mA cm^{-2} when increasing the operating temperature from 30 to 80 °C.

Xiao et al. [39] used electrocatalysts, such as Ni–Fe and Ni–Mo complexes, for the OER and HER in their MEAs. The Ni–Fe electrode was made using a solid-state electrochemical reduction procedure. Specifically, a solution containing Ni and Fe nitrates was sprayed onto a preheated Ni foam substrate and later electrochemically reduced by applying a cathodic current. The resulting loading of the catalysts was 40 mg cm^{-2} for both electrodes, and the membrane and ionomer used were xQAPS. The performance achieved was 400 mg cm^{-2} at 1.85 V in ultra-pure water. Ayers et al. [40] characterized AEMWE using non-noble metal complexes as catalysts for OER. They reported results for the ternary catalysts 30% Ni–Fe–Co/C and 30% Ni–Fe–Mo/C

compared to 30% Ni–Fe/C and IrO_2. Although they reported very low current densities, between 5 and 40 mA cm^{-2} at 1.8 V, the ternary catalysts showed higher performance compared to IrO_2 and 30% Ni–Fe/C.

Recently, Pavel et al. [41] developed and evaluated AEMWE using low cost transition metal catalysts. The commercial catalysts Acta 4030 (Ni/CeO_2-La_2O_3/C) and Acta 3030 (CuCoOx) (Acta SpA, Italy) were used as HER and OER catalysts, respectively. The loadings of the HER and OER catalysts were 7.4 and 36 mg cm^{-2}, respectively. These catalysts were designed to withstand relatively mild alkaline conditions (pH 10–11). The authors explained the effect of HER loading on the kinetic contribution and performance of the AEM electrolysis. Results showed current densities between 60 and 300 mA cm^{-2} at 1.8 V, as the HER catalyst's loading ranged from 0.6 to 7.4 mg cm^{-2}, while the OER catalyst's loading was kept constant at 36 mg cm^{-2}.

The aim of the presented work was to synthesize, characterize and electrochemically evaluate nanosized nickel-based electrocatalysts for the OER. Ni, $Ni_{90}Fe_{10}$ and $Ni_{90}Fe_{10}/CeO_2$ catalysts were synthesized by a scalable method, characterized by scanning and transmission electron microscopy (SEM and TEM), X-ray diffraction (XRD) and electrochemically evaluation using a conventional three-electrode electrochemical cell. The Ni-based electrocatalysts were also evaluated as anodes in real AEMWEs and compared to commercially available noble metal-based anode electrodes. This paper includes a study on the influence of the alkaline electrolyte concentration on the catalytic activity of the OER; ex-situ, three-electrode OER measurements and in situ AEMWE performances are compared at 1 M and 0.1 M KOH concentrations.

5.2 Results and Discussion

5.2.1 Scanning and Transmission Electron Microscopy

Figure 5.2 shows TEM images of the as-synthesized Ni and $Ni_{90}Fe_{10}$ nanoparticles (NPs), respectively. Using the scale on the image, it was possible to approximate a particle size of around 4–6 nm, agglomerated into larger clusters of NPs.

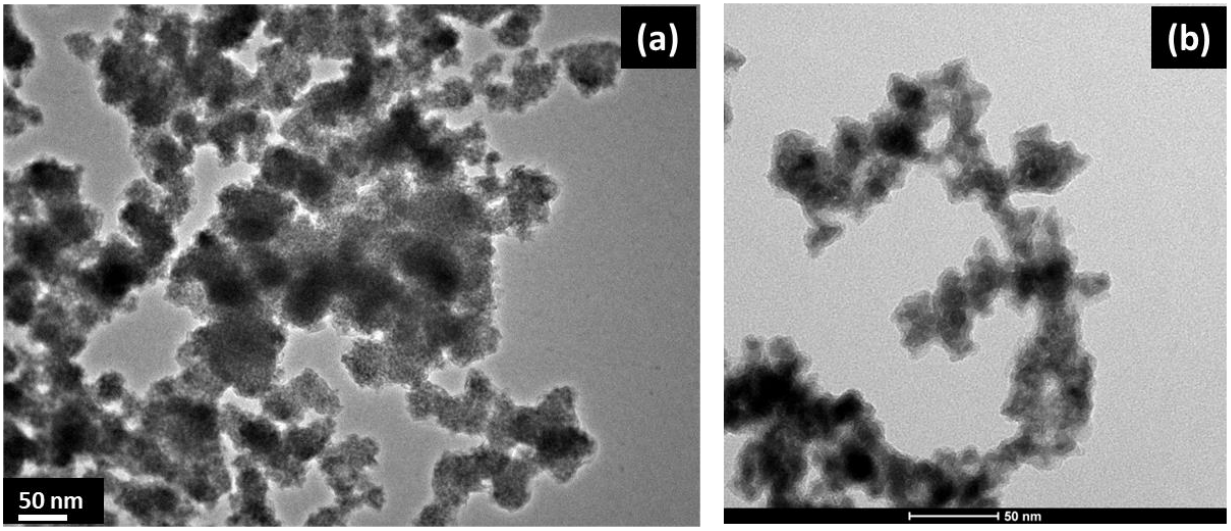

Figure 5.2: TEM of (a) Ni and (b) $Ni_{90}Fe_{10}$ nanoparticles (NPs).

Figure 5.3a-d represents SEM images of the anodes used in the AEMWE prior to experiments. Low magnitude images are displayed to show how the bulk electrode surfaces differ from each other. Comparisons with the Ni, $Ni_{90}Fe_{10}$ and $Ni_{90}Fe_{10}/CeO_2$ electrodes are shown in Figure 5.3b,c,d, respectively. The Ir black benchmark shown in Figure 5.3a, shows a more porous electrode with a clearer presence of particles making up the electrode surface. Although the same ink preparation and electrode spraying procedure was used for all electrodes, the Ni-based electrode fabrication procedure may need further optimization. The Ni anode shows an almost flaky electrode surface, which was very similar to results obtained for the $Ni_{90}Fe_{10}$ electrode surface. The $Ni_{90}Fe_{10}/CeO_2$ electrode shows relatively flat surface with large cracks in it, which is likely the result of having to spray twice as much ink onto the membrane to get the same Ni

loading, as 50 wt% of this catalyst is the CeO_2 support. Furthermore, increasing the magnification of the Ni-based anodes did not present a more detailed electrode surface, hence why they were kept at a lower magnification than Ir.

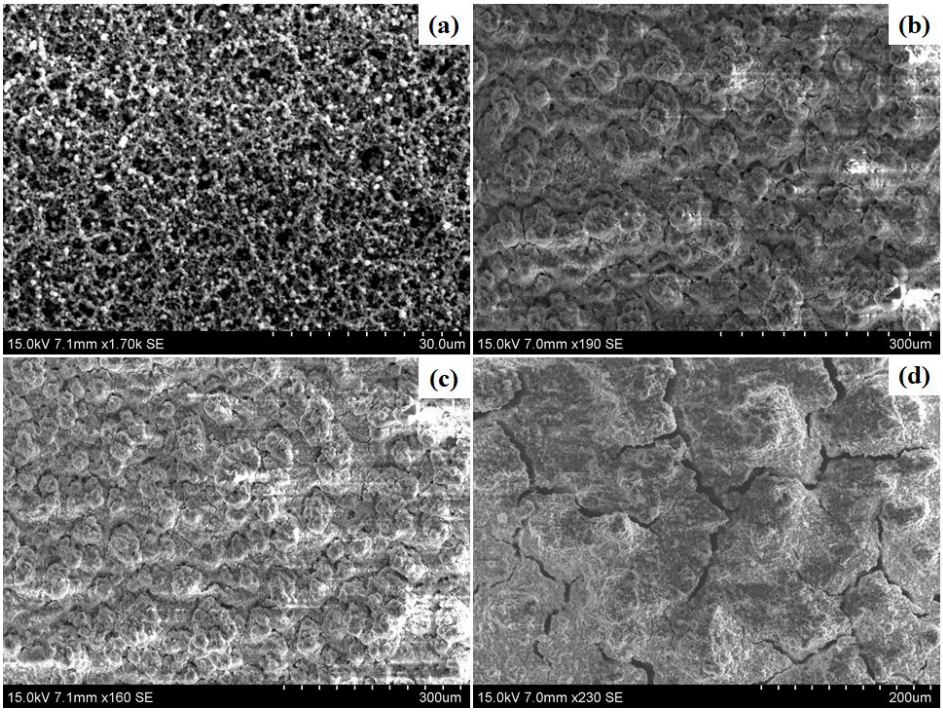

Figure 5.3: SEMs of (a) Ir black, (b) Ni, (c) $Ni_{90}Fe_{10}$ and (d) $Ni_{90}Fe_{10}/CeO_2$ anodes of the catalyst coated membranes. The magnifications of the images are 30, 300, 300 and 200 µm, respectively.

5.2.2 X-ray Diffraction

The XRD patterns of the Ni and $Ni_{90}Fe_{10}$ NPs are shown in Figure 5.4. XRD was not used to characterize the supported Ni catalyst, as ceria is also a face centered cubic (FCC) [32], and therefore, interferes with the main nickel diffraction peaks. As can be seen in Table 5.1, both samples include a mixture of Ni and β-$Ni(OH)_2$—the stable $Ni(OH)_2$ phase. In the $Ni_{90}Fe_{10}$ XRD pattern, the peak identified with the circle icon could be Ni (111) or Fe (110) [42,43]. Possible salt contamination can occur due to the synthesis method; however, catalyst samples were washed multiple times with water prior to XRD measurements to remove all NaCl. The possible presence

of NaCl was ruled out due to the absence of particular sharp peaks in the XRD spectra [44]. Having both Ni and Fe in the same peak position, and the slight shift between the Ni(III) peaks shown in the Ni XRD, indicated the potential formation of an alloy material. Additionally, the broad peak shown in the $Ni_{90}Fe_{10}$ pattern reflects the very small particle size observed in the TEM image of the synthesized materials, shown in Figure 5.2.

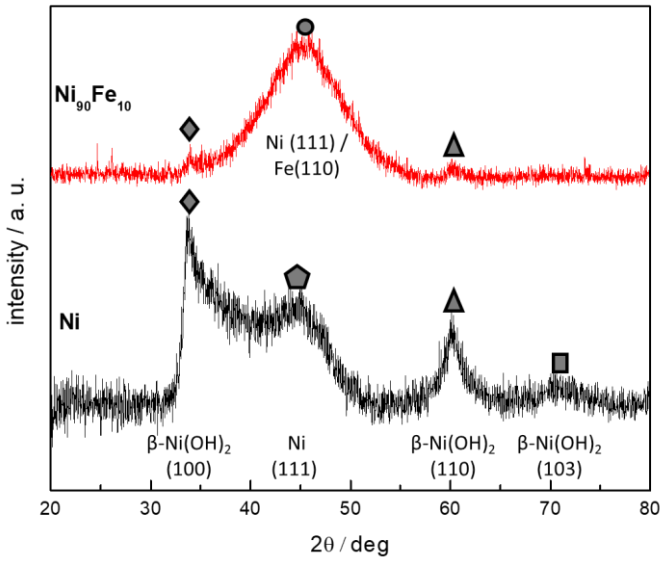

Figure 5.4: XRD results for Ni (black) and $Ni_{90}Fe_{10}$ (red) NPs.

Table 5.1: XRD results [42,43].

Icon on Figure 5.4		Experimental 2θ [deg]	Corresponding Compound; Reported 2θ [deg]
Diamond	◆	33.78	β-$Ni(OH)_2$ (100); 33.1
Pentagon	⬟	44.65	Ni (111); 44.45
Circle	●	45.37	Ni (111); 44.45 Fe (110); 44.9
Triangle	▲	59.99	β-$Ni(OH)_2$ (110); 59.1
Square	■	70.68	β-$Ni(OH)_2$ (103) ; ~71

5.2.3 Electron Energy-Loss Spectroscopy

Figure 5.5 summarizes an EELS spectrum taken for the $Ni_{90}Fe_{10}/CeO_2$ material. In Figure 5.5a, it is possible to see, in orange, the region of the STEM image where the analysis was carried out. The region in yellow was used for drift correction. As shown in Figure 5.5b, within the orange region, two sections were analyzed; the first section shows a cloudier area, while the second section shows a clearer structured area. As seen in Figure 5.5c, the first region mostly consisted of the Ni and Fe metals in the sample, while the second region mostly consisted of the CeO_2 support. This observation is also seen in the EELS mapping found in Figure D.5 of the Supplementary Information of this article. For TEM, STEM and EDX, characterization of the $Ni_{90}Fe_{10}/CeO_2$ catalyst, see Figures D.2– D.4 in the Supplementary Information.

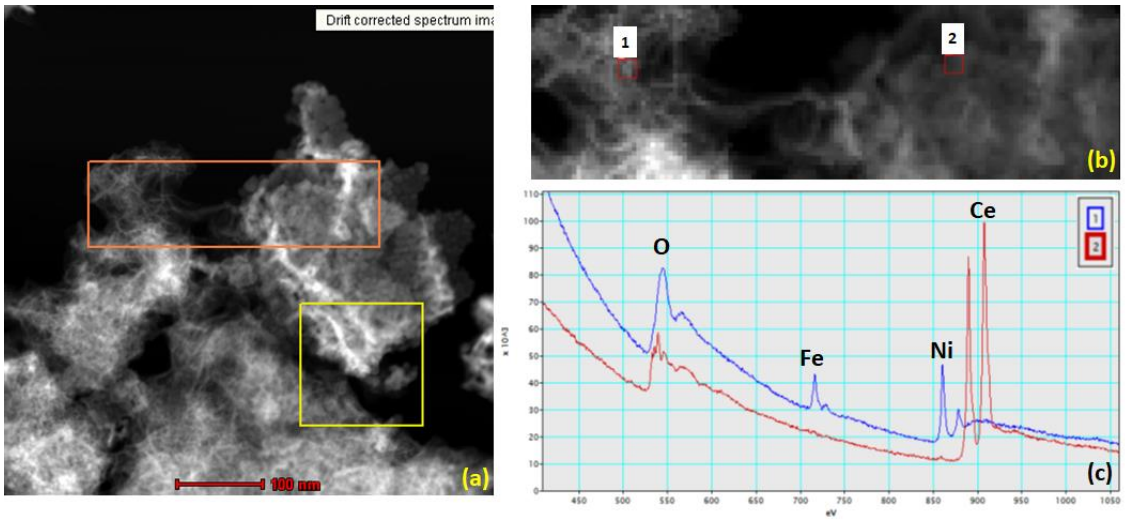

Figure 5.5: EELS results for $Ni_{90}Fe_{10}/CeO_2$. (a) The area of STEM image that was analyzed in orange, (b) shows the regions within the orange area that were analyzed and (c) shows the results of the analysis of the two regions.

5.2.4 OER Experiments

In the cyclic voltammograms (CVs) shown in Figure 5.6a, the onset overpotentials for OER in 1 M KOH can be summarize as $\eta_{\text{Ir black}} < \eta_{\text{Ni90Fe10/CeO2}} < \eta_{\text{Ni90Fe10}} < \eta_{\text{Ni}}$, where the onset potential for OER of Ir occurs at ~0.524 V (~1.449 V versus RHE). It is important to note that the onset

potentials are values taken at low currents. In addition to showing the lowest onset potential for OER, the iridium electrode also attains the highest current density and holds the lowest overpotential at 10 mA cm^{-2}, as shown in Table 5.2. Among the Ni-based electrocatalysts, the Ni electrode shows the highest current density, while the $Ni_{90}Fe_{10}/CeO_2$ sample exhibits the lowest onset potential for the OER at ~0.553 V (~1.478 V versus RHE). However, the $Ni_{90}Fe_{10}$ sample is the only sample that shows a lowered onset potential, while also attaining a high current density for OER. Additionally, it showed the second lowest overpotential at 10 mA cm^{-2}. From the CV shown in Figure 5.6b, the reaction overpotentials for OER in 0.1 M KOH can be written as $\eta_{\text{Ir black}} < \eta_{\text{Ni90Fe10/CeO2}} < \eta_{\text{Ni90Fe10}} < \eta_{\text{Ni}}$, where the onset potential for OER or Ir occurs at ~0.589 V (1.455 V versus RHE). Although the Ir black still showed the lowest onset potential for the OER in 0.1 M KOH, the catalyst performs rather poorly due to apparently slow kinetics, reaching less than 5 mA cm^{-2}. The $Ni_{90}Fe_{10}$ sample, on the other hand, continued to show a relatively high current for OER and held an overpotential of 0.404 V at 5 mA cm^{-2}. The $Ni_{90}Fe_{10}/CeO_2$ sample still exhibits the lowest onset potential amongst the Ni-based materials at around 0.635 V (1.501 V versus RHE). Figure 5.6c,d shows Tafel plots obtained from linear sweep voltammograms (LSVs) run at 1 mV s^{-1} in the OER region. Delineated on the figures are the regions in which the slopes tabulated in Table 5.2 were calculated. Note that no activity coefficients or exchange current densities were reported, as accurate estimations of a complete kinetic model require very detailed studies, such as the one reported by Reksten et al. [45] for $Ir_xRu_{(1-x)}O_2$ catalysts in acidic electrolyte.

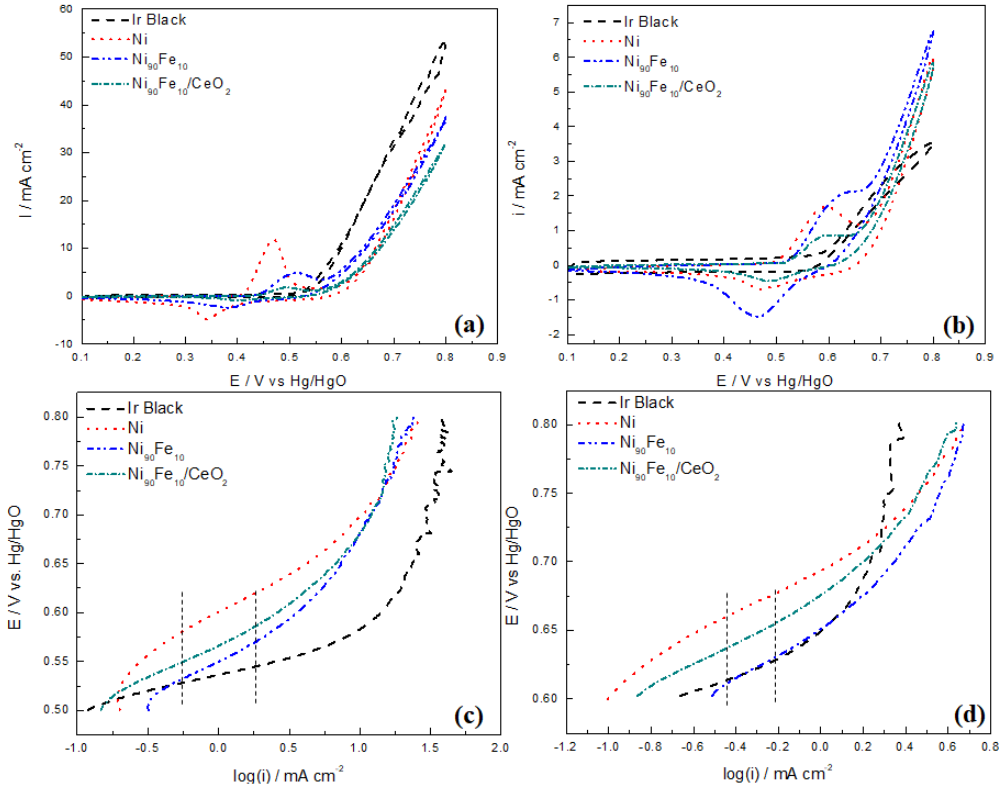

Figure 5.6: (a,b) Stable CVs run at 20 mV s^{-1} in 1 M and 0.1 M KOH, respectively. (c,d) Tafel plots obtained from LSVs run between [0.3, 0.8] V at 1 mV s^{-1} in 1 M and 0.1 M KOH, respectively. Catalysts: Ir black (black), Ni (red), $Ni_{90}Fe_{10}$ (blue) and $Ni_{90}Fe_{10}/CeO_2$ (green) NPs.

Table 5.2: Tafel slopes and overpotentials at 0.1 and 1 M for Ir black, Ni, $Ni_{90}Fe_{10}$ and $Ni_{90}Fe_{10}/CeO_2$ NPs.

Catalyst	KOH Conc. [M]	Tafel Slope [mV dec^{-1}]	η @ 5 mA cm^{-2} [mV]	η @ 10 mA cm^{-2} [mV]
Ir Black	1.0	32.0	268	295
	0.1	70.6	N/A	N/A
Ni	1.0	75.5	337	365
	0.1	73.1	424	N/A
$Ni_{90}Fe_{10}$	1.0	71.9	298	341
	0.1	83.3	404	N/A
$Ni_{90}Fe_{10}/CeO_2$	1.0	70.7	323	369
	0.1	82.1	424	N/A

The results summarized in Figure 5.6 and Table 5.2 indicate that the unsupported $Ni_{90}Fe_{10}$ catalyst is the most promising Ni-based material for OER in alkaline environment, as it shows both a lower onset potential and a higher current density in both 1 M and 0.1 M KOH. Amongst all Ni-based materials, it also shows the lowest overpotential at both 5 and 10 mA cm^{-2}. Similar results have been previously reported, where the addition of Fe increases the OER activity [18,21,23,46,47]. Increased OER overpotentials with decreasing electrolyte concentrations have also been reported [18,21,23,46,47]. When comparing values in Table 5.2, it is possible to observe that in this case, our Ni-based catalysts experience an increase in overpotential between 87 and 101 mV, when decreasing the electrolyte concentration from 1 M to 0.1 M KOH. As for the OER kinetics, it was noticed that the Tafel slopes obtained in 1 M KOH for our study were sometimes twice as high compared to the values reported in literature [18,20,21,23,46–48]. Discrepancies in the literature are common, with reported values ranging between 40 and 130 mV dec^{-1} for the Tafel slope of nickel-based oxides, and are likely combinations of the regions of LSV used to calculate the slope; it is well known that there are generally two Tafel regions for OER, separated at ~1.5 V versus RHE (~0.575 V versus Hg/HgO in 1 M KOH) [17]. Another possible cause for the different Tafel slopes for Ni-based materials could be the state of the oxide surface at the time of the measurement or the scan rate selected.

In addition, only a small increase in the Tafel slope was observed for the Ni-based catalysts when decreasing the electrolyte concentration, a clear indication that the kinetics for the OER remain unchanged in this pH region. On the other hand, it seems as though the kinetics of Ir-based catalysts are considerably more affected by the decrease in KOH concentration, more than doubling the Tafel slope from 32 to 70 mV dec^{-1}, while going from 1 M to 0.1 M KOH, respectively. These results are concurrent with observations reported in literature where Ir electrodes show a rather significant decrease in performance with decreasing electrolyte pH, either due to the development of a poorly conducting oxide film on the surface of the iridium working

electrode [49], a change in OER mechanism [49] or possible blocking of the electrode surface due to evolving oxygen [50] However, Pi et al. [51] reported Tafel slopes of 32.7, 38.4 and 40.1 mV dec^{-1} in 1 M KOH, and 42.1, 48.5, 50.2 mV dec^{-1} in 0.1 M KOH for surface-cleaned 3D Ir nanosheets, 3D Ir nanosheets and Ir NPs, respectively. The 3D nanosheets were prepared with the wet-chemical synthesis method. A study by Lyons et al. [50] also reported similar Tafel slopes of 44 and 43 mV dec^{-1} in 0.1 and 1 M KOH, respectively, for IrO_2 electrodes prepared via thermal decomposition onto a substrate. Finally, Tahir et al. [52], reported a Tafel slope of 65 mV dec^{-1} in 1 M KOH for IrO_2.

Figure 5.6 and Table 5.2 show that the $Ni_{90}Fe_{10}/CeO_2$ catalyst has a comparable overpotential for OER to those of the unsupported Ni-based materials. Although the current is not as high when including the ceria support, the material still shows promising activity through its Tafel parameters, which are very similar to the rest of the Ni-based materials. It is important to note that the CVs presented in Figure 5.6 were normalized by geometric surface area; normalizing the results by mass of metallic Ni would show that the ceria supported materials are the most promising OER catalysts, as shown in Figure 5.7, where the current densities normalized by geometric surface area and by mass of nickel at 0.8 V versus Hg/HgO (1.725 and 1.666 V versus RHE in 1 and 0.1 M KOH, respectively), are compared. Based on the interesting results of the cerium-content optimization reported in the paper by Chen et al. [34], future work on the Ni-based materials should include support content optimization of the synthesized catalysts. Figure D.6 in the Supplementary Information shows the normalization by mass of metal in the Ni-based samples.

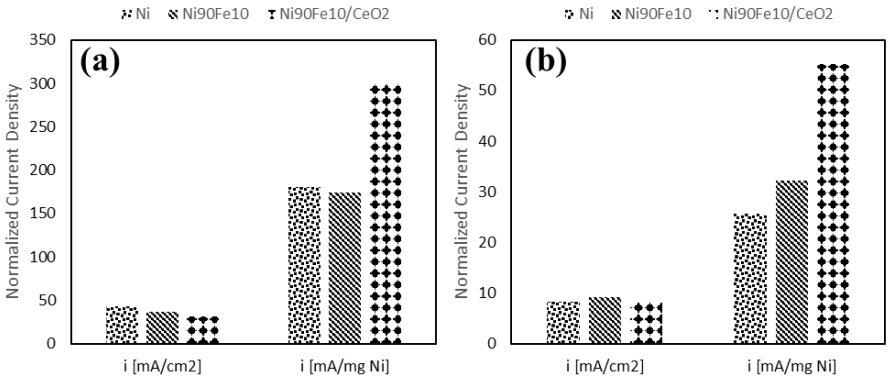

Figure 5.7: Comparison between current densities by geometric surface area and by mass of Ni at 0.8 V versus Hg/HgO in (a) 1 M KOH and (b) 0.1 M KOH. Data for Figures 5.7a and b were taken from the CVs presented in Figure 5.6a and b, respectively.

5.2.5 AEMWE Experiments

Polarization curves and electrochemical impedance spectroscopy (EIS) were carried out in an AEMWE cell. As shown in Figure 5.8a,b, polarization curves in 1 M KOH show a significantly higher performance and lower overpotential for OER than those taken in 0.1 M KOH. Achieving current densities of 2 A cm^{-2} at cell voltages of 1.85–1.9 V in 1 M KOH at 50 °C, may be regarded as an excellent result, considering the non-noble metal nature of these catalysts [2,8]. In 1 M KOH, the Ni and $Ni_{90}Fe_{10}$ electrodes show similar performance to the benchmark at only twice the intended metallic loading (6 mg cm^{-2} versus 3 mg cm^{-2} for Ir-black). As shown in Table 5.3, the $Ni_{90}Fe_{10}$ and $Ni_{90}Fe_{10}/CeO_2$ electrodes have lower overpotentials than the Ni electrode at lower current densities; however, not at higher current densities, in accordance with our ex-situ CV experiments (Figure 5.6a and b). In 0.1 M KOH, the $Ni_{90}Fe_{10}$ electrode was the only catalyst that could reach an operating current of 2 A cm^{-2}, without inducing too high an overpotential. Contrary to the non-noble catalyst results, the Ir black benchmark electrode shows a significant decrease in performance at the lower electrolyte concentration. This result not only reflects the three-electrode cell results very nicely, but also shows that Ni-based electrocatalysts, particularly the $Ni_{90}Fe_{10}$ catalyst, are promising electrocatalysts for use as AEMWE anodes. The $Ni_{90}Fe_{10}$ catalyst shows

similar performance as the Ir noble metal in 1 M KOH and outperforms the noble metal in 0.1 M. The nickel-based materials in this work also show comparable, if not better, performance than other AEMWE tests carried out with similar set ups [12,53].

EIS measurements were carried out to evaluate the overall cell resistance and charge transfer resistance for the single AEMWE cell. Figure 5.8c,d and Table 5.3 show the EIS of each cell set up at 1 A cm^{-2}. Although the EIS measurements were done for the full cell, a simple R(QR) circuit was used to fit the experimental data. The R(QR) model is shown in the corners of Figure 5.8c,d, and consists of a solution or overall cell resistance (R_{EL}) in series with a parallel combination of a charge transfer resistance (R_{CT}) and a constant phase element (Q). R_{EL} is found from the high frequency intersection of the real axis of the fitted curve, while the R_{CT} is represented by the diameter of the ensuing semicircle. All parameters were extracted from fits of the experimental data and reproduced in Table 5.3 under various conditions. Apart from the $Ni_{90}Fe_{10}/CeO_2$, all anodes exhibited similar R_{EL} in 1 M KOH. As the R_{EL} corresponds to the ohmic resistance of the cell, it was expected that it be similar for the unsupported Ni, Ir and $Ni_{90}Fe_{10}$ catalysts. It is interesting to observe that the electrolyser cell using the $Ni_{90}Fe_{10}/CeO_2$ shows more than twice the R_{EL} compared to the other cells for the same KOH concentration. This increase in ohmic resistance is caused by the rather large amount of less-conductive ceria in the catalytic layer (6 mg cm^{-2} for both the Ni catalyst and the CeO_2 support), increasing the thickness of the catalytic layer. Incorporating ceria into the catalyst therefore affected both the electrode bulk conductivity and contact resistance between the anode electrode and the porous transport layers (PTLs). Nevertheless, the $Ni_{90}Fe_{10}/CeO_2$ anode showed lower charge-transfer resistances in both 0.1 and 1 M KOH, indicating good kinetics.

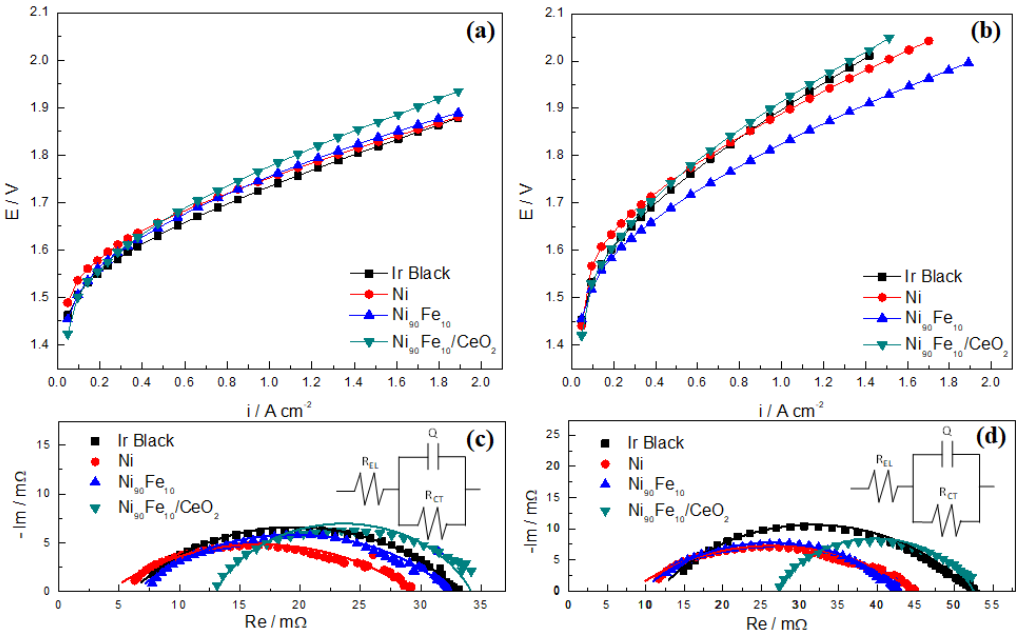

Figure 5.8: (a,b) Polarization curves up to 2 A cm^{-2} in 1 M and 0.1 M KOH, respectively. (c,d) Electrochemical impedance spectroscopy in 1 M and 0.1 M KOH, respectively. Catalysts: Ir black (black square), Ni (red circle), $Ni_{90}Fe_{10}$ (blue triangle) and $Ni_{90}Fe_{10}/CeO_2$ (green inverted triangle) NPs. Experiments were conducted at 50 °C.

Table 5.3: Summary of polarization curve and electrochemical impedance results.

Catalyst	KOH conc. [M]	*E* @ 0.4 A/cm^2 [V]	*E* @ 1.4 A/cm^2 [V]	R_{EL} [mΩ]	R_{CT} [mΩ]	*Y* [10^{-4} F $s^{(1-\alpha)}$]	α
Ir Black	1.0	1.608	1.804	6.0 ± 0.1	27 ± 0.1	3.6 ± 0.1	0.577 ± 0.005
	0.1	1.691	2.011	11.6 ± 0.2	40.2 ± 0.3	11.5 ± 0.1	0.618 ± 0.007
Ni	1.0	1.636	1.815	4.1 ± 0.2	25.2 ± 0.3	12.8 ± 0.8	0.465 ± 0.009
	0.1	1.713	1.984	8.0 ± 0.3	36.7 ± 0.5	6.4 ± 0.4	0.478 ± 0.009
$Ni_{90}Fe_{10}$	1.0	1.622	1.823	6.3 ± 0.2	26.1 ± 0.3	6.6 ± 0.5	0.53 ± 0.01
	0.1	1.659	1.911	9.4 ± 0.1	33.6 ± 0.2	2.8 ± 0.1	0.551 ± 0.005
$Ni_{90}Fe_{10}$/ CeO_2	1.0	1.627	1.854	13.0 ± 0.4	21.2 ± 0.2	10.1 ± 0.3	0.74 ± 0.04
	0.1	1.703	2.023	27.0 ± 0.4	25.6 ± 0.6	0.5 ± 0.1	0.74 ± 0.02

Table 5.3 clearly shows that decreasing that the KOH concentration decreases electrolysis performance for all materials by affecting the charge transfer resistance (R_{CT}) and kinetics of the electrochemical reactions, and the ohmic resistance or electrolyte resistance (R_{EL}) through a lack of OH^- ions. However, in the case of the $Ni_{90}Fe_{10}$ and $Ni_{90}Fe_{10}/CeO_2$, the decrease in KOH concentration does not have as large an effect on the activity and kinetics of the OER compared to the Ni and Ir catalysts. The presence of Fe in the catalysts seems to shift the OER onset potential to lower values due to the formation of a NiFe mixed oxyhydroxide ($Ni_xFe_{(1-x)}OOH$) independent of pH [25].

5.3 Materials and Methods

5.3.1 Synthesis of Ni-Based Materials by Chemical Reduction

Ni, $Ni_{90}Fe_{10}$ and $Ni_{90}Fe_{10}/CeO_2$ nanoparticles (NPs) were synthesized by a scalable chemical reduction method in ethanol using sodium borohydride as the reducing agent, similar to other reported methods[54,55]. First, the nickel chloride hexahydrate ($NiCl_2 \cdot 6H_2O$, 99.999% purity, Sigma Aldrich, St. Louis, MO, USA) precursor salt was dissolved in ethanol (EtOH, 99%, Greenfield, Grayslake, IL, USA) with magnetic stirring for 45 mins at room temperature. Depending on whether the desired compound included Fe or CeO_2, or both, the ferrous sulphate heptahydrate ($FeSO_4 \cdot 7H_2O$, ≥99%, Sigma Aldrich, St. Louis, MO, USA), precursor salt and cerium oxide nanopowder support (CeO_2, 99.5%, Alfa Aesar, Haverhill, MA, USA) were dissolved in ethanol using the same procedure. Next, the solutions were mixed together, and magnetic stirring was continued for 5 minutes to ensure that the solution was homogenous. Sodium borohydride ($NaBH_4$, ≥98%, ACROS, Geel, Belgium) was then dissolved in around 5–10 mL of ultrapure water (ultrapure water, Milli-Q® Millipore, 18.2 MΩ cm at 293 K), then added to the reaction mixture, which was then further mixed for 30 minutes to ensure everything was completely reduced. Once the reaction was complete, the nanoparticles were washed three times with ethanol using a centrifuge run at 6000 rpm for 10 minutes per wash. Finally, the particles

were left in a freeze drier overnight (around 15 h) to remove all residual ethanol from the sample. In this study, monometallic Ni nanoparticles were prepared, as were $Ni_{90}Fe_{10}$ (at%) and $Ni_{90}Fe_{10}/CeO_2$ (50 wt% $Ni_{90}Fe_{10}$ metal supported on CeO_2). Note that all glassware used in the NP synthesis was cleaned using the Aqua Regia procedure (2:1 HCl: HNO_3, 37 %, 70%, respectively, Sigma Aldrich, St. Louis, MO, USA). This synthesis procedure was easily scaled by adjusting the precursor salt quantities for the new desired material output, and by modifying the ethanol required to dissolve the salts. This ensured a similar concentration of precursor salts throughout all batches.

5.3.2 Material Characterization

The transmission electron microscopy (TEM) micrographs for the Ni and $Ni_{90}Fe_{10}$ catalysts were taken on the JEOL JEM 2100F Field Emission Transmission Electron Microscope (FETEM) (Tokyo, Japan) with an operating voltage of 200 kV. The scanning electron microscopy (SEM) micrographs of all AEMWE anodes were taken on the Hitachi Model S-3400N PC-Based Variable Pressure Scanning Electron Microscope (ON, Canada). SEM images were taken at an acceleration voltage of 15 kV. X-ray diffraction (XRD) results for the Ni and $Ni_{90}Fe_{10}$ catalysts were measured using the Rigaku Ultima IV multi-purpose diffractometer (Tokyo, Japan) using Copper Kα radiation and an X-ray wave length λ, of 1.5418 Å, at 40 kV and 44 mA. The XRD spectra were taken over a 2θ range of 20°–80° at a rate of 0.5° 2θ min^{-1}.

For the $Ni_{90}Fe_{10}/CeO_2$ material, a Field Electron and Ion Company (FEI, Hillsboro, OR, USA) Titan3 80–300 TEM operated at 300 keV, equipped with a corrected electron optical systems (CEOS) aberration corrector for the probe forming lens and a monochromated field-emission gun, was used to obtain both high-resolution TEM (HRTEM) and annular dark-field (ADF) images. The ADF images were collected using a high-angle annular dark-field (HAADF) Fischione detector in the scanning transmission electron microscopy (STEM) mode. Additionally, energy-dispersive X-ray (EDX) spectroscopy and electron energy-loss spectroscopy (EELS) were carried out on the ceria-supported material using the TEM instrument described above, equipped with an

EDX spectrometer (EDAX Analyzer, DPP-II) and an EELS spectrometer with a Gatan Tridiem 866 Image Filter. To optimize the signal intensity, EDX spectra were acquired with the specimen tilted at 15 degrees. EELS spectra were acquired in STEM with a convergence semi angle of 15 mrad and an acceptance semi angle of 40 mrad. Techniques not presented in the main article are presented in the Supplementary Information.

5.3.3 Ex-Situ Experiments

5.3.3.1 Cell Set-Up

The synthesized materials were first studied for the OER in a conventional, two-compartment, three-electrode electrochemical glass cell. The working and counter electrodes (WE and CE) were in the main compartment, while the reference electrode (RE) was in the second compartment. Prior to experiments, the glassy carbon surface of the WE was first polished with 30 micron alumina (Al_2O_3, Carveth Metallurgical Limited, Canada), then with 3 micron alumina (Al_2O_3, Buehler, Lake Bluff, IL, USA), both of which were mixed with ultrapure water. After polishing, the electrode surface was wiped with ethanol, then ultrapure water. The WE consisted of 10 μL of a catalyst ink deposited on a 0.196 cm^2 glassy carbon electrode. The catalyst ink was made with 6 mg catalyst, 1 mL of ultrapure water, 200 μL isopropanol (IPA, 99.9%, Fischer Scientific, Hampton, NH, USA) and 100 μL of Nafion® (~5%, Sigma Aldrich, St. Louis, MO, USA). Once the ink was made, it was sonicated for around 5 minutes, then the deposited ink was dried in an oven at 60 °C. The CE was a platinum mesh and the RE was mercury/mercury oxide (Hg/HgO) electrode (Koslow Scientific Company, Englewood, NJ, USA). Note that all potentials in this article are reported with respect to the Hg/HgO reference electrode unless otherwise specified. See the Supplementary Information for conversions to RHE and how the overpotentials were calculated. All electrochemistry experiments were carried out using either 1 M or 0.1 M potassium hydroxide solutions (KOH, ≥85%, Sigma Aldrich, St. Louis, MO, USA) at a room temperature of around 23 °C.

5.3.3.2 OER Experiments

Electrochemical tests were conducted using the Bio-Logic Potentiostat/Galvanostat using the EC Labs software (Bio-Logic Science Instruments, Seyssinet-Pariset, France). The OER tests included a cyclic voltammogram (CV) run between [0.1, 0.8] V for 10 cycles at a scan rate of 20 mV s^{-1}, followed by a linear sweep voltammogram (LSV) run between [0.3, 0.8] V at a scan rate of 1 mV s^{-1}. The tests mentioned were applied to the nickel-based materials, and an iridium black benchmark (Ir black, 99.8%, Alfa Aesar, Haverhill, MA, USA) catalyst. Before running the CVs and LSVs on the Ni-based materials, the WEs were polarized at –1.3 V for 5 minutes, and –0.8 V for 10 minutes [56], to first remove the oxides from the surfaces, and then to remove the hydrogen produced in the first polarization step. Only the fifth cycle of all cyclic voltammetry experiments is reported.

5.3.4 In Situ Experiments

5.3.4.1 Cell Set-Up

The AEMWE cell hardware consisted of a modified 25 cm^2 fuel cell hardware (BalticFuelCell Gmbh). The cell has parallel flow fields made with gold coated titanium, which were used as both anode and cathode endplates. The endplate material selection was based on minimizing ohmic losses in the AEMWE cell or rather to minimize the interfacial contact resistances (ICRs). The electrolyser setup also included a 5 L Teflon tank with heaters, which was used as the KOH reservoir. A double headed peristaltic pump was used to pump 300 mL min^{-1} of KOH through the AEMWE cell at both anode and cathode.

The membrane electrode assembly consisted of a commercial anionic exchange membrane (fumasep FAA-3PE-30, Fumatech, Bietigheim-Bissingen, Germany), onto which the anode and cathode were hand-sprayed with an air brush. The membrane was secured with a gasket, as shown in Figure 5.9. Furthermore, in the interest of conserving material, only 5 cm^2 of the 25 cm^2 cell

was used for the electrode area. The MEAs were assembled in the cell between two, 1 mm thick, commercially available, titanium, porous transport layers (PTLs) (Bekaert, Zwevegem, Belgium).

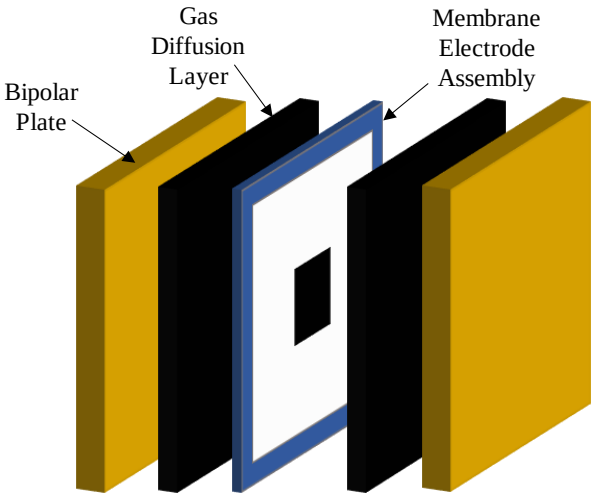

Figure 5.9: Compact alkaline exchange membrane water electrolyser cell design.

The anodes consisted of the previously mentioned Ni-based materials, and the Ir-black benchmark (Alfa Aesar, City, Haverhill, MA, USA), while the cathode consisted of platinum supported on carbon (Pt/C, 60 wt% metal on support, Alfa Aesar, Haverhill, MA, USA). The ink for the anodes were made with a solution of 50:50 by weight of ultrapure water: IPA, which included ~2 wt% metal and an anionic ionomer (fumion FAA-3-SOLUT-10, Bietigheim-Bissingen, Fumatech, Germany). The final electrode had ~7 wt% ionomer acting as both a catalyst binder and a facilitator for hydroxide ion transport. Multiple sonication and ultrasonication steps were used to ensure the solution was very fine and well dispersed. The ink for the cathodes were made in a similar way to the anode inks; however, the ionomer was present at ~23 wt% in the final electrode. Note that the ink preparation procedures were obtained by ink optimization of the benchmark electrodes; namely, the Ir-black anode and the Pt/C cathode.

In the AEMWE experiments, the anode loading for the benchmark was 3 mg cm^{-2}, while the loading for the Ni-based materials was 6 mg cm^{-2}. The cathode loading was held at a Pt loading of 1 mg cm^{-2} for all experiments. Note that those are intended metal loadings. For the actual metal

loadings, see Table D.1 in the Supplementary Information of this article. Actual metal loadings were calculated using ImageJ and a differential weight of samples taken from the template used to delimit the electrode area during spraying. The area of the template samples was calculated using the pixels that they occupied in a picture uploaded to ImageJ, with a ruler in the image for reference. It should be noted that these areas are not specific geometric surface areas (three-dimensional areas) of the sprayed catalytic layer.

5.3.4.2 AEMWE Experiments

Before starting electrolysis testing, the cell was mounted into the system, and around 2 L of 1 M KOH was circulated through the system overnight to exchange the bromine anions in the membrane with hydroxide ions from the alkaline electrolyte. The system was then cleaned by pumping ultrapure water through it. Electrolysis testing was then carried out using the HCP-803 Potentiostat equipped with the EC Labs software (Bio-Logic Science Instruments, Seyssinet-Pariset, France). First, polarization curves were taken, by stepping up the current from 0 to 10 A (0 to 2 A cm^{-2}). Next, electrochemical impedance spectroscopy (EIS) was performed by applying a direct current (DC) of 5 A (1 A cm^{-2}) and an alternating current (AC) of ±5% DC, while the frequency ranged from 20,000 to 0.1 Hz. The impedance data was fitted to a simple equivalent circuit using magnitude weighting in the Maple application "Complex Nonlinear Least Squares Fitting of Immittance Data," authored by David Harrington [57]. Polarization and EIS experiments were repeated three times in 1 M KOH, after which the system was flushed with ultrapure water, then all measurements were taken three times in 0.1 M KOH. All AEMWE experiments were performed at 50 ± 2 °C, by controlling the temperature in the cell and the KOH storage tank, individually.

5.4 Conclusions

In this study, Ni-based materials were synthesized for the promotion of the oxygen evolution reaction for applications in energy storage through anion-exchange, membrane-alkaline water electrolysis (AEMWE). Ni, $Ni_{90}Fe_{10}$ and $Ni_{90}Fe_{10}/CeO_2$ NPs were synthesized via chemical reduction in ethanol using sodium borohydride. The materials were characterized by TEM imaging and were found to be around 4–6 nm in size. Ex-situ electrochemical experiments were conducted in a conventional three-electrode cell at both 1 M and 0.1 M KOH and results were compared to an Ir-black benchmark electrode. Results indicate that on average, the $Ni_{90}Fe_{10}$ material is the best-performing material for OER, showing very low onset potentials and excellent catalytic activity. This result was also obtained for the lower electrolyte concentration, wherein the NiFe-based electrode outperformed all catalysts, including the Ir benchmark electrode.

In-situ AEMWE experiments were performed in a modified 25 cm^2 fuel cell for simultaneous O_2 and H_2 production. At twice the metallic loading compared to the Ir benchmark anode, the Ni-based materials showed state-of-the-art performance, achieving current densities of 2 A cm^{-2} at 1.85–1.9 V in 1 M KOH at 50 °C. In 0.1 M KOH, the cell set up using the $Ni_{90}Fe_{10}$ anode attained 1.99 V at 2 A cm^{-2}. These are promising results, considering the non-noble metal nature of these catalysts and that long-term stability measurements are on-going. Based on impedance results, the ceria-supported NiFe catalyst showed higher cell resistances (higher R_{EL} values), yet showed a low onset potential for the OER, and a low charge transfer resistance, indicating the $Ni_{90}Fe_{10}/CeO_2$ may be used as an anode catalyst in AEMWE if the support is further optimized in terms of electrical conductivity.

Acknowledgements

This research was conducted as part of the Engineered Nickel Catalysts for Electrochemical Clean Energy project administered from Queen's University and supported by Grant number RGPNM

477963-2015 under the Natural Sciences and Engineering Research Council of Canada (NSERC) Discovery Frontiers Program. Additionally, this work was performed within the HAPEEL project "Hydrogen Production by Alkaline Polymer Electrolyte Electrolysis," financially supported by the Research Council of Norway-ENERGIX program, contract number 268019. The Research Council of Norway is also acknowledged for the support to the Norwegian Fuel cell and Hydrogen Centre and the INTPART project 261620. The authors would also like to thank Dr. Martin Couillard from the Natural Research Council of Canada for his help in characterizing the $Ni_{90}Fe_{10}/CeO_2$ sample.

References

[1] D. Clark, N. Brandon, What's the "hydrogen economy"? *Guardian* **2012**.

[2] K. Zeng, D. Zhang, *Prog. Energy Combust. Sci.* **2010**, *36*, 307.

[3] Y. Leng, G. Chen, A. J. Mendoza, T. B. Tighe, M. A. Hickner, C.-Y. Wang, *J. Am. Chem. Soc.* **2012**, *134*, 9054.

[4] J. R. Varcoe, P. Atanassov, D. R. Dekel, A. M. Herring, M. A. Hickner, P. A. Kohl, A. R. Kucernak, W. E. Mustain, K. Nijmeijer, K. Scott, T. Xu, L. Zhuang, *Energy Environ. Sci.* **2014**, *7*, 3135.

[5] M. K. Cho, H. Y. Park, H. J. Lee, H. J. Kim, A. Lim, D. Henkensmeier, S. J. Yoo, J. Y. Kim, S. Y. Lee, H. S. Park, J. H. Jang, *J. Power Sources* **2018**, *382*, 22.

[6] I. Vincent, D. Bessarabov, *Renew. Sustain. Energy Rev.* **2018**, *81*, 1690.

[7] R. Phillips, A. Edwards, B. Rome, D. R. Jones, C. W. Dunnill, *Int. J. Hydrogen Energy* **2017**, *42*, 23986.

[8] J. E. Park, S. Y. Kang, S. H. Oh, J. K. Kim, M. S. Lim, C. Y. Ahn, Y. H. Cho, Y. E. Sung, *Electrochim. Acta* **2019**, *295*, 99.

[9] J. Hnát, M. Paidar, J. Schauer, J. Žitka, K. Bouzek, *J. Appl. Electrochem.* **2012**, *42*, 545.

[10] D. Chanda, J. Hnát, T. Bystron, M. Paidar, K. Bouzek, *J. Power Sources* **2017**, *347*, 247.

[11] J. H. Kim, J. N. Lee, C. Y. Yoo, K. B. Lee, W. M. Lee, *Int. J. Hydrogen Energy* **2015**, *40*, 10720.

[12] M. Schalenbach, O. Kasian, K. J. J. Mayrhofer, *Int. J. Hydrogen Energy* **2018**, *43*, 11932.

[13] Z. Liu, S. D. Sajjad, Y. Gao, H. Yang, J. J. Kaczur, R. I. Masel, *Int. J. Hydrogen Energy* **2017**, *42*, 29661.

[14] I. Katsounaros, S. Cherevko, A. R. Zeradjanin, K. J. J. Mayrhofer, *Angew. Chemie - Int. Ed.* **2014**, *53*, 102.

[15] S. Marini, P. Salvi, P. Nelli, R. Pesenti, M. Villa, M. Berrettoni, G. Zangari, Y. Kiros, *Electrochim. Acta* **2012**, *82*, 384.

[16] A. Faid, A. Oyarce Barnett, F. Seland, S. Sunde, *Catalysts* **2018**, *8*, 614.

[17] E. Fabbri, A. Habereder, K. Waltar, R. Kötz, T. J. Schmidt, *Catal. Sci. Technol.* **2014**, *4*, 3800.

[18] X. Li, F. C. Walsh, D. Pletcher, *Phys. Chem. Chem. Phys.* **2011**, *13*, 1162.

[19] M. K. Cho, A. Lim, S. Y. Lee, H. Kim, S. J. Yoo, Y. Sung, H. S. Park, J. H. Jang, *J. Electrochem. Sci. Technol.* **2017**, *8*, 183.

[20] L. Trotochaud, J. K. Ranney, K. N. Williams, S. W. Boettcher, *J. Am. Chem. Soc.* **2012**, *134*, 17253.

[21] M. Gong, H. Dai, *Nano Res.* **2015**, *8*, 23.

[22] X. Long, Z. Ma, H. Yu, X. Gao, X. Pan, X. Chen, S. Yang, Z. Yi, *J. Mater. Chem. A* **2016**, *4*, 14939.

[23] M. Gong, Y. Li, H. Wang, Y. Liang, J. Z. Wu, J. Zhou, J. Wang, T. Regier, F. Wei, H. Dai, *J. Am. Chem. Soc.* **2013**, *135*, 8452.

[24] H. Bode, K. Dehmelt, J. White, *Electrochim. Acta* **1966**, *11*, 1079.

[25] O. Diaz-Morales, D. Ferrus-Suspedra, M. T. M. Koper, *Chem. Sci.* **2016**, *7*, 2639.

[26] Y. Surendranath, M. W. Kanan, D. G. Nocera, *J. Am. Chem. Soc.* **2010**, *132*, 16501.

[27] T. Takashima, K. Hashimoto, R. Nakamura, *J. Am. Chem. Soc.* **2012**, *134*, 1519.

[28] M. E. G. Lyons, A. Cakara, P. O'Brien, I. Godwin, R. L. Doyle, *Int. J. Electrochem. Sci.* **2012**, *7*, 11768.

[29] M. E. G. Lyons, R. L. Doyle, M. P. Brandon, *Phys. Chem. Chem. Phys.* **2011**, *13*, 21530.

[30] C. Panaritis, M. Edake, M. Couillard, R. Einakchi, E. A. Baranova, *J. CO2 Util.* **2018**, *26*, 350.

[31] H. A. E. Dole, E. A. Baranova, *ChemCatChem* **2016**, *8*, 1977.

[32] G. R. Rao, B. G. Mishra, *Bull. Catal. Soc. India* **2003**, *2*, 122.

[33] J.-X. Feng, S.-H. Ye, H. Xu, Y.-X. Tong, G.-R. Li, *Adv. Mater.* **2016**, *28*, 4698.

[34] Z. Chen, C. X. Kronawitter, X. Yang, Y. W. Yeh, N. Yao, B. E. Koel, *Phys. Chem. Chem. Phys.* **2017**, *19*, 31545.

[35] M. Favaro, W. S. Drisdell, M. A. Marcus, J. M. Gregoire, E. J. Crumlin, J. A. Haber, J. Yano, *ACS Catal.* **2017**, *7*, 1248.

[36] J. A. Haber, Y. Cai, S. Jung, C. Xiang, S. Mitrovic, J. Jin, A. T. Bell, J. M. Gregoire, *Energy Environ. Sci.* **2014**, *7*, 682.

[37] C. C. L. McCrory, S. Jung, J. C. Peters, T. F. Jaramillo, *J. Am. Chem. Soc.* **2013**, *135*, 16977.

[38] S. Seetharaman, R. Balaji, K. Ramya, K. S. Dhathathreyan, M. Velan, *Int. J. Hydrogen Energy* **2013**, *38*, 14934.

[39] L. Xiao, S. Zhang, J. Pan, C. Yang, M. He, L. Zhuang, J. Lu, *Energy Environ. Sci.* **2012**, *5*, 7869.

[40] K. E. Ayers, E. B. Anderson, C. B. Capuano, M. Niedzwiecki, M. A. Hickner, C.-Y. Wang, Y. Leng, W. Zhao, *ECS Trans.* **2013**, *45*, 121.

[41] C. C. Pavel, F. Cecconi, C. Emiliani, S. Santiccioli, A. Scaffidi, S. Catanorchi, M. Comotti,

Angew. Chemie - Int. Ed. **2014**, *53*, 1378.

[42] Y. P. Sun, X. qin Li, J. Cao, W. xian Zhang, H. P. Wang, *Adv. Colloid Interface Sci.* **2006**, *120*, 47.

[43] D. S. Hall, D. J. Lockwood, C. Bock, B. R. MacDougall, *Proc. R. Soc. A Math. Phys. Eng. Sci.* **2014**, *471*, 20140792.

[44] E. A. Baranova, Y. Le Page, D. Ilin, C. Bock, B. MacDougall, P. H. J. Mercier, *J. Alloys Compd.* **2009**, *471*, 387.

[45] A. H. Reksten, H. Thuv, F. Seland, S. Sunde, *J. Electroanal. Chem.* **2018**, *819*, 547.

[46] M. E. G. Lyons, M. P. Brandon, *J. Electroanal. Chem.* **2010**, *641*, 119.

[47] X. Lu, C. Zhao, *Nat. Commun.* **2015**, *6*, 1.

[48] M. Tahir, L. Pan, F. Idrees, X. Zhang, L. Wang, J. J. Zou, Z. L. Wang, *Nano Energy* **2017**, *37*, 136.

[49] S. Cherevko, S. Geiger, O. Kasian, N. Kulyk, J.-P. Grote, A. Savan, R. B. Shrestha, S. Merzlikin, B. Breitbach, A. Ludwig, K. J. J. Mayrhofer, *Catal. Today* **2016**, *262*, 170.

[50] M. E. G. Lyons, S. Floquet, *Phys. Chem. Chem. Phys.* **2011**, *13*, 5314.

[51] Y. Pi, N. Zhang, S. Guo, J. Guo, X. Huang, *Nano Lett.* **2016**, *16*, 4424.

[52] M. Tahir, N. Mahmood, X. Zhang, T. Mahmood, F. K. Butt, I. Aslam, M. Tanveer, F. Idrees, S. Khalid, I. Shakir, Y. Yan, J. Zou, C. Cao, Y. Hou, *Nano Res.* **2015**, *8*, 3725.

[53] I. Vincent, A. Kruger, D. Bessarabov, *Int. J. Hydrogen Energy* **2017**, *42*, 10752.

[54] G. N. Glavee, K. J. Klabunde, C. M. Sorensen, G. C. Hadjipanayis, *Langmuir* **1994**, *10*, 4726.

[55] G. N. Glavee, K. J. Klabunde, C. M. Sorensen, G. C. Hadjipanayis, *Inorg. Chem.* **1995**, *34*, 28.

[56] M. Alsabet, M. Grden, G. Jerkiewicz, *Electrocatalysis* **2011**, *2*, 317.

[57] D. Harrington, "Complex Nonlinear Least Squares Fitting of Immittance Data," *Maple Soft; Maple 2017*, **2019**, accessed on August 26, 2019, https://www.maplesoft.com/applications/view.aspx?SID=154540.

Chapter 6. Ionomer Content Optimization in Nickel-iron-based Anodes with and without Ceria for Anion Exchange Membrane Water Electrolysis

Emily Cossar[a], Alejandro O. Barnett[b,c], Frode Seland[d], Reza Safari[e], Gianluigi A. Botton[e], Elena A. Baranova[a*]

[a] *Department of Chemical and Biological Engineering, Centre for Catalysis Research and Innovation (CCRI) University of Ottawa,161 Louis-Pasteur Ottawa, Canada, K1N 6N5*

[b] *SINTEF Industry, Sustainable Energy Technology Department, New Energy Solutions Group, Trondheim, Norway*

[c] *Department of Energy and Process Engineering, Norwegian University of Science and Technology, NO-7491 Trondheim, Norway*

[d] *Department of Materials Science and Engineering, Norwegian University of Science and Technology, NO-7491 Trondheim, Norway*

[e] *Department of Materials Science Engineering, McMaster University, 1280 Main St. W., Hamilton, Ontario, Canada L8S 4L8*

Chapter as published in: *J. Power Sources* **2021**, *514*, 230563, https://doi.org/10.1016/j.jpowsour.2021.230563.

Supplementary information for this chapter is found in Appendix E.

Abstract

Hydrogen production from anion exchange membrane water electrolysis (AEMWE) is an efficient cost-effective solution to renewable energy storage. Contrary to proton exchange membrane (PEM) electrolysis, AEMWE requires further optimization of its cell design, particularly for the kinetically unfavourable oxygen evolution anode half-cell reaction (OER). In this work we optimize the commercial Fumatech fumion ionomer content in AEMWE anodes using nickel (Ni) nanoparticles (NP) synthesized by chemical reduction. The optimal ionomer content is then applied to Ni-iron (Fe)-based NPs with and without ceria (CeO_2), all prepared using the same method. Scanning Electron Microscopy (SEM) of the resulting electrode surfaces, Particle-size Distribution (PSD) of the catalyst inks, and in-situ testing of the monometallic Ni NPs show that the best and most active catalytic layer is obtained using 15 wt% ionomer. AEMWE performance and short-term durability are evaluated in different concentrations of potassium hydroxide (KOH), where the $Ni_{90}Fe_{10}$ is the best performing Ni-based electrode showing 1.72 V at 0.8 A cm^{-2} in 1 M

KOH after IR-correction, and a degradation rate of 3.3 mV h^{-1}. The addition of ceria to the Ni-based catalysts shows more consistent mass transfer over time likely due to more efficient water transport and bubble release.

Graphical Abstract

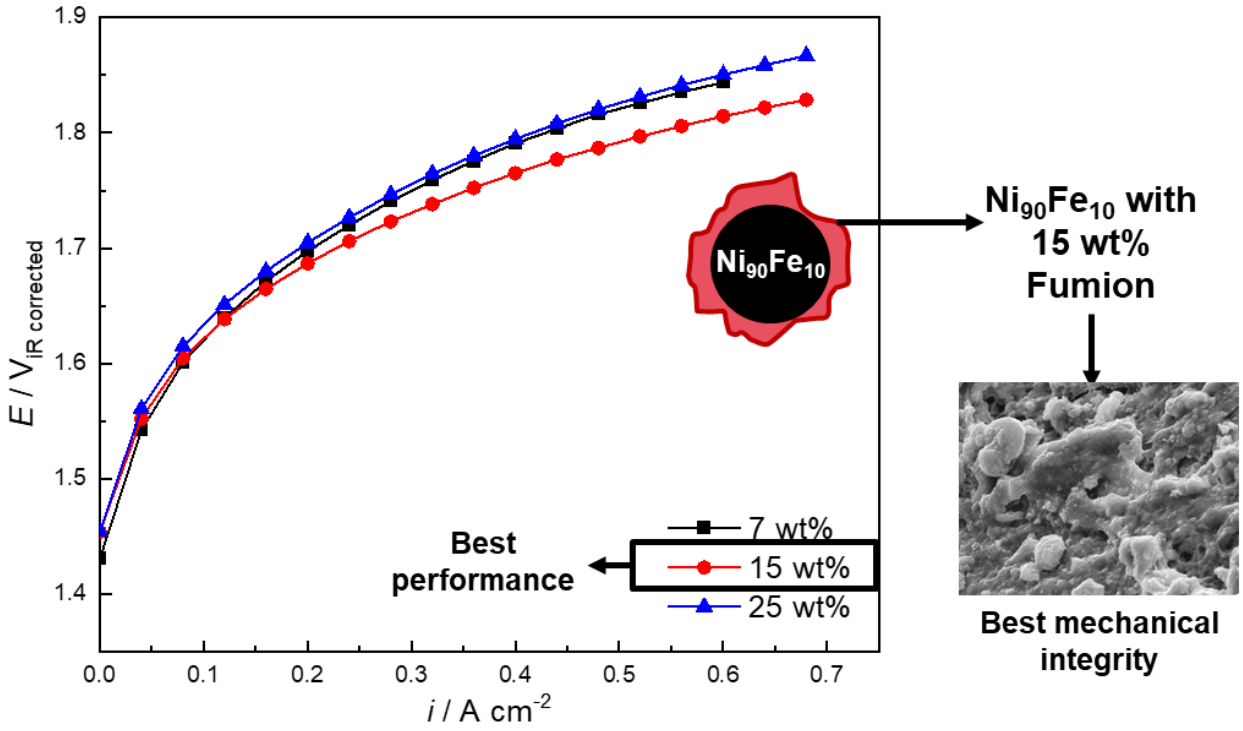

6.1 Introduction

The production of hydrogen via anion exchange membrane water electrolysis (AEMWE) is an economically feasible method for renewable energy storage, which can be easily integrated into a sustainable hydrogen-based energy system[1–4]. The advantages of AEMWE are well known[1,3,5–13]. One of the main advantages of this design comes from the use of a anion exchange membrane (AEM), which allows for a compact, low resistance cell design[6,10,11,14]. The AEM conducts hydroxide ions, while efficiently separating oxygen and hydrogen, allowing for higher operating current densities in comparison to traditional alkaline electrolyzers, which employ porous diaphragms as separators[15,16]. Additionally, contrary to its proton exchange membrane (PEM) equivalent, AEMWE systems allow the use of inexpensive non-noble metals as electrode materials due to their high stability and corrosion resistance in an alkaline environment[15,17–21]. Particularly, nickel-based catalysts have been well investigated as both anodes and cathodes in alkaline electrolysis systems[22–27]. The anode of the alkaline electrolyser is responsible for the oxygen evolution reaction (OER), a kinetically unfavourable reaction due to multiple electron transfer steps[22,28], while the cathode is responsible for the hydrogen evolution reaction (HER).

In an AEMWE system, one of the most important parts of the membrane electrode assembly (MEA) is adding the right amount of ionomer to the catalytic layers. In AEMWE, anion exchange ionomers (AEI) are used. AEIs are anion-conducting polymer electrolytes, consisting of positively charged functional groups bound to a polymer backbone[29]. In a catalytic layer, AEIs are used to form a porous network, which facilitates ion transport to the reaction sites as well as gas permeability, while also serving as a binder for the catalyst particles[30–32]. The amount of ionomer must be optimized because there are consequences to having too little or too much it. Many studies[30–36] show that having too little ionomer in the catalytic layer results in poor adhesion of the catalytic layer and low ion transport and gas permeability through the layer. On the other hand, having too much ionomer can cause particle agglomeration that can block catalyst sites as well as inhibit mass transport through the catalytic layer. Ionomers may also adsorb onto catalytic sites, reducing the active area available[37]. Having too much ionomer with readily access to water may cause the catalytic layer to lose its structural integrity due to dissolution of the ionomer into the electrolyte[31].

There are a few studies that cover ionomer optimization in AEMWE anodes. Vincent *et al.* [31] tested ionomer amounts in their electrolyser anode ranging from ~9-33% in their 5 cm^2 active area cell. They used a CuCoOx (Acta 3030®) and a Ni/(CeO_2-La_2O_3)/C) (Acta 4030®) catalyst for their OER and HER catalysts, respectively, set up in the CCS format. The loadings of the OER and HER catalysts on the porous carbon substrates were 30 and 7.4 mg cm^{-2}, respectively. The membrane used was the Tokuyama A-201 which was paired with the Acta I_2 alkaline ionomer. In their study, they found that increasing the ionomer content caused voltage drops in the cell, which were much more significant at ionomer concentrations higher than 20%. Ionomer contents lower than 9% caused large cracks in their catalyst layer, therefore the optimal ionomer content was found to be 9%. This ionomer loading resulted in a system performing at 0.5 A cm^{-2} at 1.95 V using 1% potassium carbonate at 60°C as the electrolyte.

Park *et al.* [32] tested ionomer contents of 10, 20 and 30 wt% in their 5 cm^2 active area cell. They used a catalyst coated membrane (CCM) MEA configuration with IrO_2 and 40 wt% Pt/C as OER and HER catalyst, respectively. In this work their anode loading was optimized to 4 mg cm^{-2} and the cathode was set to 0.4 mg cm^{-2}. Their cell was run with 1 M KOH at 70°C. The membrane used in their study was the Fumatech FAA-3-50, which was paired with the Fumatech FAA-3-Br anionic ionomer. In their study, Park *et al.* [32] found that the 20 wt% ionomer showed the best performance and the lowest charge transfer and cell resistance. They concluded that 20 wt% was the optimal amount when considering the trade-off between available active sites and pore morphology. The optimal performance found was 1.15 A cm^{-2} at 1.8 V at 70°C.

Cho *et al.* [33,34] tested ionomer amounts varying from 5 to 20 wt% in the anode catalytic layer in their 2.5x2.5 cm^2 active area cell in two separate works. Their OER and HER catalysts were IrO_2 and 46.5 wt % Pt/C, respectively, assembled using the CCS method. The system operated at 50°C. The membrane used was the Tokuyama A-201, while the ionomer was a 60 wt% polytetrafluoroethylene (PTFE) dispersion in water. In their first study[33], the optimal ionomer content was found to be 9 wt% showing a performance of 0.299 A cm^{-2} at 1.8 V for an anode feed supply of 0.5 M potassium hydroxide (KOH) and a cathode feed of deionized water. 9 wt% ionomer allowed for a balance between covered active sites and secondary pore formation. In the second study[34], 20 wt% ionomer content showed the best result achieving a current of 1.07 A cm^{-2} at 1.8 V for 0.5 M KOH at the anode and a dry cathode. The higher ionomer content was needed

to avoid catalyst detachment and maintain long-term performance. It is interesting to note here that simply changing the electrolyte feed conditions changed the optimal ionomer content, implying that every set of operating parameters and conditions must have its own ionomer optimization step.

In our previous work[26], we performed a preliminary evaluation of Ni-based nanoparticles (NPs) as oxygen evolution catalysts in AEMWEs. Small amounts of iron were added to the Ni NPs to enhance oxygen evolution activity as Fe is a well known OER promoter for Ni catalysts[18,20,22,38–43]. Ceria was also tested as a support to the NPs to further promote catalytic activity due to ceria's good electronic and ionic conductivity as well as its oxygen storage and release properties[28,38,39,44,45]. The results of this work were promising, showing overall cell voltages between 1.85 and 1.90 V in 1 M KOH at 50°C. The ionomer content used in the anode layers of this work was however simply set to the amount already optimized for the Ir black benchmark. Since this study as performed, we have completed an extensive ex-situ OER evaluation of multiple iron and ceria amounts in the Ni-based catalysts, showing that the best performing OER catalysts include $Ni_{90}Fe_{10}$ and $Ni_{80}Fe_{20}$, both with and without 10 wt% CeO_2[46]. As such, the goal of this study was to investigate the effects of the Fumatech fumion FAA-3-SOLUT-10 commercial ionomer content in the Ni-based anode layer of a single cell electrolyser and find the required optimal ionomer content. Ink properties such as particle size distribution measurements using different ionomer contents with Ni NP electrocatalysts are reported, and the catalytic layer morphology, mechanical stability, and electrochemical performance of the resulting electrodes are evaluated to narrow in on the optimum amount of ionomer. Finally, $Ni_{90}Fe_{10}$ and $Ni_{80}Fe_{20}$ catalysts with optimized ionomer content, both with and without the addition of 10 wt% CeO_2, are evaluated as anodes in an AEMWE single cell.

6.2 Materials and Methods

6.2.1 Material Synthesis

The Ni-based nanoparticles were synthesized by chemical reduction in ethanol using sodium borohydride as described in detail in our previous work [26]. To summarize the method to make Ni NPs, a nickel chloride hexahydrate precursor salt ($NiCl_2 \cdot 6H_2O$, 99.999%, Sigma Aldrich, St. Louis, MO, USA) is dissolved in ethanol (EtOH, 99%, Greenfield, Grayslake, IL, USA) by magnetic stirring, then chemically reduced using sodium borohydride ($NaBH_4$, ≥98%, ACROS,

Geel, Belgium). The NPs are then removed from the dispersion and washed 3x in EtOH using a centrifuge run at 6000 rpm for 10 minutes (mins) per wash. Once the materials are washed, they are freeze-dried over night to remove the remaining EtOH. To add iron or ceria to the Ni NPs, iron sulphate heptahydrate ($FeSO_4 \cdot 7H_2O$, ≥99%, Sigma Aldrich, St. Louis, MO, USA) and cerium oxide nanopowder (CeO_2, 99.5%, Alfa Aesar, Haverhill, MA, USA) are dissolve in EtOH in separate flasks. Once dissolved, the Ni, Fe and CeO_2 solutions are mixed and chemically reduced together. The prepared samples of this study include Ni, $Ni_{90}Fe_{10}$ (at%), $Ni_{80}Fe_{20}$ (at%), as well as $Ni_{90}Fe_{10}$/10 wt% CeO_2 and $Ni_{80}Fe_{20}$/10wt% CeO_2.. It is important to note that at a small quantity of 10 wt%, CeO_2 is likely present as a catalyst promoter, rather than a catalyst support. All glassware was cleaned using the Aqua Regia procedure of a volumetric 2:1 ratio of hydrochloric acid to nitric acid (HCl 37%, HNO_3 70%, Sigma Aldrich, St. Louis, MO, USA).

6.2.2 Material Characterization

The transmission electron microscopy (TEM) images of the $Ni_{90}Fe_{10}$, $Ni_{80}Fe_{10}$ and $Ni_{90}Fe_{10}$/10 wt% CeO_2 nanoparticles were taken using the Philips CM12 operating at 120 kV. The TEM images of the $Ni_{80}Fe_{20}$/10 wt% CeO_2 NPs were taken on the JEOL JEM 2010 Field Emission Transmission Electron Microscope (FETEM) (Tokyo, Japan) with an operating voltage of 200 kV. For characterization of the monometallic Ni particles, see our previous work [26]. The Brunauer-Emmett-Teller (BET) specific surface areas of the nanoparticles as well as the Barrett-Joyner-Halender (BJH) pore size distributions were evaluated using the Micrometrics 3Flex Version 5.00 analyser. Once the samples were degassed under nitrogen flow at 110°C, the measurements were taken by holding 30°C for 10 mins, 75°C for 15 h and 25°C for 4 h. The temperature ramp for all transitions was 10°C/min. Particle-size distribution (PSD) measurements of the catalyst inks were carried out using the Horiba Partica LA-960 (Kyoto, Japan) PSD analyzer. Measurements were taken under no sonication, as well as with 30 s and 180 s (3 minutes) of sonication. Finally, the catalyst coated surfaces were analyzed under the Hitachi SU6600 (Hitachi High-Tech, Krefeld, Germany) field emission gun scanning electron microscope (FEG SEM) at 20 kV.

6.2.3 In-situ Experiments

6.2.3.1 AEMWE Setup

6.2.3.1.1 Cell and System Configuration

The in-situ AEMWE measurements were carried out in a modified 25 cm^2 parallel flow field fuel cell hardware (balticFuelCells Gmbh, Schwerin, Germany). In comparison to our previous study[26], the increased active area here is used to put our catalysts to the test in a more representatively sized electrolyser, accounting for active area dependant activity. While this area is not comparable to testing in an stack, like in the work of Kim *et al.*[27], where they performed electrolysis testing on a stack of 26 unit cells having an active area of 200 cm^2, it is still on the larger side of the active areas reported in literature, which range from around 1 - 28 cm^2[6,18,31,33,47–52], with most studies conducted with an area under 10 cm^2. Aside from the cell, the electrolyser setup included a 5 L Teflon electrolyte tank and a double headed peristaltic pump, which was used to pump 300 mL min^{-1} of potassium hydroxide (KOH, ≥85%, Sigma Aldrich, St. Louis, MO, USA) electrolyte around the anode and cathode sides of the system. The KOH electrolyte was made using Milli-Q® water (H_2O, Milli-Q® Millipore, 18.2 MΩ cm et 293 K). To heat and control the system temperature to 50 ± 2°C for all experiments, the electrolyser cell as well as both sides of the KOH tank were equipped with heating elements and temperature sensors. The membrane used for all experiments was a commercial anion exchange membrane (fumasep FAA-3PE-30, Fumatech, Bietigheim-Bissingen, Germany). This membrane was paired with a 10 wt% solution of a commercial anionic ionomer (fumion FAA-3-SOLUT-10, Fumatech, Bietigheim-Bissingen, Germany). To secure the membrane and help seal the cell, the membrane was sandwiched between two gaskets (0.35 and 0.5 mm thick, 35 FC-PO 100 Ice Cube Sealing, Quintech, Göppingen, Germany). For a schematic of the electrolyser cell, see Figure E.1.

6.2.3.1.2 Ni-based Electrodes

To formulate the Ni-based anode inks, the NPs were first measured out then mixed with Milli-Q® water and the ionomer. Once the ionomer was added, the dispersion was sonicated in an ultrasonic bath (45 Hz Ultrasonic Cleaner USC300TH, VWR International, Radnor, PA, USA) for 5 mins over ice. Next, isopropanol (IPA, 99.9%, Fischer Scientific, Hampton, NH, USA) was added at a 50:50 weight ratio of water to IPA. The %solids in the ink was 3 for optimal spraying.

Once all the ink components were mixed, the ink was sonicated in an ultrasonic bath (45 Hz) for 10 mins over ice and then further mixed using an ultrasonic probe at 40% amplitude for 5 minutes, 5 s on/off (20 kHz Branson 450 Digital Sonifier, Marshall Scientific, Hampton, NH, USA) over ice. Ionomer nominal loadings of 7, 15, 25, 35 and 45 wt% in the resulting electrodes were made.

All electrolysis experiments were carried out using the catalyst coated substrate (CCS) method. When optimizing the ionomer content using the monometallic Ni NPs, the anode layer ink was hand sprayed onto a carbon fibre paper (Toray Paper 090, FuelCellStore, Texas, USA) to a final loading of 5 mg cm^{-2} (metallic weight) using an air brush (Cocraft airbrush sprayer, 0.35 mm mouthpiece). As using a carbon paper on the anode side significantly increased the initial cell resistance, a cell activation procedure was performed (keeping the cell current at 0.5 A cm^{-2} until the potential stabilized) to hydrate the carbon paper prior to polarization curve measurements. For the electrolysis experiments using the optimized ionomer in the catalytic layers, the $Ni_{90}Fe_{10}$ and $Ni_{80}Fe_{20}$ with and without CeO_2 catalysts were sprayed onto a 1 mm thick gold coated titanium porous transport layer (PTL, Ti felt, Bekaert, Zwevegem, Belgium) instead of the carbon paper.

It should be noted that the actual metal loadings obtained differ slightly from the desired amount of 5 mg cm^{-2} due to slight variations in the amount of waste generated during electrode preparation. For the actual catalyst loadings, see Table E.1 in the Supplementary Information (SI). Additionally, AEMWE testing was performed on the $Ni_{90}Fe_{10}$ electrode with less sonication prior to electrode spraying to observe whether sonication time impacted AEMWE performance. This is shown in Figure E.2, E.3 and Table E.2, with a summary of tested EIS models found in Table E.3. While the effects of ink sonication could not be properly analyzed here, the results do show that sonicating the ink for longer helps more efficiently air brush the electrode, which results in a higher electrode loading and therefore better AEMWE performance. For more information on this short study, see the SI.

6.2.3.1.3 Benchmark Electrodes

Commercial iridium black (Alfa Aesar, Haverhill, MA, USA) was used as a performance benchmark with an anode loading of 3 mg cm^{-2} hand sprayed on a gold coated Ti felt PTL. As for the cathode layer, commercial platinum supported on carbon (Pt/C, 60 wt% metal on support, Alfa Aesar, Haverhill, MA, USA) was used at a loading of 1 mg cm^{-2} hand sprayed onto a carbon paper PTL. To properly study the different electrolysis anodes, the cathode layer was identical for all

experiments. The benchmark electrode inks were prepared similarly to the Ni-based ones, however the %solids was set to 2 and the first step in the sonication sequence was done for 15 mins instead of 5. Furthermore, the resulting ionomer content in the electrode layers was 7 and 23 wt% for the Ir black benchmark anode and the Pt/C cathode, respectively.

6.2.3.2 AEMWE Performance Evaluation

6.2.3.2.1 Ionomer Optimization

To optimize the ionomer content in the monometallic Ni electrodes, the best three anodes in terms of mechanical stability, were tested in the electrolyser. The electrodes with 7, 15 and 25 wt% ionomer were chosen. The in-situ performance evaluation consisted of polarization experiments carried out using a BioLogic high current potentiostat/galvanostat (HCP-803, BioLogic Science Instruments, Seyssinet-Pariset, France) that was operated using a custom-made LabVIEW program. The polarization curves were carried out by stepping from 0 to 50 A (0 to 2 A cm^{-2}). To avoid equipment damage and maintain safe cell operation, the program was manually stopped when the measured voltage surpassed 2 V. Next, electrochemical impedance spectroscopy (EIS) measurements were carried out with the HCP-803 using the EC-Lab® software. EIS spectra were measured at a fixed direct current (DC) supply of 1, 5 and 18 A (0.04, 0.2 and 0.72 A cm^{-2}) with an alternating current (AC) supply of ± 5%DC, over a frequency range of 50 kHz down to 200 mHz. The current spectra obtained at 5 A are reported in this thesis. All experiments were carried out at 50 ± 2°C in 1 M KOH.

6.2.3.2.2 Ni-based Material Evaluation

Once the ionomer was optimized to 15 wt%, the performance of the $Ni_{90}Fe_{10}$, $Ni_{80}Fe_{20}$, $Ni_{90}Fe_{10}$/10 wt% CeO_2 and $Ni_{80}Fe_{20}$/10 wt% CeO_2 materials was evaluated. This was done by performing the experiments described in Section 6.2.3.2.1 in 1 M and 0.1 M KOH. When switching electrolytes, the system was washed by cycling 5 L of Milli-Q® water for 15 minutes. An identical experimental sequence was also performed using the Ir black benchmark anode. In addition to performing polarization and EIS measurements in both 1 M and 0.1 M KOH, preliminary electrode stability testing was carried out by fixing the cell current at 12.5 A (0.5 A cm^{-2}) for 12 hours. To observe any changes in cell resistances over time, EIS measurements were done at a DC of 12.5

A (0.5 A cm^{-2}) with an AC of ± 5%DC over a frequency range of 50 kHz down to 200 mHz after every hour during this constant current polarization.

6.3 Results and Discussion

6.3.1 Material Characterization

6.3.1.1 Nanoparticles

Figure 6.1 shows TEM images for $Ni_{90}Fe_{10}$ (Figure 6.1a), $Ni_{80}Fe_{20}$ (Figure 6.1b), $Ni_{90}Fe_{10}$/10 wt% CeO_2 (Figure 6.1c) and $Ni_{80}Fe_{20}$/10 wt% CeO_2 (Figure 6.1d). Overall, the NiFe particles are very small in size (estimated as 4-6 nm), however they are difficult to see because when taking TEM images, the particles agglomerate under the electron beam. While it can be hard to identify individual particles on the TEM images, in our previous work[26], we ran X-ray diffraction (XRD) on the particles, which shows broad diffraction peaks, which confirms the presence of nanostructures with nanocrystallites. In comparison to the $Ni_{90}Fe_{10}$ particles, the $Ni_{80}Fe_{20}$ particles show an additional flake-like phase. This flake-like phase could be due to the increased iron content or residues of the reactants or incomplete washing. As for the CeO_2-containing materials, both samples show that ceria is not well blended with the metallic content resulting in somewhat inhomogeneous samples. This can, however, be expected due to the large size of CeO_2 (15 - 30 nm) in comparison to the small nanoparticles, as well as the relatively small specific surface area of ceria (30 – 50 m^2 g^{-1}). More information on the characterization of these materials can be found in our other works[26,46].

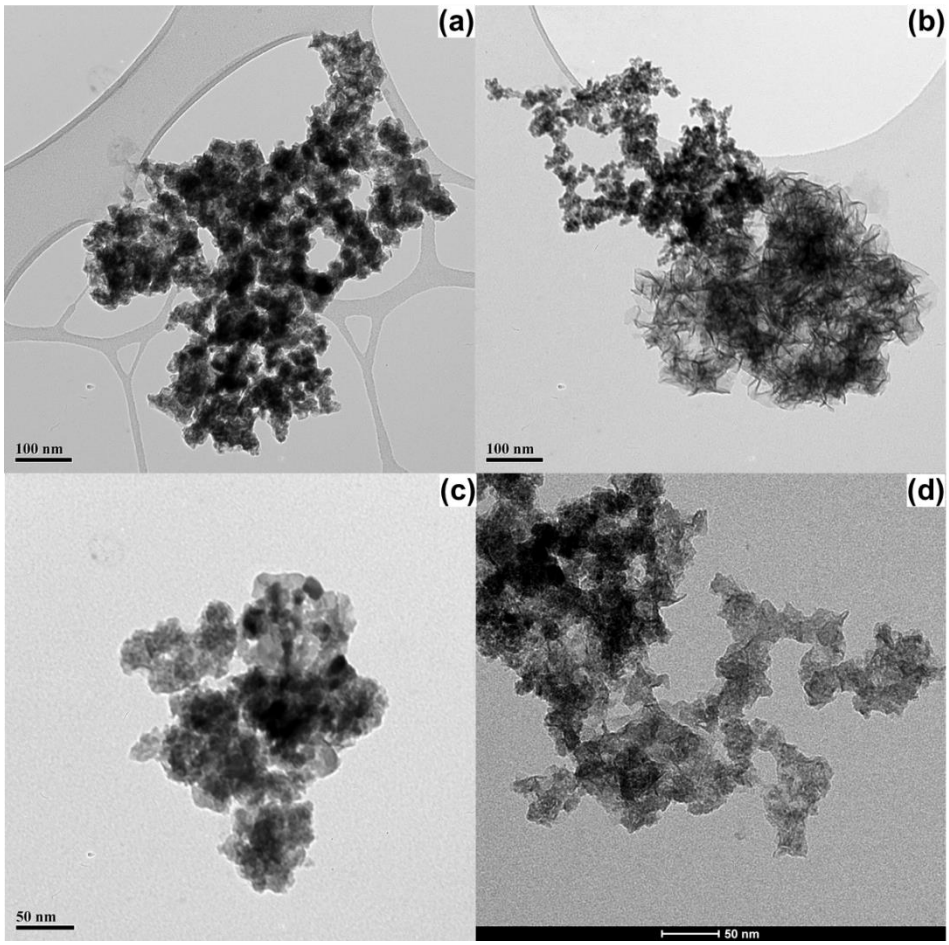

Figure 6.1: TEM image of (a) $Ni_{90}Fe_{10}$, (b) $Ni_{80}Fe_{20}$, (c) $Ni_{90}Fe_{10}$ / 10 wt% CeO_2 and (d) $Ni_{80}Fe_{20}$ / 10 wt% CeO_2 nanoparticles.

Figure E.4 in the SI shows the BJH adsorption pore size distribution by incremental volume (Figure E.4a) and by incremental area (Figure E.4b). Table 6.1 summarizes the key information for the BET and BJH analysis.

Table 6.1: Summary of BET and BJH analysis.

Material	**BET area [$m^2 g^{-1}$]**	**Ads pore D_{ave} [Å]**
Ni	91.16	122.64
$Ni_{90}Fe_{10}$	53.68	179.19
$Ni_{80}Fe_{20}$	158.10	94.21
$Ni_{90}Fe_{10}$/10 wt% CeO_2	112.74	138.36
$Ni_{80}Fe_{20}$/10 wt% CeO_2	220.76	91.62

The $Ni_{90}Fe_{10}$ particles show the smallest BET surface area of 53.68 m^2 g^{-1}. Overall, adding ceria increases the BET surface area of the sample, however, this increase is likely attributed to the presence of large ceria particles in the samples (15 – 30 nm with a specific surface area of 30 – 50 m^2 g^{-1}). While we have observed in our previous work[46] that ceria agglomerates separately from Ni and Fe, it is also possible that some NiFe NPs are dispersed on ceria, resulting in a higher specific area. As for the adsorption pore size, there is somewhat of an opposite trend. The $Ni_{90}Fe_{10}$ material has the largest pores, and the ceria containing materials show smaller pore sizes than their metallic equivalent.

6.3.1.2 Ni Catalyst Inks

Figure 6.2 shows the effect of ionomer content on the particle-size distribution measured for monometallic Ni catalyst inks containing 7, 15, 25, 35 and 45 wt% of the ionomer. The measurements were taken after 180 s of sonication. It should be noted that while there was a resting time between preparing the ink dispersions and measuring their PSDs, the measurements in Figure 6.2 are considered to be stable dispersions.

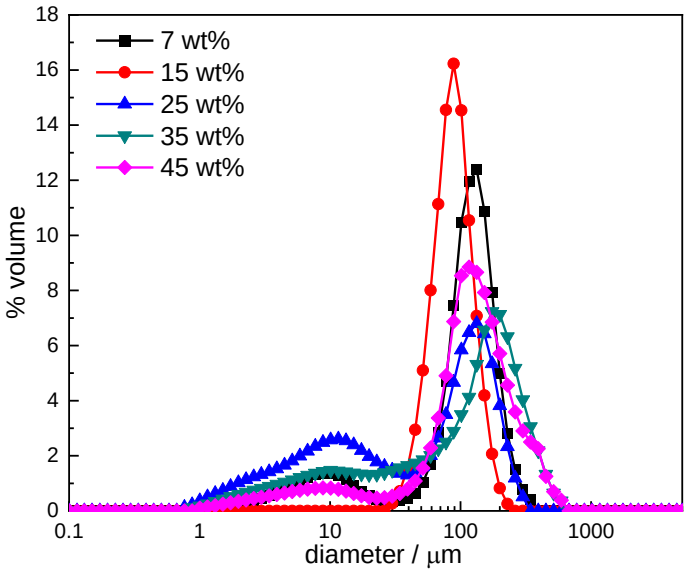

Figure 6.2: PSD measurements for Ni inks taken after 180 s of sonication for 7, 15, 25, 35 and 45 wt% ionomer.

The PSDs shown in Figure 6.2 are bimodal for the 7, 25, 35 and 45 wt% samples, showing particles, or rather agglomerates of particles, of around 10 and 100 μm. The 15 wt% sample on the other hand shows a unimodal distribution of particles or agglomerates of around 100 μm. This

effect could be due to the way the ionomer disperses itself throughout the catalyst ink when the required amount of ionomer to result in 15 wt% on the final electrode layer is used. The fact that the distribution of the 15 wt% electrode is more uniform may be beneficial for a more efficient electrode fabrication as agglomerates can result in clogging or spitting of the air brush when hand-spraying electrodes. It should be noted that the agglomerate size observed in the PSD measurements are representative of the nanoparticles in a catalyst ink containing an ionomer, and as such, will not necessarily correspond to the particle agglomerates observed in the TEM images of the materials. In this case, the agglomerates observed in the PSD measurements of the catalyst inks are larger than what is observed in the TEM images.

6.3.1.3 Ni Catalyst Coated Surfaces

Samples of the monometallic Ni catalyst coated membranes (CCM) with 7, 15, 25, 35 and 45 wt% ionomer were prepared and evaluated. Images of every CCM after being treated in KOH for 12 h are shown in Figure E.5 of the SI. From the images, the 7, 15 and 25 wt% (Figure E.5a, b and c, respectively) ionomer electrode surfaces maintain more or less their initial physical form during the ion exchange step, while the structure of the 35 and 45 wt% ionomer electrodes (Figure E.5d and e, respectively) have started to break down due to excessive swelling. We therefore consider that an ionomer content of 35 and above is too high for efficient cell operation. Although a higher ionomer content is favoured for improved transport of anions through the catalytic layer, too high of an ionomer content ultimately results in an overhydrated catalytic layer leading to its destruction. Note that initially, the CCM format was going to be used for electrolysis because it is known to be more advantageous due to a lower cell resistances[32], however when using high material loadings on the full 25 cm^2 membrane, the catalytic layer started to peel off once submerged in KOH. This effect can be seen in Figure E.6 of the SI. As such, AEMWE experiments were set up using the CCS format.

The physical impact of ionomer content on the catalytic layer morphology was observed with SEM. Representative SEM images of the 7, 15 and 25 wt% ionomer electrode surfaces are shown in Figure 6.3.

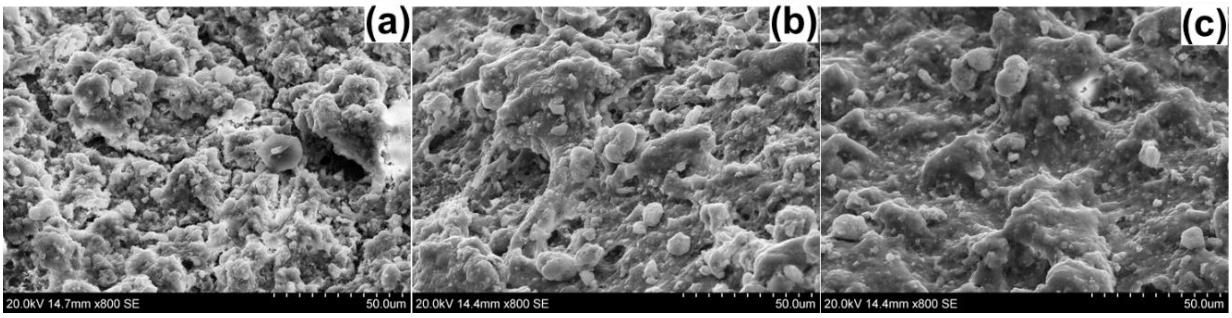

Figure 6.3: SEM images for (a) 7, (b) 15 and (c) 25 wt% ionomer electrode surfaces.

From inspection of the SEM images, it is possible to see that at lower ionomer concentrations such as the 7 wt% electrode (Figure 6.3a), the catalytic layer looks more textured and porous. When increasing the ionomer amount, the catalytic layer starts to have less texture and starts to show more agglomerates on its surface. Similar effects of the ionomer on the morphology of catalytic layers have recently been reported[30–34], where electrodes with lower ionomer loadings are less mechanically stable (more cracks) with more access to active sites, and electrodes with higher ionomer content show better mechanical stability with more particle coating and agglomerates. From the SEM images it is possible to say that there is a trade-off between catalytic layer texture and structure, where is more favourable to expose more active sites for oxygen evolution, while the other is more favourable from a durability perspective. However, to properly assess this potential trade-off, in-situ testing of all three electrodes was done and is presented and discussed in the next section.

6.3.2 In-situ Ionomer Optimization of the Monometallic Ni NPs

The ultimate test for the ionomer optimization is its electrochemical performance. Figure 6.4 shows IR-corrected polarization curves (Figure 6.4a) and impedance spectra (Figure 6.4b) for the 7, 15 and 25 wt% ionomer electrodes prepared using monometallic Ni NPs. The data before IR-correction can be seen in Figure E.7 of the SI. Table 6.2 summarizes key data extracted from Figure 6.4. The complex-impedance plane plots indicate that an equivalent circuit with at least two relaxations must be used to fit the data. The equivalent circuit should account for charge transfer, adsorption, and double layer capacitance in the porous catalytic layer, although no detailed interpretation is attempted here. After testing a few EIS models, the $LR_{EL}(Q_1R_1)(Q_2R_2)$ circuit is chosen, similar to the one used by Faid *et al.*[25] when studying the hydrogen evolution reaction in the same AEM electrolyser test station. The fitted data is provided so that the first Q_1R_1 parallel

represents the high frequency arc, commonly assigned to kinetics contributions at the electrodes, i.e charge transfer (R_{ct}) of both electrodes and a constant phase element that represents the electrode roughness. The second Q_2R_2 parallel represents the low-frequency arc and is commonly assigned to mass transfer and bubble formation [25,53,54]. The R_{EL} represents the uncompensated ohmic resistance, frequently referred to as the high frequency resistance (HFR) and estimated from the real axis approach at high frequency. Finally, the L term represents an inductor term and was added in series to better fit the high frequency data. It should be noted that parameters were only added to the equivalent circuits if it was statistically significant to do so, according to the F-ratio test method[55,56]. Supplementary data for the EIS models are reported in Table E.4 of the SI.

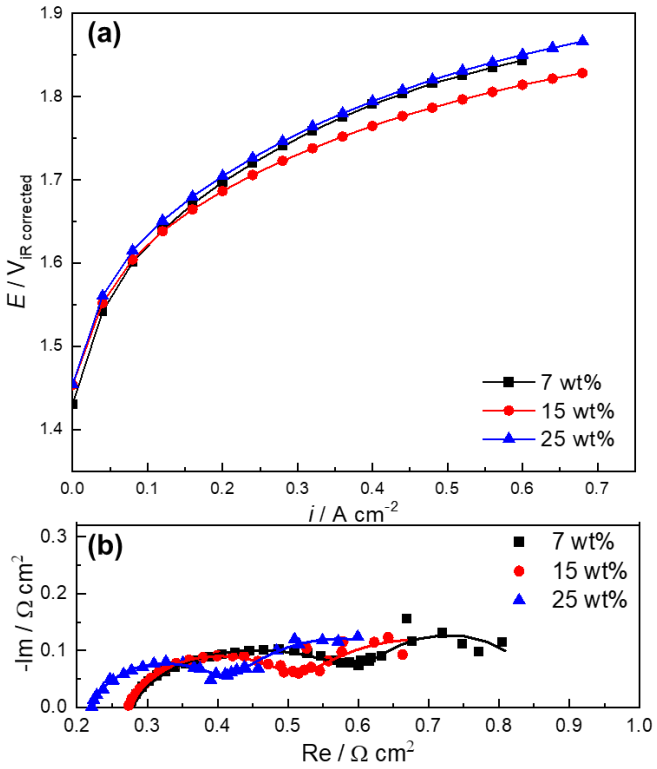

Figure 6.4: (a) Polarization curves and (b) EIS at 5 A for the monometallic Ni NPs, using 7, 15 and 25 wt% ionomer. Experiments were run at 50°C in 1 M KOH. In (b), the solid lines represent the EIS fit to the equivalent circuit.

Table 6.2: Summary of polarization and EIS data extracted from Figure 6.4 for different wt% ionomer.

Ni wt% ionomer	*E* at 0.4 A cm^{-2} [V]	Tafel Impedance [mV]	R_{EL} [mΩ cm^2]	R_1 [mΩ cm^2]	R_2 [mΩ cm^2]
7	1.791	64	254 ± 5	387 ± 19	221 ± 32
15	1.766	48	269 ± 4	354 ± 164	243 ± 29
25	1.793	37	213 ± 3	199 ± 20	338 ± 83

As shown in Figure 6.4a, the 15 wt% ionomer shows the best catalytic activity by showing a slightly smaller increase in cell potential with increasing current density. At 0.40 A cm^{-2}, it is 250 and 270 mV lower than the 7 and 25 wt% electrodes, respectively. The Ni NPs with 15 wt% ionomer show current densities of 0.280 and 0.538 A cm^{-2} at 1.8 V for the original and IR-corrected graphs, respectively. This is comparable to what others have found in literature where the ionomer content was optimized for the anode catalytic layer[31–34]. Interestingly, the observation that the ionomer content influences the Ni anode activity is opposite to what Faid *et al.*[36] found in their recent work covering the Fumatech fumion FAA-3 ionomer content optimization for a NiO anode and Ni/C cathode. Through both rotating disc electrode (RDE) measurements and in-situ half-cell AEMWE measurements, Faid *et al.*[36] found that the cathode layer was dependent on the ionomer content, showing an optimal of 10 wt% ionomer, while the anode layer did not show a significant change in activity with varying amounts of ionomer. It should be noted that prior to IR-correction, the 15 and 25 wt% electrodes perform similarly, however this is likely due to the 25 wt% electrode having a thicker catalytic layer, resulting in a more favourable contact between the catalyst layer and the membrane, as further discussed below. To properly factor out effects of cell compression, the IR-corrected polarization curves were used to identify the optimal amount of ionomer.

As for the impedance spectra in Figure 6.4b, for an increasing ionomer content, the first semicircle resistance (R_1) decreases. Park *et al.* [32] found a similar change in charge transfer resistance with increasing ionomer content, and attributed this effect to the increased size of secondary pores. The second semicircle resistance (R_2) increases with increasing ionomer content, which could be attributed to large quantities of ionomer inhibiting mass transport. The 25 wt% ionomer shows a noticeably lower ohmic resistance (R_{EL}) than the 7 and 15 wt% electrodes. Interestingly, a lower ohmic resistance for the 25 wt% ionomer electrode was observed despite a

thicker catalyst layer. This is in line with the observed reduced ohmic resistance that Faid *et al.*[25] observed when employing a NiMo/C catalyst instead of a Pt/C catalyst for the hydrogen evolution reaction in the same set-up using 1 M KOH. In addition to the electrolyte resistance, constriction or contact resistances, ohmic resistance in pores and pore distribution, as well as uneven reaction distribution will contribute to the impedance spectra and impact the measured high frequency resistance. Furthermore, Tafel impedances were extracted from the impedance measurements as the diameter of the impedance arc, assuming only kinetic contributions (i.e. subtracting the ohmic resistance from the impedance spectra and multiplying it with the steady state current [57,58]). This showed that the 25 wt% sample led to the lowest Tafel slope of 37 mV. The validity of the Tafel impedance calculations may however be questioned as the low frequency tail observed, likely due to bubble formation or mass transport[53], was not taken into account.

After AEMWE testing was completed, the cells were opened and the anode catalytic layer residue on the membrane (anode catalytic layer that broke off the carbon paper) was observed. This is shown in Figure 6.5 for all 3 samples. From the images, it is possible to observe that the 15 wt% ionomer layer (Figure 6.5b) lost the least amount of material. The 7 wt% layer (Figure 6.5a) did not have enough ionomer to bind the catalytic layer, causing it to detach when the parallel flow field was pressed into it, and the 25 wt% layer (Figure 6.5c) was over hydrated during electrolysis causing the catalytic layer to partially disintegrate. In other words, the 15 wt% ionomer electrode was the only one that had: (i) enough ionomer to keep all the particles adhered to the GDL, despite the imposed shear stress, which causes the particles to be forced off the catalytic layer, and (ii) not too much ionomer to cause excessive swelling and thus loss of the catalytic layer structure. The effects of swelling with increased ionomer content are also apparent on the MEAs that were made, then exchanged in 1 M KOH in Figure E.5 of the SI. As such, although the 15 and 25 wt% ionomer electrodes both showed good performance, the 15 wt% showed a better adhesion of the catalytic layer and was therefore chosen as the optimal ionomer content for the Ni-based materials. It is important to note that observing the state of the anode GDL post-testing is only a preliminary indicator of the efficiency of catalytic layer under operating conditions. Running electrolysis for thousands of hours under various conditions would be required to truly put the mechanical durability of an electrode to the test.

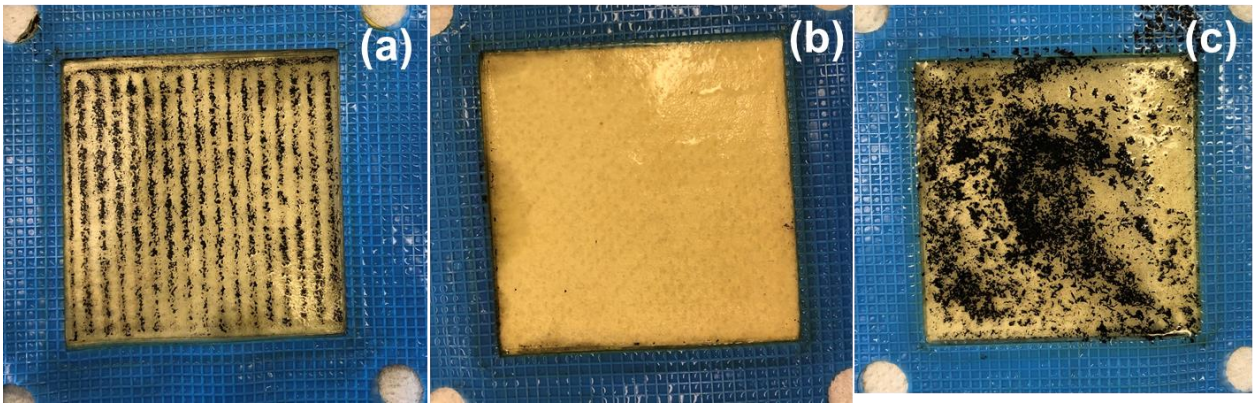

Figure 6.5: Anode catalytic residue on the AEM after electrolysis for (a) 7, (b) 15 and (c) 25 wt% ionomer.

6.3.3 AEMWE Performance Evaluation of the Ni-based NPs

6.3.3.1 Polarization Curves and Electrochemical Impedance

Once the ionomer content for the Ni electrodes was optimized, the 15 wt% ionomer content was used when fabricating the anodes for the $Ni_{90}Fe_{10}$, $Ni_{80}Fe_{20}$, $Ni_{90}Fe_{10}$/10 wt% CeO_2 and $Ni_{80}Fe_{20}$/10 wt% CeO_2 catalysts. Figure 6.6 shows polarization curves (Figure 6.6a, b) and EIS measurements (Figure 6.6c, d) for all the mentioned Ni-based materials in addition to the Ir black benchmark catalyst in 1 (Figure 6.6a, c) and 0.1 (Figure 6.6b, d) M KOH. Tables 6.3 and 6.4 summarize key information extracted from the plots in Figure 6.6 in 1 and 0.1 M KOH, respectively. To see polarization curves without IR-correction, see Figure E.8 in the SI. The EIS data for the materials tested in 1 and 0.1 M KOH were analyzed using a similar equivalent circuit as the ionomer optimization study. Here however, it was not always statistically significant to use a more complex circuit, such as the $LR_{EL}(Q_1R_1)(Q_2R_2)$ model described above. In some cases, the circuit was not improved by adding the inductor term, L, and in other cases, a simple $R_{EL}(QR_P)$ circuit best fit the experimental data. In the latter case, the polarization resistance R_P would represent both the previous R_1 and R_2. For data of the best fitted EIS models in 1 and 0.1 M KOH, see Tables E.5 and E.6, respectively, in the SI.

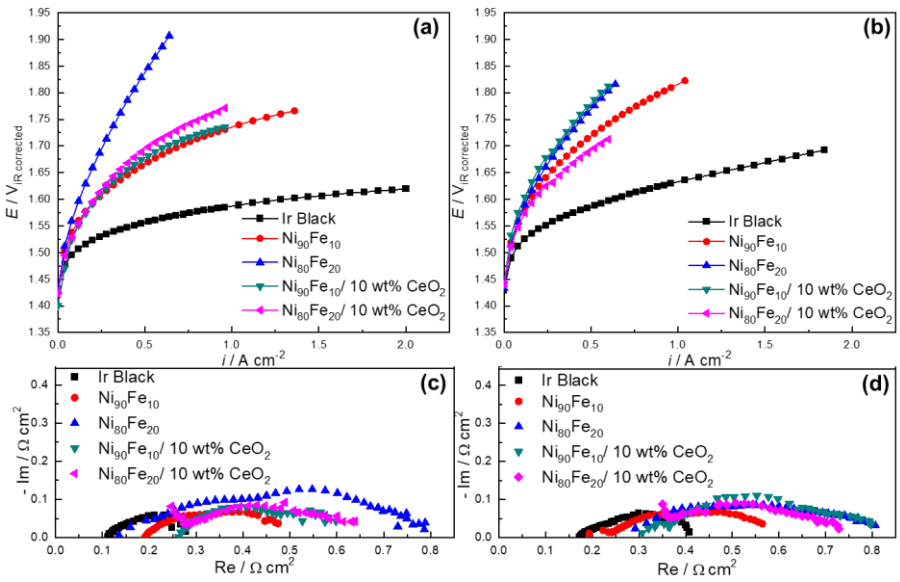

Figure 6.6: Polarization curves (a, b) and electrochemical impedance spectroscopy run at 5 A (c, d) run in 1 (a, c) and 0.1 (b, d) M KOH at 50°C.

Table 6.3: Summary of in-situ performance in 1 M KOH extracted from Figure 6.6a and c.

Material	***E* at 0.4 A cm^{-2} [V]**	***E* at 0.8 A cm^{-2} [V]**	**Tafel Impedance [mV]**	**R_{EL} [mΩ cm^2]**
Ir Black	1.547	1.578	34	109 ± 1
$Ni_{90}Fe_{10}$	1.645	1.717	63	170 ± 3
$Ni_{80}Fe_{20}$	1.785	N/A	131	130 ± 10*
$Ni_{90}Fe_{10}$/10 wt% CeO_2	1.655	1.723	70	250 ± 3
$Ni_{80}Fe_{20}$/10 wt% CeO_2	1.688	1.751	73	232 ± 6

*It should be noted that this value may be misrepresenting the actual R_{EL} of the system because the impedance of this sample in the high frequency region is not ideal. See the SI for more details.

Table 6.4: Summary of in-situ performance in 0.1 M KOH extracted from Figure 6.6b and d.

Material	*E* at 0.4 A cm^{-2} [V]	*E* at 0.8 A cm^{-2} [V]	Tafel Impedance [mV]	R_{EL} [mΩ cm^2]
Ir Black	1.577	1.617	47	158 ± 12
$Ni_{90}Fe_{10}$	1.692	1.782	70	220 ± 2
$Ni_{80}Fe_{20}$	1.732	N/A	108	144 ± 32*
$Ni_{90}Fe_{10}$/10 wt% CeO_2	1.743	N/A	102	314 ± 9
$Ni_{80}Fe_{20}$/10 wt% CeO_2	1.666	N/A	74	338 ± 5

*It should be noted that this value may be misrepresenting the actual R_{EL} of the system because the impedance of this sample in the high frequency region is not ideal.

In 1 M KOH, Ir black is the best performing electrode showing voltages of around 1.58 at 0.8 A cm^{-2}. This is closely followed by $Ni_{90}Fe_{10}$ showing a cell voltage of 1.72 V at that same current. The ceria containing materials are not too far behind the $Ni_{90}Fe_{10}$ performance, where the $Ni_{90}Fe_{10}$/10 wt% CeO_2 electrode outperforms the $Ni_{80}Fe_{20}$/10 wt% CeO_2. The $Ni_{80}Fe_{20}$ is the least performing catalyst, which is unexpected considering it shows better three-electrode cell OER performance than all other Ni-based materials in this study[46]. It is however important to note that although a catalyst presents high activity in a three-electrode cell, it will not necessarily show high performance in an electrolyser, as discussed in the works of Xu *et al.*[18]. Additionally, it is known that iron is not stable at the anode in electrolyser systems[59], therefore it is possible that here, the stability of the $Ni_{80}Fe_{20}$ electrode is lower due to its higher iron content.

In the EIS data shown in Figure 6.6c, the lowest ohmic resistance of around 109 mΩ cm^2 was found for the Ir electrode, with the $Ni_{80}Fe_{20}$ electrode showing the next the lowest ohmic resistance of around 130 mΩ cm^2. Overall, the samples containing 20 at% Fe show lower electrolyte resistances than their 10 at% Fe equivalents. Additionally, while we have dramatically reduced the ceria content from 50 to 10 wt% following our previous AEMWE study[26], the ceria containing samples still show higher R_{EL} values than their metallic equivalent. This result is in agreement with our recent detailed ex-situ study on the effects of CeO_2 on the OER performance of NiFe nanoparticles[46], where we find that while CeO_2 can be beneficial to electrochemical performance, it also introduces additional ohmic resistances to the catalyst, which can lower its overall catalytic activity. It is important to note that while poor conductivity and constriction resistance between electrical and ionic conductors, as well as electrolyte solution resistance can

affect the R_{EL}, the observed changes in R_{EL} with different catalyst materials are likely more importantly related to changes in the resistance of the electrolyte solution within the system.

In terms of the charge transfer resistance shown in Figure 6.6c, Ir black has the lowest resistance of 132 mΩ cm^2, followed by $Ni_{90}Fe_{10}$/ 10 wt% CeO_2, which has a resistance of around 242 mΩ cm^2. Overall, the 10 at% iron samples show lower observed polarization resistances than their 20 at% Fe equivalents. When preparing the CCS of the materials containing 20 at% iron, the material was readily oxidizing. This effect, in combination with the aforementioned possible low stability of Fe in the $Ni_{80}Fe_{20}$ catalyst, could be negatively affecting AEMWE performance and the observed polarization resistance. The low relative activity of the $Ni_{80}Fe_{20}$ electrode is reflected in its extremely high charge transfer resistance of 774 mΩ cm^2. The $Ni_{80}Fe_{20}$ electrode also shows a Tafel impedance value of 131 mV, 58 mV higher than any other electrode. With respects to the ceria-containing materials, they each show lower observed polarization resistances than their metallic equivalents, possibly due to electronic effects that ceria has on NiFe. This result is in accordance with our previous work[26], showing that ceria has beneficial effects on the charge transfer of the process.

In 0.1 M KOH, the iridium electrode still shows the best performance in terms of lowest reaction overpotential and low cell resistances. Aside from Ir, the only other material to reach 0.8 A cm^{-2} was $Ni_{90}Fe_{10}$, which shows a cell voltage of 1.78 V at that current, which is 165 mV higher than what was obtained for Ir. Interestingly, in 0.1 M KOH, the $Ni_{80}Fe_{20}$/10 wt% CeO_2 electrode shows the best performance of all Ni-based materials, showing a cell voltage of 1.67 V at 0.4 A cm^{-2} after IR-correction. It also shows a low charge transfer resistance in comparison to $Ni_{80}Fe_{20}$ and $Ni_{90}Fe_{10}$/ 10 wt% CeO_2. Reasons for the change in relative behaviour of the $Ni_{80}Fe_{20}$/ 10 wt% ceria electrode with pH, could be related to ceria's oxygen storage capacity and reducibility, which may favourably affect the local pH in the vicinity of the electrode, improving electrochemical activity. While this effect is likely also present in the $Ni_{90}Fe_{10}$/ 10 wt% CeO_2, it is possible that having more Fe in comparison to Ni in the $Ni_{80}Fe_{20}$/ 10 wt% CeO_2 material, alters the properties of the catalyst to further boost the surface oxygen ion (O^{2-}) conductivity of ceria, making it outperform $Ni_{90}Fe_{10}$/ 10 wt% CeO_2 in 0.1 M KOH. It should be noted that prior to IR-correction, $Ni_{90}Fe_{10}$ was the best performing Ni-based electrode, followed by the $Ni_{80}Fe_{20}$/ 10% CeO_2. This is illustrated in Figure E.8.

Overall, the $Ni_{90}Fe_{10}$ electrode is the best Ni-based AEMWE anode, however, when analyzing the IR-corrected data in 0.1 M KOH, the $Ni_{80}Fe_{20}$/10 wt% CeO_2 outperforms $Ni_{90}Fe_{10}$. Recalling the results of the BET measurements of the respective catalyst powders, the $Ni_{90}Fe_{10}$ has a low BET area but a high average pore size, while the $Ni_{80}Fe_{20}$/10 wt% CeO_2 has a high BET area with a low average pore size. It could therefore be said that at the higher electrolyte concentrations, it is more important to have larger pores to allow for better mass and ion transport through the catalytic layer, while at lower concentrations, it is more important to have a higher area to expose more active sites. It would of course be ideal to combine having a large average pore size with a high BET area to expose the most active sites, while allowing for optimal ion and mass transport through the catalytic layer.

Overall, although a direct comparison cannot be made due to many different cell variables, it is possible to say that these results are comparable to what has previously been reported in literature[7,32,60–63]. Based on the above results in both 1 and 0.1 M KOH, it is not evident whether incorporating ceria into the catalyst helps very much with performance. The ceria-containing materials have a larger high frequency resistance, which makes their IR-corrected catalytic performance more comparable to the other catalysts. When looking at the actual electrode loadings reported in Table E.1 of the SI, both the $Ni_{90}Fe_{10}$/10 wt%CeO_2 and $Ni_{80}Fe_{20}$/10 wt% CeO_2 materials have a lower loading than their metallic counterpart. It could therefore be possible that the lower performance of those materials was due to the lower resulting anode loadings. Interestingly, in most cases, the addition of CeO_2 to the $Ni_{90}Fe_{10}$ and $Ni_{80}Fe_{20}$ materials results in a lower charge transfer resistance indicating more favourable kinetics.

6.3.3.2 Electrode Stability

Many authors[11,18,31,64–67] have done durability investigations of their systems for times ranging from hours to days of operation. In this study, preliminary durability measurements were performed over 12 h on the Ni-based catalysts to see how well their performance holds over time in an AEMWE setup. This can be seen in Figure 6.7 with key information of that plot presented in Table 6.5.

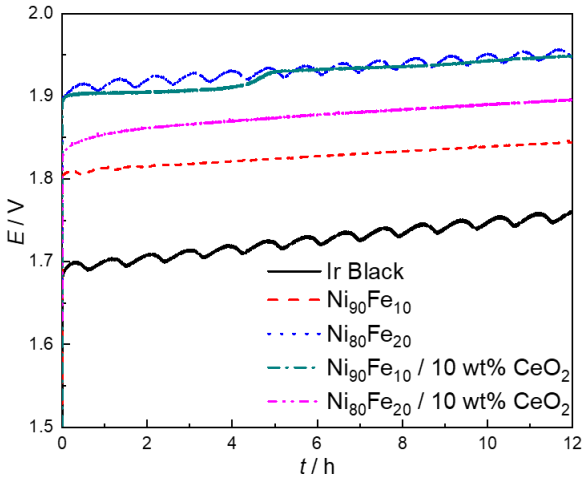

Figure 6.7: Chronopotentiometry (CP) experiments at 0.5 A cm^{-2} in 0.1 M KOH at 50°C. Catalysts: Ir black, $Ni_{90}Fe_{10}$, $Ni_{80}Fe_{20}$, $Ni_{90}Fe_{10}$/ 10 wt% CeO_2 and $Ni_{80}Fe_{20}$/ 10 wt% CeO_2.

Table 6.5: Summary of in-situ stability performance evaluation in 0.1 M KOH extracted from Figures 6.7 and 6.8.

Material	**ΔE [mV]**	**Degradation Rate [mV h^{-1}]**	**ΔTafel Impedance [mV]**
Ir Black	67	5.6	16
$Ni_{90}Fe_{10}$	40	3.3	3
$Ni_{80}Fe_{20}$	47	3.9	5
$Ni_{90}Fe_{10}$/10 wt% CeO_2	52	4.3	4
$Ni_{80}Fe_{20}$/10 wt% CeO_2	62	5.2	3

In addition to the long-term polarization, an EIS spectrum was taken every hour during the 12 hour polarization experiment. Figure 6.8 shows the spectrum taken at the 1st, 6th and 12th hour for every material. The change in Tafel impedance over 12 hours is reported in Table 6.5. To see the EIS spectra taken every hour, see Figure E.9 in the SI. See Table E.7 of the SI for the best fitted EIS models for the spectra shown in Figure 6.8 at hours 1 and 12.

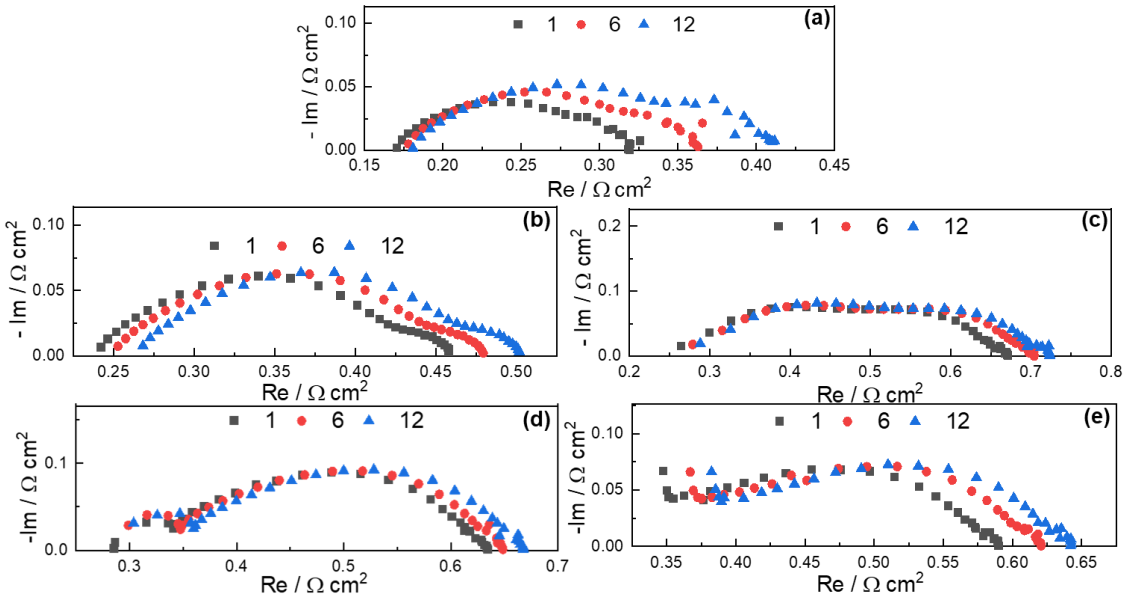

Figure 6.8: Electrochemical impedance spectroscopy of (a) Ir black, (b) $Ni_{90}Fe_{10}$, (c) $Ni_{80}Fe_{20}$, (d) $Ni_{90}Fe_{10}$/10 wt% CeO_2 and (e) $Ni_{80}Fe_{20}$/10 wt% CeO_2 taken at the 1st, 6th and 12th hour of polarization.

As shown in Figure 6.7, the best performing material in terms of lowest cell potential is Ir black, which is followed by $Ni_{90}Fe_{10}$ and then $Ni_{80}Fe_{20}$/10 wt% CeO_2. This is as expected following the results of the polarization experiments presented above. As shown in Table 6.5, although the Ir benchmark shows the lowest current, its change in potential over the 12 hours is higher than all Ni-based materials, likely due to its low stability in an alkaline environment[68]. Based on the calculated degradation rate, it could be possible that over a longer period, the Ni-based electrodes would outperform Ir black. Overall, the materials containing 10 at% iron are more stable that their 20 at% iron equivalents, where the most stable Ni-based material is the $Ni_{90}Fe_{10}$ catalyst showing a change in voltage of 40 mV over 12 hours or a degradation rate of 3.3 mV h^{-1}. It should be noted that a degradation rate of 3.3 mV h^{-1} is not practical for commercial scale operation. An example of an AEMWE that shows a more commercially stable performance is presented in the works of Motealleh *et al.*[67], where they run electrolysis testing for 10 000 h at 1 A/cm^2. Their cell, constructed using a Sustainion® membrane, a commercial $NiFe_2O_4$ anode and a commercial modified Raney Ni cathode, can hold around 1.85 V over 10 000 h at 60°C in 1 M KOH, showing a degradation rate of less than 1 µV h^{-1}. It should however be noted that in their work, a different AEMWE unit was used with different system components, including catalysts and membranes/ionomers, all of which could affect the overall stability of the system. Finally,

incorporating ceria into the $Ni_{90}Fe_{10}$ and $Ni_{80}Fe_{20}$ catalysts did not help the catalysts' overall stability as both materials with ceria showed higher degradation rates than their respective metallic counterpart. These stability results are all in accordance with the results found in our three-electrode study for the NiFe materials with and without 10 wt% ceria[46].

The observed positive degradation rate of the NiFe materials without ceria shown in Figure 6.7 could be due to iron dissolution under applied currents[59] and could be more important for the samples with 20 at% Fe. As for the materials containing ceria, a possible reason for this decrease in stability over time could be the phase segregation of a redox inactive CeO_2 phase[38,69,70], however a more detailed investigation into the interactions of Ni, Fe and CeO_2 under constant applied current would need to be done to know for sure. Additionally, while short term durability testing can be informative, running longer durability experiments (over thousands of hours) would be required to know whether the voltage drift observed in Figure 6.7 is maintained over time.

When analyzing the EIS data in Figure 6.8, all materials have an increase in the ohmic resistance over time. Furthermore, contrary to the ceria containing materials, the Ir black, $Ni_{90}Fe_{10}$ and $Ni_{80}Fe_{20}$ cells seem to have a more prominent second semicircle with time. This could mean that incorporating ceria into the catalysts helps with the transport of water to the surface and the bubble release from the surface allowing for more consistent mass transfer overtime, all while maintaining the integrity of the pores in the catalytic layer. The Ir black electrode also shows the largest increase in observed polarization resistance over time, possibly related to its higher degradation rate in comparison to the Ni-based materials.

6.4 Conclusions

In this work, we have determined the optimal amount of commercial Fumatech anionic ionomer content to be 15 wt% in $Ni_{90}Fe_{10}$ and $Ni_{80}Fe_{20}$ NPs, both with and without 10% CeO_2 catalysts for the oxygen evolution reaction in anion exchange membrane water electrolysis (AEMWE). The optimization was based on particle size distribution measurements of the catalyst inks, scanning electron microscopy images of the prepared electrode surfaces and electrochemical performance in an operating AEMWE single cell. 15 wt% ionomer provided the highest activity, while showing the best adhesion of the catalyst particles within the catalytic layer. The $Ni_{90}Fe_{10}$ and $Ni_{80}Fe_{20}$ NPs with and without 10% CeO_2 catalysts were evaluated using the optimal 15 wt%

ionomer. $Ni_{90}Fe_{10}$ is found to be the best-performing non-noble metal catalyst, showing 1.72 V at 0.8 A cm^{-2} in 1 M KOH after IR-correction. However, in 0.1 M KOH the $Ni_{80}Fe_{20}$/10 wt% CeO_2 catalyst obtained a higher activity than $Ni_{90}Fe_{10}$, achieving an IR-corrected cell voltage of 1.67 V at 0.4 A cm^{-2}. This increase in relative activity of the $Ni_{80}Fe_{20}$/ 10 wt% CeO_2 electrode at lower pH, could be due to ceria's oxygen storage capacity and reducibility. Based on the calculated degradation rates during stability measurements, it is likely that the Ni-based electrodes, particularly the $Ni_{90}Fe_{10}$ electrode, will outperform Ir black when operated over an extended period. Upon measuring electrochemical impedance over the course of the durability experiments, it was observed that incorporating ceria into electrodes may assist mass transport within the catalytic layer over time perhaps by maintaining the porous structure of the catalytic layer.

Acknowledgements

This research was conducted as part of the Engineered Nickel Catalysts for Electrochemical Clean Energy project administered from Queen's University and supported by Grant number RGPNM 477963-2015 under the Natural Sciences and Engineering Research Council of Canada (NSERC) Discovery Frontiers Program. This work was also carried out within the HAPEEL project "Hydrogen Production by Alkaline Polymer Electrolyte Electrolysis," financially supported by the Research Council of Norway-ENERGIX program, contract number 268019. Additionally, the Research Council of Norway is acknowledged for the support to the Norwegian Fuel cell and Hydrogen Centre and the INTPART project 261620. Finally, funding was also provided by NSERC's Alexander Graham Bell Canada Graduate Scholarship – Doctoral (CGS D).

References

[1] D. M. F. Santos, C. A. C. Sequeira, *Quim. Nova* **2013**, *36*, 1176.

[2] M. Carmo, D. L. Fritz, J. Mergel, D. Stolten, *Int. J. Hydrogen Energy* **2013**, *38*, 4901.

[3] K. Zeng, D. Zhang, *Prog. Energy Combust. Sci.* **2010**, *36*, 307.

[4] J. Turner, G. Sverdrup, M. K. Mann, P.-C. Maness, B. Kroposki, M. Ghirardi, R. J. Evans, D. Blake, *Int. J. energy Res.* **2008**, *32*, 379.

[5] M. David, C. Ocampo-martínez, R. Sánchez-peña, *J. Energy Storage* **2019**, *23*, 392.

[6] R. Phillips, A. Edwards, B. Rome, D. R. Jones, C. W. Dunnill, *Int. J. Hydrogen Energy* **2017**, *42*, 23986.

[7] Y. Leng, G. Chen, A. J. Mendoza, T. B. Tighe, M. A. Hickner, C.-Y. Wang, *J. Am. Chem. Soc.* **2012**, *134*, 9054.

[8] M. M. Rashid, M. K. Al Mesfer, H. Naseem, M. Danish, *Int. J. Eng. Adv. Technol.* **2015**, *4*, 80.

[9] M. Bodner, A. Hofer, V. Hacker, *Wiley Interdiscip. Rev. Energy Environ.* **2015**, *4*, 365.

[10] D. Pletcher, X. Li, *Int. J. Hydrogen Energy* **2011**, *36*, 15089.

[11] S. Marini, P. Salvi, P. Nelli, R. Pesenti, M. Villa, M. Berrettoni, G. Zangari, Y. Kiros, *Electrochim. Acta* **2012**, *82*, 384.

[12] I. Vincent, D. Bessarabov, *Renew. Sustain. Energy Rev.* **2018**, *81*, 1690.

[13] M. K. Cho, A. Lim, S. Y. Lee, H. Kim, S. J. Yoo, Y. Sung, H. S. Park, J. H. Jang, *J. Electrochem. Sci. Technol.* **2017**, *8*, 183.

[14] R. Phillips, C. W. Dunnill, *RSC Adv.* **2016**, *6*, 100643.

[15] H. A. Miller, K. Bouzek, J. Hnat, S. Loos, C. I. Bernäcker, T. Weißgärber, L. Röntzsch, J. Meier-Haack, *Sustain. Energy Fuels* **2020**, *4*, 2114.

[16] D. Henkensmeier, M. Najibah, C. Harms, J. Žitka, J. Hnát, K. Bouzek, *J. Electrochem. Energy Convers. Storage* **2021**, *18*, 024001.

[17] M. E. G. Lyons, R. L. Doyle, M. P. Browne, I. J. Godwin, A. A. S. Rovetta, *Curr. Opin. Electrochem.* **2017**, *1*, 40.

[18] D. Xu, M. B. Stevens, M. R. Cosby, S. Z. Oener, A. M. Smith, L. J. Enman, K. E. Ayers, C. B. Capuano, J. N. Renner, N. Danilovic, Y. Li, H. Wang, Q. Zhang, S. W. Boettcher, *ACS Catal.* **2019**, *9*, 7.

[19] P. Du, R. Eisenberg, *Energy Environ. Sci.* **2012**, *5*, 6012.

[20] M. Tahir, L. Pan, F. Idrees, X. Zhang, L. Wang, J. J. Zou, Z. L. Wang, *Nano Energy* **2017**, *37*, 136.

[21] F. Safizadeh, E. Ghali, G. Houlachi, *Int. J. Hydrogen Energy* **2015**, *40*, 256.

[22] M. Gong, H. Dai, *Nano Res.* **2015**, *8*, 23.

[23] M. Gong, D. Y. Wang, C. C. Chen, B. J. Hwang, H. Dai, *Nano Res.* **2016**, *9*, 28.

[24] M. Schalenbach, O. Kasian, K. J. J. Mayrhofer, *Int. J. Hydrogen Energy* **2018**, *43*, 11932.

[25] A. Faid, A. Oyarce Barnett, F. Seland, S. Sunde, *Catalysts* **2018**, *8*, 614.

[26] E. Cossar, A. O. Barnett, F. Seland, E. A. Baranova, *Catalysts* **2019**, *9*, 814.

[27] J. H. Kim, J. N. Lee, C. Y. Yoo, K. B. Lee, W. M. Lee, *Int. J. Hydrogen Energy* **2015**, *40*, 10720.

[28] Z. Chen, C. X. Kronawitter, X. Yang, Y. W. Yeh, N. Yao, B. E. Koel, *Phys. Chem. Chem. Phys.* **2017**, *19*, 31545.

[29] J. R. Varcoe, P. Atanassov, D. R. Dekel, A. M. Herring, M. A. Hickner, P. A. Kohl, A. R. Kucernak, W. E. Mustain, K. Nijmeijer, K. Scott, T. Xu, L. Zhuang, *Energy Environ. Sci.* **2014**, *7*, 3135.

[30] G.-F. Li, D. Yang, P. Y. A. Chuang, *ACS Catal.* **2018**, *8*, 11688.

[31] I. Vincent, A. Kruger, D. Bessarabov, *Int. J. Hydrogen Energy* **2017**, *42*, 10752.

[32] J. E. Park, S. Y. Kang, S. H. Oh, J. K. Kim, M. S. Lim, C. Y. Ahn, Y. H. Cho, Y. E. Sung, *Electrochim. Acta* **2019**, *295*, 99.

[33] M. K. Cho, H. Park, S. Choe, S. J. Yoo, J. Y. Kim, H.-J. Kim, D. Henkensmeier, S. Y. Lee, Y. Sung, H. S. Park, J. Hyun Jang, *J. Power Sources* **2017**, *347*, 283.

[34] M. K. Cho, H. Y. Park, H. J. Lee, H. J. Kim, A. Lim, D. Henkensmeier, S. J. Yoo, J. Y. Kim, S. Y. Lee, H. S. Park, J. H. Jang, *J. Power Sources* **2018**, *382*, 22.

[35] T. W. Koo, C. S. Park, Y. Do Kim, D. Lee, S. Park, J. H. Lee, S. M. Choi, C. Y. Choi, *J. Korean Phys. Soc.* **2015**, *67*, 1558.

[36] A. Y. Faid, L. Xie, A. O. Barnett, F. Seland, D. Kirk, S. Sunde, *Int. J. Hydrogen Energy* **2020**, *45*, 28272.

[37] M. K. Bates, Q. Jia, N. Ramaswamy, R. J. Allen, S. Mukerjee, *J. Phys. Chem. C* **2015**, *119*, 5467.

[38] L. J. Enman, M. S. Burke, A. S. Batchellor, S. W. Boettcher, *ACS Catal.* **2016**, *6*, 2416.

[39] C. C. L. McCrory, S. Jung, J. C. Peters, T. F. Jaramillo, *J. Am. Chem. Soc.* **2013**, *135*, 16977.

[40] S. Lee, L. Bai, X. Hu, *Angew. Chemie - Int. Ed.* **2020**, *59*, 8072.

[41] L. Trotochaud, J. K. Ranney, K. N. Williams, S. W. Boettcher, *J. Am. Chem. Soc.* **2012**, *134*, 17253.

[42] M. B. Stevens, C. D. M. Trang, L. J. Enman, J. Deng, S. W. Boettcher, *J. Am. Chem. Soc.* **2017**, *139*, 11361.

[43] D. Friebel, M. W. Louie, M. Bajdich, K. E. Sanwald, Y. Cai, A. M. Wise, M. Cheng, D. Sokaras, T. Weng, R. Alonso-mori, R. C. Davis, J. R. Bargar, J. K. Nørskov, A. Nilsson, A. T. Bell, *J. Am. Chem. Soc.* **2015**, *137*, 1305.

[44] J.-X. Feng, S.-H. Ye, H. Xu, Y.-X. Tong, G.-R. Li, *Adv. Mater.* **2016**, *28*, 4698.

[45] J. A. Haber, Y. Cai, S. Jung, C. Xiang, S. Mitrovic, J. Jin, A. T. Bell, J. M. Gregoire, *Energy Environ. Sci.* **2014**, *7*, 682.

[46] E. Cossar, K. Agarwal, V. B. Nguyen, R. Safari, G. A. Botton, E. A. Baranova, *Electrocatalysis* **2021**.

[47] V. N. Kuleshov, N. V Kuleshov, S. A. Grigoriev, E. Y. Udris, P. Millet, A. S. Grigoriev,

Int. J. Hydrogen Energy **2016**, *41*, 36.

[48] J. Xiao, A. M. Oliveira, L. Wang, Y. Zhao, T. Wang, J. Wang, B. P. Setzler, Y. Yan, *ACS Catal.* **2021**, *11*, 264.

[49] H. Ito, N. Kawaguchi, S. Someya, T. Munakata, N. Miyazaki, M. Ishida, A. Nakano, *Int. J. Hydrogen Energy* **2018**, *43*, 17030.

[50] H. Ito, N. Miyazaki, S. Sugiyama, M. Ishida, Y. Nakamura, S. Iwasaki, Y. Hasegawa, A. Nakano, *J. Appl. Electrochem.* **2018**, *48*, 305.

[51] A. Y. Faid, A. O. Barnett, F. Seland, S. Sunde, *ACS Appl. Energy Mater.* **2021**, *4*, 3327.

[52] S. Ghoshal, B. S. Pivovar, S. M. Alia, *J. Power Sources* **2021**, *488*, 229433.

[53] I. Dedigama, P. Angeli, K. Ayers, J. B. Robinson, P. R. Shearing, D. Tsaoulidis, D. J. L. Brett, *Int. J. Hydrogen Energy* **2014**, *39*, 4468.

[54] S. Siracusano, S. Trocino, N. Briguglio, V. Baglio, A. S. Aric, *Materials (Basel).* **2018**, *11*, 1368.

[55] F. Seland, R. Tunold, D. A. Harrington, *Electrochim. Acta* **2006**, *51*, 3827.

[56] P. Bevington, "Data reduction and error analysis for the physical sciences," McGraw-Hill, New York **1969**, p. 200.

[57] F. Jaouen, G. Lindbergh, G. Sundholm, *J. Electrochem. Soc.* **2002**, *149*, A437.

[58] F. Jaouen, G. Lindbergh, *J. Electrochem. Soc.* **2003**, *150*, A1699.

[59] F. D. Speck, K. E. Dettelbach, R. S. Sherbo, D. A. Salvatore, A. Huang, C. P. Berlinguette, *Chem* **2017**, *2*, 590.

[60] J. Chang, Q. Lv, G. Li, J. Ge, C. Liu, W. Xing, *Appl. Catal. B Environ.* **2017**, *204*, 486.

[61] C. C. Pavel, F. Cecconi, C. Emiliani, S. Santiccioli, A. Scaffidi, S. Catanorchi, M. Comotti, *Angew. Chem. Int.* **2014**, *53*, 1378.

[62] S. Seetharaman, R. Balaji, K. Ramya, K. S. Dhathathreyan, M. Velan, *Int. J. Hydrogen Energy* **2013**, *38*, 14934.

[63] L. Xiao, S. Zhang, J. Pan, C. Yang, M. He, L. Zhuang, J. Lu, *Energy Environ. Sci.* **2012**, *5*, 7869.

[64] X. Li, F. C. Walsh, D. Pletcher, *Phys. Chem. Chem. Phys.* **2011**, *13*, 1162.

[65] C. C. Pavel, F. Cecconi, C. Emiliani, S. Santiccioli, A. Scaffidi, S. Catanorchi, M. Comotti, *Angew. Chemie - Int. Ed.* **2014**, *53*, 1378.

[66] D. Chanda, J. Hnát, T. Bystron, M. Paidar, K. Bouzek, *J. Power Sources* **2017**, *347*, 247.

[67] B. Motealleh, Z. Liu, R. I. Masel, J. P. Sculley, Z. R. Ni, L. Meroueh, *Int. J. Hydrogen Energy* **2021**, *46*, 3379.

[68] Y. Zhao, N. M. Vargas-Barbosa, E. A. Hernandez-Pagan, T. E. Mallouk, *Small* **2011**, *7*, 2087.

[69] J. A. Haber, E. Anzenburg, J. Yano, C. Kisielowski, J. M. Gregoire, *Adv. Energy Mater.* **2015**, *5*, 1402307.

[70] M. Favaro, W. S. Drisdell, M. A. Marcus, J. M. Gregoire, E. J. Crumlin, J. A. Haber, J. Yano, *ACS Catal.* **2017**, *7*, 1248.

Chapter 7. The Role of Ionomers in Anion Exchange Membrane Water Electrolysis; Is Aemion™ the Answer for Nickel-based Anodes?

Emily Cossar[a], Frédéric Murphy[a], Jaspreet Walia[b,c], Arnaud Weck[b,c,d], Elena A. Baranova[a*]

[a] *Department of Chemical and Biological Engineering, Centre for Catalysis Research and Innovation (CCRI) University of Ottawa,161 Louis-Pasteur Pvt., Ottawa, Canada, K1N 6N5*

[b] *Department of Mechanical Engineering, University of Ottawa, 161 Louis-Pasteur Pvt., Ottawa, Canada, K1N 6N5*

[c] *Center for Research in Photonics, University of Ottawa, 25 Tempelton St., Ottawa, Canada, K1N 6N5*

[d] *Department of Physics, University of Ottawa, 150 Louis-Pasteur Pvt., Ottawa, Canada, K1N 6N5*

Chapter as submitted to: *ACS Appl. Energy Mater.*, **2022.**

Supplementary information for this chapter is found in Appendix F.

Abstract

The anode oxygen evolution reaction (OER) in anion exchange membrane water electrolysis (AEMWE) limits the process' overall hydrogen production efficiency. Studies show that nickel-iron (NiFe)-based catalysts show excellent activity towards OER. In anode catalyst layers, electrocatalysts must be paired with anion exchange ionomers (AEI) to bind the catalyst and conduct hydroxide ions. This work covers the first investigation of the commercial Aemion™ AEI with a non-noble metal $Ni_{90}Fe_{10}$ nanoparticle anode catalyst for applications in AEMWE. The effects of Aemion™ are also studied for the first time in a three-electrode cell and compared to the commercial Fumion® and Nafion™ ionomers. Cyclic voltammetry (CV) results show that Aemion™ distinctly interacts with NiFe to supresses the $Ni(OH)_2$/NiOOH transition peak current by 39 % (vs. 11 and 17 % for Nafion™ and Fumion®, respectively), thus decreasing the OER activity of NiFe with a high overpotential of 369 mV at 10 mA cm^{-2} in 1 M potassium hydroxide (KOH). This effect was not alleviated by prolonged CV cycling, pre-conditioning the electrode in KOH, stabilizing the electrode deposition, or by modifying the Aemion™ solvent. NiFe anode catalytic layers were also prepared for AEMWE testing with varying amount of Aemion™ (7, 15, 25 and 35 wt%). Scanning Electron Microscopy (SEM) of the catalyst layers show catalyst-rich

and ionomer-rich phases, each becoming more prominent with increasing ionomer. AEMWE testing shows that 7 wt% Aemion^{TM} is the best ionomer loading, achieving a cell voltage of 1.941 V at 0.4 A cm^{-2} in 1 M KOH at 50°C, 62 mV higher than our previously optimized 15 wt% Fumion® anode. While less performing than Fumion®, $Ni_{90}Fe_{10}$ with 7 wt% Aemion^{TM} is more stable over time. Ex-situ Raman spectroscopy of the spent 7 wt% Aemion^{TM} electrode, supports the CV results, where the electrode remains mostly in the $Ni(OH)_2$ phase after polarization.

Graphical Abstract

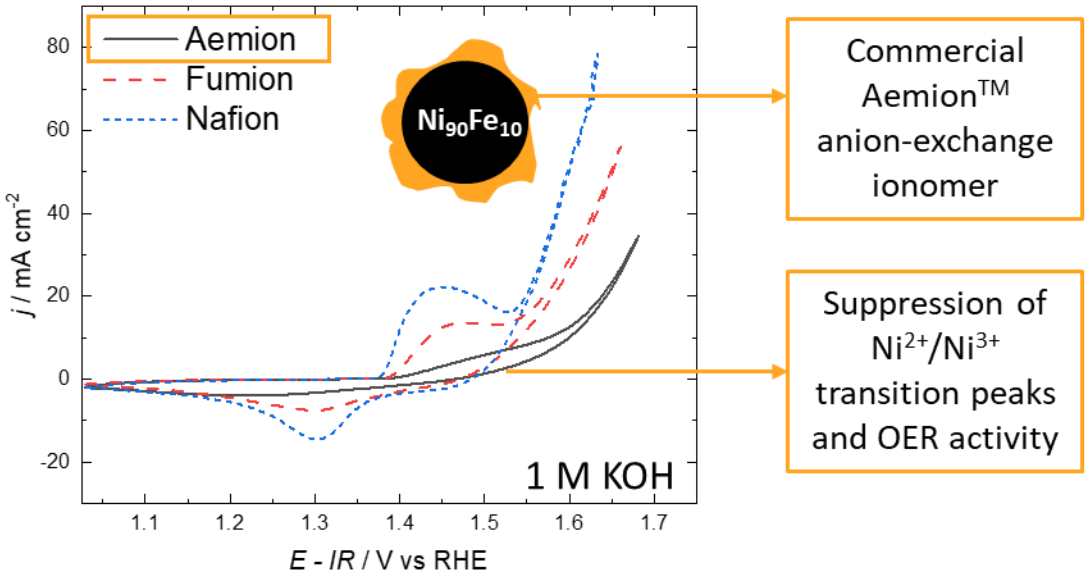

7.1 Introduction

In recent years, many efforts have been made to move away from fossil fuel utilization in an effort to reduce the anthropogenic causes of climate change. Hydrogen (H_2), is one of the most promising clean alternative fuels, however currently, around 95% of global hydrogen is produced from natural gas and coal[1–3] (grey hydrogen). While pairing fossil fuel-based hydrogen with carbon capture and storage technologies (blue hydrogen) can significantly reduce the carbon footprint of hydrogen production by capturing around 85-90% of the produced carbon dioxide (CO_2)[3], the cleanest and most sustainable method of hydrogen production is by water electrolysis powered using renewable energy sources (green hydrogen).

Water electrolysis systems, which utilize solid polymer electrolytes, are the most promising type of water electrolysis due to their favourable operating conditions and their compact cell design. In comparison to anion exchange membrane water electrolysis (AEMWE), proton exchange membrane water electrolysis (PEMWE) is currently the leading technology in terms of cell performance. In a recent review[4], it was reported that PEMWEs can achieve currents ranging from 0.6 - 2.0 A cm^{-2} at cell voltages ranging from 1.8 - 2.2 V and cell temperatures of 50 - 80°C. AEMWEs on the other hand are achieving currents of 0.2 – 1.0 A cm^{-2} at voltages of 1.8 – 2.2 V at temperatures of 50 – 60°C. While the AEMWE may currently be lacking in performance compared to the PEMWE, the alkaline environment of the AEM system allows for the use of non-noble metal catalysts and inexpensive cell materials, resulting in significant capital cost reductions[5], which are imperative for industrial applications.

Nickel (Ni)-based materials are some of the most promising catalysts for both hydrogen and oxygen evolution (HER and OER) in AEMWE as they are active and stable in alkaline media[4,6–8]. Particularly, nickel (Ni) iron (Fe)-based materials are well studied for their high catalytic activity towards the OER, a kinetically unfavourable process due to a complex mechanism involving multiple electron transfer steps[4,6–8]. For example, fluoride-incorporated nickel-iron oxyhydroxide nanosheet arrays on a compressed Ni foam have recently been synthesized by a dissolved oxygen and galvanic corrosion method, for improved OER activity and stability in a water-fed AEMWE[9]. The authors tested the self-supported Fe_xNi_yOOH-20F catalyst at the anode with 47 wt% platinum on carbon (Pt/C) at the cathode, and a poly(aryl piperidinium) hydroxide exchange membrane and ionomer, achieving a cell performance of 1.02 A cm^{-2} at 1.8

V in a water-fed system at 90°C. Those tests were carried out in a 5 cm^2 cell using anode and cathode catalyst loadings of 4.8 and 0.94 mg cm^{-2}, and an anode and cathode ionomer loading of 0.8 mg cm^{-2} and 30 wt%, respectively. The novel catalyst was also stable for over 160 h at 0.2 A cm^{-2} at 80°C.

When using nanoparticle catalysts in AEMWE systems, it is particularly important to optimize the membrane electrode assembly (MEA), which consists of the anode and cathode catalysts as well as the membrane and ionomer. Simply modifying the type or amount of ionomer used with a specific catalyst can result in improvements in AEMWE performance[5,10–16]. In a recent work[10], the authors studied catalyst-ionomer interactions in a 25 cm^2 single-cell AEMWE using lab-synthesized Ni-MoO_2 and $Ni_{0.6}Co_{0.2}Fe_{0.2}$ as cathode and anode catalysts, respectively. By varying the type and amount of ionomer used, they achieved competitive AEMWE performance of 1.15 A cm^{-2} at 2 V in 1 M KOH at 50°C using 10 wt% Nafion™ and 10 wt% Fumion® in and on top of the catalytic layer, respectively. The anode and cathode loadings used to achieve this performance were 5 and 3 mg cm^{-2}, respectively.

In PEMWE applications, one of the most common membranes/ionomers used is DuPont's Nafion™[17]. Nafion™ is composed of a polytetrafluoroethylene (PTFE) backbone with a polysulfonyl fluoride vinyl ether side chain with sulfonic acid ionic group (SO^{3-})[18]. Nafion™'s PTFE backbone and perfluorosulfonic acid (PSFA) side chain result in efficient transport of cations and solvent, while inhibiting the transport of electrons and anions[18,19]. These proton exchange membranes provide good mechanical, thermal and chemical stability[18,20] and are often used as performance comparisons in AEMWE. While these membranes exhibiting benchmark performance of zero-gap electrolyzers, they are very costly and release hydrogen fluoride (HF) upon chemical decomposition[18,21–23]. Although Nafion™ can also be used in AEMWE, ideally anion exchange polymer electrolytes should be utilized due to their ability to conduct hydroxide ions throughout the MEA. Common membranes and ionomers in AEMWE applications are made with a hydrocarbon-based backbone and quaternary ammonium ion exchange groups (QA), providing a more environmentally friendly and economically feasible option[8,15,22,24].

In our previous work[12], we optimized the amount of Fumatech Fumion® FAA-3 ionomer required for enhanced anode performance of NiFe-based particles with and without CeO_2 tested in the catalyst coated surface (CCS) configuration. We found that 15 wt% Fumion® provided the

highest AEMWE performance and showed the best adhesion of the catalyst particles within the anodic layer. The highest achieved performance of 1.72 V at 0.8 A cm^{-2} was found for the $Ni_{90}Fe_{10}$ catalyst in combination with 15 wt% Fumion®. This electrode was also found to be the most stable over 12 h at 0.5 A cm^{-2} in 0.1 M KOH at 50°C. To further test the durability of the $Ni_{90}Fe_{10}$ catalysts over time, it was of interest to use the Aemion™ ionomer from Ionomer Innovations Inc. In comparison to the Fumatech FAA-3 ionomer, which is an aromatic hydrocarbon backbone polymer with a QA side chain functionality[25,26], the Aemion™ ionomer is a form of alkylated poly(benzimidazolium) polymer (referred to as HMT-PMBI when methylated)[27], where the QA cation is located on the backbone itself, rather than on a side chain.

Not only have the Aemion™ materials been proven to perform relatively similar to the Fumion® materials[16], the Aemion™ materials are reported to be more stable over time. A recent study[27] compared the Fumion® FAA-3 ionomer and membrane to the HMT-PMBI ionomer and membrane by preparing catalyst coated membranes (CCM) of each of them respectively, using 0.5 mg_{Pt} cm^{-2} of 46.4 wt% platinum supported on graphitized carbon (Pt/C) on both the anode and cathode sides of the membranes. When polarizing both systems to similar currents in the range of 20 mA cm^{-2} in 1 M KOH at 60°C, the Fumion® materials lasted on average around 16 h, while the HMT-PMBI materials lasted around 195 h, with one stop at the 144 h mark, to re-condition the cell. Other longer-term AEMWE stability tests were performed using the HMT-PMBI membrane with a NiAlMo cathode and various Ni-based anodes, both prepared by direct current plasma-spraying onto gradient porous metal frameworks (GPMF)[28]. While the NiAlMo anode was the most active, the NiAl anode showed stable operation for over 150 h at 1 mA cm^{-2} in 1 M KOH at 60°C.

While the ultimate performance evaluation of a catalyst-ionomer combination is in an AEMWE, insight can be gained from studying the electrochemical interactions that occur between the catalyst and ionomer under applied potential in three-electrode cell experiments[10,11,19,29–32]. To the best of our knowledge, investigating the effects of the Aemion™ ionomer on OER electrocatalysts in a three-electrode cell has yet to be done. Additionally, the Aemion™ ionomer has yet to be evaluated in an AEMWE with non-noble metal anode catalysts, such as NiFe materials. As such, in this study we use three-electrode cell electrochemical techniques to investigate the interactions between our highly active lab-synthesized $Ni_{90}Fe_{10}$ electrocatalyst[12,33]

and the Aemion™ ionomer at various ionomer loadings, for alkaline oxygen evolution. The three-electrode cell tests are also performed using Nafion™ and Fumion® for comparison. We then evaluate the physical morphology and electrochemical effects of different Aemion™ nominal loadings used in the $Ni_{90}Fe_{10}$ anode of a single-cell AEMWE. Finally, the results obtained with the Aemion™ ionomer are compared to the best performing electrode configuration from our previous ionomer optimization study conducted using the commercial Fumion® ionomer[12].

7.2 Experimental Section

7.2.1 Material Synthesis

$Ni_{90}Fe_{10}$ nanoparticles were synthesized by the easily scalable method of chemically reducing nickel chloride hexahydrate ($NiCl_2 \cdot 6H_2O$, 99.999% purity, Sigma Aldrich, St. Louis, MO, USA) and iron sulphate heptahydrate ($FeSO_4 \cdot 7H_2O$, ≥99%, Sigma Aldrich, St. Louis, MO, USA) in ethanol (EtOH, 99%, Greenfield, Grayslake, IL, USA) using sodium borohydride (NaBH4, ≥98%, ACROS, Geel, Belgium). For more information on the synthesis method, see our previous works[12,33,34].

7.2.2 Material Characterization

7.2.2.1 Scanning Electron Microscopy

Scanning electron microscopy (SEM) images of the $Ni_{90}Fe_{10}$ catalyst used in three-electrode cell experiments in combination with 42 wt% of the Aemion™ anion exchange polymer resin for CO_2 (Aemion™ AP1-HNN8-00-X Low IEC, Ionomr Innovations Inc., Vancouver, BC, Canada), Fumion® anion exchange ionomer (Fumion® FAA-3-SOLUT-10, Fumatech, Bietigheim-Bissingen, Germany) and Nafion™ cation exchange ionomer (Nafion™ 5 wt%, Sigma Aldrich, St. Louis, MO, USA) were taken using the Phenom Pro desktop SEM (Nanoscience Instruments, Pheonix, AZ, USA) operating at 5 kV. The samples were prepared drop-casting a portion of catalyst ink (see Section 7.2.4.1 for more details) onto a boron-doped diamond (BDD) support. $Ni_{90}Fe_{10}$ anode CCS's containing 7, 15, 25 and 35 wt% Aemion™ were also analyzed under the same SEM. Each of the CCS samples were prepared by making sample electrolysis anodes, where the electrode inks were each sprayed onto a 2 cm^2 piece of 5 wt% Teflon treated carbon paper (Toray carbon paper, Fuel Cell Store, College Station, TX, USA).

7.2.2.2 Raman Spectroscopy

Raman spectroscopy experiments were carried out using the WITec a300 Raman microscope (WITec, Ulm, Germany) using an excitation wavelength of 785 nm, operating in the backscattering configuration. A total laser power of 0.25 mW was used, in combination with 300 g mm^{-1} grating blazed at 750 nm to disperse the signal on the charge coupled device (CCD) array. Raman spectral images were acquired over a 150 x 150 μm area at a resolution of 75 points per line, and 75 lines per image. In all cases, suitable integration times were chosen to balance between good signal to noise ratio and experimental acquisition time. Spectra were collected for the $Ni_{90}Fe_{10}$ nanoparticles, the Aemion™ ionomer, as well as the best performing CCS electrode surface ($Ni_{90}Fe_{10}$ with 7 wt% Aemion™) before and after polarization. Anode CCS samples before polarization were prepared as explained in Section 7.2.2.1, and anode CCS samples after polarization were obtained directly after electrolysis testing, by cutting, then drying the sample in air at RT overnight.

7.2.3 Ionomer Solution Preparation for Three-electrode Cell Experiments

7.2.3.1 Aemion™ Ionomer

To prepare the commercial Aemion™ anion exchange ionomer solution, the Aemion™ ionomer pellets were dissolved in methanol (MeOH, 99.9%, Fischer Scientific, Hampton, NH, USA) by magnetic stirring as per company recommendations[35]. Ionomer solutions of 5 and 0.3 wt% were used in this study. To evaluate the effects of solvents on OER performance, 2.5 wt% Aemion™ solutions were prepared using (*i*) 1-Methyl-2-pyrrolidone (NMP, 99.5%, Sigma Aldrich, St. Louis, MO, USA) and (*ii*) 33.5 wt% Milli-Q® water (H_2O, Milli-Q® Millipore, 18.2 MΩ cm at 293 K) and 64 wt% isopropanol (IPA, 99.9% Fisher Scientific, Hampton, NH, USA) as a solvent. These solvents were evaluated as they are the solvents used with the Fumion® and Nafion™ ionomers, as explained below.

7.2.3.2 Fumion® Ionomer

For comparison, the commercial anionic Fumatech Fumion® ionomer was used in this study. For three-electrode cell experiments, the as-purchased 10 wt% Fumion® solution was further diluted to 2.5 wt%, using NMP.

7.2.3.3 Nafion™ Ionomer

The benchmark ionomer for three-electrode cell testing used in this study is the cation exchange ionomer, Nafion™. This ionomer is widely used for three-electrode cell characterization. The as-purchased 5 wt% Nafion™ solution was diluted to 2.5 wt% with Milli-Q® water and IPA to result in a solution containing around 33.5 wt% Milli-Q® water and 64 wt% IPA.

7.2.4 Electrochemical Methods

7.2.4.1 Three-electrode Cell Setup and Electrode Preparation

Three-electrode electrochemical experiments were run in a Teflon conventional three-electrode cell with an upward facing working electrode, as described in our previous work[33]. The counter electrode (CE) used was a platinum mesh and the reference electrode (RE) was a mercury/mercury oxide (Hg/HgO, Koslow Scientific Company, Englewood, NJ, USA) electrode. The working electrode (WE) consisted of a 0.196 cm^2 glassy carbon (GC) electrode (London Scientific Limited, St. Thomas, ON, CAN) onto which a portion of catalyst ink was drop-cast using a micropipette. Prior to experiments, the GC surface was polished with a slurry of 30, then 5-micron alumina (Al_2O_3, Carveth Metallurgical Limited, Canada) in Milli-Q® water. The WE was then wiped clean with EtOH, followed by Milli-Q® water. In this study, two methods of preparation of the WE were studied, namely “Method 1” and “Method 2”. Method 1 consists of a drop-cast electrode made from an ink containing both the catalyst and ionomer, while Method 2 consists of a drop-cast electrode where the catalyst is deposited first, and the ionomer is added on top. The two working electrode preparation methods are described in detail in the Supplementary Information (SI). These two methods were considered for reasons which are later explained in the discussion of this work.

7.2.4.2 Three-electrode Cell Electrochemical Methods

Potentiostatic electrochemical impedance spectroscopy (EIS) experiments were carried out to quantify the ohmic losses of the system. The EIS experiments were run using a sinusoidal amplitude of 5 mV around the open circuit from 50 kHz to 0.1 Hz. Next, chronoamperometry (CA) experiments at -1.3 and -0.8 V vs Hg/HgO for 5 and 10 minutes, respectively, were carried out to pre-treat the electrode[36]. To assess the OER activity of the prepared electrodes, cyclic

voltammetry (CV) experiments were run between 0.1 and 0.8 V vs Hg/HgO at 25 mV s^{-1} for 10 cycles. Then, linear sweep voltammetry (LSV) experiments were run between 0.3 and 0.8 V vs Hg/HgO for 1 sweep at 1 mV s^{-1}. CV experiments were also run from 0.1 to 0.8 V vs Hg/HgO for 200 cycles at 50 mV s^{-1} to further study the effects of Aemion^{TM} on $Ni_{90}Fe_{10}$. Finally, to explore the preliminary durability of the electrodes, chronopotentiometry experiments were run for 3 h at 10 mA cm^{-2}. All electrochemical experiments were conducted in 1 M potassium hydroxide solution (KOH, ≥ 85%, Sigma-Aldrich, St. Louis, MO, USA) at room temperature (RT). To convert the gathered data from the Hg/HgO reference electrode to the reversible hydrogen electrode (RHE), Equation 7.1 was used.

$$E_{RHE} = E_{Hg/HgO} + 0.925 \qquad \textbf{\textit{Equation 7.1}}$$

7.2.4.3 Single-cell Electrolysis Setup and Electrode Preparation

The single-cell AEMWE experiments were run in a custom-built 5 cm^2 parallel flow field single-cell zero-gap electrolyser as shown in Figure F.1 of the SI, along with a schematic of the AEMWE cell. The AEMWE system was temperature controlled and included a two compartment 2 L electrolyte tank and a peristaltic pump, which circulated the electrolyte around the anode and cathode sides of the system at 10 mL min^{-1}. All AEMWE experiments were run at 50 ± 2°C in 1 M KOH with nitrogen (N_2 Grade 4.8, Linde plc, Dublin, Ireland) bubbled through the anode side of the electrolyte tank for safety reasons. See the SI for a more detailed description of the AEMWE experimental setup.

In this study, electrodes were prepared in the CCS configuration by hand-spraying catalytic inks using an air brush (Iwata Eclipse HP-BCS, Maple Airbrush Supplies Inc., Edmonton, AB, Canada) onto a gas diffusion layer, which is held on a hot plate at 60°C, similarly to our previous work[12]. Here however, the ink preparation method was altered to accommodate the properties of the Aemion^{TM} ionomer. The inks prepared using Aemion^{TM} were done in two steps to aid in the mixing of the ionomer in the Milli-Q® water:MeOH solvent. Note that to avoid using the Aemion^{TM} ionomer with incompatible solvents, MeOH was used in the catalyst ink instead of IPA. This procedure was adapted from the ink formulation procedure previously reported for the HTM-PMBI ionomer[27] and company recommendations from Ionomr Innovations Inc.[35]. First, the required catalyst and amount of Milli-Q® water was measured into a vial (Vial 1). This vial was

sonicated in an ultrasonic bath for 2 x 5 mins over ice. In a separate vial (Vial 2), the required amount of ionomer was added using a 5 wt% Aemion™ in MeOH solution. This solution was diluted with the required amount of MeOH for the ink. For the $Ni_{90}Fe_{10}$ anodes, the amount of ionomer was varied to result in a final nominal ionomer loading of 7, 15, 25 and 35 wt% Aemion™. For the cathodes, the final ionomer loading was kept constant at 23 wt%. The inks were made to have 2 wt% solids and a 50:50 ratio of Milli-Q® water:MeOH. With Vial 1 and 2 prepared, the contents of Vial 2, containing the ionomer and MeOH, were added to the contents of Vial 1, containing the catalyst and water, by drop-wise addition on a stir plate with magnetic mixing. Then, the combined ink was sonicated in an ultrasonic bath (40 kHz Ultrasonic Bath 15,337,409, Fischer Scientific, Hampton, NH, USA) over ice for 6 x 5 mins for a total of 40 minutes of sonication. While an ultrasonic probe was used in our previous work[12,34] to better mix the ink for spraying, this step was not performed here so as not to damage the Aemion™ ionomer[35].

The anode catalytic inks were sprayed onto gold (Au)-coated titanium (Ti) felt (2GDL20-1,0, 1 mm thick, Bekaert Corporation, Marietta, GA, USA) and the cathode inks were sprayed onto 5 wt% Teflon treated carbon paper. The Ti felts were coated with Au using a Quorum sputter coater (Q150R ES, Quorum Technologies Inc., Puslinch, ON, Canada) to coat each side of the gas diffusion layer (GDL) with 50 nm of gold. All anodes were tested with a target loading of 5 mg cm^{-2} of the synthesized $Ni_{90}Fe_{10}$ catalyst and all cathodes were tested with a loading of 1 mg cm^{-2} of commercial platinum on carbon (Pt/C, 60 wt% metal on support, Thermo Fisher Scientific, Tewksbury, MA, USA). To see the experimental anode loadings, see Table F.1 in the SI. It should be noted that like the three-electrode cell experiments, ink stability and homogeneity issues were still encountered despite forming the inks in two steps when using the Aemion™ ionomer. More difficulties were encountered when spraying electrode inks prepared with lower amounts of Aemion™. It appears that having more ionomer in the ink helps reduce clogging of the air brush to ensure a smoother spraying process. This is reflected in the data presented in Table F.1, where the experimental catalyst loadings of $Ni_{90}Fe_{10}$ increase with increasing ionomer content. Difficulties with ink preparation and stability when using an Aemion+™ ionomer are also mentioned in the works of Koch *et al.*[15], indicating the need for ink optimization studies with this group of ionomers. When using the Aemion™ ionomer, the commercial Aemion™ High IEC Anion Exchange Membrane for CO_2 (Aemion™ AF1-HNN8-50-X, Ionomr Innovations Inc.,

Vancouver, BC, Canada) was used. The membrane was pre-conditioned by soaking it in 1 M KOH for around 15 h prior to experiments.

For comparison, catalytic layers were prepared using the commercial Fumatech Fumion® ionomer. The inks prepared using Fumion® were prepared in two steps, similar to our previous work[12]. First, the required catalyst mass, amount of water and ionomer were added to a vial. Then, the ink was sonicated for 3 x 5 mins over ice. Next, the required amount of IPA was added to the ink. The ink was then sonicated for 5 x 5 mins. For consistency with the Aemion™ experiments, the ultrasonic probe was not utilized to further mix the ink. The inks using Fumion® were also prepared for an anode and cathode loading of 5 and 1 mg cm^{-2}, respectively, 2 wt% solids in the ink, and a Milli-Q® water:IPA ratio of 50:50. To see the experimental catalyst loadings, see Table F.1 in the SI. Following the results of our previous study[12], the anode nominal ionomer loading was 15 wt% and the cathode was 23 wt%. When using the Fumion® ionomer, the commercial Fumatech fumasep membrane (Fumasep FAA-3PE-30, Fumatech, Bietigheim-Bissingen, Germany) was used. The Fumatech membrane was also pre-conditioned in 1 M KOH for around 15 h prior to experiments.

7.2.4.4 Single-cell Electrolysis Electrochemical Methods

Polarization curves in AEMWE were run by stepping 0.1 A from 0 to 10 A (0 to 2 A cm^{-2}) using the Kikusui Bipolar Power Supply (PBX 20-10, Kikusui Electronics Corporation, Kanagawa Japan). A safety cut off of 2 V was set in place to protect the electrolyzer hardware. Constant current polarization experiments were also run to assess the preliminary durability of the prepared electrodes. This was done by holding the current which results in a cell voltage of 1.8 V for 6 h. For the 7, 15, 25 and 35 wt% electrodes, these currents were 1.5, 0.8, 0.4 and 0.2 A. As is evident from the provided current values, the anode ionomer content dramatically changes the applied current to result in a cell voltage of 1.8 V.

7.3 Results and Discussion

7.3.1 Three-electrode Cell Electrochemical Characterization for OER

7.3.1.1 Methods of Working Electrode Preparation

As mentioned in Section 7.2.4.1, two methods were used to prepare the WE in this study. Initially, Method 1 was to be used to carry out the entire ionomer optimization study because this method of ionomer incorporation into catalytic layers is known to offer good reproducibility and a more consistent distribution of ionomer in the catalyst layer[37,38]. However, for Method 1 to be reproducible, a well-mixed system must be obtained in the catalyst ink. As the Aemion^{TM} ionomer is insoluble in water, variability was introduced in the experiments using Method 1 because a well-mixed ink could not be achieved, despite ultrasonication. The issues with the experimental reproducibility of Method 1 are evident in Figure F.2 of the SI, where dramatic differences between repeated CV trials using 15 wt% Aemion^{TM} are shown. To reduce experimental variability between trials, Method 2 was used. In this method, the issue of mixing Aemion^{TM} with water in a catalyst ink is by-passed by adding the catalyst and the ionomer to the GC electrode surface in layers. While utilizing a different electrode preparation method could alter the CV behaviour of the $Ni_{90}Fe_{10}$ catalyst[37], in Figure F.3 of the SI, it is possible to observe that both Method 1 and 2 show very similar CV profiles and OER activity when applied using the Nafion^{TM} ionomer, indicating that the behaviour of the $Ni_{90}Fe_{10}$ catalyst is not significantly disturbed by the change in methods. Additionally, in comparison to Method 1, it was found that little to no change in experimental reproducibility occurred when using the Nafion^{TM} ionomer with Method 2. Placing the ionomer on top of the catalyst did however impede bubble detachment from the electrode surface, as shown in Figure F.4.

Figure 7.1 shows a comparison of both working electrode preparation methods using 42 wt% of the Aemion^{TM} ionomer with the $Ni_{90}Fe_{10}$ catalyst. Note that the current density in Figure 7.1 is also normalized by mass of $Ni_{90}Fe_{10}$ due to the different catalyst loadings used in Method 1 and 2. As was also observed with the Nafion^{TM} ionomer, there is a slight increase in reaction overpotential between Method 1 and 2, likely resulting from the change in ionomer placement. What is most interesting however, is the introduction of a type of charging behaviour, shown by

the difference in currents observed between Cycle 2 and Cycle 10, a result which was not observed for the Nafion™ ionomer. This behaviour will be further addressed later in the discussion.

Concerning experimental reproducibility, when using Method 2 with the Aemion™ ionomer, the overall reproducibility between trials is significantly improved to much more acceptable values of standard deviation between experimental trials. Differences in experimental trials is still however larger than with Nafion™. It should be noted that when applying Method 2 using the Fumion® ionomer, there was only a very slight difference between experimental trials, meaning that when using the Aemion™ ionomer, there are other factors, in addition to the solubility of Aemion™ in water, that are affecting the way the catalyst is behaving in the presence of the ionomer. This in turn affects the reproducibility of experiments. Some of these factors could include the way the ionomer interacts with the different phases of the catalyst or how much of each particle is covered with the ionomer. Although some potential interactions are being observed, the experiments are considered to be more controlled using Method 2, therefore Method 2 will be used for the remainder of the three-electrode tests in this study. We refer the reader to the supplemental information for details on the statistical evaluation of Method 1 and 2 with the different ionomeric binders.

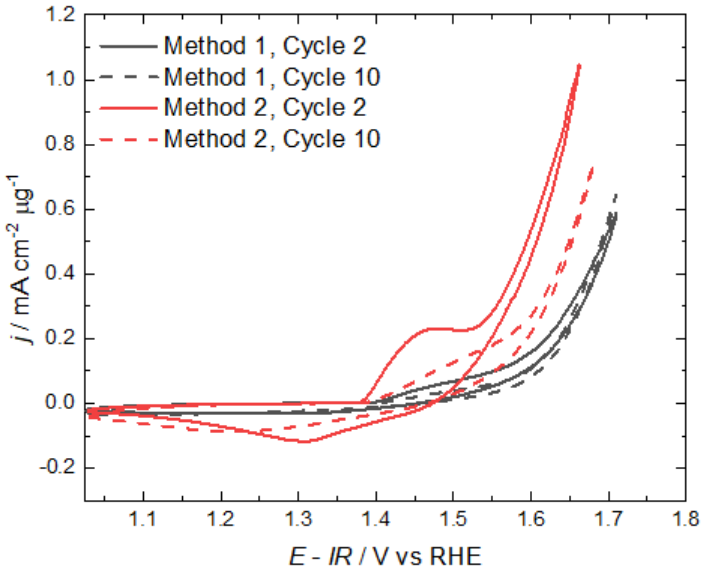

Figure 7.1: Cyclic voltammograms for the $Ni_{90}Fe_{10}$ catalyst with 42 wt% Aemion™ in 1 M KOH at RT, comparing Method 1 and Method 2 of working electrode preparation. v = 25 mV s^{-1}. Method and cycle number shown in the legend.

7.3.1.2 Effects of Aemion™ Loading on OER Activity

To evaluate the effects of the Aemion™ ionomer loading on OER activity, the nominal ionomer loading was tested at 42, 20, 10 and 5 wt%. The bounds of this study were chosen to start from our standard Nafion™ nominal loading for three-electrode cell testing (42 wt%) and work downwards until the ionomer was no longer able to bind the catalyst particles on the GC surface. Higher ionomer concentrations were not tested as exceeding amounts of 42 wt% is not practical in AEMWE applications. In literature, optimal amounts of anion exchange ionomers in anode catalytic layers are found to lie within the range of around 10 to 20 wt%, where the studied ranges for ionomer optimization do not generally exceed around 40 wt% ionomer[5,11,39,40]. Figure 7.2 shows representative graphs of the OER performance for ionomer loadings of 42, 20 and 10 wt% prepared using Method 2, and Table 7.1 summarizes key data extracted from Figure 7.2b. To see only Cycle 10 of the CVs in Figure 7.2a, see Figure F.5 of the SI. The vertical dotted lines on Figure 7.2b show where the Tafel slopes were calculated. The linear regressions of the Tafel region can be seen in Figure F.6 of the SI. Although it was possible to gather data at 5 wt% ionomer (see Figure F.7 of the SI), this experiment was not easily reproduced due to the detachment of particles from the GC surface upon adding KOH to the Teflon cell. As such, the 5 wt% Aemion™ loading will be excluded from further analysis.

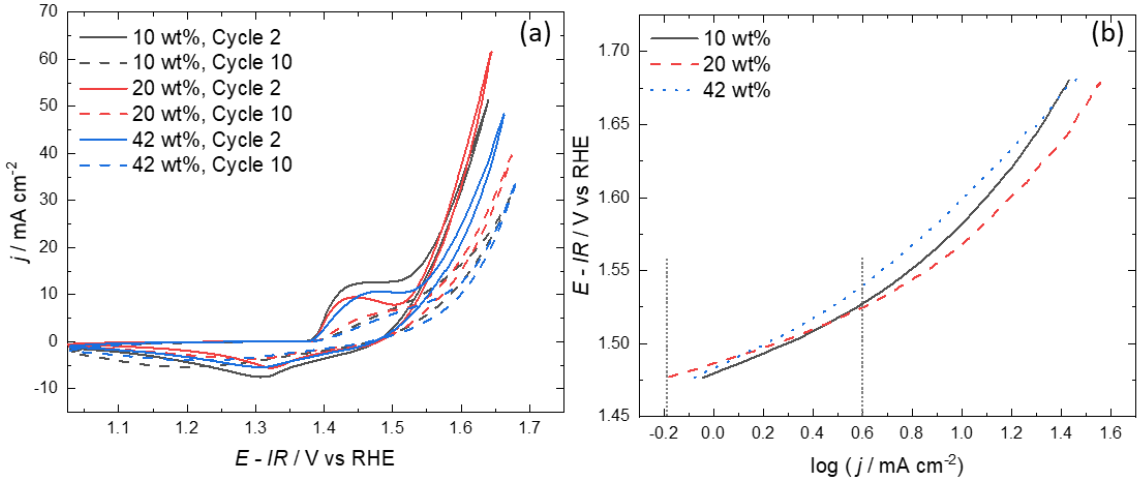

Figure 7.2: (a) Cyclic voltammograms (v = 25 mV s^{-1}) and (b) Tafel plots obtained from linear sweep voltammograms (v = 1 mV s^{-1}) for the $Ni_{90}Fe_{10}$ catalyst in 1 M KOH at RT using Method 2 of electrode preparation, comparing Aemion™ ionomer loadings of 10, 20 and 42 wt%. Ionomer loading and cycle number shown in the legend.

Table 7.1: Summary of OER overpotentials and Tafel slopes obtained from Figure 7.2b.

Aemion™ Loading [wt%]	**η at 10 mA cm^{-2} [mV]**	**Tafel Slope [mV dec^{-1}]**
10	352	78
20	338	61
42	369	92

Although it may be concluded that the 20 wt% Aemion™ electrode shows the best OER performance with a low overpotential of 338 mV at 10 mA cm^{-2} and a low Tafel slope of 61 mV dec^{-1}, the current range of the 10th CV cycle across all ionomer concentrations at 0.8 V vs Hg/HgO is around 8 mA cm^{-2} with a SD of 4 mA cm^{-2}, which is lower than the range of variability seen between experimental trials for a certain ionomer loading (see the SI for more details). As such, it could also be argued that there are no significant effects of varying the Aemion™ nominal loading on OER activity. The observed effects of ionomer loading on OER performance in a three-electrode cell are therefore not significant enough to draw any definitive conclusion. In literature for three-electrode electrochemical cell testing, less ionomer provides better OER performance[11,19]. However Faid *et al.*[11] show that the difference in performance when decreasing ionomer content from 50 to 17 wt% Fumion® was not significant. Following the inconclusive results of Figure 7.2, the nominal loading of 42 wt% was used for the remainder of this study.

7.3.1.3 Analysis of the Effects of Aemion™ on $Ni_{90}Fe_{10}$ OER Activity

As previously mentioned, when running experiments using Method 2 with the Aemion™ ionomer, there is a loss in current over 10 cycles. Not only is there a loss in current, but the redox transition peaks associated to the $Ni(OH)_2$/NiOOH couple are supressed. To see whether this was a permanent transformation of the Ni electrode, CVs were continuously run for 200 cycles. This is shown in Figure 7.3a. When inspecting the CVs in Figure 7.3a, it can be observed that the OER current continuously decreases until after around 40 cycles where it changes very minimally. It would therefore seem that the transformation of the $Ni_{90}Fe_{10}$ with Aemion™ electrode with continued cycling in the OER region is irreversible.

A possible reason for the decrease in OER current and suppression of the $Ni(OH)_2$/NiOOH couple could be due to the ionomer not stabilizing the catalyst under applied potential. This hypothesis comes from the observation that there was no change in electrochemical behaviour over

10 cycles when using Method 1 of working electrode preparation. This can be observed in Figure F.8 of the SI, where Cycle 2 and 10 of the CVs using 15 wt% Aemion^{TM} completely overlap each other. This result was consistent for all trials and ionomer loadings tested using Method 1. It appears that dispersing the ionomer in the ink prior to electrode deposition results in a more stable catalyst layer with continuous cycling. Additionally, higher OER currents when using the Aemion^{TM} ionomer were only ever achieved using Method 1 of electrode preparation, which is possibly an indication of the formation of a more favourable three-phase boundary when the ionomer is mixed in with the ink. It should however be noted that while Method 1 showed a stable current with cycling, the trials exhibiting lower OER currents (see Trial 5 of Figure F.8) had redox behaviour resembling that of the $Ni(OH)_2$/NiOOH suppression occurring over 10 cycles when employing Method 2 with Aemion^{TM}. In an attempt to recreate the ionomer-catalyst stabilizing effect using Method 2, a working electrode was prepared by layering the catalyst and ionomer in three stages, each stage consisting of the deposition of a portion of catalyst ink and a portion of ionomer. This is shown in Figure 7.3b. As evident from the CVs, layering the catalyst and ionomer does not help stabilize the catalyst in the same way mixing the ionomer in the ink does.

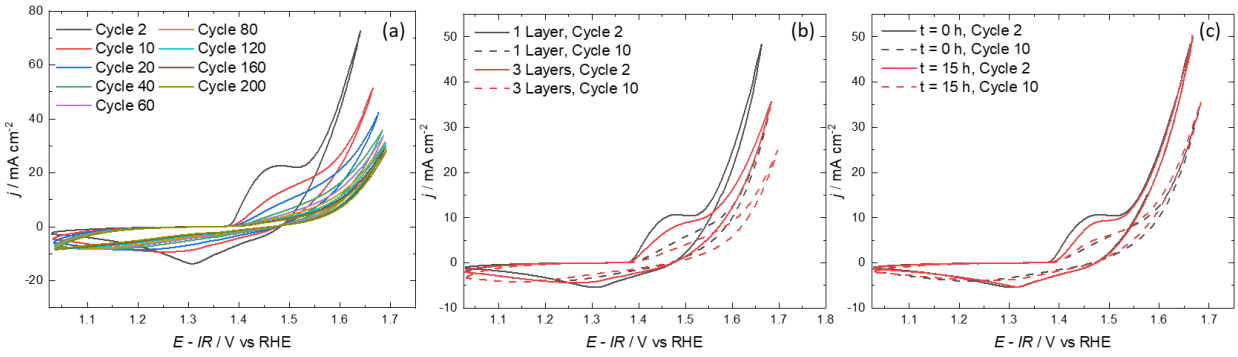

Figure 7.3: Cyclic voltammograms of the $Ni_{90}Fe_{10}$ catalyst with 42 wt% Aemion^{TM} in 1 M KOH at RT using Method 2 of electrode preparation, showing the effects of (a) 200 continuous CV cycles at 50 mV s^{-1}, (b) electrode layering, and (c) pre-conditioning the electrode in 1 M KOH for 15 h. For (b) and (c), v = 25 mV s^{-1}. Studied effect and cycle number shown in the legend.

Another important factor to consider when working with Aemion^{TM} is that when it is purchased, the ionomer is in its stable iodide (I^-) form. It is possible that the I^- impurities in the drop-cast electrode is causing the decrease in OER activity and change in NiFe redox behaviour with cycling. When working with ionomers or membranes that are fabricated in their halide ion form, there is always a pre-conditioning step done prior to AEMWE testing, where the ionomer

and membrane are soaked in 1 M KOH (or other hydroxide salt) to replace the stabilizing halide ions with OH^- ions. As such, a drop-cast electrode was prepared using Method 2, then soaked in 1 M KOH overnight (~15 h). Next, fresh electrolyte was put in the cell and electrochemical OER testing was performed. As shown in Figure 7.3c, pre-conditioning the electrode in 1 M KOH did not influence OER activity and did not improve the behaviour of the NiFe electrode with continued cycling. This result could possibly be due to a minimal effect that hydroxide ion conduction has on performance in a three-electrode cell in comparison to an anode catalytic layer in an electrolyzer. This hypothesis is supported by the results further discussed in Section 7.3.1.4, where Nafion™, a proton conducting ionomer, is the best performing binder for OER performance in three-electrode cell testing.

7.3.1.4 Comparison of Aemion™ to Fumion® and Nafion™

Scanning electron microscopy (SEM) was used to characterize the drop-cast electrodes using Aemion™, Fumion® and Nafion™. These microscopy images are shown in Figure F.9 in the SI, where a brief discussion of the observed surface morphology is also provided. Figure 7.4 shows the effects of the Aemion™ ionomer on OER activity of the $Ni_{90}Fe_{10}$ electrode in comparison to the Fumion® and Nafion™ ionomers. Data extracted from Figure 7.4b is tabulated in Table 7.2. To only see Cycle 10 of the CVs in Figure 7.4a, see Figure F.10 of the SI. To see the linear regressions of the Tafel region shown by the vertical dotted lines on Figure 7.4b, see Figure F.11 of the SI.

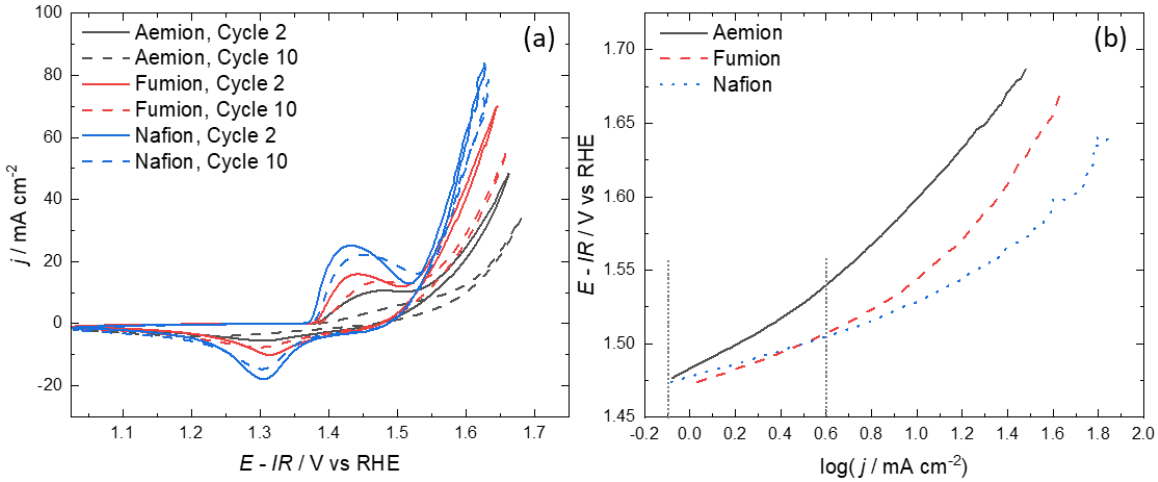

Figure 7.4: (a) Cyclic voltammograms (v = 25 mV s^{-1}) and (b) Tafel plots obtained from linear sweep voltammograms (v = 1 mV s^{-1}) for the $Ni_{90}Fe_{10}$ catalyst in 1 M KOH at RT using Method 2 of electrode preparation, comparing 42 wt% of the Aemion™, Fumion®, and Nafion™ ionomers. Ionomer type and cycle number shown in the legend.

Table 7.2: Summary of OER overpotentials and Tafel slopes obtained from Figure 7.4b, and voltage drift obtained from Figure 7.5.

Ionomer Type	**η at 10 mA cm^{-2} [mV]**	**Tafel Slope [mV dec^{-1}]**	***(E - IR)* Drift [mV h^{-1}]**
Aemion™	369	92	8
Fumion®	314	58	10
Nafion™	298	45	7

Overall, the $Ni_{90}Fe_{10}$ electrode in combination with Nafion™ shows the best OER performance with an overpotential of 298 mV at 10 mA cm^{-2} and a Tafel slope of 45 mV dec^{-1}. This is a common trend found in literature when comparing Nafion™ to anionic ionomers for OER[11,19,29]. The better OER performance obtained using Nafion™ in combination with a $NiCoO_2$ catalyst has been attributed to a lower resistance in the electrode layer in comparison to when anionic ionomers are employed[29]. Nafion™ has also been shown to provide better charge transfer than Fumion® for OER using a NiO catalyst[11]. When comparing the two anionic ionomers, Fumion® outperforms Aemion™ with an overpotential at 10 mA cm^{-2} of 314 mV, 55 mV lower than that of Aemion™, and a Tafel slope of 58 mV dec^{-1}, 34 mV dec^{-1} lower than that of Aemion™.

When inspecting Figure 7.4a, it is possible to see that unlike Nafion™, both anionic ionomers show a decrease in OER current with cycling, with the Aemion™ electrode showing the fastest decrease over 10 cycles. At 0.8 V vs Hg/HgO, Nafion™ shows a decrease in current of 7%, while Fumion® and Aemion™ show a decrease of 22 and 29%, respectively. Additionally, the peak current position of the $Ni(OH)_2$/NiOOH transition decreases by 11, 17 and 39% for Nafion™, Fumion® and Aemion™, respectively. Reasons for the overall lower OER activity, as well as decrease in OER current with continued cycling using the anionic ionomers in comparison to Nafion™, could be due to phenyl group adsorption to the catalyst surface[5,41–43]. Phenyl group adsorption could lead to the formation of acidic phenol, a component which can neutralize the hydroxides of the ammonium functional groups in the ionomer at the catalyst-ionomer interface[41]. This can lower the electrochemical activity of the Ni-based catalyst by lowering the local pH of the electrode. Additionally, phenyl adsorption to the catalyst surface can potentially block otherwise OER active sites. The more dramatic decrease in activity with continued cycling when using Aemion™ in comparison to Fumion® implies either a more severe amount of phenyl adsorption of Aemion™ on $Ni_{90}Fe_{10}$ or the presence of an additional OER performance inhibiting effect. The suppression of an oxidation peak was also observed in the works of Ghoshal *et al.*[44], where they evaluated the effects of multiple membrane, ionomer and supporting electrolyte combinations on the activity of a commercial cobalt nanoparticle anode. They observe that the Co^{3+}/Co^{4+} transition is absent when running CV experiments with the Gen 2 membrane and ionomer [perfluorinated backbone, hexyl trimethylammonium (HTMA)-based cation] at 60°C in a 0.1 M potassium bicarbonate electrolyte. They hypothesize that the observed inhibiting effect could be due to the chemical structure of the Gen 2 ionomer and how it interacts (adsorbs) to the Co catalyst.

To assess the preliminary durability of the Aemion™ ionomer in comparison to Fumion® and Nafion™, a CP was run at 10 mA cm^{-2} for 3 h in 1 M KOH. This is shown in Figure 7.5, with the drift over 3 h tabulated in Table 7.2.

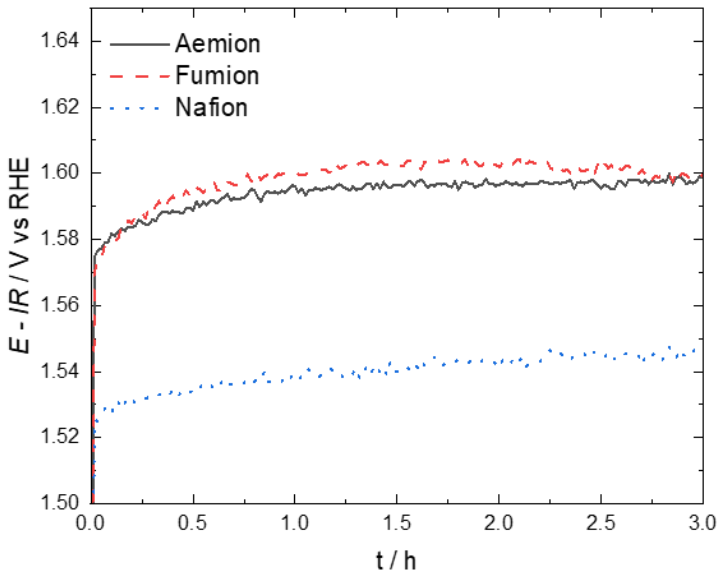

Figure 7.5: Chronopotentiometry experiment for the $Ni_{90}Fe_{10}$ catalyst run at 10 mA cm^{-2} for 3 h in 1 M KOH at RT using Method 2 of electrode preparation, comparing 42 wt% of the Aemion™, Fumion®, and Nafion™ ionomers. Ionomer type shown in the legend.

Of the 3 tested electrodes in Figure 7.5 and Table 7.2, Nafion™ shows the lowest overpotential at 10 mA cm^{-2}. Both anionic ionomers show similar overall currents, where the Fumion® has a lower starting overpotential than Aemion™. This trend is expected following the results from the CV and LSV experiments. Aemion™ and Nafion™ have the best stability for 3 h under OER currents. However, it is important to observe that while the Fumion® electrode has the highest drift over 3 h, it seems to start to stabilize itself just before the 3 h mark. While these CP results are informative, longer-term experiments under harsher conditions would be a better indicator of the true durability of the drop-cast electrodes[45,46].

7.3.1.5 Analysis of the Effects of Aemion™ Solvent on OER Activity

When comparing the different ionomers together in Section 7.3.1.4, it is important to note that the solvent used to dissolve each ionomer is different due to different solvent-ionomer compatibilities. Aemion™, Fumion® and Nafion™ are dissolved in MeOH, NMP and water:IPA, respectively. Recent studies show that the solvent used in catalyst inks can modify catalyst-ionomer interactions, which can in turn affect the formed electrode surface and affect electrochemical activity[47–49]. While in traditional ink systems, Method 1 of ink preparation is used (catalyst, ionomer and solvent are all mixed prior to catalyst layer formation), changing the solvent used to dissolve the ionomer prior to depositing it onto the catalyst, can affect the ionomer

conformation in solution as well as the way the ionomer disperses itself throughout the particles on the GC electrode. Furthermore, adding the ionomer solution to the dry particles will slightly re-disperse them, creating a form of catalyst ink and allow for interactions between the solvent, ionomer and catalyst as the ink is drying. To study the effects of the ionomer solvent on the OER activity of Aemion^{TM}, $Ni_{90}Fe_{10}$ electrodes were prepared where Aemion^{TM} was dissolved in H_2O:IPA as well as NMP, which are the solvents used for Nafion^{TM} and Fumion$^{®}$, respectively. This is shown in Figure 7.6 and data extracted from Figure 7.6b can be found in Table 7.3. Cycle 10 of each tested solvent is shown in Figure F.12 of the SI, and the linear regressions of the Tafel slopes are found in Figure F.13. It should be noted that of the tested solvents, only MeOH and NMP were recommended by Ionomr Innovations Inc. as suitable solvents for Aemion^{TM}[35]. MeOH was recommended as the most ideal solvent.

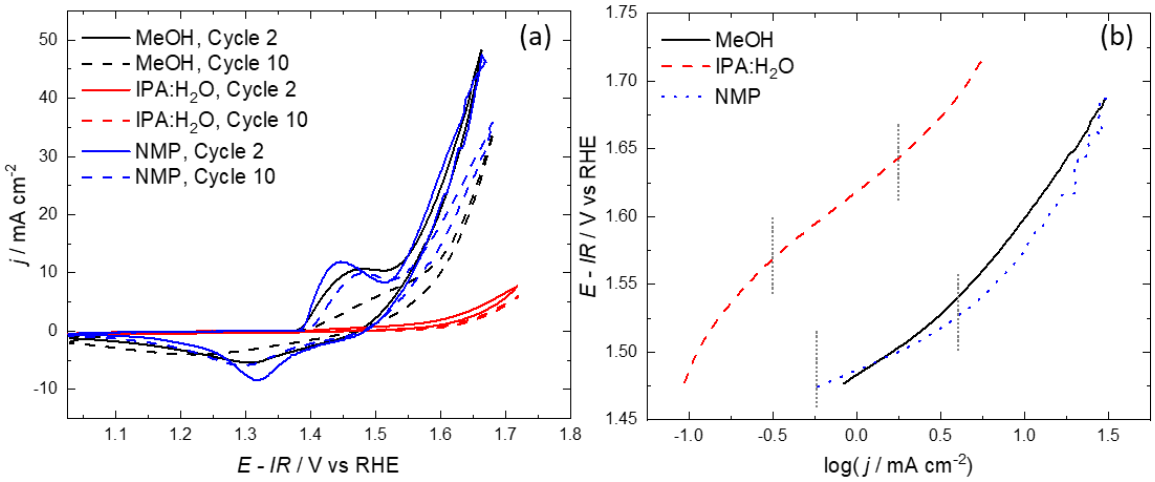

Figure 7.6: (a) Cyclic voltammograms (v = 25 mV s^{-1}) and (b) Tafel plots obtained from a linear sweep voltammogram (v = 1 mV s^{-1}) for the $Ni_{90}Fe_{10}$ catalyst in 1 M KOH at RT using Method 2 of electrode preparation, comparing 42 wt% of Aemion^{TM} dissolved in MeOH, H_2O:IPA and NMP. Ionomer solvent shown in the legend.

Table 7.3: Summary of OER overpotentials and Tafel slopes obtained from Figure 7.6b.

Ionomer Solvent	**η at 10 mA cm^{-2} [mV]**	**Tafel Slope [mV dec^{-1}]**
MeOH	369	92
H_2O:IPA	N/A	98
NMP	346	61

As shown in Figure 7.6 and Table 7.3, when Aemion^{TM} is dissolved in NMP, the OER activity is only slightly improved, showing an overpotential of 346 mV at 10 mA cm^{-2} and a Tafel slope of 61 mV dec^{-1}, values which are respectively 23 mV and 31 mV dec^{-1} lower than when MeOH is used. While the change in OER current at 0.8 V vs Hg/HgO with cycling is very similar, is appears that using NMP slows the process which supresses the $Ni(OH)_2$/NiOOH redox couple. The changes with cycling are very similar to what is observed with Fumion®, where the decrease in current of the $Ni(OH)_2$/NiOOH transition peak when using Aemion^{TM} with NMP is 17%. When using H_2O:IPA as a solvent, the OER activity is dramatically decreased indicating that using H_2O and IPA as solvents for Aemion^{TM} affect the way the ionomer interacts with the $Ni_{90}Fe_{10}$ catalyst under operating conditions. Further understanding the complex interactions between solvents, ionomers and catalysts in an electrode ink would require a detailed ink analysis and optimization study for efficient formation of catalytic layers for high OER activity[48]. While Aemion^{TM} and NMP appear to show some favourable effects on OER performance, the single-cell AEMWE experiments in the following section were performed using MeOH, the solvent most recommended to use with Aemion^{TM} by Ionomr Innovations Inc.[35].

7.3.2 Single-cell Electrolysis Experiments

7.3.2.1 Scanning Electron Microscopy of Anode Catalytic Layers

SEM was used to physically characterize the $Ni_{90}Fe_{10}$ catalytic layers used for AEMWE testing with different nominal loadings of the Aemion^{TM} ionomer. This is shown in Figure F.14 of the SI for electrodes prepared with 7 (Figure F.14a), 15 (Figure F.14b), 25 (Figure F.14c) and 35 (Figure F.14d) wt% ionomer. It is possible to observe in the micrographs that each of the electrode surfaces shows two phases. A catalyst rich phase, which appears uniform, and an ionomer rich phase, which appears to create channels or cracks throughout the catalytic layer. When increasing the amount of Aemion^{TM} ionomer in the catalytic layers, the cracks in the electrode surfaces, which seem to be agglomerated ionomer, get larger. A similar physical effect of increasing Aemion^{TM} content in the catalytic layer is mentioned in the works of Mayerhöfer *et al.*[50] where they describe a uniform IrO_2 catalyst layer at a low ionomer loading of 10 wt%, and an increasingly inhomogeneous catalytic layer when increasing ionomer loading to 20 and 50 wt%.

We relate the formation of inhomogeneous catalytic layers to catalyst ink stability issues, similar to Koch *et al.*[15]. The observed ionomer channels in the Aemion^{TM} catalytic layers are

different from what we have previously observed when forming Ni catalytic layers with Fumion®[12]. In that study, the prepared surfaces were uniform, where less Fumion® ionomer showed a more textured, porous surface and more ionomer showed a smoother surface with ionomer agglomerates on top. The Fumion® observations are more in line with other previously reported changes in electrode surfaces with increasing ionomer content[39,51]. Overall, from inspection of the SEM images in Figure F.14, it can be said that less Aemion™ forms a surface with less cracks or ionomer channels, which could be beneficial for AEMWE activity. For more details on the analysis of the electrode surfaces, see Figures F.14-F.16 along with an accompanying discussion, in the SI.

7.3.2.2 Effects of Aemion™ Loading on AEMWE Performance

Preliminary AEMWE testing of the $Ni_{90}Fe_{10}$ catalyst in the presence of different nominal Aemion™ loadings was performed and the results are shown in Figure 7.7, with key information from the plots summarized in Table 7.4.

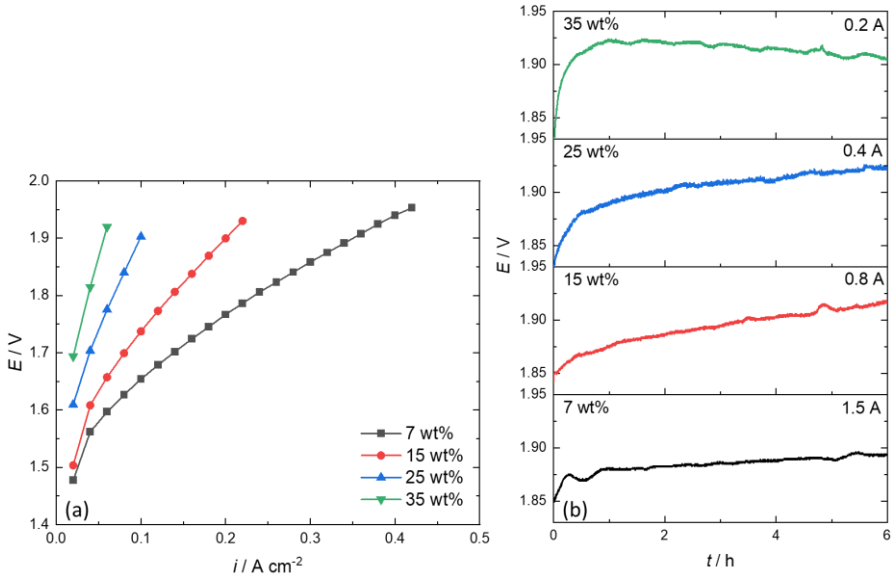

Figure 7.7: (a) Polarization curves and (b) chronopotentiometry experiments run for 6 h for the $Ni_{90}Fe_{10}$ catalyst in 1 M KOH at 50°C, comparing Aemion™ ionomer loadings of 7, 15, 25 and 35 wt%. Ionomer loadings shown in the legend. The currents for Figure b are 0.2, 0.4, 0.8 and 1.5 A for the 7, 15, 25 and 35 wt% electrodes, respectively, each resulting in a starting cell voltage of around 1.8 V.

Table 7.4: Summary of polarization curve performance and voltage drift obtained from Figure 7.7.

Aemion™ Loading [wt%]	***i* at 1.8 V [mA cm^{-2}]**	**Drift [mV h^{-1}]**
7	235	7
15	136	11
25	68	15
35	37	11

In Figure 7.7 it is possible to see that the best performing $Ni_{90}Fe_{10}$ electrode contains a nominal loading of 7 wt% Aemion™, showing a current of 234 mA cm^{-2} at 1.8 V, 99 mA cm^{-2} higher than the other tested loadings. While the results shown in Figure 7.7b cannot be directly compared, the 7 wt% electrode also showed the lowest drift of 7 mV h^{-1}over 6 h. This drift was also measured at higher currents (1.5 A), therefore under harsher conditions than the other tested loadings, indicating a more durable electrode. These results are in accordance with a recent study by Koch *et al.*[15] where they test varying amount of Aemion+™ ionomer (4 – 15 wt%) in the anode side of their AEMWE using a 1 mg cm^{-2} IrO_x anode and 0.5 mg_{Pt} cm^{-2} cathode configured in the catalyst coated membrane (CCM) format on a reinforced Aemion+™ membrane. In their work, they discuss that having higher amounts of ionomer can lead to a decreased number of active sites and increased mass transport resistances throughout the catalytic layer. They too find that 7 wt% ionomer provides the best and most stable performance. As the electrode loadings shown in Table F.1 of the SI vary quite significantly between electrodes, the polarization curves in Figure 7.7a were normalized by mass in Figure F.17a. Results in Figure F.17a further support the 7 wt% electrode being the most appropriate amount of Aemion™ to use with the $Ni_{90}Fe_{10}$ catalyst as this electrode shows the best activity with the least amount of catalyst on the gold-coated Ti support. It should however be noted that it is possible that 7 wt% Aemion™ provided the best activity because the proportion of ionomer-rich areas on the catalyst surface shown in Figure F.14 are less important than what was observed for the 15, 25 and 35 wt% electrodes. It is therefore possible that the best AEMWE performance may be found with a different ionomer loading when a more uniform electrode layer, formed using an optimized ink formulation and ink deposition conditions, is used.

7.3.2.3 Comparison of Aemion™ to Fumion®

While it can be informative to compare the behaviour of different ionomers in three-electrode cell experiments, it is more representative to get a comparison in an AEMWE cell. Figure 7.8 shows a comparison between Aemion™ and Fumion® tested in a single-cell AEMWE. Following Section 7.3.2.2, the Aemion™ loading used in this comparison is 7 wt%, while the Fumion® loading is 15 wt%, based on the results of our previous work[12]. Table 7.5 summarizes key data extracted from Figure 7.8.

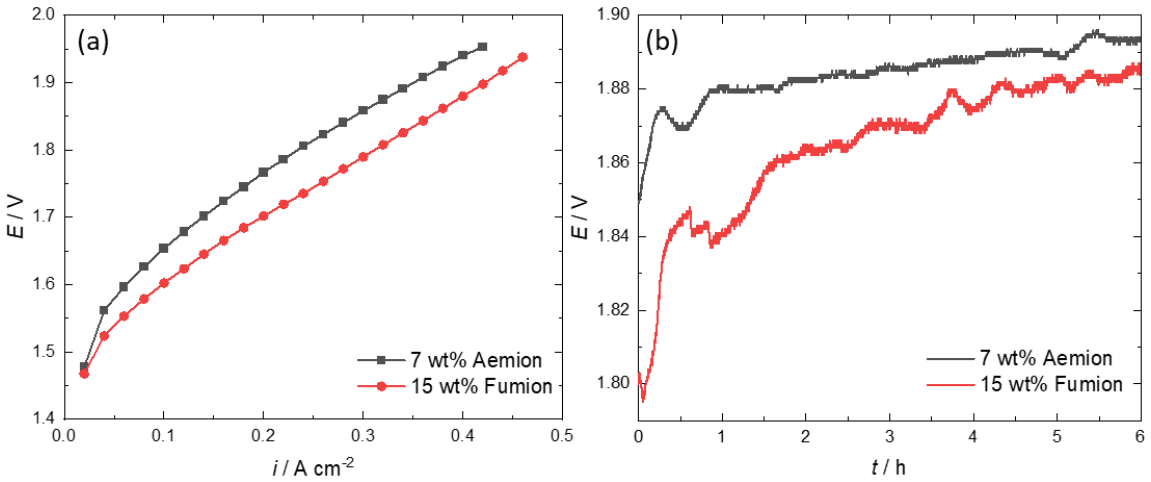

Figure 7.8: (a) Polarization curves and (b) chronopotentiometry experiments run at 1.5 A for 6 h for the $Ni_{90}Fe_{10}$ catalyst in 1 M KOH at 50°C, comparing 7 wt% Aemion™ and 15 wt% Fumion®. Ionomer type and loading shown in the legend.

Table 7.5: Summary of polarization curve performance and voltage drift obtained from Figure 7.8.

Electrode	*E* at 0.4 A cm^{-2} [V]	*i* at 1.8 V [mA cm^{-2}]	Drift [mV h^{-1}]
7 wt% Aemion™	1.941	235	7
15 wt% Fumion®	1.879	312	14

As shown in Figure 7.8, the 15 wt% Fumion® electrode shows a lower cell voltage with applied current. At 0.4 A cm^{-2}, the Fumion® electrode achieves a cell voltage of 1.879 V, 62 mV lower than that of 7 wt% Aemion™. However, when looking at Figure F.17b, it is possible to see that when normalizing the activity by mass of $Ni_{90}Fe_{10}$, both electrodes perform very similarly, where

the Aemion™ electrode outperforms the Fumion® electrode at higher currents. Although the cell components are not identical, our results support the work of Fortin *et al.*[16], where they find that Fumion® outperforms Aemion™ in a cell consisting of an Ir black anode (3.5-3.8 mg cm^{-2}) and 60 wt% Pt/C cathode (1 mg_{Pt} cm^{-2}) with an Aemion™ membrane (AF1-HNN8-50-X, like in this study). They however find that after the curves are IR-corrected for ohmic losses, the AEMWE performance of the Aemion™ electrode is slightly better than Fumion®. In their study, the higher observed ohmic resistance of the Aemion™ catalytic layer is attributed to its inability to provide intimate contact between the catalyst layer and the membrane[16].

In Figure 7.8b, over the 6 h at 1.5 A, the Aemion™ electrode shows a lower potential drift of 7 mV h^{-1}, compared to 14 mV h^{-1}, shown by the Fumion® electrode. It should however be noted that these are preliminary durability experiments, and it is possible that over an extended period of time, the Fumion® electrode stabilizes itself to show a lower voltage drift, more similar to what we have previously observed[12]. Additionally, we previously observed that 15 wt% Fumion® provided enough ionomer to properly adhere the catalyst particles to the GDL, while not providing too much ionomer to result in the loss of the catalyst layer structure due to excessive swelling. In Figure F.18 of the SI, it is possible to see that compared to the Fumion® electrode, which is still mostly intact, the 7 wt% Aemion™ layer shows catalyst layer dissolution or delamination of the anode layer, which over a longer period of time, can more importantly affect electrochemical performance and result in poor electrode durability. This effect of the ionomer on the structure of the catalytic layer is also observed in the work of Fortin *et al.* [16], where their Ir black anode layers prepared using the Aemion™ ionomer do not properly adhere the particles after a short-term durability experiment at 0.5 A cm^{-2} in 0.1 M KOH at 50°C.

Overall, in a single-cell AEMWE, Aemion™ and Fumion® perform very similarly, where Aemion™ shows slightly lower performance than Fumion®, a result which is expected following the three-electrode cell testing. However, the Aemion™ electrode is potentially more stable over time. Longer-term experiments under harsher conditions would be required to completely evaluate the stability of both ionomers in comparison to each other. It should be noted that the achieved potential drift values are orders of magnitudes higher than commercially feasible degradation rates, such as the ones in the work of Motealleh *et al.*[21], which are under 1 μV h^{-1} over 10 000 h at 1 A cm^{-2}.

7.3.2.4 Ex-situ Raman Spectroscopy

Following the three-electrode cell results showing that the $Ni(OH)_2$/NiOOH transition is inhibited in the presence of Aemion^{TM}, it was of interest to perform ex-situ Raman spectroscopy on the electrolysis anodes to observe whether any changes occurred to the $Ni_{90}Fe_{10}$ catalyst in the presence of Aemion^{TM} after single-cell polarization. As a base line analysis, the $Ni_{90}Fe_{10}$ particles as well as the dry Aemion^{TM} ionomer were evaluated. This can be seen in Figure F.19 of the SI. As evident from the spectra in Figure F.19a, the ionomer shows some fluorescence with some discernible features in the 1250 – 1600 cm^{-1} spectral range, which are likely features associated to benzene and imidazolium found in the methylated poly(benzimidazolium) polymer[27,52,53]. More specifically, peaks are readily resolved at 1250, 1365, 1430, 1535 and 1600 cm^{-1}. As for the nanoparticles in Figure F.19b, the overwhelming fluorescence of the sample does not allow for the identification of any of the Ni or Fe phases. However, in our previous work[34], we determined by X-ray diffraction (XRD) that the $Ni_{90}Fe_{10}$ catalyst consists of metallic Ni and Fe as well as β-$Ni(OH)_2$.

Figure F.20 shows the Raman spectrum of an anode layer containing 7 wt% Aemion^{TM} before electrolysis and Figure 7.9 shows the anode layer after electrolysis. In Figure F.20, the broad fluorescence background can be attributed to the presence of $Ni_{90}Fe_{10}$ nanoparticles, a characteristic shown by the nanoparticles in Figure F.19b. While Aemion^{TM} is also present here, Raman spectral features associated with the ion exchange polymer are masked by the fluorescence background.

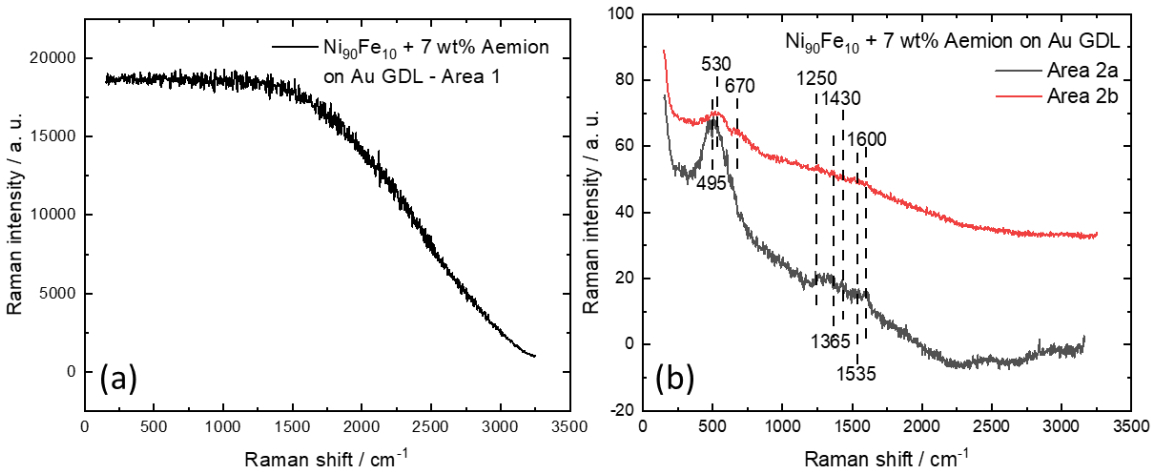

Figure 7.9: Raman spectra of the $Ni_{90}Fe_{10}$ electrolysis anodes with 7 wt% Aemion™ scanned post-electrolysis testing in (a) Area 1, and (b) Areas 2a and 2b (see Figure F.21).

Figure 7.9 shows two different areas of the anode post-electrolysis as two different spectra were observed. In Figure 7.9a, the Raman spectrum shows a lot of fluorescence, as in Figure F.20, indicating that the nature of the electrode surface has not changed in some areas of the electrode. This lack of surface modification under operating conditions is possible due to the relatively short duration of the electrolysis experiments. In Figure 7.9b, the observation that some areas of the anode surface show a very distinct spectrum is quite clear. The two displayed spectra were taken at two different locations on the electrode, showing a consistent change in electrode modification. This result was only observed on the post-electrolysis sample and could be related to changes in the catalyst-ionomer interfaces upon hydrating the electrode in 1 M KOH prior to experiments. In Figure 7.9b, it is possible to see low intensity peaks around 1250 – 1600 cm^{-1}, showing that Aemion™ peaks at 1250, 1365, 1430, 1535 and 1600 cm^{-1} are still present, indicating the ionomer likely maintains its chemical structure during electrolysis operation. However, as the features in the spectra shown in Figure 7.9b are not as clear and evident as in Figure F.19a, it is not possible to definitively answer whether the Aemion™ ionomer has undergone changes during polarization.

Also present in Figure 7.9b are peaks around 495 and 530 cm^{-1}, which have been previously attributed to Ni-O vibrations in defective or disordered α and β-$Ni(OH)_2$ phases under no applied current[54–61]. While a high current was applied to the anode during electrolysis operation, which should result in the oxidation of $Ni(OH)_2$ to NiOOH, no Raman shift values of around 475 - 480 and 555 - 560 cm^{-1} were found, which are the shift values associated to Ni-O vibrations in NiOOH[56,57,62–64]. It should be noted that Cole *et al.*[65] attributed peaks at 460 and 530 cm^{-1} to Ni-

O vibrations in NiOOH, indicating the possibility of both $Ni(OH)_2$ and NiOOH vibrations at 530 cm^{-1} in our work. Finally, the peak shown around 670 cm^{-1} in Area 2b of Figure 7.9b is likely a contribution from the iron present in the sample. Reports have attributed Raman shift values of 670 cm^{-1} to Fe_3O_4[54,66]. This peak cannot be identified in Area 2a of Figure 7.9b, likely due to the high relative intensity of the Ni peak at 495 cm^{-1}. It should also be noted that a peak around 540 cm^{-1} has also been attributed to Fe_3O_4[66], a Raman shift value relatively close to 530 cm^{-1}. The peak at 530 cm^{-1} could therefore reflect contributions from Ni and Fe. To further understand the spatial distribution of the observed changes in Figure 7.9b, a Raman spectral image, which maps the peak intensity at 530 cm^{-1} over a 150 x 150 μm area, as well as an overlay of the Raman map with the corresponding brightfield microscope image of the sample, are shown in Figures F.21 and F.22, respectively. A clear differentiation between the modified and unmodified areas is readily observed. In this connection, when combined with other imaging techniques, Raman scattering measurements can provide correspondence between structure and chemistry.

With the information gathered from the Raman analysis, it is possible to say that the post-electrolysis anode remains mostly in the $Ni(OH)_2$ phase, indicating that the Ni^{2+}/Ni^{3+} transition is also inhibited under polarization in the electrolyser. These findings support the observed three-electrode electrochemical results which show that the $Ni(OH)_2$/NiOOH transition peaks are suppressed with continued CV cycling, which again could be related to phenyl adsorption of Aemion^{TM} on $Ni_{90}Fe_{10}$ or the occurrence of an additional OER performance inhibiting phenomenon. In-situ characterization, such as in-situ Raman spectroscopy would likely help further define specifically what occurs between Aemion^{TM} and $Ni_{90}Fe_{10}$ under polarization to inhibit the Ni^{2+}/Ni^{3+} transition, and consequentially, lower OER activity.

7.4 Conclusions

In this work, the Aemion^{TM} anion exchange ionomer is studied for the first time with a non-noble metal oxygen evolution electrocatalyst, consisting of our lab synthesized $Ni_{90}Fe_{10}$ nanoparticles, for application in anion exchange membrane water electrolysers. In addition to evaluating the ionomer in an AEMWE, to the best of our knowledge, this study is also the first to utilize three-electrode cell electrochemical testing to evaluate how the Aemion^{TM} ionomer affects the electrochemical behaviour of the NiFe OER electrocatalyst. Three-electrode cell electrochemical results showed that Aemion^{TM} distinctly interacts with NiFe to inhibit the

$Ni(OH)_2$/NiOOH transition and lower OER activity. In comparison to Nafion™ and Fumion®, this electrochemical behaviour is most significant in the presence of the Aemion™, showing a peak current decrease of the Ni^{2+}/Ni^{3+} transition of 11, 17 and 39 % for Nafion™, Fumion® and Aemion™, respectively. Further investigation of this inhibitory effect showed that it is not alleviated with prolonged CV cycling, electrode stabilization by layering of catalyst and ionomer, or pre-conditioning the drop-cast ink in 1 M KOH prior to experiments. Additionally, while utilizing different solvents to dissolve the Aemion™ ionomer affected the resulting OER activity of the catalyst, it was not the factor responsible for the change in redox behaviour of NiFe in the presence of Aemion™.

Single-cell electrolysis testing was performed to evaluate the $Ni_{90}Fe_{10}$ anodes with 7, 15, 25 and 35 wt% Aemion™. SEM images of the prepared electrode surfaces showed that they are inhomogeneous, with a catalyst-rich and an ionomer-rich phase, each becoming more pronounced with increasing ionomer content. Experimental observations related the instability of the catalyst ink dispersion using Aemion™ as a possible reason for the poor architecture of the $Ni_{90}Fe_{10}$ catalytic layers. Preliminary AEMWE experiments in 1 M KOH at 50°C showed that the 7 wt% Aemion™ electrode achieved a cell voltage of 1.941 V at 0.4 A cm^{-2} with a voltage drift of 7 mV h^{-1} when held at 1.5 A for 6 h, which was the best and most stable electrolysis performance of all the Aemion™-containing membrane electrode assemblies. The performance of the 7 wt% Aemion™ electrode was comparable to the performance of our previously optimized $Ni_{90}Fe_{10}$ electrode with 15 wt% Fumion®. Ex-situ Raman spectroscopy was performed on the 7 wt% Aemion™ electrolysis anode before and after polarization to study possible changes to Aemion™ or NiFe with polarization. Results indicated that the electrode surface remained mostly in the $Ni(OH)_2$ phase after polarization, supporting the CV findings. Overall, this study demonstrated that Aemion™ does not appear to be compatible with Ni-based anodes in AEMWE. A deeper understanding of the mechanisms behind this negative interaction would lead to a better ability to pair catalysts and ionomers for efficient anode performance.

Acknowledgements

This research was conducted as part of the Engineered Nickel Catalysts for Electrochemical Clean Energy project administered from Queen's University and supported by Grant number RGPNM 477963-2015 under the Natural Sciences and Engineering Research Council of Canada (NSERC) Discovery Frontiers Program. Additional funding was also provided by NSERC's Alexander Graham Bell Canada Graduate Scholarship – Doctoral (CGS D). We would also like to thank Dr. Fabio Variola for access to the Raman spectrometer.

References

[1] M. Bodner, A. Hofer, V. Hacker, *Wiley Interdiscip. Rev. Energy Environ.* **2015**, *4*, 365.

[2] I. Dincer, C. Acar, *Int. J. Hydrogen Energy* **2014**, *40*, 11094.

[3] G. Kakoulaki, I. Kougias, N. Taylor, F. Dolci, J. Moya, A. Jäger-Waldau, *Energy Convers. Manag.* **2021**, *228*, 113649.

[4] H. A. Miller, K. Bouzek, J. Hnat, S. Loos, C. I. Bernäcker, T. Weißgärber, L. Röntzsch, J. Meier-Haack, *Sustain. Energy Fuels* **2020**, *4*, 2114.

[5] D. Li, E. J. Park, W. Zhu, Q. Shi, Y. Zhou, H. Tian, Y. Lin, A. Serov, B. Zulevi, E. D. Baca, C. Fujimoto, H. T. Chung, Y. S. Kim, *Nat. Energy* **2020**, *5*, 378.

[6] F. Dionigi, P. Strasser, *Adv. Energy Mater.* **2016**, *6*, 1600621.

[7] A. L. Santos, M.-J. Cebola, D. M. F. Santos, *Energies* **2021**, *14*, 3193.

[8] C. Li, J.-B. Baek, *Nano Energy* **2021**, *87*, 106162.

[9] J. Xiao, A. M. Oliveira, L. Wang, Y. Zhao, T. Wang, J. Wang, B. P. Setzler, Y. Yan, *ACS Catal.* **2021**, *11*, 264.

[10] A. Y. Faid, A. O. Barnett, F. Seland, S. Sunde, *ACS Appl. Energy Mater.* **2021**, *4*, 3327.

[11] A. Y. Faid, L. Xie, A. O. Barnett, F. Seland, D. Kirk, S. Sunde, *Int. J. Hydrogen Energy* **2020**, *45*, 28272.

[12] E. Cossar, A. O. Barnett, F. Seland, R. Safari, G. A. Botton, E. A. Baranova, *J. Power Sources* **2021**, *514*, 230563.

[13] R. Soni, S. Miyanishi, H. Kuroki, T. Yamaguchi, *ACS Appl. Energy Mater.* **2021**, *4*, 1053.

[14] D. Chanda, J. Hnát, T. Bystron, M. Paidar, K. Bouzek, *J. Power Sources* **2017**, *347*, 247.

[15] S. Koch, P. A. Heizmann, S. K. Kilian, B. Britton, S. Holdcroft, M. Breitwieser, S. Vierrath, *J. Mater. Chem. A* **2021**, *9*, 15744.

[16] P. Fortin, T. Khoza, X. Cao, S. Y. Martinsen, A. Oyarce Barnett, S. Holdcroft, *J. Power Sources* **2020**, *451*, 227814.

[17] K. A. Mauritz, R. B. Moore, *Chem. Rev.* **2004**, *104*, 4535.

[18] A. Kusoglu, A. Z. Weber, *Chem. Rev.* **2017**, *117*, 987.

[19] G.-F. Li, D. Yang, P. Y. A. Chuang, *ACS Catal.* **2018**, *8*, 11688.

[20] M. Carmo, D. L. Fritz, J. Mergel, D. Stolten, *Int. J. Hydrogen Energy* **2013**, *38*, 4901.

[21] B. Motealleh, Z. Liu, R. I. Masel, J. P. Sculley, Z. R. Ni, L. Meroueh, *Int. J. Hydrogen Energy* **2021**, *46*, 3379.

[22] D. Henkensmeier, M. Najibah, C. Harms, J. Žitka, J. Hnát, K. Bouzek, *J. Electrochem. Energy Convers. Storage* **2021**, *18*, 024001.

[23] M. David, C. Ocampo-martínez, R. Sánchez-peña, *J. Energy Storage* **2019**, *23*, 392.

[24] J. R. Varcoe, P. Atanassov, D. R. Dekel, A. M. Herring, M. A. Hickner, P. A. Kohl, A. R. Kucernak, W. E. Mustain, K. Nijmeijer, K. Scott, T. Xu, L. Zhuang, *Energy Environ. Sci.* **2014**, *7*, 3135.

[25] B. Bauer, H. Strathmann, F. Effenberger, *Desalination* **1990**, *79*, 125.

[26] A. Carbone, S. C. Zignani, I. Gatto, S. Trocino, A. S. Aricò, *Int. J. Hydrogen Energy* **2020**, *45*, 9285.

[27] A. G. Wright, J. Fan, B. Britton, T. Weissbach, H.-F. Lee, E. A. Kitching, T. J. Peckham, S. Holdcroft, *Energy Environ. Sci.* **2016**, *9*, 2130.

[28] L. Wang, T. Weissbach, R. Reissner, A. Ansar, A. S. Gago, S. Holdcroft, K. A. Friedrich, *ACS Appl. Energy Mater.* **2019**, *2*, 7903.

[29] I. Spanos, S. Neugebauer, R. Guterman, J. Yuan, R. Schlögl, M. Antonietti, *Sustain. Energy Fuels* **2018**, *2*, 1446.

[30] F. Zhang, M. Yang, S. Zhang, P. Fang, *Polymers (Basel).* **2019**, *11*, 1268.

[31] R. Jervis, N. Mansor, A. J. Sobrido, S. Jones, C. Gibbs, T. P. Neville, J. Millichamp, P. R. Shearing, D. J. L. Brett, *J. Electrochem. Soc.* **2017**, *164*, F1551.

[32] T. W. Koo, C. S. Park, Y. Do Kim, D. Lee, S. Park, J. H. Lee, S. M. Choi, C. Y. Choi, *J.*

Korean Phys. Soc. **2015**, *67*, 1558.

[33] E. Cossar, K. Agarwal, V. B. Nguyen, R. Safari, G. A. Botton, E. A. Baranova, *Electrocatalysis* **2021**.

[34] E. Cossar, A. O. Barnett, F. Seland, E. A. Baranova, *Catalysts* **2019**, *9*, 814.

[35] Ionomr Innovations Inc., Aemion^{TM} Dispersion and Ink Formulation (FM-7005-C) **2020**.

[36] M. Alsabet, M. Grden, G. Jerkiewicz, *Electrocatalysis* **2011**, *2*, 317.

[37] M. S. McGovern, E. C. Garnett, C. Rice, R. I. Masel, A. Wieckowski, *J. Power Sources* **2003**, *115*, 35.

[38] M. S. Wilson, S. Gottesfeld, *J. Electrochem. Soc.* **1992**, *139*, L28.

[39] J. E. Park, S. Y. Kang, S. H. Oh, J. K. Kim, M. S. Lim, C. Y. Ahn, Y. H. Cho, Y. E. Sung, *Electrochim. Acta* **2019**, *295*, 99.

[40] I. Vincent, A. Kruger, D. Bessarabov, *Int. J. Hydrogen Energy* **2017**, *42*, 10752.

[41] D. Li, I. Matanovic, A. S. Lee, E. J. Park, C. Fujimoto, H. T. Chung, Y. S. Kim, *ACS Appl. Mater. Interfaces* **2019**, *11*, 9696.

[42] I. Matanovic, S. Maurya, E. J. Park, J. Y. Jeon, C. Bae, Y. S. Kim, *Chem. Mater.* **2019**, *31*, 4195.

[43] D. Li, H. T. Chung, S. Maurya, I. Matanovic, Y. S. Kim, *Curr. Opin. Electrochem.* **2018**, *12*, 189.

[44] S. Ghoshal, B. S. Pivovar, S. M. Alia, *J. Power Sources* **2021**, *488*, 229433.

[45] Y. Kuroda, T. Nishimoto, S. Mitsushima, *Electrochim. Acta* **2019**, *323*, 134812.

[46] M. I. Jamesh, X. Sun, *J. Power Sources* **2018**, *400*, 31.

[47] S. A. Berlinger, B. D. McCloskey, A. Z. Weber, *ACS Energy Lett.* **2021**, *6*, 2275.

[48] S. A. Berlinger, S. Garg, A. Z. Weber, *Curr. Opin. Electrochem.* **2021**, *29*, 100744.

[49] C. Lei, F. Yang, N. Macauley, M. Spinetta, G. Purdy, J. Jankovic, D. A. Cullen, K. L. More, Y. S. Kim, H. Xu, *J. Electrochem. Soc.* **2021**, *168*, 044517.

[50] B. Mayerhöfer, K. Ehelebe, F. D. Speck, M. Bierling, J. Bender, J. A. Kerres, K. J. J. Mayrhofer, S. Cherevko, R. Peach, S. Thiele, *J. Mater. Chem. A* **2021**, *9*, 14285.

[51] M. K. Cho, H. Park, S. Choe, S. J. Yoo, J. Y. Kim, H.-J. Kim, D. Henkensmeier, S. Y. Lee, Y. Sung, H. S. Park, J. Hyun Jang, *J. Power Sources* **2017**, *347*, 283.

[52] L. M. Markham, L. C. Mayne, B. S. Hudson, M. Z. Zgierski, *J. Phys. Chem.* **1993**, *97*, 10319.

[53] M. Wahadoszamen, A. Rahaman, N. M. R. Hoque, A. I. Talukder, K. M. Abedin, A. F. M. Y. Haider, *J. Spectrosc.* **2015**, *2015*, 1.

[54] M. W. Louie, A. T. Bell, *J. Am. Chem. Soc.* **2013**, *135*, 12329.

[55] M. Vidotti, R. P. Salvador, S. I. Córdoba de Torresi, *Ultrason. Sonochem.* **2009**, *16*, 35.

[56] K. S. Joya, X. Sala, *Phys. Chem. Chem. Phys.* **2015**, *17*, 21094.

[57] J. Desilvestro, D. A. Corrigan, M. J. Weaver, *J. Electrochem. Soc.* **1988**, *135*, 885.

[58] D. S. Hall, D. J. Lockwood, S. Poirier, C. Bock, B. R. MacDougall, *J. Phys. Chem. A* **2012**, *116*, 6771.

[59] M. C. Bernard, R. Cortes, M. Keddam, H. Takenouti, P. Bernard, S. Senyarich, *J. Power Sources* **1996**, *63*, 247.

[60] B. C. Cornilsen, P. J. Karjala, P. L. Loyselle, *J. Power Sources* **1988**, *22*, 351.

[61] M. Vidotti, R. P. Salvador, E. A. Ponzio, S. I. C. De Torresi, *J. Nanosci. Nanotechnol.* **2007**, *7*, 3221.

[62] M. W. Louie, A. T. Bell, *J. Am. Chem. Soc.* **2013**, *135*, 12329.

[63] B. S. Yeo, A. T. Bell, *J. Phys. Chem. C* **2012**, *116*, 8394.

[64] B. J. Trzešniewski, O. Diaz-Morales, D. A. Vermaas, A. Longo, W. Bras, M. T. M. Koper, W. A. Smith, *J. Am. Chem. Soc.* **2015**, *137*, 15112.

[65] K. M. Cole, D. W. Kirk, S. J. Thorpe, *J. Electrochem. Soc.* **2018**, *165*, J3122.

[66] M. Hanesch, *Geophys. J. Int.* **2009**, *177*, 941.

Chapter 8. Conclusions and Recommendations

8.1 Conclusions

Hydrogen production via water electrolysis is a booming field of research due to the current environmental crisis stemming from fossil fuel utilization. Of the many types of water electrolysis that can be used to produce green hydrogen, anion exchange membrane water electrolysis is one of the most promising technologies due to its ability to accommodate low-cost cell materials and non-noble metal cell catalysts, such as nickel, as well as its favourable low resistance cell design. This technology is however very new, and as such relatively little research has been done on optimizing the many system components for commercially relevant performance and stability. One of the most important system limitations is the anode catalytic layer, as the oxygen evolution reaction (OER) is kinetically unfavourable. This catalytic layer consists of an OER electrocatalyst and an anion exchange ionomer, which binds the catalyst and conducts hydroxide ions through the layer. This thesis covers multiple studies which aid in the research, development and understanding of nickel-based nanostructured electrocatalysts for the promotion of the OER in AEMWE systems. In addition to thoroughly investigating Ni-based nano-catalysts for OER, this thesis also covers an investigation of two commercial AEIs and their effect on the efficiency of the Ni-based catalysts in anode catalytic layers.

The electrochemical active surface area is an important criterion used to evaluate the intrinsic activity of an electrocatalyst. The ECSA is however very difficult to identify for Ni materials. In Chapter 3 of this thesis, four ECSA methods were assessed for five different Ni structures (different size, shape, and phases) to determine whether one method was better than the other, or whether each method was applicable under certain conditions. This fundamental electrochemical study showed that the most appropriate method to apply will depend strongly on the nature of the Ni material analyzed and on the end application of the electrocatalyst. This study therefore helped further understand of the applicability and validity of electrochemical active surface area methods for Ni electrocatalysts. As such, researchers will be able to better determine the ECSA of their Ni catalysts under study through the better selection of the ECSA method to apply. This study also showed the need to develop or modify existing methods when other metals or supports are combined with the Ni catalysts.

A detailed three-electrode electrochemical study was performed in Chapter 4 of this thesis to analyze the effects of Fe and CeO_2 addition into Ni nanoparticles for the promotion of the OER. A simple chemical reduction synthesis method carried out at room temperature using sodium borohydride as the reducing agent, was successfully used to produce the nanoparticles in this study. Physicochemical characterization of the materials showed Ni and Fe, 4-6 nm in size, co-distributed throughout the samples, with CeO_2 agglomerated separately. Of the studied materials [$Ni_{100-x}Fe_x$/ 50 wt% CeO_2 (x = 0, 5, 10, 20, 40 at%) as well as $Ni_{90}Fe_{10}$/ *y* wt% CeO_2 and $Ni_{80}Fe_{20}$/ *y* wt% CeO_2 (*y* = 0, 5, 7, 10, 20, 50)], it was observed that incorporating 20 wt% Fe into Ni provided the best electrochemical activity, which was better performing than the IrO_2 benchmark catalyst, as well as similar materials reported in literature. While slightly less active for OER, the 10 at% Fe catalysts were found to provide better stability than the 20 at% Fe materials, likely due to less severe Fe dissolution under applied currents. While catalysts with lower amounts of CeO_2 (7 and 10 wt%) showed better OER performance, overall, incorporating ceria did not further promote the OER of the NiFe catalysts. This was suggested to be due to CeO_2 introducing an additional ohmic resistance to the NiFe catalysts, which outweighed any beneficial effects that CeO_2 could have on catalytic performance. Overall, this study demonstrated that NiFe-based nanoparticles can be successfully synthesized using a scalable and reproducible synthesis method. Additionally, the resulting Ni particles with 10-20 at% Fe showed excellent OER activity and stability.

The evaluation of the NiFe-based catalysts with and without CeO_2 in an AEMWE was performed in the studies presented in Chapters 5-7. In Chapter 5 the synthesis of the nanoparticles was successfully scaled to produce material quantities necessary to make single cell AEMWE anode catalytic layers. The electrochemical activity of the materials was maintained when producing around 0.5 and 1 g of material at a time. As a preliminary evaluation of the catalysts in an electrolyser device, the Ni-based anodes were evaluated using an ionomeric binder loading of 7 wt%, which was previously optimized for a commercial IrO_2 anode. The work shown in Chapter 5 demonstrated great promise for the Ni-based nanoparticles as high-performing anodes in AEMWE using the commercial Fumatech Fumion® ionomer. Following this study, in Chapter 6, the ionomer loading in the NiFe-based anodes with and without CeO_2 was optimized for enhanced AEMWE performance. Results indicated that 15 wt% Fumion® provided the best performance and mechanical adhesion of the particles within the catalytic layer. When evaluating the anode performance of the best NiFe-based anodes with and without CeO_2 developed in Chapter 4, it was

observed that $Ni_{90}Fe_{10}$ was the most active and stable material reaching 0.8 A cm^{-2} at 1.72 V in 1 M KOH at 50°C. The electrochemical impedance spectroscopy analysis performed in Chapters 5 and 6 showed that incorporating ceria into the NiFe materials reduced the observed charge transfer resistance of the cell and helped better maintain mass transfer over time under a continuously applied current. However, in accordance with the results from Chapter 4, the CeO_2-containing anodes had a higher ohmic resistance, which resulted in increased cell overpotential, even when CeO_2 was only present in small amounts. Overall, the AEMWE studies carried out with the Fumion® ionomer showed promise for the NiFe-based catalysts as efficient AEMWE anodes. These results, in combination with the three-electrode cell results from Chapter 4, indicated that the CeO_2-containing materials could have some promotional effect on the OER when present in small amounts (around 7-10 wt%), however the catalyst compositions evaluated in these studies did not show those effects to be significant enough to overcome the added ohmic resistance from the low electronic conductivity of CeO_2. Finally, the work carried out on optimizing the Fumion® ionomer loading in the anode layers showed the importance of optimizing this parameter to find a balance between electrode morphology, exposed catalyst active sites, and electrode durability.

In Chapter 7, the best performing $Ni_{90}Fe_{10}$ AEMWE anode was evaluated in combination with the more durable commercial Aemion™ ionomer from Ionomr Innovations. A detailed three-electrode electrochemical study was first conducted to observe the influence of Aemion™ on the $Ni_{90}Fe_{10}$ electrochemical activity. It was observed that in the presence of Aemion™, the $Ni(OH)_2$/NiOOH redox peaks were supressed, which in turn lowered the OER activity of the catalyst. This effect was not observed when using Fumion®, or Nafion™, which is the most widely used ionomer for three-electrode electrochemical studies. Further investigation into this electrochemical behaviour showed that this inhibiting effect is permanent and likely due to interactions between $Ni_{90}Fe_{10}$ and Aemion™ under applied currents. When employing different loadings of the Aemion™ ionomer in a $Ni_{90}Fe_{10}$ AEMWE anode layer, it was found that 7 wt% ionomer offered the best electrochemical performance, which was close to the performance obtained using 15 wt% Fumion®. Results from ex-situ Raman spectroscopy performed on the Aemion™ catalytic layers before and after electrolysis experiments, indicated that the Ni catalyst remained in the $Ni(OH)_2$ phase after polarization, supporting the findings from the three-electrode electrochemical testing. This work demonstrated the importance of properly pairing catalyst and ionomer together to yield efficient AEMWE anodes. Additionally, in this study, observations of

poor catalyst ink stability using Aemion^{TM} and its effects on electrode morphology indicated that optimization of the catalyst ink and electrode preparation conditions should be carried out. The work in this chapter was performed on a custom-built single cell AEMWE. Although the design and construction of this unit was successful, the specific design characteristics of the AEMWE unit need to be optimized for more accurate electrolyser performance.

8.2 Recommendations

While the work presented in this thesis was relatively successful, there is still much experimental and theoretical work to be done to further understand and optimize Ni-based anode performance in AEMWE. As such, the following is a list of recommendations for future work of this thesis:

1. An extensive analysis of the current ECSA methods of Ni materials was performed in Chapter 3. The analysis of this study showed that all methods present an amount of inherent uncertainty primarily related to the use of a theoretical value for the Ni surface charge density or capacitance in the calculation of the ECSA. As such, when incorporating other metals into the Ni-materials, the application of those theoretical values in the ECSA calculations becomes even less relevant. To estimate the ECSA of Ni bimetallic or supported materials more accurately, it is recommended to study the ECSA methods of the additional metal or support, to understand how those materials can affect the results of the existing Ni ECSA methods. Following this investigation, a new ECSA method could be developed, where contributions from Ni as well as the additional metal or support are considered.
2. A detailed analysis was performed on the effects of Fe and CeO_2 on Ni nanoparticles towards the OER. While the effects of Fe on Ni were relatively clear and well supported by literature, the results of CeO_2 incorporation in the Ni-based catalysts should be further investigated. Results indicated that the interactions between Ni, Fe and CeO_2 could be very sensitive to the composition of the catalyst. As such, it is recommended to do a more complete screening of the Ni, Fe and CeO_2 variations to find whether specific catalyst compositions allow the observed positive effects of CeO_2 to become more important. As fine-tuning the catalyst is likely required, it is recommended to carry out this study using both theoretical modelling, such as density functional theory (DFT) calculations, and experimental work.
3. While the chemical reduction synthesis procedure was successfully applied and scaled to produce the nanoparticles used in this thesis, it is recommended to carry out a synthesis optimization procedure to see whether changing some parameters can further boost the OER activity. For example, using different precursor salts, or modifying the rate of sodium

borohydride addition could modify the physicochemical properties of the resulting materials to benefit electrochemical performance. Additionally, while this synthesis procedure was successfully scaled to 0.5 and 1 g batches, it is recommended to carry out a study analyzing the effects of scaling the synthesis to larger batches on OER activity. In this way, the synthesis method can be controlled to ensure the performance of the particles can still be achieved when carrying out large scale synthesis batches.

4. The results of the ionomer optimization studies demonstrated that ionomers can significantly affect the catalytic activity of the Ni-based materials. As such, it is recommended to study a variety of anion exchange ionomers to observed whether one works better than the other and why. If possible, ionomers should be specifically tailored to the Ni-based materials as they work closely to carry out the OER. It is also recommended to evaluate combining ionomers together to take advantage of each of their strengths. For example, PTFE is commonly used for its durability, however it does not conduct hydroxide ions. Combining PTFE with an AEI could result in a durable electrode layer, with efficient hydroxide ion conduction.
5. When working with the Aemion^{TM} ionomer in Chapter 7, multiple experimental observations pointed towards the need to optimize catalyst ink formulations and electrode fabrication conditions. Catalyst ink formulations are often not modified when different catalysts or ionomers are being evaluated. It is however important to do so as each of the ink components interact together and form a dispersion, which is then used to form catalytic layers. While utilizing a pre-established ink formulation worked relatively well with the Fumion® ionomer, it did not also work as well in the case of the Aemion^{TM} ionomer. Some effort was put towards stabilizing the ink formulation using Aemion^{TM}, however the ink formulation was not optimal and the resulting electrode layers were not uniform. It is therefore recommended to carry out an ink optimization study, where different catalyst-ionomer-solvent ratios, types of solvent, and mixing methods are evaluated to yield better catalyst layers. The ink dispersion must also be optimized for efficient spraying, and the spraying conditions (spraying rate, hot plate temperature, etc.) should also be tailored to the materials at hand.
6. In this work, AEMWE testing was performed in both 1 and 0.1 M KOH to evaluate the effects of pH on electrochemical activity. Results demonstrate a decrease in performance

with pH. To remain competitive with PEMWE, which shows high performance in a water-fed system, it is recommended to further investigate the effects of electrolyte type and concentration on AEMWE performance. This is something to consider once the catalyst and ionomer in the anode layers are better understood.

7. The preliminary stability of the Ni-based catalysts was tested in both a three-electrode electrochemical cell and a single cell AEMWE. While these tests were informative, it is recommended to carry out long-term durability of the electrocatalysts in an AEMWE. Accelerated stability testing should also be performed to see whether the system can endure the simulation of repeatedly starting up and shutting down due to intermittent renewable energy supplies. It should however be noted that based on the presented preliminary durability results, further optimization of the anode catalytic layer and AEMWE system stability will need to be performed before evaluating the system's long-term and accelerated stability. This could include testing other ionomers with the Ni-based catalysts or evaluating methods to reduce iron dissolution under applied currents.

Appendix A. Supplementary Information for Chapter 2

Content as published in: *J. Chem. Technol. Biotechnol.*, **2022,** https://doi.org/10.1002/jctb.7094.

Tables A.1 and A.2 present more details on the particle synthesis and electrode fabrication methods summarized in Tables 2.3 and 2.4 of the main article.

Table A.1: Part 1 - Details of Ni-based anode catalyst synthesis and electrode fabrication.

Ni-based AN	Particle Synthesis	Electrode Fabrication	Ref.# (year)
$NiCoO_x$, $NiFeO_xH_y$, **$NiCoO_x$:Fe**, $NiCoFeO_x$ NPs	*Hydrothermal method:* 1. Dissolve metal precursors in H_2O & EtOH, add NH_3 under stirring. 2. Transfer to a Parr bomb, heat to 150°C for 3 h. 3. Centrifuge NPs, wash 3x with EtOH, dry at 80°C overnight. 4. For NiCoOx:Fe, Fe added by stirring NiCoOx NPs in $FeCl_{2(aq)}$ for 30 min.	1. Spray coat a stirred catalyst ink onto a Pt-coated sintered titanium frit on a hot plate at 80°C. 2. Spray coat supplemental ionomer sln onto the formed layer.	[1] (2019)
Fe_xNi_yOOH-20F powder	*Hydrothermal method:* 1. Dissolve Fe and Ni precursor, NaF and urea in H_2O. 2. Transfer to a Teflon vessel, heat to 100°C for 12 h. 3. Wash powders with H_2O, dry.	1. Spray coat an ultrasonicated catalyst ink onto both sides of a compressed Ni foam.	[2] (2021)
Ni, $Ni_{90}Fe_{10}$, $Ni_{90}Fe_{10}$/50 wt% CeO_2 NPs	*Chemical reduction:* 1. Dissolve Ni and Fe precursors and CeO_2 nanopowder in ethanol. 2. Reduce combined sln by adding $NaBH_4$ sln in EtOH under stirring at RT. 3. Centrifuge NPs, wash 3x with EtOH, freeze dry overnight.	1. Spray coat an ultrasonicated catalyst ink onto a membrane on a hot plate at 60°C.	[3] (2019)
Ni, **$Ni_{90}Fe_{10}$**, $Ni_{80}Fe_{20}$, $Ni_{90}Fe_{10}$/ 10 wt% CeO_2, $Ni_{80}Fe_{20}$/ 10 wt% CeO_2 NPs		1. Spray coat an ultrasonicated catalyst ink onto a gold-coated titanium felt on a hot plate at 60°C.	[4] (2021)
Ni_2Fe_1 nanofoam	*Chemical reduction:* 1. Dissolve Ni and Fe precursor in H_2O. 2. Reduce by injecting the Ni and Fe sln into $NaBH_4$ sln in H_2O under stirring at RT. 3. Stir 1 min and let sit until the next day. 4. Recover settled nanofoams and freeze dry.	1. Paint a mixed catalyst ink onto a platinized titanium GDL.	[5] (2020)
NiO nanosheets	*Chemical reduction*: 1. Dissolve Ni precursor in H_2O. 2. Reduce by adding $NaBH_4$ sln, stir for 1 h. 3. Centrifuge particles, wash with H_2O and EtOH 3x. 4. Dry at 80°C overnight in a vacuum oven. 5. Anneal in air at 500°C for 6 h.	1. Spray coat an ultrasonicated catalyst ink onto a carbon paper GDL on a hot plate at 60°C.	[6] (2020)
$NiCo_2O_4$ particles	*Coprecipitation using NaOH:* 1. Dissolve Ni and Co precursor in H_2O. 2. Coprecipitate by adding NaOH sln under stirring at RT, stir for 1 h, let stand for 12 h. 3. Wash particles 5x with H_2O, filter, further wash with H_2O. 4. Dry at 80°C. 5. Calcinate at 325°C for 4 h.	1. Spray coat an ultrasonicated catalyst ink onto a Ni foam GDL on a hot plate.	[7] (2017)
$NiCo_2O_4$ particles		1. Spray coat an ultrasonicated catalyst ink onto a Ni foam GDL (CCS-MEA) or a membrane (CCM-MEA) on a hot plate at 50°C.	[8] (2019)
$NiCo_2O_4$ particles		1. Spray coat an ultrasonicated catalyst ink onto a Ni foam on a hot plate at 120°C. 2. Heat CCS to 325°C for 15 min to bind the catalyst to the Ni foam.	[9] (2016)
$Ni_{0.6}Co_{0.2}Fe_{0.2}$ particles	*Laboratory synthesized**	1. Spray coat a sonicated catalyst ink onto a Au-coated Ti felt at 60°C. 2. Coat additional ionomer onto the formed layer.	[10] (2021)

Note: In bold is the material or the specifications for which the performance is reported in the main text. * Synthesis method not specified.

Table A.2: Part 2 - Details of Ni-based anode catalyst synthesis and electrode fabrication.

Ni-based AN	Particle Synthesis	Electrode Fabrication	Ref.# (year)
NiFe (2:1)-LDH/KB (2/1)	*Gelation-deflocculation method*: 1. Dissolve Ni and Fe precursor H_2O and EtOH, add acetylacetone and stir for 30 min at RT. 2. Add propylene oxide and stir for 1 min. 3. Let mixture stand for a few days to form gel then sol. 4. Dry mixture in an oven.	1. Spray coat a ball-milled and ultrasonicated catalyst ink onto a carbon paper.	[11] (2020)
NiFe-BTC-GNPs MOF	*Chemical reduction:* 1. Dissolve Ni and Fe precursor and trimesic acid (BTC) in H_2O:DMF:EtOH (1:1:1) sln. 2. Sonicate graphene powder (GNP) in the same solvent then add to sln from Step 1. 3. Heat mixture to 85°C for 24 h under stirring, cool to RT. 4. Filter, wash with DMF, immerse in dichloromethane overnight. 5. Repeat Step 4. 6. Filter and dry at 65°C for 18 h under vacuum.	1. Coat a sonicated catalyst ink onto a nickel foam. 2. Hot press the CCS onto a pre-treated membrane using a pressure of 5 MPa at 40°C for 2-3 min.	[12] (2020)
$Ni_{0.9}Fe_{0.1}Co_{1.975}Li_{0.025}O_4$, $Ni_{0.9}Fe_{0.1}Co_2O_4$ particles	*Electrochemical precipitation:* 1. Dissolve Ni, Co, Li and Fe precursor in H_2O. 2. Precipitate by applying 10 V for 1 h. 3. Filter, wash with hot H_2O. 3. Dry at 80°C, calcinate at 325°C for 4 h in air.	1. Spray coat an ultrasonicated catalyst ink onto a Ni foam GDL on a hot plate. 2. Sinter the binder in the CCS at 325°C for 15 min.	[13] (2018)
$NiMnO_x$ NPs	*Oxalate method*: 1. Dissolve Ni and Mn precursor H_2O at 60°C. 2. Mix with oxalic acid sln and neutralize with NaOH. 3. Heat to 80°C, add hydrogen peroxide dropwise to form precipitate. 4. Filter, wash with H_2O, dry at 100°C for 24 h. 5. Calcinate at 350°C for 120 min.	1. Spray coat a catalyst ink onto a membrane.	[14] (2020)
$NiFeO_x$ 70wt% / KB, $NiFe_2O_x$ 70 wt%/KB NPs	*Oxalate method*: 1. Dissolve Ni and Fe precursor in H_2O at 60°C. 2. Mix with oxalic acid sln and neutralize with NaOH. 3. Heat to 80°C, add hydrogen peroxide dropwise to form precipitate. 4. Filter, wash with hot H_2O, dry at 100°C for 24 h. 5. Calcinate at 450°C for 120 min.	1. Spray coat a catalyst ink onto a carbon cloth backing GDL.	[15] (2020)
$NiMn_2O_4$ (20 wt%)/CNF, **$NiCo_2O_4$ (40 wt%)/CNF** fibers	*Electrospinning method*: 1. Solubilize Ni, Mn and Co precursors and polyacrylonitrile (carbon nanofiber precursor) in DMF under stirring at 60°C for 1 h. 2. Load sln into electrospinning system, apply an electrical field of 17 kV to the sln jet at 21°C and <40% RH to form layer. 3. Stabilize layer by heating to 270°C in air for 30 min. 4. Carbonize by heating to 900°C for 1 h under He flow. 5. Oxidize by heating to 350°C in static air for 1 h.	1. Spray coat a catalyst ink onto a carbon cloth backing GDL.	[16] (2019)
$NiCo_2O_4$ particles	*Thermal decomposition:* 1. Dissolve Ni and Co precursor in MeOH. 2. Heat to 338 K (65°C) to evaporate solvent. 3. Calcinate at 648 K (375°C) for 20 h. 4. Ball mill for 12 h.	1. Spray coat a catalyst ink onto a **Ti fibre felt GDL** or coat the ink onto a membrane.	[17] (2018)
commercial $NiFe_2O_4$ NPs	N/A	1. Spray coat a sonicated catalyst ink onto a stainless fiber paper.	[18] (2017)
commercial $NiFe_2O_4$ NPs	N/A	1. Spray coat an ultrasonicated catalyst ink onto a Ni fiber paper. 2. Dry CCS in an oven at 80°C for 20 min.	[19] (2020)
commercial $NiFe_2O_4$ NPs	N/A	1. Spray coat an ultrasonicated catalyst ink onto a 316L sintered SS fiber felt. 2. Dry CCS in an oven at 80°C for 20 min.	[20] (2017)

Notes: In bold is the material or the specifications for which the performance is reported in the main text. "sln" is short for solution.

References

[1] D. Xu, M. B. Stevens, M. R. Cosby, S. Z. Oener, A. M. Smith, L. J. Enman, K. E. Ayers, C. B. Capuano, J. N. Renner, N. Danilovic, Y. Li, H. Wang, Q. Zhang, S. W. Boettcher, *ACS Catal.* **2019**, *9*, 7.

[2] J. Xiao, A. M. Oliveira, L. Wang, Y. Zhao, T. Wang, J. Wang, B. P. Setzler, Y. Yan, *ACS Catal.* **2021**, *11*, 264.

[3] E. Cossar, A. O. Barnett, F. Seland, E. A. Baranova, *Catalysts* **2019**, *9*, 814.

[4] E. Cossar, A. O. Barnett, F. Seland, R. Safari, G. A. Botton, E. A. Baranova, *J. Power Sources* **2021**, *514*, 230563.

[5] D. Li, E. J. Park, W. Zhu, Q. Shi, Y. Zhou, H. Tian, Y. Lin, A. Serov, B. Zulevi, E. D. Baca, C. Fujimoto, H. T. Chung, Y. S. Kim, *Nat. Energy* **2020**, *5*, 378.

[6] A. Y. Faid, L. Xie, A. O. Barnett, F. Seland, D. Kirk, S. Sunde, *Int. J. Hydrogen Energy* **2020**, *45*, 28272.

[7] D. Chanda, J. Hnát, T. Bystron, M. Paidar, K. Bouzek, *J. Power Sources* **2017**, *347*, 247.

[8] J. Hnát, M. Plevova, R. A. Tufa, J. Zitka, M. Paidar, K. Bouzek, *Int. J. Hydrogen Energy* **2019**, *44*, 17493.

[9] R. A. Tufa, E. Rugiero, D. Chanda, J. Hnàt, W. van Baak, J. Veerman, E. Fontananova, G. Di Profio, E. Drioli, K. Bouzek, E. Curcio, *J. Memb. Sci.* **2016**, *514*, 155.

[10] A. Y. Faid, A. O. Barnett, F. Seland, S. Sunde, *ACS Appl. Energy Mater.* **2021**, *4*, 3327.

[11] H. Koshikawa, H. Murase, T. Hayashi, K. Nakajima, H. Mashiko, S. Shiraishi, Y. Tsuji, *ACS Catal.* **2020**, *10*, 1886.

[12] P. Thangavel, M. Ha, S. Kumaraguru, A. Meena, A. N. Singh, A. M. Harzandi, K. S. Kim, *Energy Environ. Sci.* **2020**, *13*, 3447.

[13] D. Chanda, S. Basu, *Int. J. Hydrogen Energy* **2018**, *43*, 21999.

[14] A. Carbone, S. C. Zignani, I. Gatto, S. Trocino, A. S. Aricò, *Int. J. Hydrogen Energy* **2020**, *45*, 9285.

[15] S. C. Zignani, M. Lo Faro, S. Trocino, A. S. Aricò, *Energies* **2020**, *13*, 1720.

[16] C. Busacca, S. C. Zignani, A. Di Blasi, O. Di Blasi, M. Lo Faro, V. Antonucci, A. S. Aricò, *Int. J. Hydrogen Energy* **2019**, *44*, 20987.

[17] G. Gupta, K. Scott, M. Mamlouk, *J. Power Sources* **2018**, *375*, 387.

[18] Z. Liu, S. D. Sajjad, Y. Gao, J. J. Kaczur, R. I. Masel, *ECS Trans.* **2017**, *77*, 71.

[19] I. V Pushkareva, A. S. Pushkarev, S. A. Grigoriev, P. Modisha, D. G. Bessarabov, *Int. J. Hydrogen Energy* **2020**, *45*, 26070.

[20] Z. Liu, S. D. Sajjad, Y. Gao, H. Yang, J. J. Kaczur, R. I. Masel, *Int. J. Hydrogen Energy* **2017**, *42*, 29661.

Appendix B. Supplementary Information for Chapter 3

Content as published in: *J. Electroanal. Chem.* **2020**, *870*, 114246,
http://dx.doi.org/10.1016/j.jelechem.2020.114246.

B.1 The Oxidation Cycle of Ni in an Alkaline Environment

As shown in the blue curve of Figure B.1, when metallic nickel is cycled in the cathodic region, it oxidizes to an unstable α-$Ni(OH)_2$ phase. This process is reversible, as shown by the reduction peak of that same CV. When Ni gets prolonged exposure to an alkaline environment, the unstable α-$Ni(OH)_2$ phase is reorganized to a stable β-$Ni(OH)_2$ phase. This process is irreversible, therefore once you have this stable structure, you cannot see any of the alpha features in a CV. This is evident by comparing Cycles 1 and 2 (black and red plots, respectively); Cycle 2 shows a relatively flat cathodic region. Further anodic polarization, shown in the black and red curves, oxidises the β-$Ni(OH)_2$ to a β-NiOOH phase. That oxidation process is reversible as shown by the reduction peaks of those two CVs. In Figure B.1 it is also shown that in the far left of the graph, the hydrogen evolution reaction occurs (HER), while in the far right, the oxygen evolution reaction (OER) occurs.

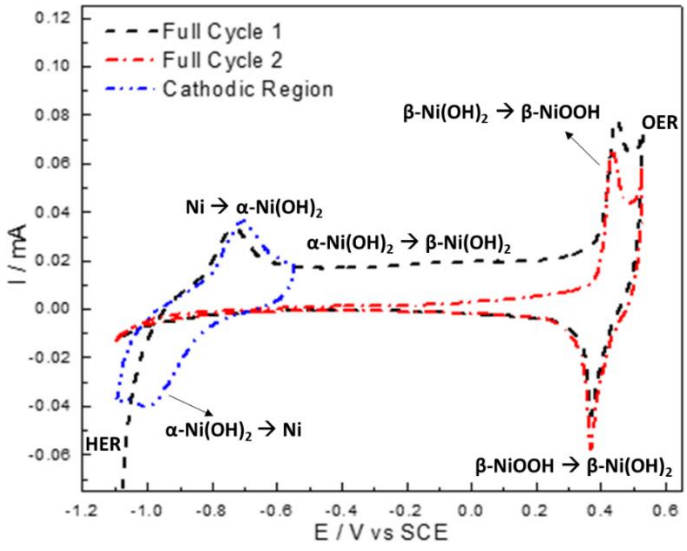

Figure B.1: CVs of Ni wire in 0.1 M potassium hydroxide (KOH) solution from -1.096 to 0.575 V vs SCE in black (Cycle 1) and red (Cycle 2), and from -1.096 to -0.546 V vs SCE in blue, run at a scan rate of 20 mVs^{-1}.

B.2 The "Alpha" Method

Figure B.2 shows an example of the 200 mV idea area in which the Alpha ECSA was calculated.

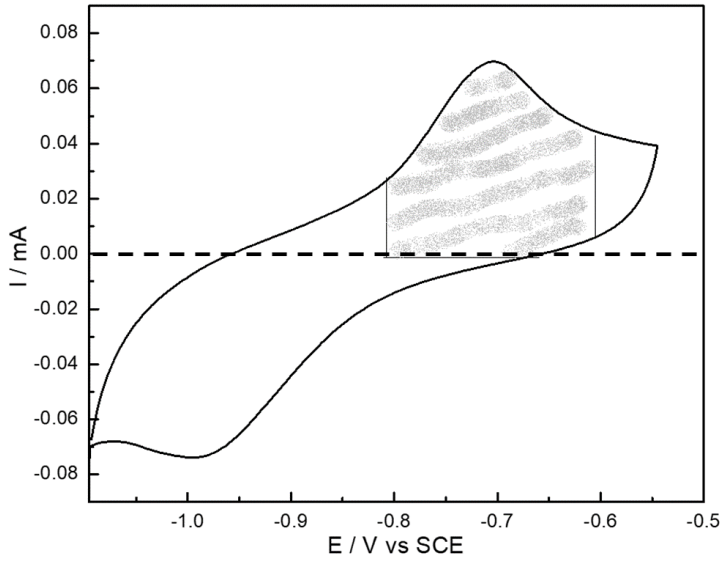

Figure B.2: The Alpha method; Example of the integration area for Ni wire from Cycle 10 of a CV from -1.096 to -0.546 V vs SCE in 0.1 M KOH + 0.08 M $C_2H_2O_4$ run at a scan rate of 50 mVs^{-1}.

The equation used to calculate the charge associated to a certain oxidation or reduction peak is described by Equation B.1.

$$Q\,[\mu C] = 10^6 \left(\frac{\int E\,[V]\, I\,[mA]}{\frac{dE\,[mV]}{dt\,[s]}} \right) \qquad \textit{Equation B.1}$$

Figure B.3 shows how the addition of oxalate in the alkaline electrolyte does not affect the cathodic region of the Ni CV.

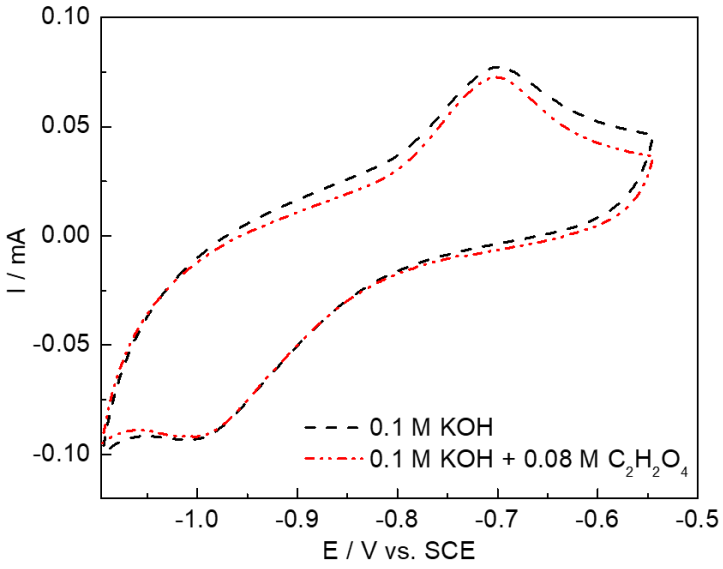

Figure B.3: The Alpha method; Effect of adding oxalic acid to the electrolyte on the cathodic region of Cycle 10 of a CV from -1.096 to -0.546 V vs SCE run at a scan rate of 50 mVs^{-1}. The electrolytes used are 0.1 M KOH (black) and 0.1 M KOH + 0.08 M $C_2H_2O_4$ (red).

B.3 The "Oxalate" Method

Figure B.4 shows the area that was integrated for the Oxalate region, which stretched across 350 mV. Table B.1 tabulates the CV bounds for each material as their overpotential for OER was not the same.

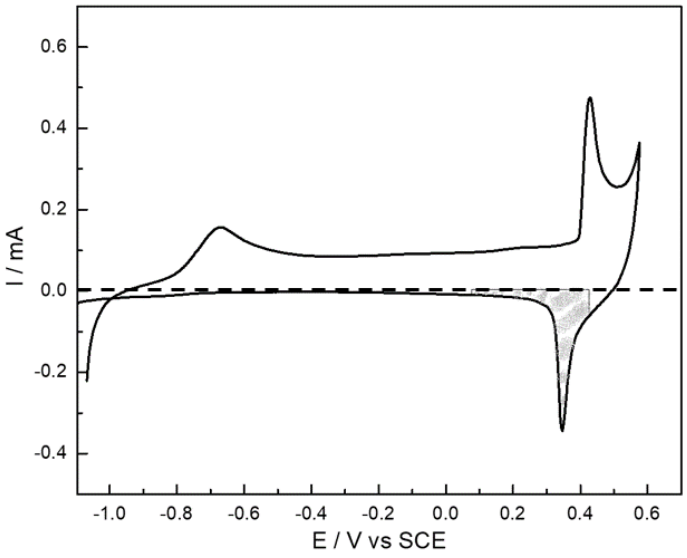

Figure B.4: The Oxalate method; Example of the integration area for Ni wire from Cycle 1 of a CV from -1.096 to 0.575 V vs SCE in 0.1 M KOH + 0.08 M $C_2H_2O_4$ run at a scan rate of 150 mVs^{-1}.

Table B.1: The Oxalate method; CV range for every Ni material.

Material	**CV Window vs SCE**
Ni Wire	-1.096 to 0.575
Ni Foams	-1.096 to 0.625
Ni Triangle	-1.096 to 0.575
Ni Urchin	-1.096 to 0.600
Ni Spherical	-1.096 to 0.750

Figure B.5 shows Cycle 1 and 2 of the Oxalate method, illustrating how the α-$Ni(OH)_2$ transition peak is no longer present after the first scan since the transformation to the β-$Ni(OH)_2$ phase is irreversible.

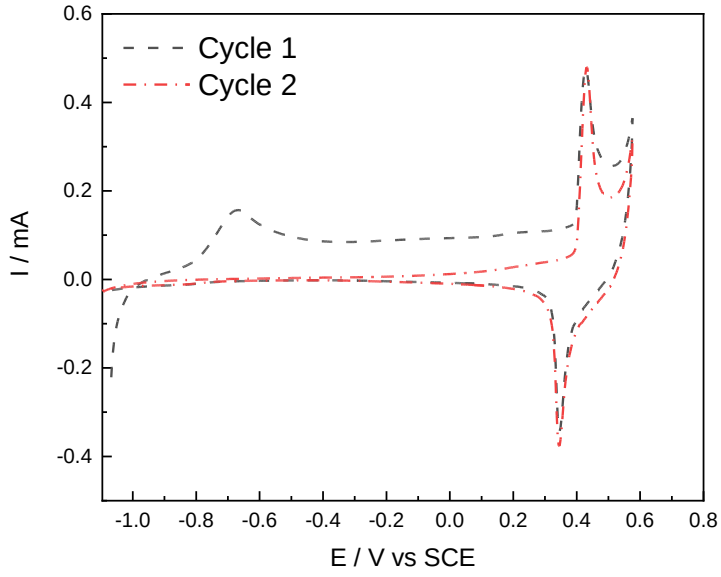

Figure B.5: The Oxalate method; Example of Cycle 1 (black) and Cycle 2 (red) of a CV from -1.096 to 0.575 V vs SCE in 0.1 M KOH + 0.08 M $C_2H_2O_4$ run at a scan rate of 150 mVs^{-1} for Ni wire.

B.4 The "Capacitance" Method

Open circuit values for every material are shown in Table B.2 below. It is important to note that the OCP changes per electrode ink deposition, therefore the values reported below are not absolute.

Table B.2: The Capacitance method; Summary of open circuit potentials (OCP) for every Ni material.

Ni Structure	OCP [mV vs Hg/HgO]
Ni Wire	-220
Ni Foams	130
Ni Triangle	12
Ni Urchin	8
Ni Spherical	274
Ni Spherical / 70 wt% C	295

B.5 The "Beta" Method

Figure B.6 shows the 430 mV integrated area for the beta method. Specific CV bounds are tabulated per material in Table B.3.

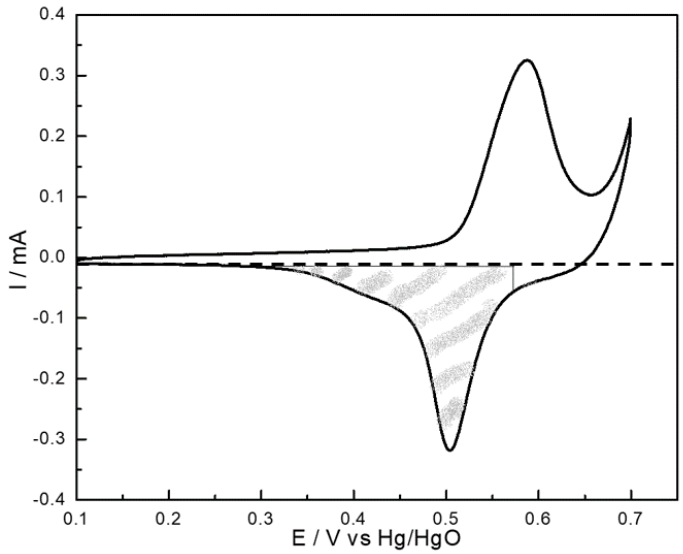

Figure B.6: The Beta method; Example of the integration area for Ni wire from Cycle 100 of a CV from 0.1, 0.7 V vs Hg/HgO in 0.1 M KOH run at a scan rate of 100 mVs^{-1}.

Table B.3: The Beta method; CV range for every Ni material.

Material	CV Window vs Hg/HgO
Ni Wire	0.10 to 0.70
Ni Foams	0.10 to 0.75
Ni Triangle	0.10 to 0.75
Ni Urchin	0.10 to 0.75
Ni Spherical	0.10 to 0.85

B.6 Material Characterization

Figure B.7 below shows other images taken for all materials. Figures B.7c and d were taken on the JEOL JSM-7500F field-emission scanning electron microscope with the FEI Magellan ultrahigh-resolution scanning electron microscope.

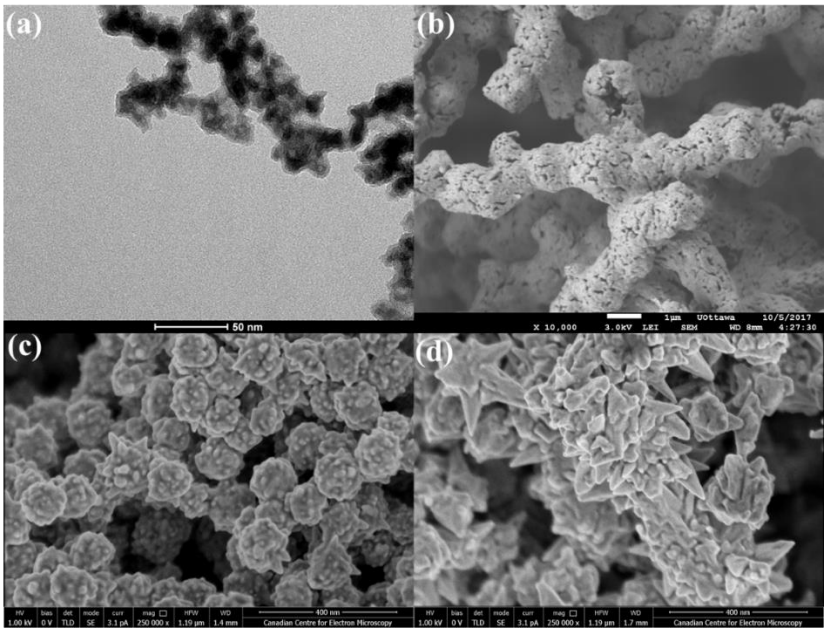

Figure B.7: Ni nanostructures (a) TEM of Ni spherical, (b) SEM of Ni foams, (c) SEM of Ni urchin, and (d) SEM of Ni triangle.

B.7 Confirming the Applicability of the Oxalate Method

Figure B.8 was used to determine whether a limiting cathodic charge is attained at high scan rates. Aside from the spherical NPs that continue to show a slow charge in cathodic charge, a limiting $Q_{cathodic}$ seems to be reached past around 150 to 200 mVs^{-1}.

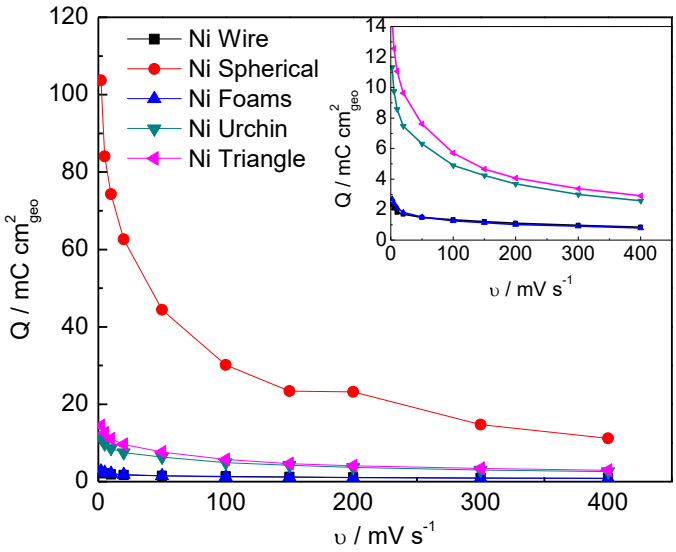

Figure B.8: The Oxalate method; Cathodic charge at different scan rates for CV experiments from -0.046 to 0.575 V* vs SCE in 0.1 M KOH + 0.08 M $C_2H_2O_4$ run at a scan rate of 150 mVs^{-1}. Catalysts; Ni wire (black), Ni spherical (red), Ni foams (blue), Ni urchin (green) and Ni triangle (magenta). The inset figure shows details of the plots with lower currents.

B.8 Capacitance Experiments using Ni Spherical / 70 wt% C

As mentioned in the Section 3.3.3.3 of the main article, the spherical Ni particles did not respond to the capacitance method due to the presence of non-conductive β-Ni(OH)$_2$ species in the material. To confirm this, Ni spherical particles were supported on carbon (30 wt% metal on support) to allow for conduction though the catalytic layer. The synthesis was done by adding Carbon Black (Vulcan XC72, 100%, Cabot Corporation, Boston, MA, USA) and acetone (CH_3COCH_3, ≥99.5%, Sigma Aldrich, St. Louis, MO, USA) directly to the Ni nanoparticle dispersion after it was reduced. After mixing this Ni-C dispersion together for 20 minutes, the particles were washed 3x with acetone. Finally, the bulk of the washing fluid was removed by vacuum filtration, then the sample was further dried in an oven at 40°C for 12 h. As shown in Figure B.9 below, the carbon supported Ni sample shows an extremely steep slope in comparison to the Ni spherical particles, indicating a strong response to the double layer charging. Although this material yielded a high ECSA of 25.55 cm^2 (shown in Table 3.2 of the main text), this value was not further compared to other ECSA values for other methods and materials due to the addition of carbon, which could have multiple promotional effects on the Ni particles, aside from simply promoting electronic conduction in the material.

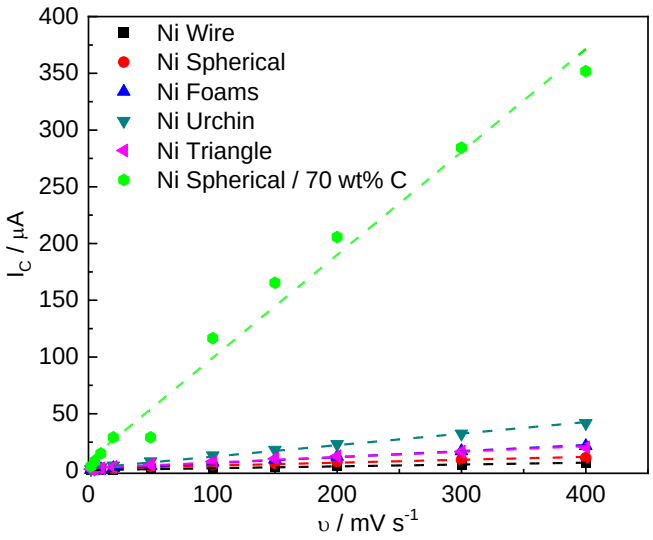

Figure B.9: The Capacitance method; Experimental data of charging current vs scan rate as well as a linear regression of each data set in dotted lines, obtained from CV experiments done ± 50 mV around the OCP in 0.1 M KOH. Catalysts; Ni wire (black), Ni spherical (red), Ni foams (blue), Ni urchin (green), Ni triangle (magenta) and Ni spherical/70 wt% C (lime green).

B.9 Results for ECSA and RF Values for All 4 Methods

Tables B.4 and B.5 include the standard error values between trials for the calculated ECSA and RF values.

Table B.4: Summary of electrochemical active surface area (ECSA) values.

Material	$ECSA_{alpha}$ [cm^2]	$ECSA_{oxalate}$ [cm^2]	$ECSA_{capacitance}$ [cm^2]	$ECSA_{beta}$ [cm^2]
Ni Wire	0.42 ± 0.00	0.74 ± 0.00	0.43 ± 0.01	0.75 ± 0.04
Ni Foams	0.43 ± 0.00	0.75 ± 0.07	1.19 ± 0.14	2.09 ± 0.16
Ni Triangle	2.48 ± 0.23	3.55 ± 0.17	1.27 ± 0.06	2.93 ± 0.12
Ni Urchin	1.86 ± 0.03	3.39 ± 0.27	2.62 ± 0.08	5.08 ± 0.13
Ni Spherical	N/A	21.90 ± 2.73	0.47 ± 0.17	13.37 ± 0.13

Table B.5: Summary of roughness factor (RF) values.

Material	RF_{alpha} [-]	$RF_{oxalate}$ [-]	$RF_{capacitance}$ [-]	RF_{beta} [-]
Ni Wire	2.62 ± 0.03	4.66 ± 0.01	2.18 ± 0.05	3.85 ± 0.18
Ni Foams	2.19 ± 0.02	3.83 ± 0.36	6.06 ± 0.73	10.67 ± 0.84
Ni Triangle	12.67 ± 1.17	19.27 ± 0.29	6.48 ± 0.31	14.97 ± 0.60
Ni Urchin	9.51 ± 0.13	17.28 ± 1.37	13.37 ± 0.41	25.91 ± 0.67
Ni Spherical	N/A	111.71 ± 13.94	2.41 ± 0.86	68.22 ± 0.67

As previously mentioned in the main text, when applying the Oxalate and the Beta methods, some uncertainty arose when selecting the integration window for calculating the charge, *Q*, due to changes in overpotentials between each material as well as system ohmic losses. To see how changing the integration window could affect the results, an alternate integration window was also chosen when applying both methods. Rather than using a larger, fixed integration window as described in Sections 3.2.3.3 and 3.2.3.5 of the main article to calculate the ECSA, a smaller window that encompasses the peak maximum of the reduction of Ni^{3+} was chosen. For the Oxalate method, this window was 125 mV wide, while for the Beta method, this window was 200 mV wide. A summary of the alternate integration windows for each material is shown in Table B.6.

Table B.6: Summary of integration windows used for the Oxalate and Beta methods.

Ni Structure	**Oxalate Integrated Area [V vs SCE]**	**Beta Integrated Area [V vs Hg/HgO]**
Ni Wire	0.300 to 0.425	0.400 to 0.600
Ni Foams	0.250 to 0.375	0.325 to 0.425
Ni Triangle	0.200 to 0.325	0.300 to 0.500
Ni Urchin	0.225 to 0.350	0.275 to 0.475
Ni Spherical	0.150 to 0.275	0.175 to 0.375

When comparing the ECSA results from Table 3.1 in the main text, to the ones shown in Table B.7 below, it is possible to see that aside from sometimes decreasing the obtained ECSA value due to the smaller integration area, changing the window did not have a difference on the relative ECSA values, and thus does not affect the discussion points in the main article.

Table B.7: Results of ECSA values using alternate integration windows.

Ni Structure	**$ECSA_{oxalate}$ [cm^2]**	**$ECSA_{beta}$ [cm^2]**
Ni Wire	0.58 ± 0.03	0.65 ± 0.02
Ni Foams	0.53 ± 0.01	1.67 ± 0.12
Ni Triangle	2.78 ± 0.03	2.27 ± 0.11
Ni Urchin	2.46 ± 0.16	3.71 ± 0.27
Ni Spherical	13.89 ± 1.67	8.89 ± 0.19

The same can of course be said for the difference in the roughness factor values shown in Table B.8 in comparison to the ones shown in Table B.5.

Table B.8: Results of RF values using alternate integration windows.

Ni Structure	**RF_{oxalic} [-]**	**RF_{beta} [-]**
Ni Wire	3.67 ± 0.19	3.30 ± 0.09
Ni Foams	2.72 ± 0.03	8.50 ± 0.60
Ni Triangle	14.18 ± 0.14	11.57 ± 0.56
Ni Urchin	12.54 ± 0.80	18.94 ± 1.38
Ni Spherical	70.88 ± 8.53	45.36 ± 0.95

Appendix C. Supplementary Information for Chapter 4

Content as published in: *Electrocatalysis* **2021**, https://doi.org/10.1007/s12678-021-00674-7.

Figure C.1 shows the three-electrode cell setup used during electrochemical testing. As described in the main text, the working electrode is facing upward for bubble evolution.

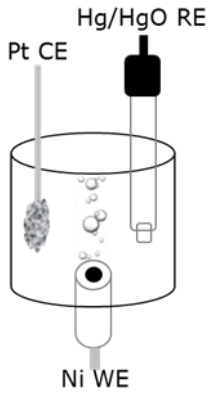

Figure C.1: Schematic of three-electrode electrochemical cell. CE= counter electrode, RE= reference electrode and WE= working electrode.

Figure C.2 shows the OER performance comparing Ni/50 wt% CeO_2 to Ni NPs and CeO_2.

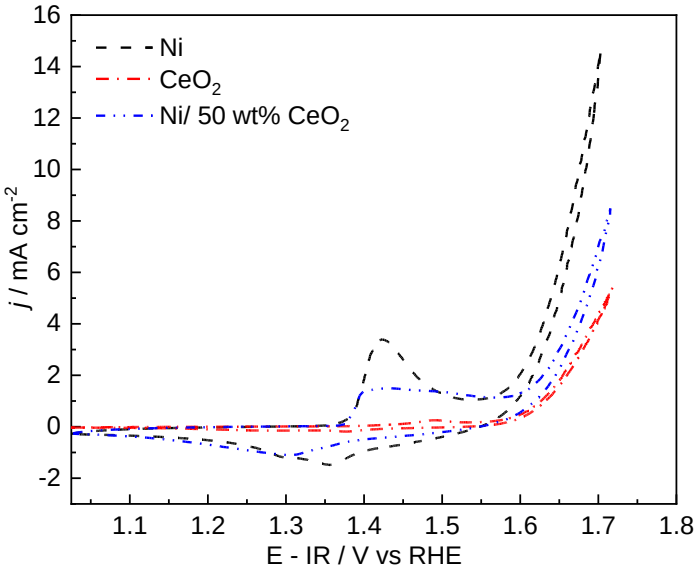

Figure C.2: Cyclic voltammetry cycle 10 run at 25 mV s^{-1} between 0.1 and 0.8 V vs Hg/HgO in 1 M KOH for the Ni, CeO_2 and Ni/ 50 wt% CeO_2 catalysts, as indicated in the figure.

Figures C.3 to C.7 show the areas where the Tafel plots were calculated for Figures 4.4 to 4.7 and 4.9 in the main text, respectively.

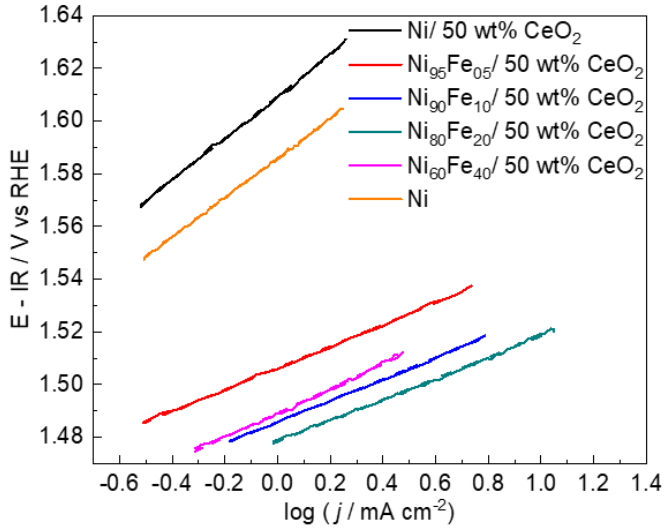

Figure C.3: Tafel regions used for the analysis of Figure 4.4b for the $Ni_{100-x}Fe_x$/ 50 wt% CeO_2 (x = 0, 5, 10, 20, 40 at%) catalysts as well as Ni, as indicated in the figure.

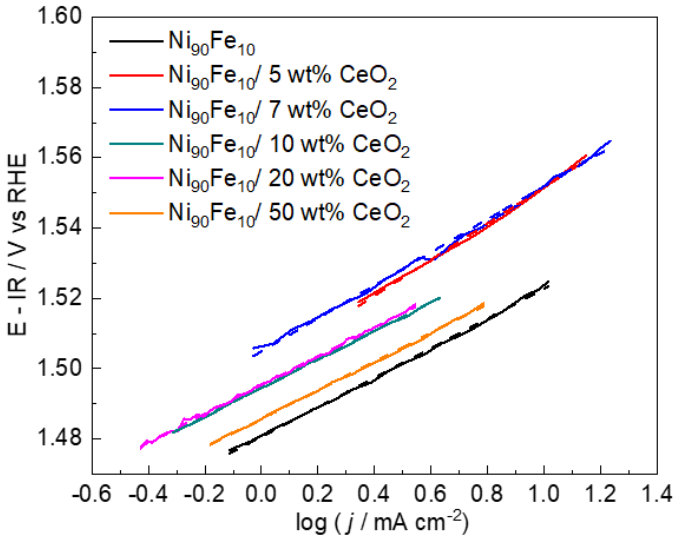

Figure C.4: Tafel regions used for the analysis of Figure 4.5b for the $Ni_{90}Fe_{10}$/ y wt% CeO_2 (y=0, 5, 7, 10, 20, 50 wt%) catalysts, as indicated in the figure.

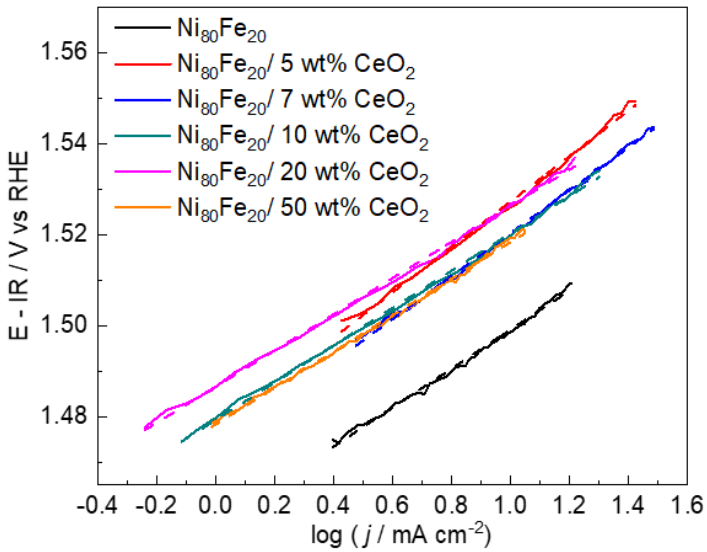

Figure C.5: Tafel regions used for the analysis of Figure 4.6b for the $Ni_{80}Fe_{20}$/ y wt% CeO_2 (y=0, 5, 7, 10, 20, 50 wt%) catalysts, as indicated in the figure.

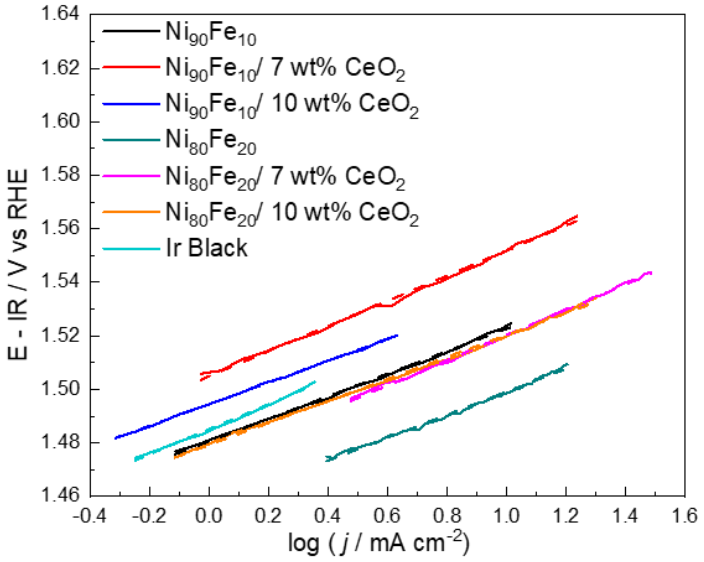

Figure C.6: Tafel regions used for the analysis of Figure 4.7b for the Ir black as well as $Ni_{90}Fe_{10}$/ y wt% CeO_2 and $Ni_{80}Fe_{20}$/ y wt% CeO_2 (y=0, 7, 10 wt%) catalysts, as indicated in the figure.

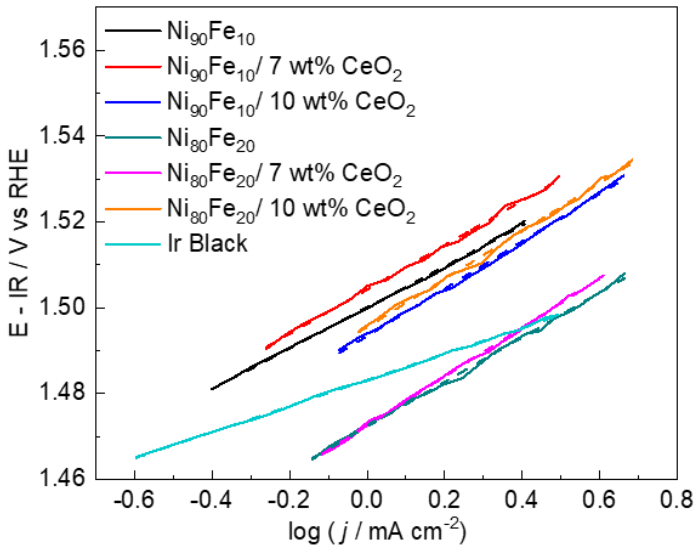

Figure C.7: Tafel regions used for the analysis of Figure 4.9b for the Ir black as well as $Ni_{90}Fe_{10}$/ y wt% CeO_2 and $Ni_{80}Fe_{20}$/ y wt% CeO_2 (y=0, 7, 10 wt%) catalysts, as indicated in the figure.

Figure C.8 shows the comparison of two trials for the stability test (CP for 12 h at 10 mA cm^{-2}) of the $Ni_{80}Fe_{20}$/ 10 wt% CeO_2 sample.

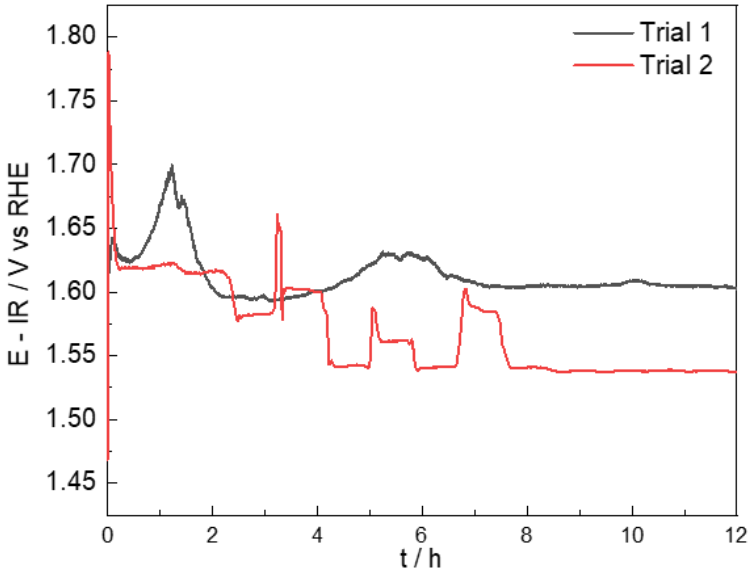

Figure C.8: Stability testing trials for $Ni_{80}Fe_{20}$/10 wt% CeO_2 showing unstable results

Appendix D. Supplementary Information for Chapter 5

Content as published in: *Catalysts* **2019**, *9*, 814, doi:10.3390/catal9100814.

D.1 Target and Final Metal Loadings for the Anodes

As the electrodes for the AEMWE set up were made by hand-spraying a catalyst ink, there is always a certain amount of ink waste that occurs. Although that waste is accounted for in the ink formulation, the target electrode loading is not always obtained. Furthermore, the ink formulation was optimized for the Ir-black reference catalyst therefore the error on the Ni-based electrode loadings was higher, as shown in Table D.1, where the intended metal loading is compared to the actual metal loading of each of the anodes.

Table D.1: Anode metal loadings on the membrane electrode assemblies.

Catalyst	**Intended Metal Loading [mg_{metal} cm^{-2}]**	**Actual Loading [mg_{metal} cm^{-2}]**
Ir Black	3	2.9
Ni	6	3.5
$Ni_{90}Fe_{10}$	6	3.6
$Ni_{90}Fe_{10}/CeO_2$	6	5.3

D.2 Activity of CeO_2 towards OER

Figure D.1 shows a cyclic voltammogram of the promotional effect that the ceria support has on the pure nickel nanoparticles.

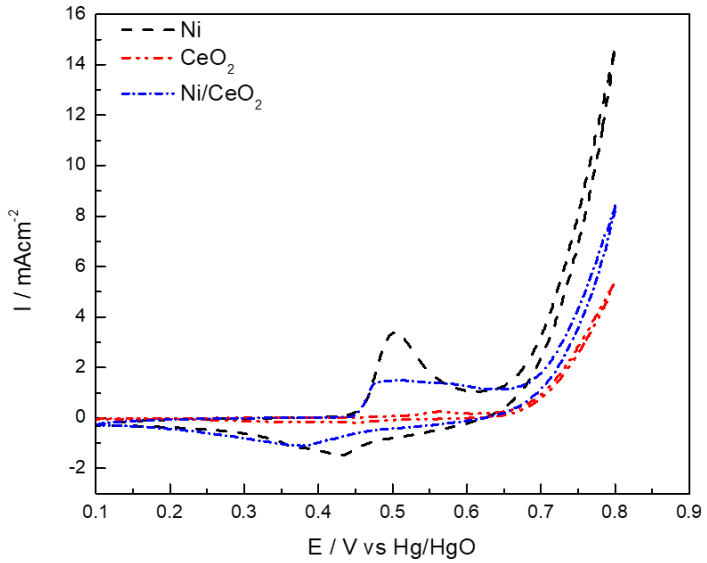

Figure D.1: CVs from 0.1 to 0.8 V of Ni (black), CeO_2 (red) and Ni/CeO_2 (blue) run at 20 mV s^{-1} in 1 M KOH.

D.3 Reference Conversions

Conversions from the Hg/HgO to the RHE reference electrode are done with the following equation:

$$E_{RHE} = E_{Hg/HgO} + E^{0}_{Hg/HgO} + 0.0591(pH) \qquad \textit{Equation D.1}$$

Based on the instrumentation specifications,

$$E^{0}_{Hg/HgO} = 0.098\,V$$

At pH 14,

$$E_{RHE} = E_{Hg/HgO} + 0.925 \qquad \textit{Equation D.2}$$

Using Equation D.2, knowing $E^{\text{water electrolysis}}_{\text{theoretical}} = 1.23\,V$ vs RHE,

$$E^{\text{water electrolysis}}_{\text{theoretical}} = 0.305\,V \text{ vs } Hg/HgO \text{ at pH} = 14$$

Similarly, at pH 13,

$$E_{RHE} = E_{Hg/HgO} + 0.866 \qquad \textit{Equation D.3}$$

Therefore,

$$E^{\text{water electrolysis}}_{\text{theoretical}} = 0.364\ \text{V vs Hg / HgO at pH} = 13$$

D.4 Characterization of the $Ni_{90}Fe_{10}/CeO_2$ Catalyst

As explained in the main article, there are two regions of the $Ni_{90}Fe_{10}/CeO_2$ sample. Figure D.2a shows a TEM image of the cloudier region of the ceria supported sample, which corresponds mostly to the metal in the sample. Figure D.2b shows a TEM image of the more structured area of the sample, which is mostly from the support.

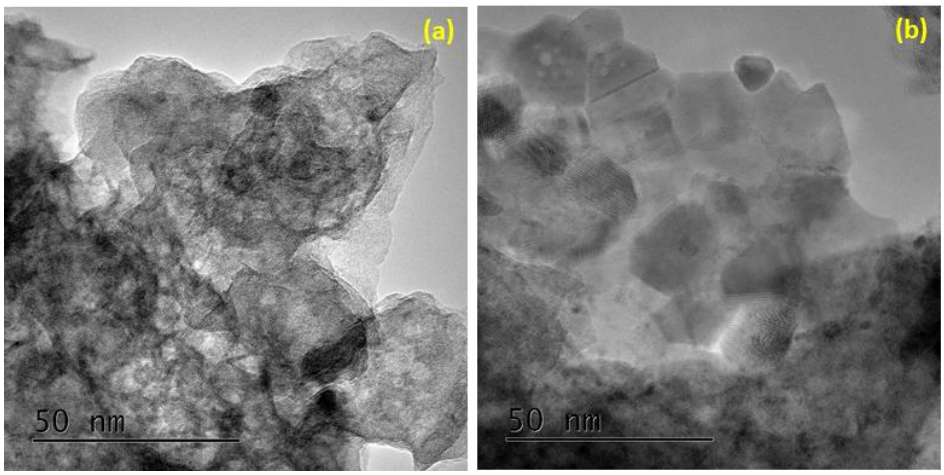

Figure D.2: TEM images of $Ni_{90}Fe_{10}/CeO_2$ showing (a) mostly the Ni and Fe and (b) mostly the CeO_2 support.

Similarly, the STEM images shown in Figure D.3 show a cloudier area (Figure D.3a) as well as a more structured area (Figure D.3b).

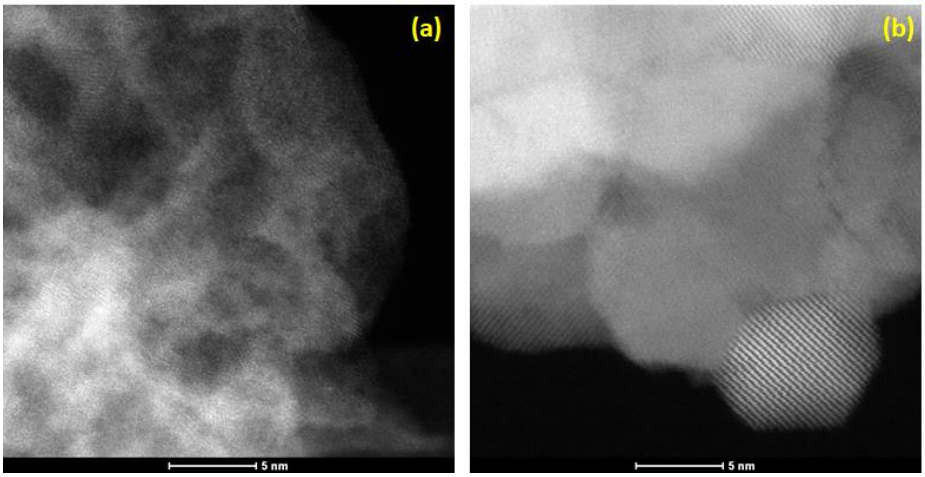

Figure D.3: STEM images of $Ni_{90}Fe_{10}/CeO_2$ showing (a) mostly the Ni and Fe and (b) mostly the CeO_2 support.

The EDX spectrum below shows that the cloudier area of the STEM image shown in Figure D.4a (Region 1) is mostly Ni and Fe, while the more structured area of the image (Region 2) is mostly the ceria support.

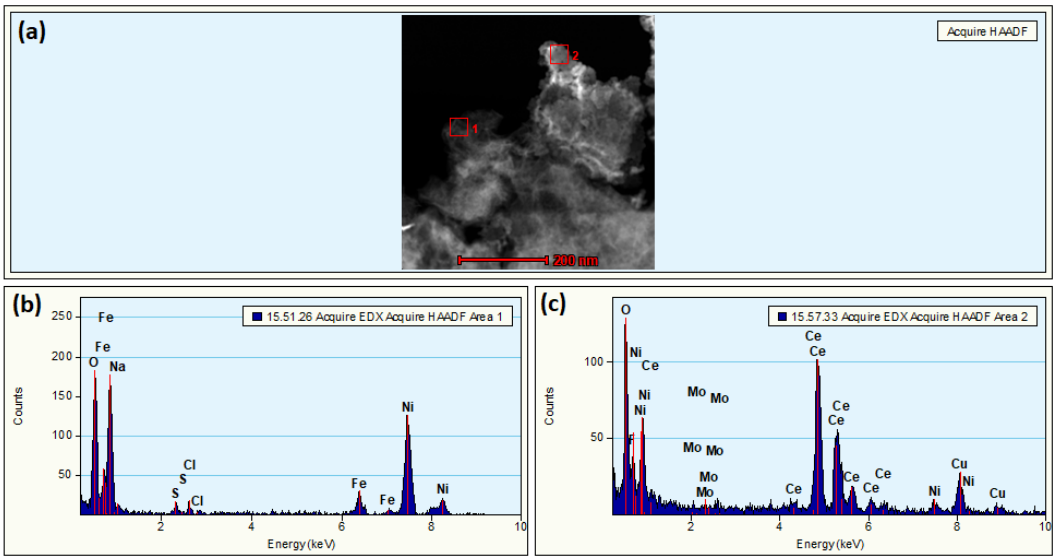

Figure D.4: Spatially-resolved EDX of $Ni_{90}Fe_{10}/CeO_2$. (a) Shows the two selected regions of the STEM image, (b) Shows the analysis of Region 1 and (c) Shows the analysis of Region 2.

Finally, Figure D.5 shows the EELS mapping of the ceria-supported sample. Figure D.5c shows, in orange, the region in which the mapping was carried out. As previously mentioned,

the cloudier area to the left of the area delimited in orange, consist mainly of the Fe and Ni, as shown in Figures D.5a and b, respectively. The more structured area on the right of the orange area can be attributed to the ceria support by looking at the lack of Ni and Fe on the right sides of Figures D.5a and b. Due to issues with how the material was arranged and background subtraction, it was not possible to get a good mapping of the ceria support.

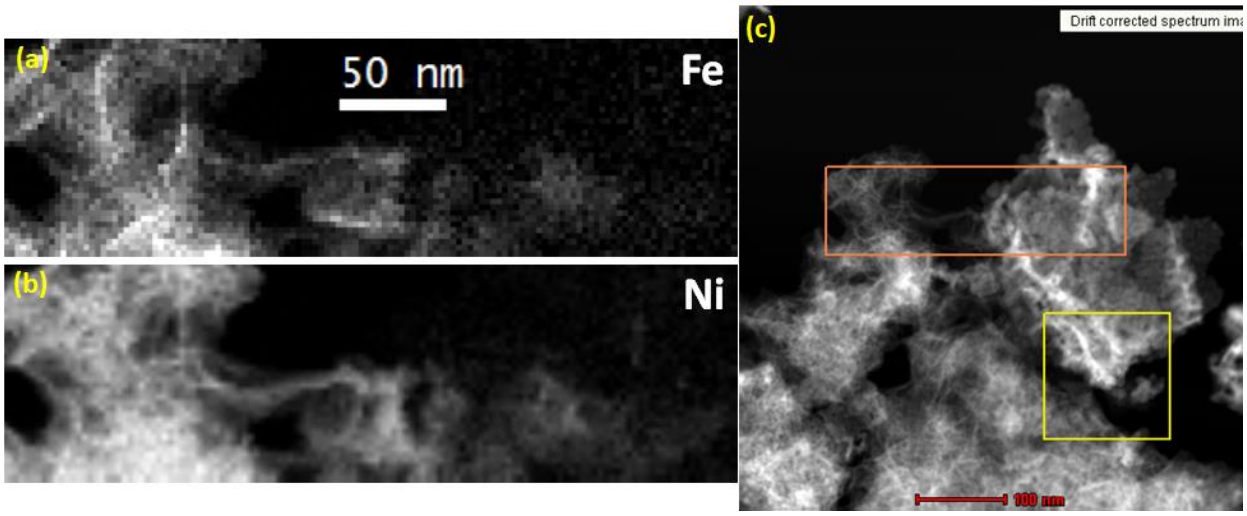

Figure D.5: EELS mapping of $Ni_{90}Fe_{10}/CeO_2$. (a) Shows the Fe mapping, (b) Shows the Ni mapping and (c) Shows the analyzed region in orange.

D.5 Cyclic Voltammogram Results Normalized by Mass of Metal for the Ni-based Catalysts

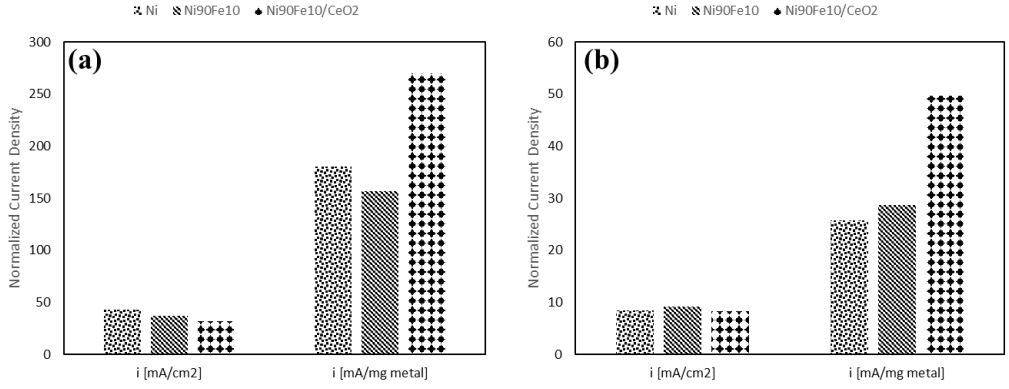

Figure D.6: Comparison between current densities by geometric surface area and by mass of metal at 0.8 V vs. Hg/HgO in (a) 1 M KOH and (b) 0.1 M KOH.

Appendix E. Supplementary Information for Chapter 6

Content as published in: *J. Power Sources* **2021**, *514*, 230563, https://doi.org/10.1016/j.jpowsour.2021.230563.

E.1 Experimental Setup

Figure E.1 shows the experimental setup for the AEMWE experiments.

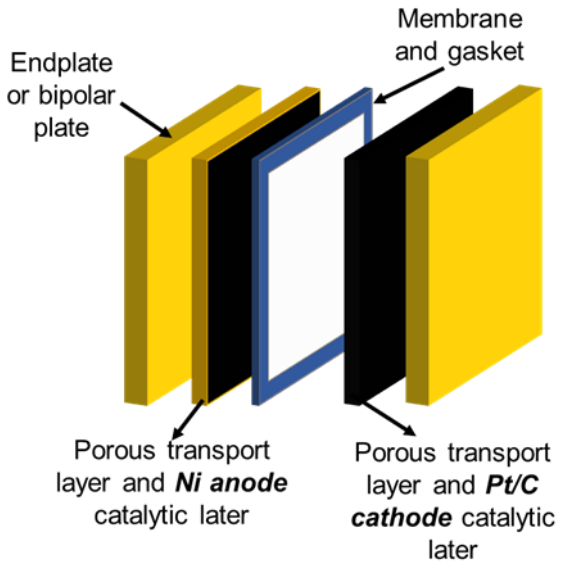

Figure E.1: Electrochemical experiment setup for in-situ AEMWE experiments.

E.2 Anode Catalytic Layer Loading

Table E.1 shows the actual anode loadings used during every experiment.

Table E.1: Anode catalytic layer loadings.

Material	**wt% ionomer**	**Desired Loading [mg_{metal} cm^{-2}]**	**Actual Loading [mg_{metal} cm^{-2}]**
Ni	7	5	5.7
Ni	15	5	6.2
Ni	25	5	5.8
$Ni_{90}Fe_{10}$	15	5	5.9
$Ni_{80}Fe_{20}$	15	5	5.4
$Ni_{90}Fe_{10}$ /10 wt% CeO_2	15	5	3.5
$Ni_{80}Fe_{20}$ /10 wt% CeO_2	15	5	3.3
$Ni_{90}Fe_{10}$ *no sonication*	15	5	4.0

E.3 Effect of Ink Preparation on AEMWE Performance

To evaluate the impact of ink sonication on the AEMWE performance, the experiments in Section 6.2.3.2.2 of the main article were repeated for the $Ni_{90}Fe_{10}$ catalysts, however the amount of sonication used in the ink preparation was reduced. After water and the ionomer was added to the nanoparticles, the sample was sonicated for using 2 mins, then once the IPA was added, the sample was sonicated for 5 mins, both in an ultrasonic bath (45 kHz) over ice. The ultrasonic probe was not used to further sonicate the ink for this experiment. The results of these experiments are presented in Figure E.2, with key data presented in Table E.2. To see polarization curves without IR-correction, see Figure E.3, and to see the best fitted EIS models of the tested electrodes, see Table E.3.

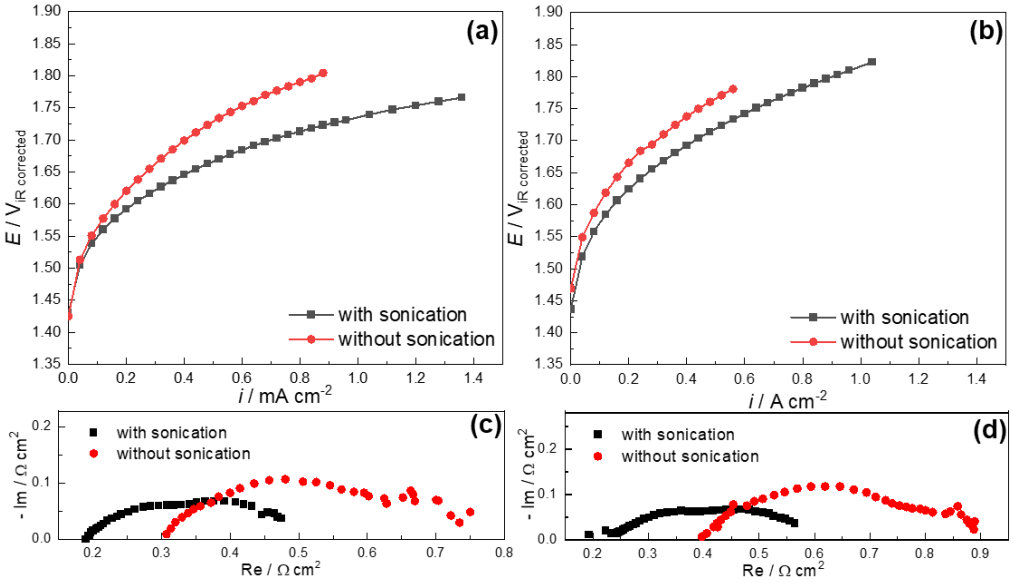

Figure E.2: Polarization curves (a, b) and electrochemical impedance spectroscopy run at 5 A (c, d) in 1 (a, c) and 0.1 (b, d) M KOH at 50°C, of the $Ni_{90}Fe_{10}$ catalyst ink with and without sonication.

Table E.2: Summary of in-situ sonication performance in 1 and 0.1 M KOH extracted from Figure E.2 for the $Ni_{90}Fe_{10}$ ink prepared with and without sonication.

Electrolyte conc. [M]	**$Ni_{90}Fe_{10}$ sonication**	***E* at 0.4 A cm^{-2} [V]**	***E* at 0.8 A cm^{-2} [V]**	**Tafel Impedance [mV]**	**R_{EL} [mΩ cm^2]**
1	with	1.645	1.717	63	170 ± 3
	without	1.698	1.790	86	286 ± 4
0.1	with	1.692	1.782	70	220 ± 2
	without	1.738	N/A	98	397 ± 3

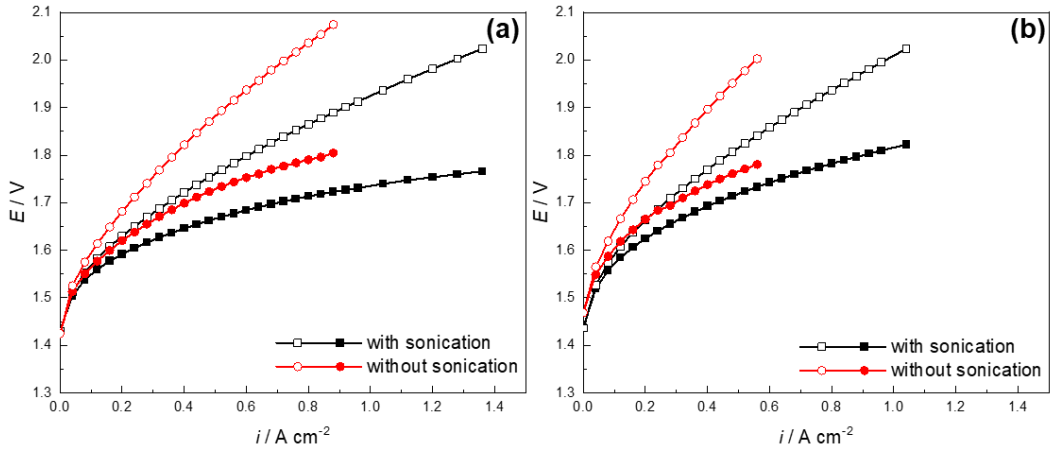

Figure E.3: Polarization curves in (a) 1 and (b) 0.1 M KOH at 50°C for $Ni_{90}Fe_{10}$ with and without sonication. The full symbols are the IR-corrected graphs.

As can be seen in Figure E.2 and Table E.2, sonicating the ink prior to electrode spraying significantly enhances the catalytic activity. However, the electrode loading for the non-sonicated sample was significantly lower (4.0 vs 5.9 mg cm^{-2}) due to lots of waste due to clogging during the spraying. It is therefore possible that the effect of sonication on electrode preparation is mixed with the effect of catalyst loading in the obtained result. As for the polarization and ohmic resistances, they both decreased when the catalyst ink was sonicated. It is possible that this occurs because the lack of sonication resulted in the particles not being properly coated with ionomer and are therefore not well connected to each other within the catalytic layer. Additionally, the low loading of the non-sonicated sample could decrease the contact between the membrane and the catalyst layer, increasing the ohmic resistance of the system.

E.4 Material Characterization

Figure E.4 shows the BJH adsorption pore size distribution measurements by incremental volume (Figure E.4a) and area (Figure E.4b).

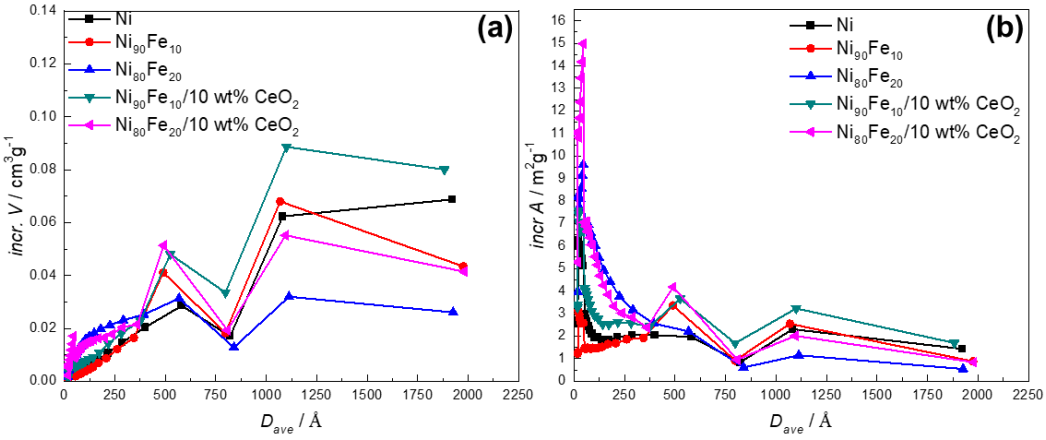

Figure E.4: BJH adsorption pore size distribution by incremental (a) volume and (b) area.

E.5 Ionomer Optimization

Figure E.5 shows the catalyst coated membranes formed with monometallic Ni nanoparticles and different amount of ionomer, after having been exchanged in KOH for 12 h.

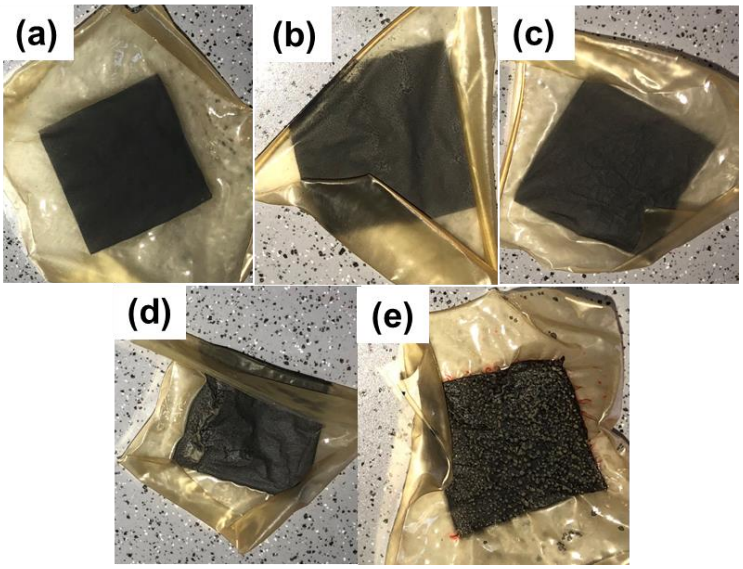

Figure E.5: Dried AEMs after ion exchange in 1 M KOH but prior to electrolysis for (a) 7, (b) 15, (c) 25, (d) 35 and (e) 45 wt% ionomer content.

Figure E.6 shows how a CCM of Ni NPs with a 5 mg cm^{-2} started to crack and come apart as it was submerged in 1 M KOH.

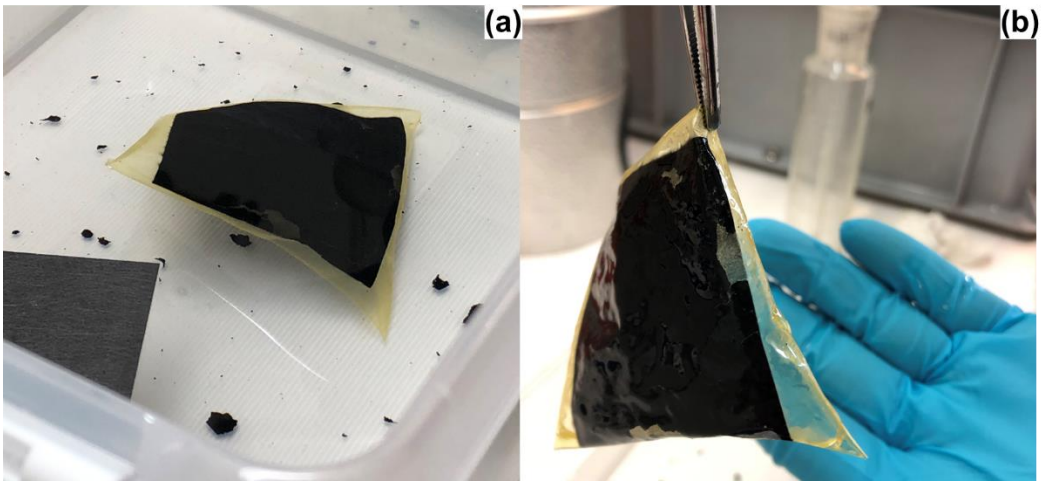

Figure E.6: 25 cm^2 CCM (a) exchanging in 1 M KOH (b) removed from KOH when catalytic layer fell off.

Figure E.7 shows the polarization curves in 1 M KOH of the ionomer optimization study both with and without IR-correction.

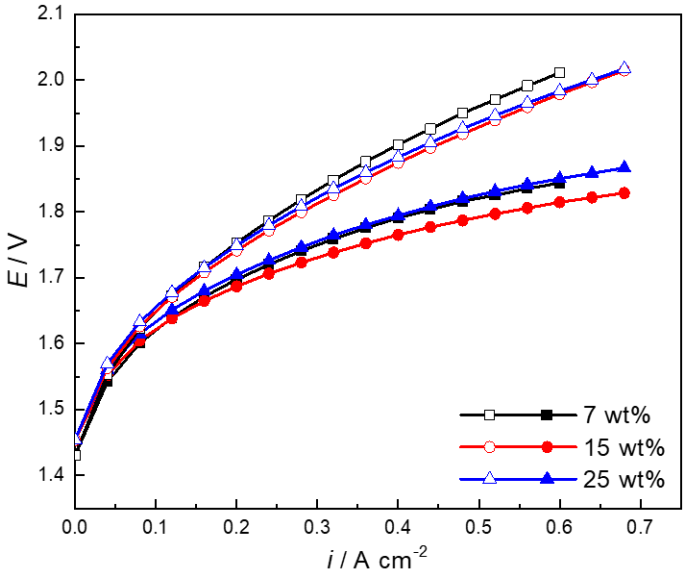

Figure E.7: Polarization curves run at 50°C in 1 M KOH for 7, 15, 25 wt% ionomer. The full symbols are the IR-corrected graphs.

Figure E.8 shows the polarization curves with and without IR-correction in 1 and 0.1 M for the Ni-based materials tested with the optimized 15 wt% ionomer. Figure E.8 also includes the Ir black benchmark electrode.

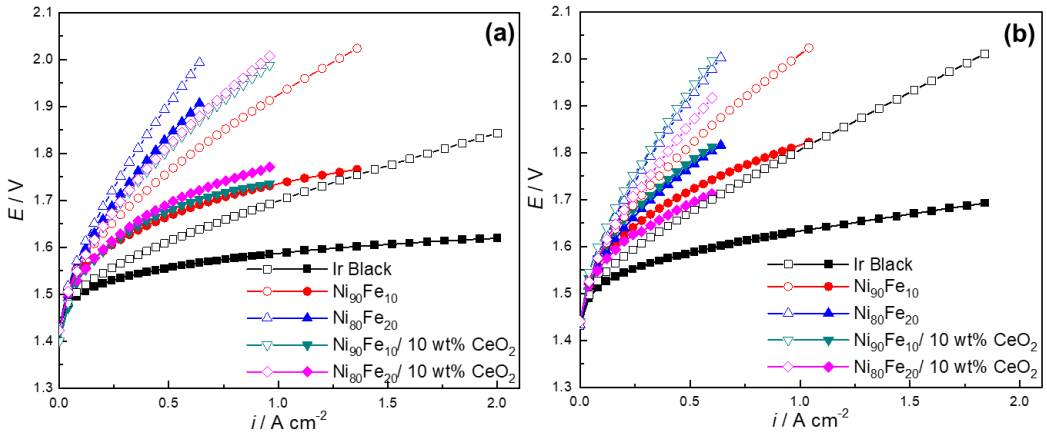

Figure E.8: Polarization curves in (a) 1 and (b) 0.1 M KOH run at 50°C. The full symbols are the IR-corrected graphs.

Figure E.9 shows the EIS spectra that were obtained every hour over 12 hours during the durability experiments.

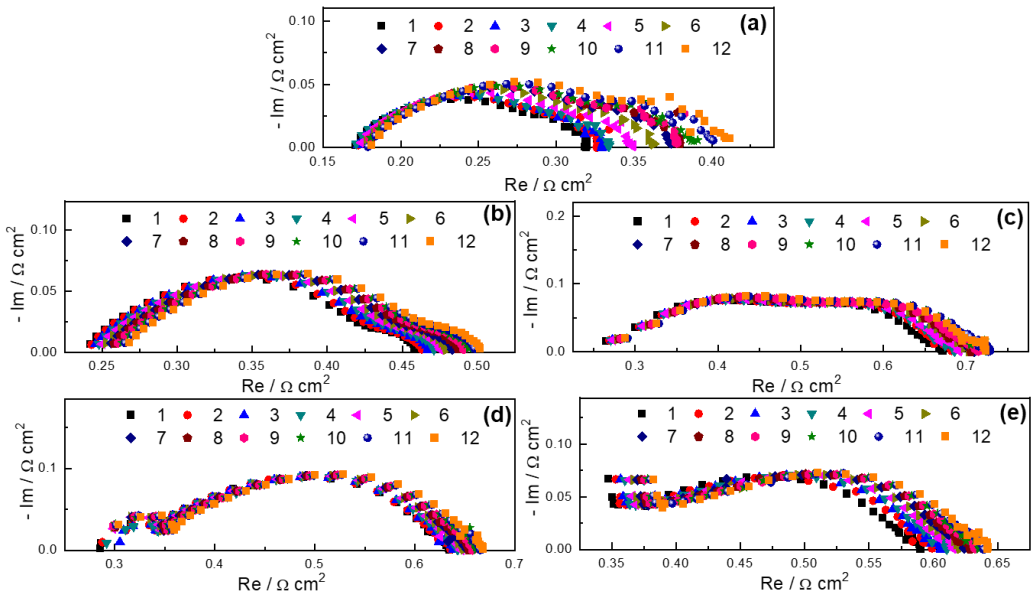

Figure E.9: Electrochemical impedance spectroscopy run at 0.5 A cm^{-2} every hour for 12 hours (time indicated in legend) in 0.1 M KOH at 50°C.

E.6 Summary of EIS Fittings

Tables E.3 to E.7 show the EIS fittings that used to model the experimental data from Figures E.2c and d, 6.4b, 6.6c and d as well as 6.8. The data for all EIS spectra was analyzed below 30 kHz, unless otherwise indicated.

Table E.3: Summary of EIS models for the plots in Figure E.2c and d for $Ni_{90}Fe_{10}$ particles with and without ink sonication in 1 and 0.1 M KOH.

Electrolyte conc. [M]	Material	Circuit Model	L	R_{EL} [mΩ cm^2]	Q_1	n_1	R_1 [mΩ cm^2]	Q_2	n_2	R_2 [mΩ cm^2]
1	$Ni_{90}Fe_{10}$	LR(QR)(QR)	2.44E-04 ± 1.13E-05	170 ± 3	251 ± 59	0.455 ± 0.028	318 ± 64	876 ± 326	1.000 ± 0.405	30 ± 45
	$Ni_{90}Fe_{10}$ no sonication	LR(QR)(QR)	4.88E-04 ± 2.46E-05	286 ± 4	37 ± 7	0.604 ± 0.024	393 ± 21	613 ± 188	1.000 ± 0.158	83 ± 25
0.1	$Ni_{90}Fe_{10}$	R(QR)	---	220 ± 2	250 ± 14	0.415 ± 0.009	406 ± 8	---	---	---
	$Ni_{90}Fe_{10}$ no sonication	R(QR)(QR)	---	397 ± 3	16 ± 2	0.646 ± 0.019	412 ± 17	421 ± 116	0.906 ± 0.119	97 ± 20

Table E.4: Summary of EIS models tested for the plots in Figure 6.4b for Ni NPs with different %ionomer in 1 M KOH.

Material	Circuit Model	L	R_{EL} [mΩ cm^2]	Q_1	n_1	R_1 [mΩ cm^2]	Q_2	n_2	R_2 [mΩ cm^2]
Ni 7 wt%	LR(QR)(QR)	5.33E-04 ± 3.02E-05	254 ± 5	31 ± 6	0.605 ± 0.027	387 ± 19	361 ± 61	1.000 ± 0.084	221 ± 32
Ni 15 wt%	LR(QR)(QR)	7.62E-04 ± 4.45E-05	269 ± 4	848 ± 345	0.737 ± 0.189	354 ± 164	16 ± 6	0.780 ± 0.051	243 ± 29
Ni 25 wt%	LR(QR)(QR)	1.19E-03 ± 3.97E-05	213 ± 3	14 ± 5	0.807 ± 0.048	199 ± 20	589 ± 159	0.778 ± 0.118	338 ± 83

Table E.5: Summary of EIS models for the plots in Figure 6.6c for Ni-based particles in 1 M KOH.

Material	Circuit Model	L	R_{EL} [mΩ cm^2]	Q_1	n_1	R_1 [mΩ cm^2]	Q_2	n_2	R_2 [mΩ cm^2]
Ir Black	LR(QR)(QR)	1.56E-04 ± 1.08E-05	109 ± 1	273 ± 43	0.833 ± 0.070	132 ± 29	184 ± 126	0.722 ± 0.102	46 ± 26
$Ni_{90}Fe_{10}$	LR(QR)(QR)	2.44E-04 ± 1.13E-05	170 ± 3	251 ± 59	0.455 ± 0.028	318 ± 64	876 ± 326	1.000 ± 0.405	30 ± 45
$Ni_{80}Fe_{20}$*	R(QR)	---	130 ± 10	58 ± 5	0.406 ± 0.013	704 ± 18	---	---	---
	LR(QR)(QR)	1.62E-04 ± 3.82E-05	0 ± 54	78 ± 7	0.308 ± 0.030	774 ± 48	14 ± 8	1.000 ± 0.126	77 ± 26
$Ni_{90}Fe_{10}$/ 10 wt% CeO_2	LR(QR)(QR)	8.94E-04 ± 2.26E-05	250 ± 3	34 ± 9	0.683 ± 0.035	242 ± 32	817 ± 221	0.733 ± 0.167	141 ± 49
$Ni_{80}Fe_{20}$/ 10 wt% CeO_2	R(QR)	---	232 ± 6	142 ± 16	0.426 ± 0.018	452 ± 16	---	---	---

*While the LR(QR)(QR) circuit provides a statistically significant better fit, the R(QR) circuit provides an R_{EL} value that is more in line with the value obtained with the raw data. As such, the R_{EL} of the R(QR) circuit is reported in the main text.

Table E.6: Summary of EIS models for the plots in Figure 6.6d for Ni-based particles in 0.1 M KOH.

Material	Circuit Model	L	R_{EL} [mΩ cm^2]	Q_1	n_1	R_1 [mΩ cm^2]	Q_2	n_2	R_2 [mΩ cm^2]
Ir Black	LR(QR)(QR)	1.13E-04 ± 2.39E-05	158 ± 12	247 ± 48	0.790 ± 0.152	144 ± 101	336 ± 617	0.436 ± 0.215	117 ± 127
$Ni_{90}Fe_{10}$	R(QR)	---	220 ± 2	250 ± 14	0.415 ± 0.009	406 ± 8	---	---	---
$Ni_{80}Fe_{20}$	LR(QR)(QR)	2.24E-04 ± 4.10E-05	144 ± 32	117 ± 9	0.296 ± 0.020	695 ± 68	0 ± 0	1.000 ± 0.208	44 ± 35
$Ni_{90}Fe_{10}$/ 10 wt% CeO_2	R(QR)(QR)	---	314 ± 9	448 ± 186	0.320 ± 0.039	438 ± 33	8 ± 3	0.865 ± 0.070	154 ± 35
$Ni_{80}Fe_{20}$/ 10 wt% CeO_2	LR(QR)(QR)	-3.47E-04 ± -2.65E-05	338 ± 5	30 ± 10	0.601 ± 0.045	314 ± 69	1173 ± 616	0.601 ± 0.284	108 ± 86

Table E.7: Summary of EIS models for the durability measurement plots in Figure 6.8 for Ni-based particles in 0.1 M KOH.

Material	Hour	Circuit Model	L	R_{EL} [mΩ cm^2]	Q_1	n_1	R_1 [mΩ cm^2]	Q_2	n_2	R_2 [mΩ cm^2]
Ir Black	1*	LR(QR)(QR)	3.42E-04 ± 1.80E-03	101 ± 13544	163 ± 14	0.543 ± 0.025	165 ± 13	1 ± 328	0.672 ± 2.644	58 ± 13543
	12	LR(QR)	3.06E-04 ± 1.60E-05	155 ± 3	190 ± 13	0.455 ± 0.012	256 ± 5	---	---	---
$Ni_{90}Fe_{10}$	1	LR(QR)(QR)	2.23E-04 ± 8.61E-06	202 ± 5	412 ± 77	0.347 ± 0.029	196 ± 6	16 ± 3	0.956 ± 0.041	73 ± 10
	12*	LR(QR)(QR)	1.62E-04 ± 4.30E-03	11 ± 3.99E07	81 ± 9	0.571 ± 0.029	246 ± 18	0 ± 0	0.866 ± 1.19E10	242 ± 3.99E07
$Ni_{80}Fe_{20}$	1	LR(QR)(QR)	2.80E-04 ± 3.68E-05	0 ± 65	21 ± 3	0.362 ± 0.014	621 ± 60	20 ± 6	0.960 ± 0.067	57 ± 10
	12	LR(QR)(QR)	2.79E-04 ± 4.95E-05	10 ± 81	21 ± 4	0.359 ± 0.017	671 ± 76	22 ± 10	1.000 ± 0.101	50 ± 12
$Ni_{90}Fe_{10}$/ 10 wt% CeO_2	1*	R(QR)(QR)	---	3 ± 9067	0 ± 0	1.000 ± 0.708	325 ± 9074	22 ± 1	0.659 ± 0.012	306 ± 6
	12*	R(QR)(QR)	---	10 ± 8037	0 ± 0	0.957 ± 0.684	338 ± 8043	25 ± 2	0.656 ± 0.013	321 ± 7
$Ni_{80}Fe_{20}$/ 10 wt% CeO_2	1	R(QR)(QR)	---	12 ± 744	0 ± 0	0.967 ± 0.232	329 ± 749	34 ± 3	0.623 ± 0.018	249 ± 9
	12**	LR(QR)(QR)	-2.35E-04 ± -4.48E-06	361 ± 3	61 ± 17	0.534 ± 0.032	240 ± 31	23 ± 17	1.000 ± 0.215	44 ± 33

*The circuit fit has a large error, however it was still kept in the table for comparison. ** The data between 50 and 30 kHz of this plot was included to get a better fit.

Appendix F. Supplementary Information for Chapter 7

Content as submitted to: *ACS Appl. Energy Mater.*, **2022.**

F.1 Methods of Working Electrode Preparation in Three-electrode Cell Experiments

For the sake of simplicity, the explanation of the two WE electrode preparation methods will be provided for a WE with a final nominal ionomer loading of 42 wt%, which is the loading of ionomer used in our other work[1].

For the first method of WE preparation, herein referred to as "Method 1", a catalyst ink was prepared using 6 mg of catalyst, 1000 μL of Milli-Q® water, 200 μL of IPA and 100 μL of 5 wt% Aemion™ solution in MeOH. Once mixed, the ink was sonicated in an ultrasonic bath (40 kHz Ultrasonic Bath 15,337,409, Fischer Scientific, Hampton, NH, USA) for 5 minutes. Then, 5 μL of the catalyst ink was drop cast onto the GC surface of the WE electrode, resulting in an electrode loading of 118 μg cm^{-2}. The WE was then dried in an oven at 60°C for 5 mins. To vary the ionomer concentration on the final WE, the amount of 5 wt% Aemion™ solution in the ink was modified, while adjusting the amount of Milli-Q® water and IPA to maintain a total liquid volume of 1300 μL with a water to IPA ratio of 83:17. This method was however not used to complete this study due to ink instability issues, as will be discussed later in this work.

For the second method of WE preparation, herein referred to as "Method 2", the WE electrode was prepared in 2 steps; (*i*) depositing the catalyst and (*ii*) depositing the ionomer. To deposit the catalyst, an ink was prepared with 6 mg of catalyst, 1000 μL of Milli-Q® water and 200 μL of IPA. This ink was then sonicated in an ultrasonic bath for 5 minutes, after which 9.23 μL of ink was drop cast onto the GC surface. This resulted in a catalyst loading of 235 μg cm^{-2}. The WE was then dried under the fume hood for 15 minutes. Next, to deposit the ionomer, 13.21 μL of a 0.3 wt% Aemion™ solution was added to the GC surface in increments of 2.5 μL or less, to fully cover the GC surface, while minimizing spillage of the solution off the GC surface. The WE was dried in between each added increment of ionomer solution. To vary the ionomer loading on the final WE, the amount of 0.3 wt% ionomer solution deposited onto the electrode surface was modified. Ionomer nominal loadings of 42, 20, 10 and 5 wt% were evaluated in this work. Note

that since this method requires the addition of very small volumes of ionomer solution onto the GC surface, the ionomer solution used was diluted from its initial 5 to 0.3 wt%, and the catalyst loading used was doubled to 235 μg cm^{-2} (equivalent to a 10 μL ink prepared using Method 1). Although diluting the Aemion^{TM} solution allowed for a more manageable volume of drop cast ionomer solution, the required amount of ionomer needed when studying very low ionomer loadings was still too low when working with a catalyst loading of 118 μg cm^{-2} (equivalent to a 5 μL ink prepared using Method 1). Further diluting the ionomer solution past 0.3 wt% resulted in too much spillage outside of the GC surface due to the lack of surface tension resulting from higher quantities of MeOH in the ionomer solution. It should be noted that in both Method 1 and Method 2, the prepared drop-cast electrodes have low loadings meaning that there will likely be experimental error between trials. This error is managed through experimental design and by performing multiple experimental trials to achieve reproducible results.

F.2 Schematic of the Electrolyser and Electrode Loadings

Figure F.1 shows the custom-designed single-cell AEMWE laboratory setup, along with a schematic of the single-cell electrolyser assembly.

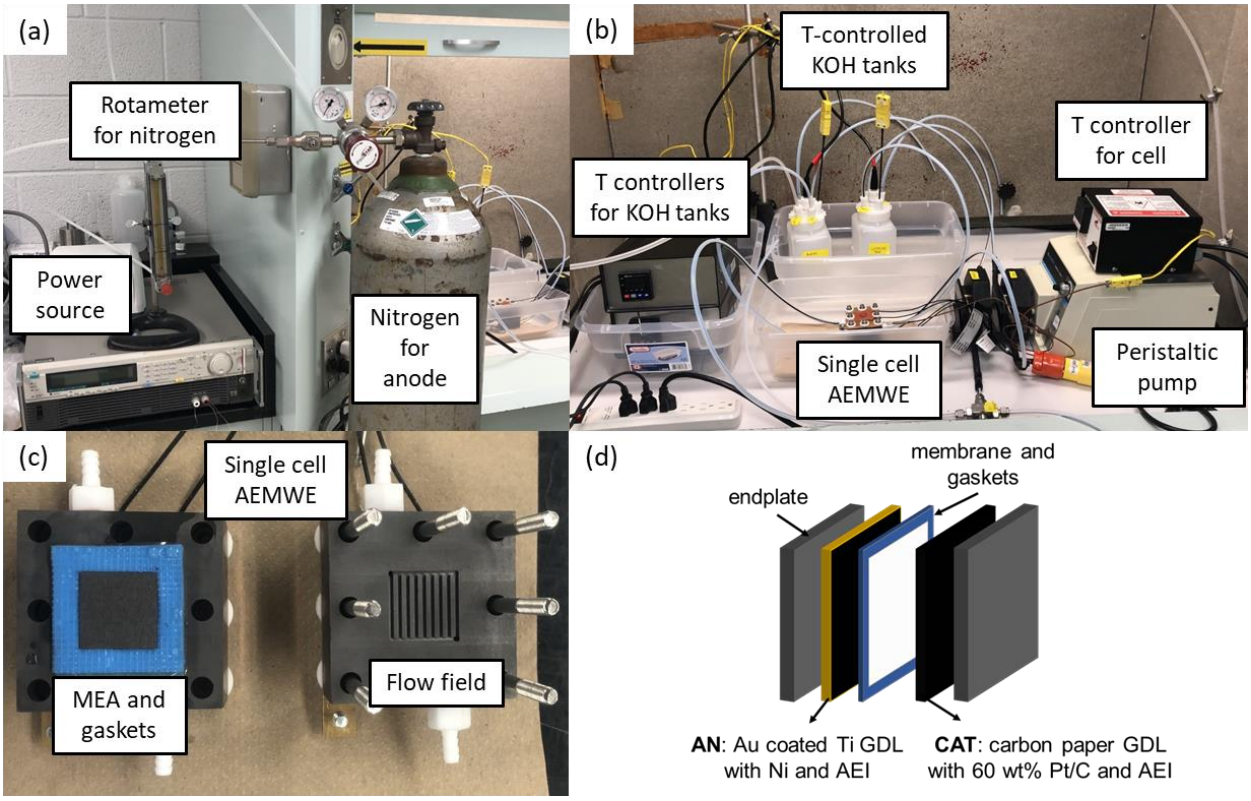

Figure F.1: (a, b, c) Custom built single-cell AEMWE laboratory setup and (b) schematic of single-cell AEMWE.

The AEMWE unit was constructed with two graphite endplates and two gold-coated copper plates, which served as current collectors. The cell was bolted together to a torque of 0.8 Nm using an adjustable torque driver (Vario-S 0.5-2.0 Nm, Wiha Tools Canada LTD., Burlington, ON, Canada). To secure the membrane and seal the cell, polyolefin elastomer gaskets were used (0.35 and 0.5 mm thick, 35 FC-PO 100 Ice Cube Sealing, Quintech, Göppingen, Germany). The anode and cathode sides of the electrolyser were connected to respective sides of a 2 L electrolyte tank made from two square 1 L polyethylene bottles (Dynamic Aqua-Supply Ltd., Surrey, BC, Canada) connected with a custom Teflon salt bridge. Temperature control of the electrolyser active area was achieved by connecting two square silicone rubber flexible heater blankets (1" x 1", 10 W, 120 VAC, Omega, St.-Eustache, QC, Canada) and a thin thermocouple probe (D=0.02", L=2", K-type, Omega, St.-Eustache, QC, Canada) to the FUZYPRO Pro Temp Precision Controller (FUZYPRO No. 1215, Heating Controls and Sensors, LTD., London, ON, Canada). The two silicone heater blankets were placed on either side of the cell, with the thin thermocouple placed between the graphite endplate and current collector on the cathode side. Temperature control of

the electrolyte tank was achieved by pairing two PFA-coated stainless steel self-regulating immersion heaters (L=7", 100 W, 120 VAC, Omega, St.-Eustache, QC, Canada) and two PFA-coated thermocouple probes, (D=0.125", L=12", K-type, Omega, St.-Eustache, QC, Canada) to two SOLO temperature controllers (SOLO4848, AutomationDirect, Cumming, GA, USA). Each side of the electrolyte tank had one thermocouple and one immersion heater. The temperature was held at 50 ± 2°C for all experiments. The electrolyte, consisting of 1 M KOH, was pumped through the system in ¼" Teflon tubing (3/16" ID, ¼" OD, McMaster-Carr, Elmhurst, IL, USA) at 10 mL min^{-1} using a double-headed peristaltic pump (MasterFlex L/S Console Drive 77521-50, Cole-Parmer, Montreal, QC, Canada) with two pump heads (MasterFlex L/S Easy Load II pump heads, 77200-62, Cole-Parmer, Montreal, QC, Canada). Due to the low electrolyte flowrate, two magnetic stirrers (Hanna HI 190M-0, ITM Instruments Inc., Sainte-Anne-de-Bellevue, QC, Canada) were placed under each side of the electrolyte tank to ensure the temperature was uniform throughout the electrolyte. For safety reasons, nitrogen (N_2 Grade 4.8, Linde plc, Dublin, Ireland) was bubbled in the anode chamber at ~ 30 mL min^{-1} during cell operation.

Table F.1 summarized the anode loadings of all AEMWE experiments. The target loading of $Ni_{90}Fe_{10}$ for all anodes was 5 mg cm^{-2}.

Table F.1: $Ni_{90}Fe_{10}$ anode loadings for AEMWE experiments.

Ionomer	**Ionomer Loading [wt%]**	**$Ni_{90}Fe_{10}$ loading [mg cm^{-2}]**
Aemion™	7	3.4
	15	3.7
	25	5.6
	35	7.1
Fumion®	15	4.3

F.3 Three-electrode Cell Electrochemical Methods

F.3.1 Methods of Working Electrode Preparation

As mentioned in the main article, two methods were used to prepare the WE in this study. Initially, Method 1 was to be used to carry out this study, as it is known to form more reproducible and consistent catalytic layers[2,3]. However, for this method to be reproducible, a well-mixed ink

must be prepared. When using 42 wt% Nafion™ in Method 1, reproducibility is very consistent, showing very little to no change over experimental trials [standard deviation (SD) between trials = 0 mA cm^{-2}], a result also reported by McGovern *et al.*[2] when mixing Nafion™ into the inks used to evaluate the formic acid oxidation activity of various unsupported noble metal nanoparticle catalysts. As previously mentioned, since the Aemion™ ionomer is insoluble in water, a well-mixed catalytic ink could not be formed, despite ultrasonication. This resulted in higher experimental variability during three-electrode cell testing using Method 1 due to inconsistencies when preparing the drop-cast electrodes. When testing 42 wt% of the Aemion™ ionomer using Method 1, the current densities achieved at 0.8 V vs Hg/HgO lied within a ~14 mA cm^{-2} range with a SD of 5 mA cm^{-2} between trials. While this range in currents for a repeated experiments is high compared to what is observed using Nafion™, when the ionomer concentration in the ink was decreased, the variability stemming from the poor dispersion of Aemion™ in the ink became much more important. For example, for a final nominal Aemion™ loading of 15 wt%, the current density range at 0.8 V vs Hg/HgO was found to be around ~88 mA cm^{-2}, showing a standard deviation of 35 mA cm^{-2} between trials. This can be seen in Figure F.2. It is possible that in Method 1, having a larger amount of ionomer solution in the ink was helping the dispersion of Aemion™ throughout the ink, however the difficulties in forming a well-mixed system were still present.

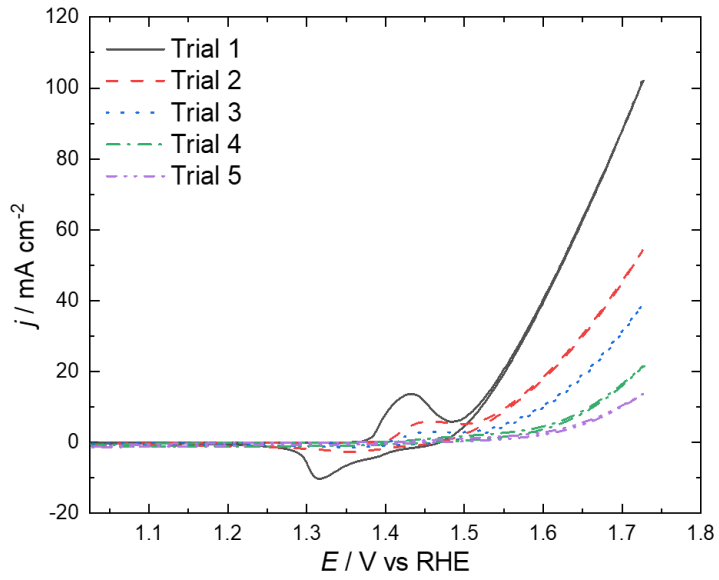

Figure F.2: Cyclic voltammograms for the $Ni_{90}Fe_{10}$ catalyst with 15 wt% Aemion™ in 1 M KOH at RT using Method 1 of working electrode preparation, comparing Cycle 10 of various experimental trials. v = 25 mV s^{-1}. Trial numbers shown in legend.

To reduce experimental variability between trials, Method 2 was used. In this method, mixing Aemion^{TM} with water is avoided by adding the catalyst and the ionomer in layers. It has however previously been reported that depending on the catalyst type and studied reaction, adding Nafion^{TM} either on top of the catalyst or in the ink can alter the shape and peak position of CVs obtained using the catalyst without any ionomer[2]. These results have been attributed to the ionomer causing site blocking effects and, in some cases, preferential activation or deactivation of the tested catalyst. To evaluate whether Method 2 would modify or impair OER activity, both Methods 1 and 2 were evaluated using 42 wt% Nafion^{TM} as the ionomer and an electrode loading of 235 μg cm^{-2}, equivalent to a 10 μL ink.

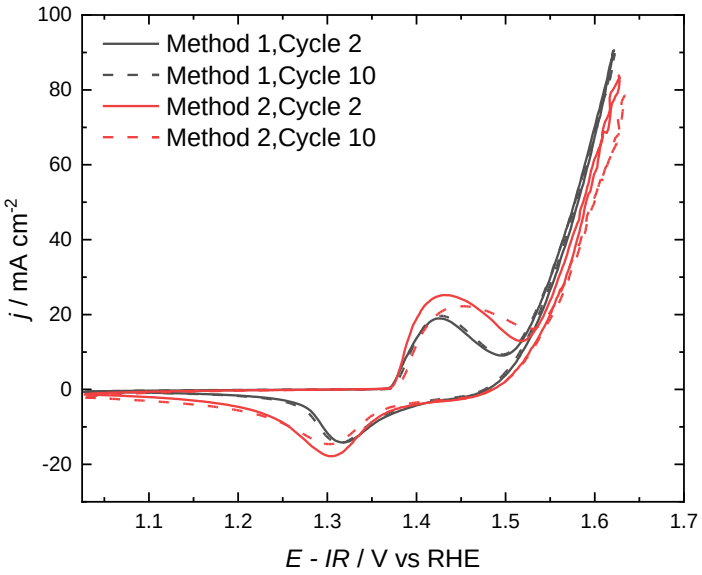

Figure F.3: Cyclic voltammograms for the $Ni_{90}Fe_{10}$ catalyst in combination with 42 wt% Nafion^{TM} in 1 M KOH at RT, comparing Method 1 and Method 2 of working electrode preparation. v = 25 mV s^{-1}. Method and cycle number shown in the legend.

As shown in Figure F.3, both methods show very similar CV profiles and OER activity, meaning the behaviour of the $Ni_{90}Fe_{10}$ catalyst is not significantly disturbed by the change in electrode configuration. While the CV profiles are similar, a slight increase in OER overpotential can be observed between Method 1 and 2, which could be attributed to an increase in the blocking of active sites when the ionomer is placed on top of the catalyst rather than mixed into the ink. Concerning experimental reproducibility, using Method 2 with 42 wt% Nafion^{TM} showed once again, little to no change in currents at 0.8 V vs Hg/HgO with a SD of 0 mA cm^{-2} between trials, meaning that the reproducibility of Method 2 is comparable, if not the same as Method 1. It should

however be noted that bubble detachment from the electrode surface is negatively affected with the ionomer placed on top of the catalyst. This can be seen in Figure F.3 where noise starts to appear on the curve for Method 2 at higher currents, signifying that there is interference from bubble formation/detachment. Additionally, as shown in Figure F.4, multiple small bubbles remained on the 42 wt% Nafion electrode post-OER testing when using Method 2, a phenomenon which was not observed when using Method 1. Reasons for this change in bubble detachment could be due to the modification of the three-phase boundary that occurs when the ionomer is simply placed on top of the catalyst vs. mixed in with the particles in the ink.

Figure F.4: The $Ni_{90}Fe_{10}$ electrode with 42 wt% Nafion™ post-OER testing using Method 2 of working electrode preparation.

Figure 7.1 of the main text shows a comparison of both electrode preparation methods using 42 wt% of the Aemion™ ionomer. As previously mentioned, the change in CV behaviour was similar to what was also observed with the Nafion™ ionomer, where a slight increase in reaction overpotential between Method 1 and 2 is observed, likely due to increased blocking of active sites from the change in ionomer placement in the drop-cast catalytic layer. When employing the Aemion™ ionomer with Method 2 however, a type of charging behaviour between CV cycles is obtained, which was not observed for the Nafion™ ionomer.

In terms of reproducibility, when using Method 2 with the Aemion™ ionomer, the reproducibility of the 42 wt% electrode was slightly worse than in Method 1, where the tested

trials covered a range of 22 mA cm^{-2} at 0.8 V vs Hg/HgO with a SD of 10 mA cm^{-2} between trials. However, when lowering the ionomer concentration, reproducibility was significantly improved. For example, at 10 wt% Aemion™, the current range at 0.8 V vs Hg/HgO was around ~14 mA cm^{-2} with a SD of 7 mA cm^{-2}, a much more acceptable value. It should be noted that when applying Method 2 using 42 wt% of the Fumion® ionomer, there was only a slight difference in currents at 0.8 V vs Hg/HgO between trials of around 2 mA cm^{-2} and a SD of 1 mA cm^{-2}. This indicates that when using the Aemion™ ionomer, other factors are affecting the way the catalyst is behaving, which in turn affects the reproducibility of three-electrode cell experiments. These factors could include the way the ionomer interacts with the catalyst or how the ionomer disperses itself around the catalyst.

F.3.2 Effects of Aemion™ Loading on OER Activity of $Ni_{90}Fe_{10}$

Figure F.5 shows Cycle 10 of the CVs characterizing the OER activity using different amounts of Aemion™.

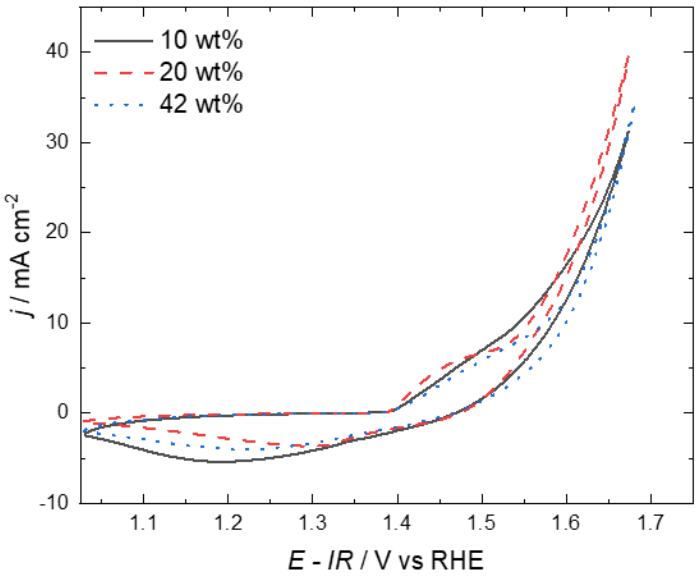

Figure F.5: Cyclic voltammograms for the $Ni_{90}Fe_{10}$ catalyst in 1 M KOH at RT using Method 2 of working electrode preparation, comparing cycle 10 of Aemion™ ionomer loadings of 10, 20 and 42 wt%. v = 25 mV s^{-1}. Ionomer loadings shown in the legend.

Figure F.6 shows the region in which the Tafel slopes were calculated from the LSVs obtained for different amounts of Aemion™.

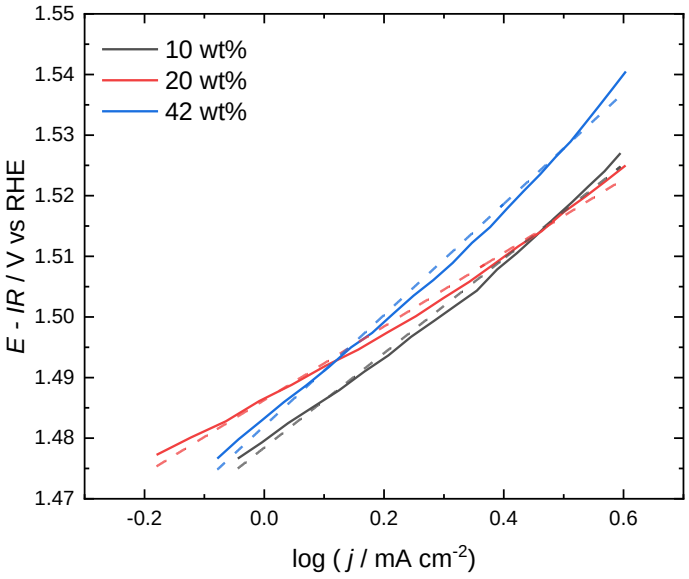

Figure F.6: Tafel plots for the $Ni_{90}Fe_{10}$ catalyst obtained from linear sweep voltammograms (v = 1 mV s^{-1}) in 1 M KOH at RT using Method 2 of working electrode preparation, comparing Aemion™ ionomer loadings of 10, 20 and 42 wt%. Ionomer loadings shown in the legend.

Figure F.7 shows the effects of Aemion™ loading on the OER performance of $Ni_{90}Fe_{10}$. In comparison to Figure 7.2, Figure F.7 includes the 5 wt% loading of Aemion™, which was not included in the main text due to issues reproducing the experiment with so little ionomer binding the catalyst to the GC surface.

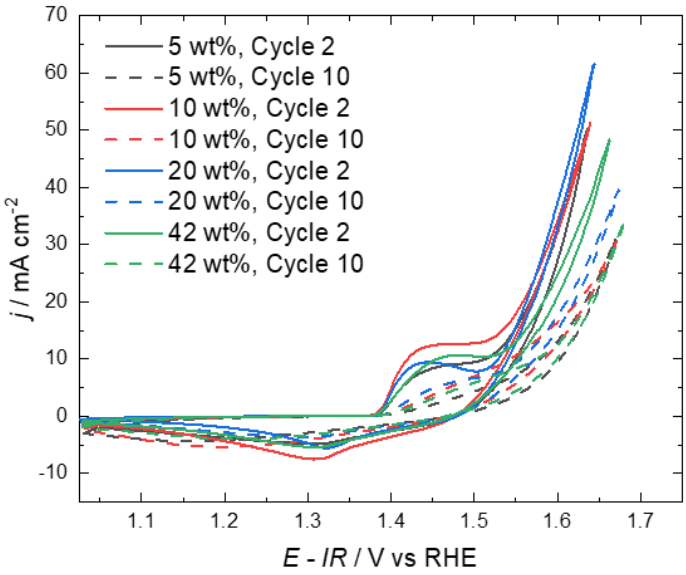

Figure F.7: Cyclic voltammograms for the $Ni_{90}Fe_{10}$ catalyst in 1 M KOH at RT using Method 2 of working electrode preparation, comparing Aemion™ ionomer loadings of 5, 10, 20 and 42 wt%. (v = 25 mV s^{-1}). Ionomer loading and cycle number shown in the legend.

Figure F.8 shows Cycle 2 and 10 of two trials run using 15 wt% Aemion^{TM} using Method 1 of electrode preparation. This figure illustrated that when the ionomer is mixed into the ink directly, there is little to no change in activity with continued cycling.

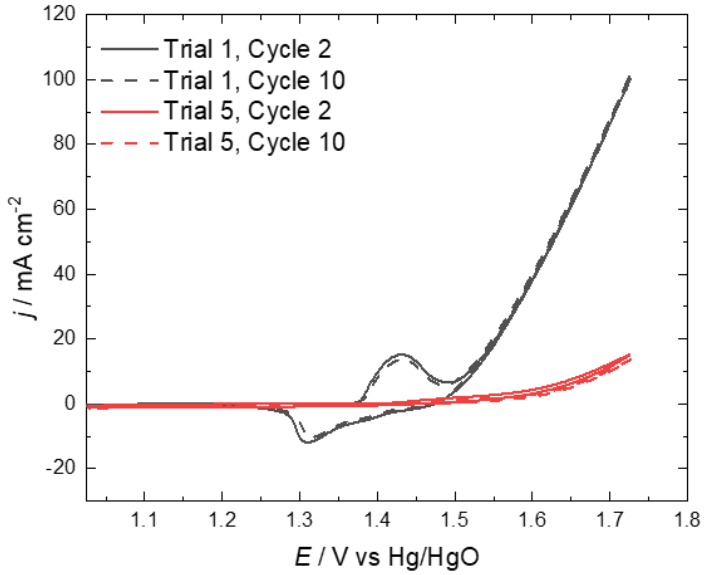

Figure F.8: Cyclic voltammograms for the $Ni_{90}Fe_{10}$ catalyst in 1 M KOH at RT using Method 1 of working electrode preparation, comparing Cycle 2 and 10 of experimental trials in combination with 15 wt% Aemion^{TM}. $v = 25$ mV s^{-1}.

F.3.3 Comparison of Aemion^{TM} to Fumion® and Nafion^{TM}

Figure F.9 shows SEM images of the drop-cast inks prepared using Method 2 of electrode deposition using Aemion^{TM} dissolved in MeOH (Figure F.9a, b), Fumion® in NMP (Figure F.9c) and Nafion^{TM} dissolved in water:IPA (Figure F.9d).

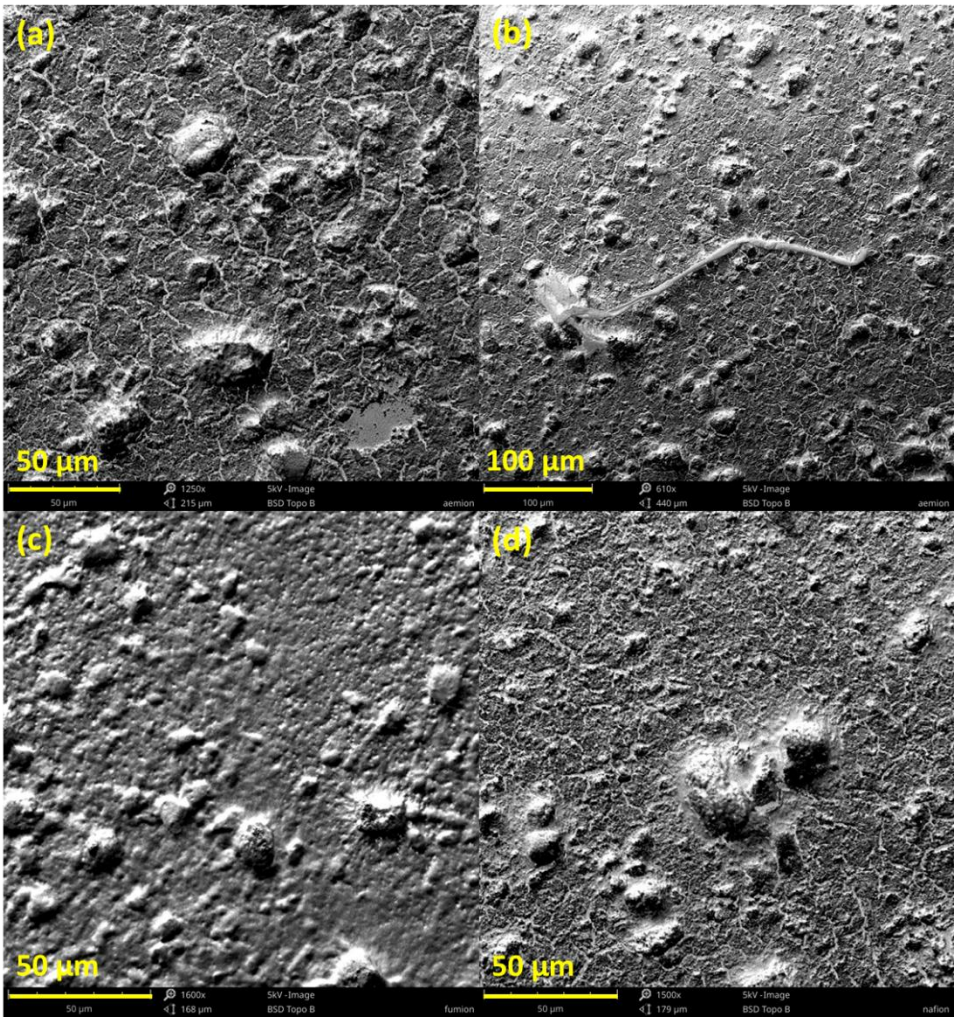

Figure F.9: SEM of the $Ni_{90}Fe_{10}$ drop-cast electrodes prepared using 42 wt% of (a) and (b) Aemion™, (c) Fumion® and (d) Nafion™.

When comparing the surfaces of the different drop-cast electrodes, it is possible to see that both Aemion™ and Nafion™ show cracks in the prepared surface, while Fumion® shows a more continuous surface. This effect could be due to the way the ionomers are interacting with their respective solvent or the catalyst during the electrode drying process. In Figure F.9b, it is possible to see that the Aemion™ electrode has an agglomeration of polymer on its surface, a phenomenon which it not observed on the surfaces of the other electrodes. This could be an indication that Aemion™ does not disperse itself as well across the electrode surface and throughout the particles, which could result in the blocking of active $Ni_{90}Fe_{10}$ sites. It should be noted that using SEM to analyze drop-cast electrode surfaces prepared using Method 2 will not necessarily provide any

concrete information on the effects the various ionomers on the $Ni_{90}Fe_{10}$ catalyst. As such, further interpretation of the observed results in Figure F.9 will not be performed.

Figure F.10 shows Cycle 10 of the CVs characterizing the OER activity using different types of ionomer, namely Aemion™, Fumion® and Nafion™.

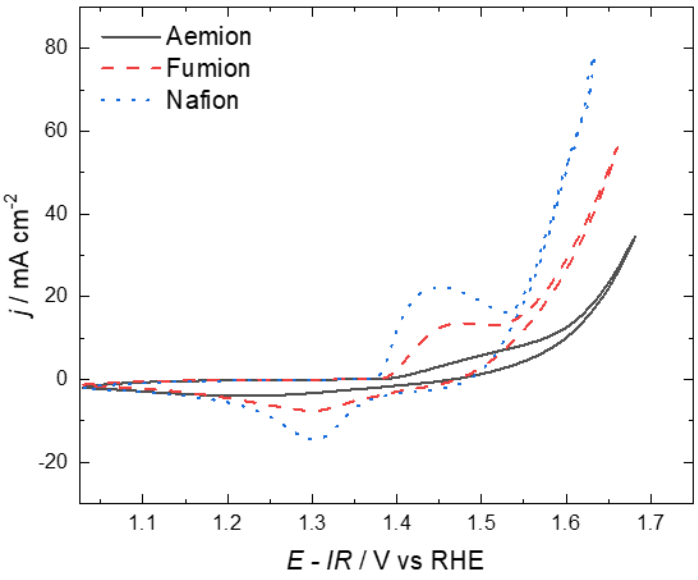

Figure F.10: Cyclic voltammograms for the $Ni_{90}Fe_{10}$ catalyst in 1 M KOH at RT using Method 2 of working electrode preparation, comparing cycle 10 of 42 wt% of the Aemion™, Fumion® and Nafion™ ionomers. $v = 25\ mV\ s^{-1}$. Ionomer type shown in the legend.

Figure F.11 shows the region in which the Tafel slopes were calculated from the LSVs obtained for different types of ionomer.

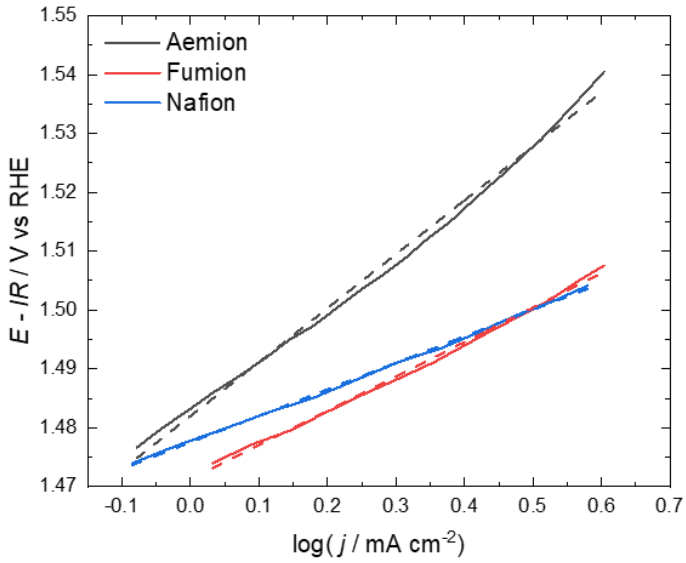

Figure F.11: Tafel plots for the $Ni_{90}Fe_{10}$ catalyst obtained from linear sweep voltammograms (v = 1 mV s^{-1}) in 1 M KOH at RT using Method 2 of working electrode preparation, comparing 42 wt% of the Aemion™, Fumion® and Nafion™ ionomers. Ionomer type shown in the legend.

F.3.4 Analysis of the Effects of Aemion™ Solvent on OER Activity

Figure F.12 shows Cycle 10 of the CVs characterizing the OER activity using different ionomer solvents for the Aemion™ ionomer, namely MeOH, H_2O:IPA and NMP.

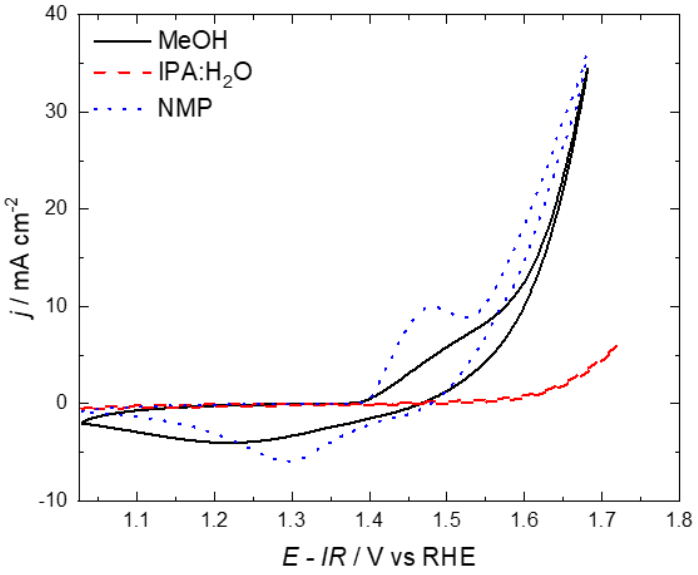

Figure F.12: Cyclic voltammograms for the $Ni_{90}Fe_{10}$ catalyst in 1 M KOH at RT using Method 2 of working electrode preparation, comparing cycle 10 of 42 wt% of the Aemion™ ionomer dissolved in MeOH, H_2O:IPA and NMP. v = 25 mV s^{-1}. Ionomer solvent shown in the legend.

Figure F.13 shows the region in which the Tafel slopes were calculated from the LSVs obtained using different types of solvents for the Aemion^{TM} ionomer.

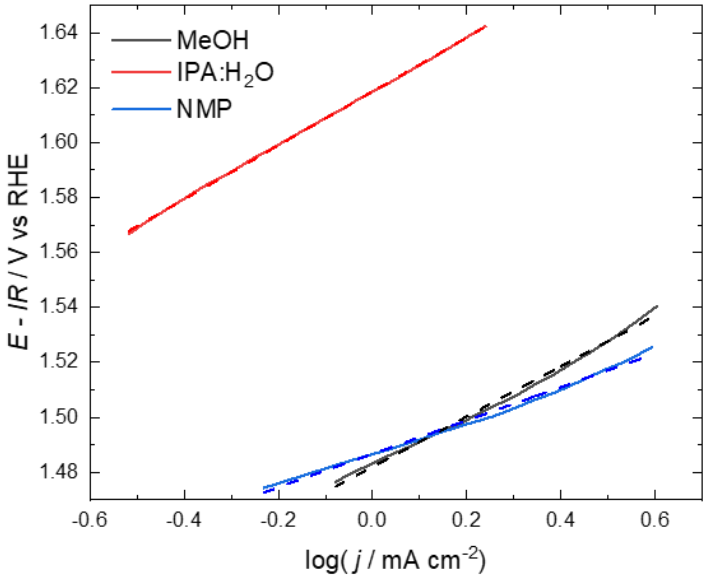

Figure F.13: Tafel plots for the $Ni_{90}Fe_{10}$ catalyst obtained from linear sweep voltammograms (v = 1 mV s^{-1}) in 1 M KOH at RT using Method 2 of working electrode preparation, comparing 42 wt% of the Aemion^{TM} ionomer dissolved in MeOH, H_2O:IPA and NMP. Ionomer solvent shown in the legend.

F.4 Single-cell Electrolysis Experiments

F.4.1 Scanning Electron Microscopy

SEM was used to physically characterize the $Ni_{90}Fe_{10}$ catalytic layers used for AEMWE testing with different nominal loadings of the Aemion^{TM} ionomer. This is shown in Figure F.14 for ionomer loadings of 7, 15, 25 and 35 wt%.

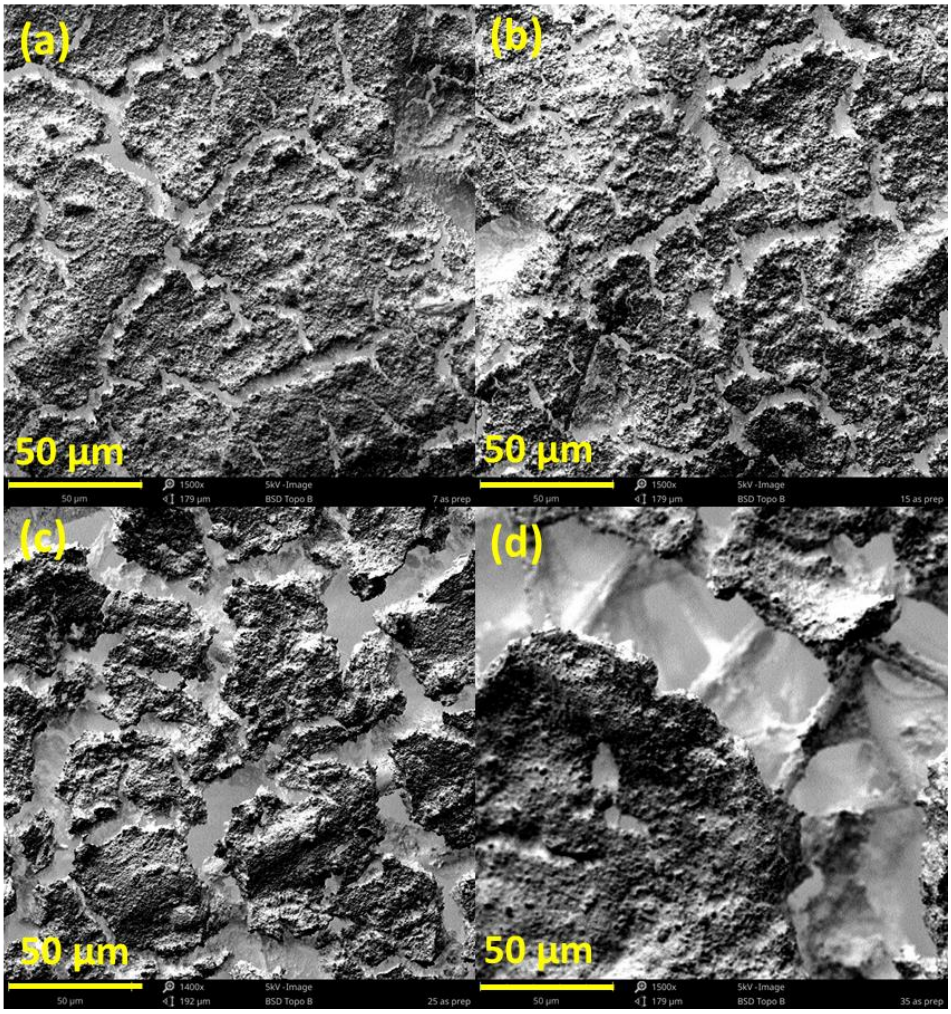

Figure F.14: SEM of the as-prepared $Ni_{90}Fe_{10}$ catalytic layers using 7, 15, 25 and 35 wt% Aemion™.

As previously discussed in the main text, it is possible to observe in Figure F.14 that each of the electrode surfaces shows two phases. A catalyst rich phase, which appears uniform, and an ionomer rich phase, which appears to create channels or cracks throughout the catalytic layer. When increasing the amount of Aemion™ ionomer in the catalytic layers, the cracks in the electrode surfaces, which seem to be agglomerated ionomer, get larger. A similar physical effect of increasing Aemion™ content in the catalytic layer is described in the works of Mayerhöfer *et al.*[4] where they describe a uniform IrO_2 catalyst layer at a low ionomer loading of 10 wt%, and an increasingly inhomogeneous catalytic layer when increasing ionomer loading to 20 and 50 wt%. They also observe two separate phases; a catalyst rich phase, which seems relatively uniform, and a polymer rich phase, which consist of bulges of polymer on the porous layer.

Ideally, the ionomer would help the formation of a uniform, very porous catalytic layer by slowly binding the particles throughout the air brushing process. For this to occur, a well-mixed, optimized ink formulation and spraying process would need to be employed when making the electrode using an air brush. Despite the preliminary measures taken to assist in the formation of a well-mixed ink using Aemion^{TM} (see Section 7.2.4.3 of the main article), the ionomer was still not properly dispersing itself in the ink, resulting in an inhomogeneous electrode surface. Koch *et al*.[5] similarly relate ink stability issues to the formation an inhomogeneous IrO_x catalytic layer with higher Aemion+^{TM} ionomer loadings. They however mention that the ink is less stable with more ionomer, which is the opposite of our observations when hand-spraying the electrodes. It should however be noted that in comparison to the ink formulation used by Koch *et al*.[5], different solvents, catalysts and types of Aemion^{TM} ionomers were used in this study, all of which could affect the interactions within the ink dispersion, therefore affecting the ink stability and resulting electrode morphology[6,7]. While our ink dispersion appeared to be more stable with increasing ionomer content, this result was not carried forward onto the resulting electrodes, indicating that more factors are at play. For example, Lei *et al.*[8] demonstrated that the ink solvent has an effect on catalyst layer morphology. When using a 2-propanol/water solvent in the inks used to prepare a Pt/C catalytic layer using the Nafion^{TM} ionomer, the resulting layer formed large cracks, whereas other solvents such as ethylene glycol, 1, 2-butanediol and 1-propanol/water resulted in more uniform surfaces with no cracks. In addition to factors related to ink formulations, the electrode fabrication method, i.e. the ink deposition method and ink deposition conditions, will also have an impact on the resulting catalytic surfaces[9].

The observed ionomer channels in the Aemion^{TM} catalytic layers are different from what we have previously observed when forming Ni catalytic layers with Fumion$^{®}$[10]. In that study, the prepared surfaces were uniform, where less Fumion$^{®}$ ionomer showed a more textured, porous surface and more ionomer showed a smoother surface with agglomerates on top. The Fumion$^{®}$ observations are more in line with other previously reported changes in electrode surfaces with increasing ionomer content[11,12]. Overall, from inspection of the SEM images in Figure F.14, it can be said that less Aemion^{TM} forms a surface with less cracks or ionomer channels, which could be beneficial for AEMWE activity. It is possible that the larger ionomer channels will result in the blocking of active sites by (*i*) pushing more particles together and (*ii*) covering of the particles once the catalytic layer is exchanged in 1 M KOH. This effect can be seen in Figures F.15 and

F.16, which show electrode surfaces after being in exchanged in 1 M KOH at two different magnifications. It can be observed that as the ionomer content increases, more ionomer covers the catalyst particles. It should be noted that the surfaces shown in Figures F.15 and F.16 are not completely representative of the ones used during AEMWE operation because here, the effects of exchanging the layers in 1 M KOH in preparation for electrolysis testing are combined with the effects of drying the layers in preparation for taking SEM images.

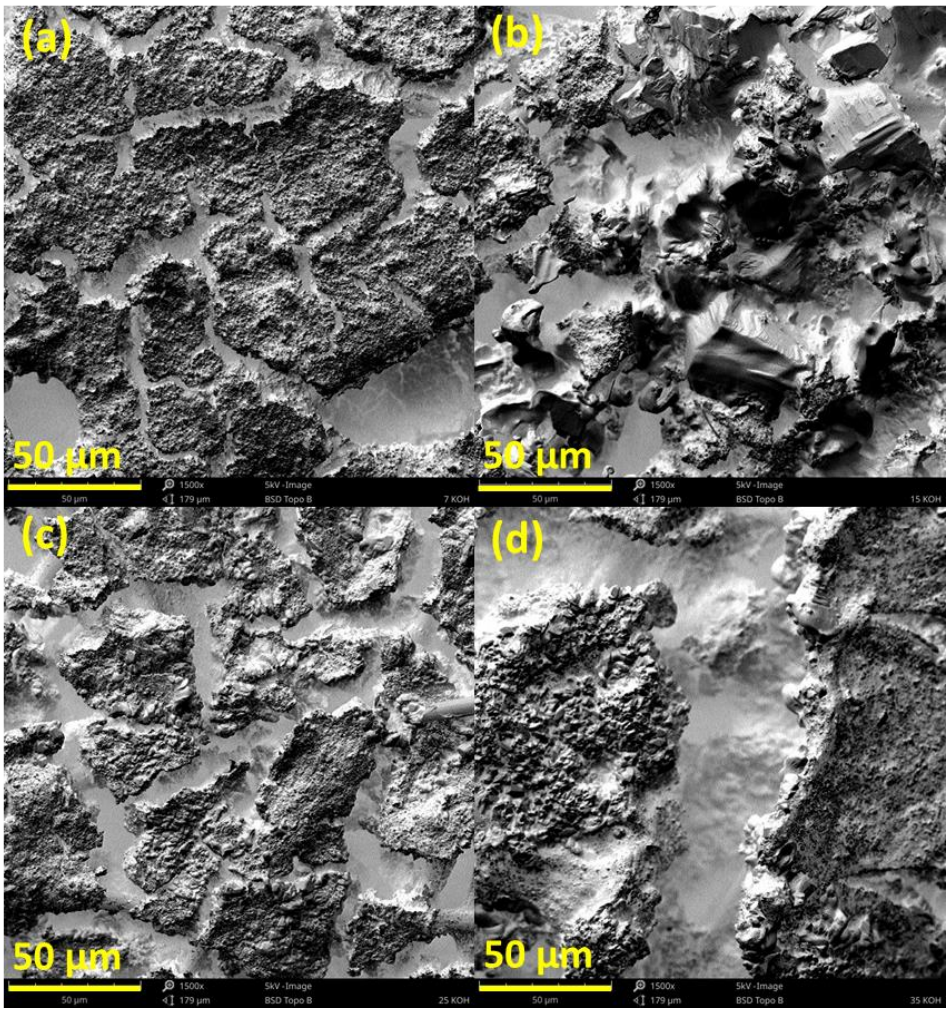

Figure F.15: SEM of the $Ni_{90}Fe_{10}$ electrolysis anodes after exchanging in 1 M KOH, prepared using 7, 15, 25 and 35 wt% Aemion™.

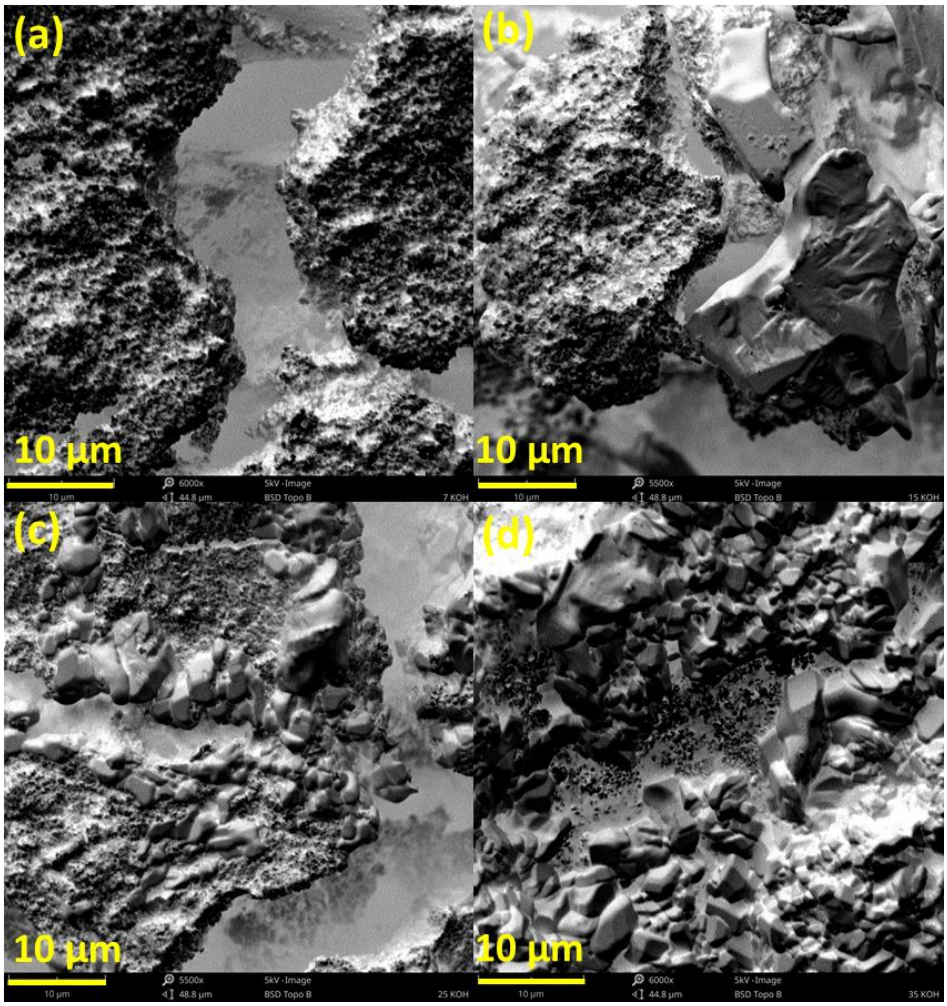

Figure F.16: SEM at higher magnification of the $Ni_{90}Fe_{10}$ electrolysis anodes after exchanging in 1 M KOH, prepared using 7, 15, 25 and 35 wt% Aemion™.

F.4.2 Single-cell Electrolysis Electrochemical Testing

Figure F.17 shows polarization curves obtained in a single-cell AEMWE when comparing different loadings of Aemion™ (Figure F.17a) and when comparing 7 wt% Aemion™ to 15 wt% Fumion® (Figure F.17b). Unlike Figures 7.7a and 7.8a, the data presented here is normalized by the mass of $Ni_{90}Fe_{10}$ (see Table F.1) at the anode of the AEMWE.

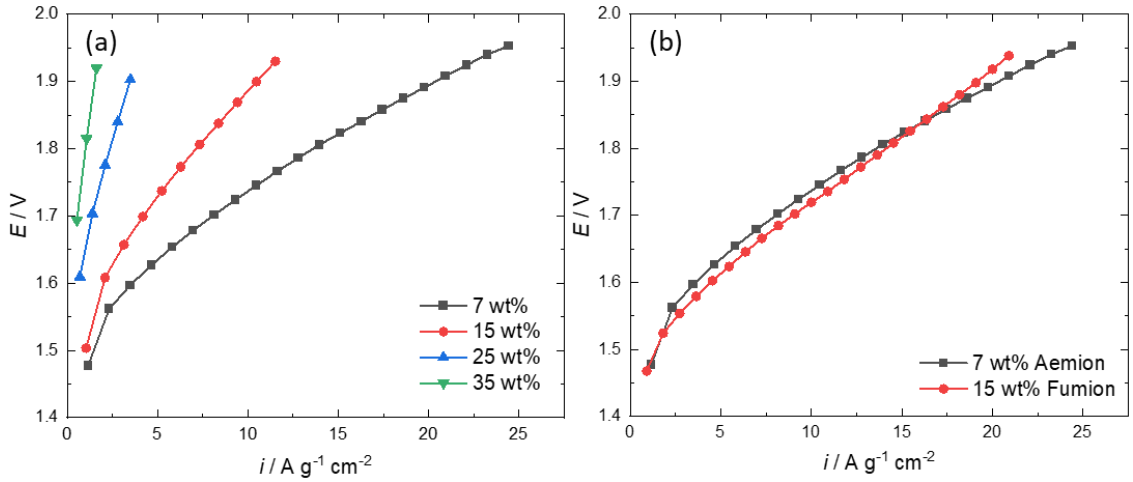

Figure F.17: Polarization curves for the $Ni_{90}Fe_{10}$ catalyst in 1 M KOH at 50°C, comparing (a) Aemion™ ionomer loadings of 7, 15, 25 and 35 wt% and (b) 7 wt% Aemion™ and 15 wt% Fumion®. Ionomer type and loadings shown in the legend. Data is normalized by mass of $Ni_{90}Fe_{10}$.

Figure F.18 shows the $Ni_{90}Fe_{10}$ catalytic layers after single-cell electrolysis experiments, showing differences in the remaining $Ni_{90}Fe_{10}$ catalyst still attached to the GDL. The samples were photographed directly after opening the electrolysis cell post-testing and the images were taken under laboratory lighting.

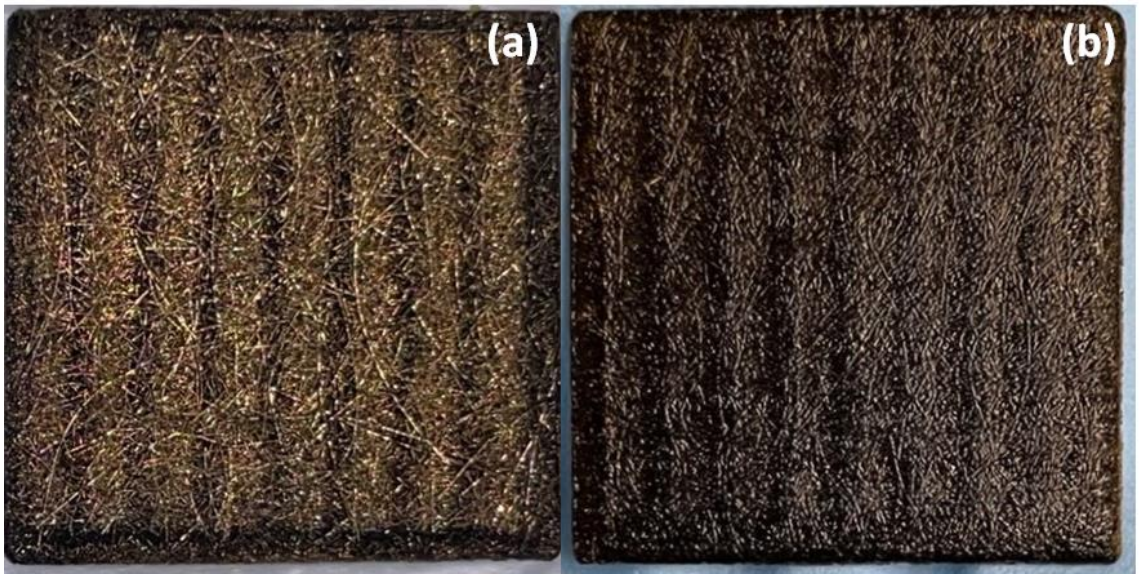

Figure F.18: Comparison of the $Ni_{90}Fe_{10}$ catalytic layers post-electrolysis testing using (a) 7 wt% Aemion™ and (b) 15 wt% Fumion®.

F.4.3 Raman Spectroscopy

Figure F.19 and F.20 show Raman spectra obtained for dry Aemion^{TM} (Figure F.19a), the $Ni_{90}Fe_{10}$ nanoparticles (Figure F.19b) and the as-prepared $Ni_{90}Fe_{10}$ anode with 7 wt% Aemion^{TM} (Figure F.20).

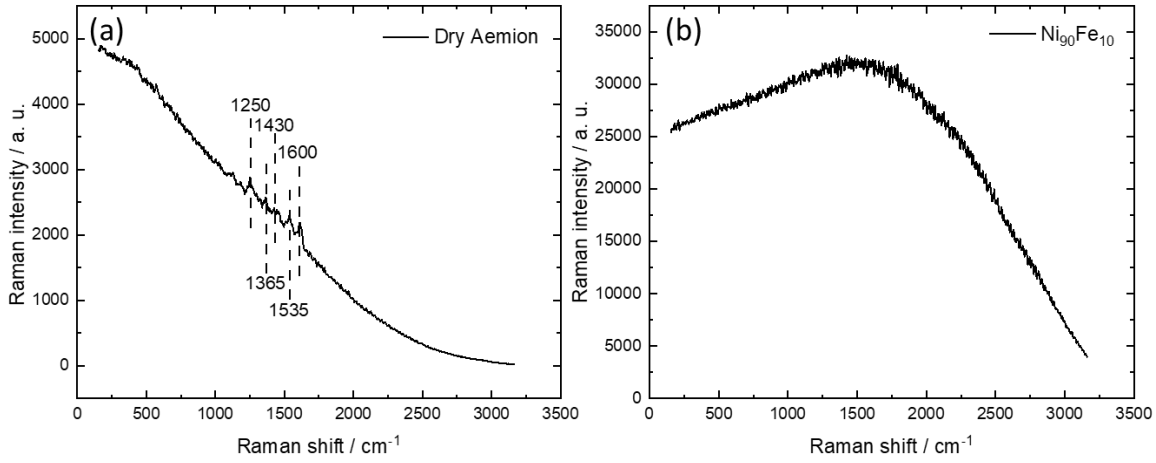

Figure F.19: Raman spectra of the as-prepared (a) dry Aemion^{TM} ionomer, and (b) $Ni_{90}Fe_{10}$ nanoparticles.

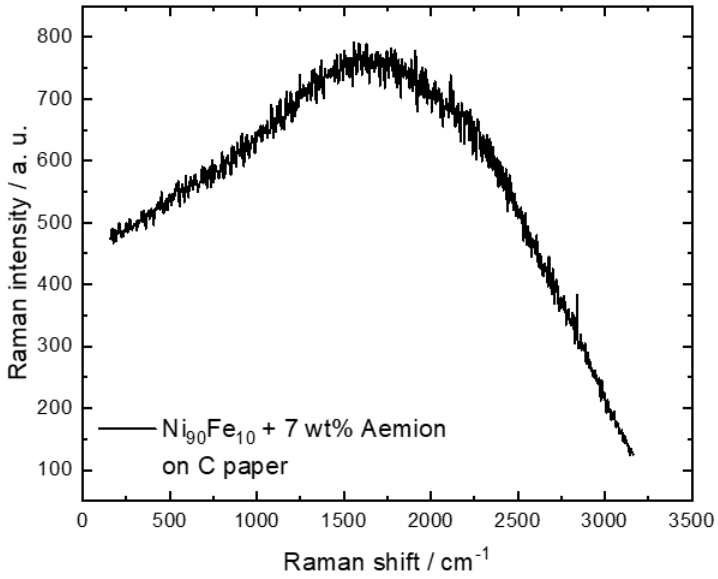

Figure F.20: Raman spectra of the $Ni_{90}Fe_{10}$ electrolysis anode with 7 wt% Aemion^{TM} scanned prior to electrolysis experiments.

To understand the spatial distribution of the two Raman spectra (Area 1 and Area 2) observed on the $Ni_{90}Fe_{10}$ anode with 7 wt% Aemion^{TM} post-electrolysis, Figure F.21 shows a

Raman spectral image, mapping the peak intensity at 530 cm^{-1} over a 150 x 150 µm area. Figure F.22 shows an overlay of the Raman mapping with a brightfield microscopy image of the $Ni_{90}Fe_{10}$ with 7 wt% Aemion^{TM} electrode surface.

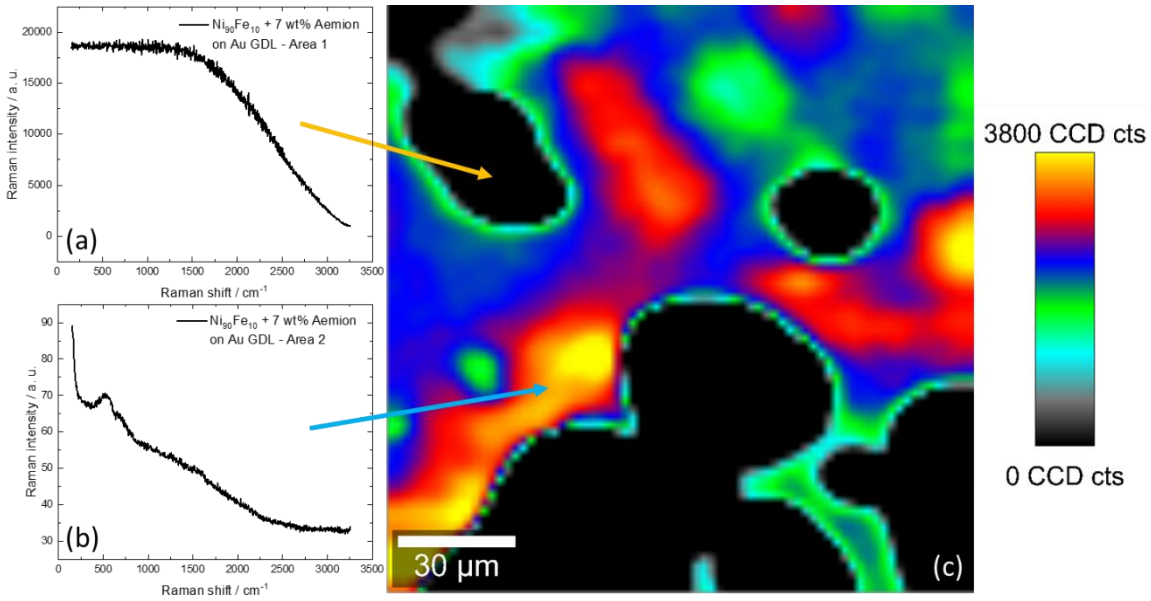

Figure F.21: Raman spectral image of the $Ni_{90}Fe_{10}$ electrolysis anode with 7 wt% Aemion^{TM} post-electrolysis testing showing the spatial distribution of the unmodified and modified areas (Area 1 and Area 2, respectively) achieved by mapping the peak intensity at 530 cm^{-1} (above the background noise) over a 150 x 150 µm area.

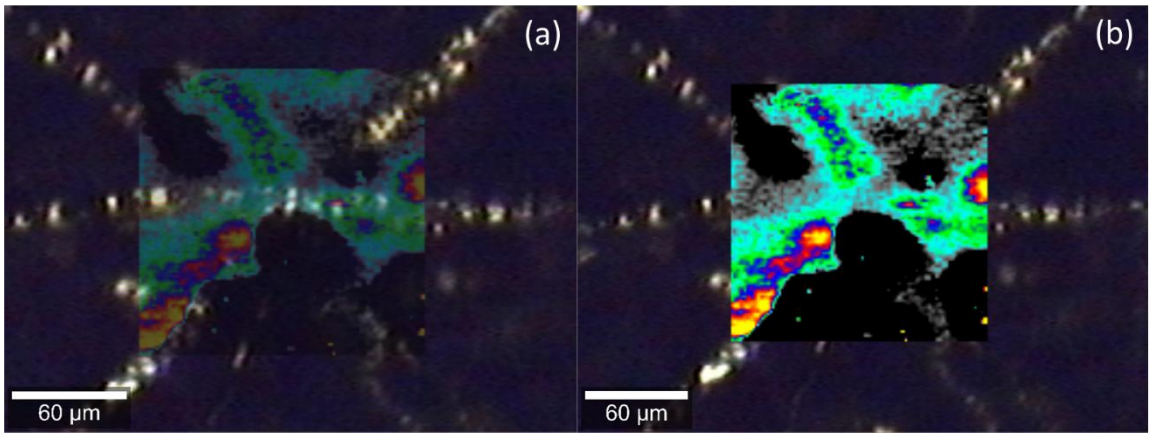

Figure F.22: Overlay of the Raman map of the $Ni_{90}Fe_{10}$ electrolysis anode with 7 wt% Aemion™ post-electrolysis testing in Figure F.21 with the corresponding brightfield microscope image of the sample. It is difficult to assign a 1:1 correspondence between the microscope image and the Raman map, however it appears the bright regions in the optical image correspond to regions where the 530 cm^{-1} vibrational mode is observed.

References

[1] E. Cossar, K. Agarwal, V. B. Nguyen, R. Safari, G. A. Botton, E. A. Baranova, *Electrocatalysis* **2021**.

[2] M. S. McGovern, E. C. Garnett, C. Rice, R. I. Masel, A. Wieckowski, *J. Power Sources* **2003**, *115*, 35.

[3] M. S. Wilson, S. Gottesfeld, *J. Electrochem. Soc.* **1992**, *139*, L28.

[4] B. Mayerhöfer, K. Ehelebe, F. D. Speck, M. Bierling, J. Bender, J. A. Kerres, K. J. J. Mayrhofer, S. Cherevko, R. Peach, S. Thiele, *J. Mater. Chem. A* **2021**, *9*, 14285.

[5] S. Koch, P. A. Heizmann, S. K. Kilian, B. Britton, S. Holdcroft, M. Breitwieser, S. Vierrath, *J. Mater. Chem. A* **2021**, *9*, 15744.

[6] S. A. Berlinger, B. D. McCloskey, A. Z. Weber, *ACS Energy Lett.* **2021**, *6*, 2275.

[7] S. A. Berlinger, S. Garg, A. Z. Weber, *Curr. Opin. Electrochem.* **2021**, *29*, 100744.

[8] C. Lei, F. Yang, N. Macauley, M. Spinetta, G. Purdy, J. Jankovic, D. A. Cullen, K. L. More, Y. S. Kim, H. Xu, *J. Electrochem. Soc.* **2021**, *168*, 044517.

[9] B. Bladergroen, H. Su, S. Pasupathi, V. Linkov, "Overview of Membrane Electrode Assembly Preparation Methods for Solid Polymer Electrolyte Electrolyzer," *Electrolysis*, **2012**.

[10] E. Cossar, A. O. Barnett, F. Seland, R. Safari, G. A. Botton, E. A. Baranova, *J. Power Sources* **2021**, *514*, 230563.

[11] J. E. Park, S. Y. Kang, S. H. Oh, J. K. Kim, M. S. Lim, C. Y. Ahn, Y. H. Cho, Y. E. Sung, *Electrochim. Acta* **2019**, *295*, 99.

[12] M. K. Cho, H. Park, S. Choe, S. J. Yoo, J. Y. Kim, H.-J. Kim, D. Henkensmeier, S. Y. Lee, Y. Sung, H. S. Park, J. Hyun Jang, *J. Power Sources* **2017**, *347*, 283.